Dissertation

SUBMITTED TO THE

Combined Faculty of Mathematics, Engineering and Natural Sciences

of Heidelberg University, Germany

FOR THE DEGREE OF

Doctor of Natural Sciences

PUT FORWARD BY

Eduard Jürgen Braun

BORN IN: **Homburg**

ORAL EXAMINATION: **04.02.2026**

Frustrated Magnetism and Localization in a Long-Range Interacting Spin System

---

Referees: Prof. Dr. Matthias Weidemüller
Prof. Dr. Markus Oberthaler

Abstract Frustration, bond disorder, and long-range interactions can produce novel, highly nontrivial phases of matter. This thesis investigates a bond-disordered, dipolar-interacting XY spin model, studied through both numerical simulations and experiments on a Rydberg quantum simulator. Three major results are achieved: (i) We analyze energetic-magnetic hysteresis in two disorder configurations, and find pronounced hysteresis in the strongly disordered configuration for low energies. This is a first experimental evidence of energetic-magnetic hysteresis in putative isolated glasses. (ii) We develop an extension of the generalized Kibble-Zurek mechanism for reverse quenches, which allows to characterize putative spin glass quantum phase transitions by global magnetization measurements. We validate this extension numerically exactly for one-dimensional systems, and subsequently experimentally extract a critical exponent consistent with spin glass critical exponents measured in other systems. This is a first tentative experimental evidence of a spin glass phase in an isolated dipolar interacting spin system. (iii) We studied time reversal on a Rydberg quantum simulator and showed numerically that, in bond-disordered power-law interacting models, time-reversal–based protocols reveal a localization mechanism distinct from conventional many-body localization at finite sizes.

Zusammenfassung Frustration, Kopplungsunordnung und langreichweitige Wechselwirkungen können neuartige, hochkomplexe Phasen der Materie erzeugen. Diese Arbeit untersucht ein kopplungsungeordnetes, dipolares XY-Spinmodell, das sowohl numerisch als auch experimentell auf einem Rydberg-Quantensimulator untersucht wurde. Drei zentrale Ergebnisse wurden erzielt: (i) Wir analysieren die energetisch-magnetische Hysterese in zwei Unordnungskonfigurationen und beobachten eine ausgeprägte Hysterese in der stark ungeordneten Konfiguration bei niedrigen Energien. Dies ist ein erster experimenteller Nachweis einer energetisch-magnetischen Hysterese in mutmaßlichen isolierten Gläsern. (ii) Wir entwickelen eine Erweiterung des verallgemeinerten Kibble-Zurek-Mechanismus für Rückwärts-Quenches, die es ermöglicht, mutmaßliche Spin-Glas-Quantenphasenübergänge mittels globaler Magnetisierungsmessungen zu charakterisieren. Wir validieren diese Erweiterung numerisch exakt für eindimensionale Systeme, und extrahieren anschließend experimentell einen kritischen Exponenten, der mit den in anderen Spingläsern gemessenen kritischen Exponenten konsistent ist. Dies liefert erste vorläufige experimentelle Hinweise auf eine Spinglasphase in einem isolierten dipolaren Spin-System. (iii) Wir untersuchten Zeitumkehr auf einer Rydberg-Quantensimulationsplattform und zeigten numerisch, dass zeitumkehrbasierte Protokolle in kopplungsungeordneten, nach Potenzgesetzen wechselwirkenden Modellen einen Lokalisierungsmechanismus aufdecken, der sich bei endlichen Systemgrößen von konventioneller Vielteilchenlokalisierung unterscheidet.

List of publications

This thesis is based on the following manuscripts and publications:

- **Observation of hysteresis in an isolated quantum system of disordered Heisenberg spins**
  Moritz Hornung*, Eduard J. Braun*, Sebastian Geier, Titus Franz, Gerhard Zürn, Matthias Weidemüller
  arXiv:2508.18197 **(Submitted)**

- **Universal Defect Statistics in Reverse Quenches**
  Eduard J. Braun, Daniel Rubin, Margaux Cartier, Gerhard Zürn and Matthias Weidemüller
  In preparation

- **Time-reversal in a dipolar quantum many-body spin system**
  Sebastian Geier, Adrian Braemer, Eduard Braun, Maximilian Müllenbach, Titus Franz, Martin Gärttner, Gerhard Zürn and Matthias Weidemüller
  Phys. Rev. Research 6, 033197 (2024)

- Time-Reversal Signatures of Bond-Disordered Algebraic Localization in an Isolated Quantum Spin Chain
  Eduard J. Braun, Matthias Lotze, Gerhard Zürn and Matthias Weidemüller
  In preparation

The author further contributed to the following manuscripts and publications:

- **Observation of anisotropy-independent magnetization dynamics in spatially disordered Heisenberg spin systems**
  T. Franz*, S. Geier*, C. Hainaut, A. Braemer, N. Thaicharoen, M. Hornung, E. Braun, M. Gärttner, G. Zürn and M. Weidemüller 1
  Phys. Rev. Research 6, 033131 (2024)

- **Efficient and Accurate Calculation of Rydberg Interactions and Its Implementation in the *PairInteraction* Software**
  Johannes Mögerle, ..., Eduard J. Braun et. al.
  In preparation

* These authors contributed equally.

Contents

CHAPTER 1

Introduction

Competing constraints shape both our everyday decisions and the behavior of complex systems. Politicians must negotiate priorities that may conflict, financial markets must balance risk and reward, and project management must reconcile precision and speed. In all these cases, no solution can fully satisfy every requirement, often resulting in multiple nearly optimal, and sometimes unexpected outcomes. This idea that competing constraints produce rich, sometimes unexpected behavior extends also to physical systems, where interactions between components can similarly compete, preventing the system from finding a single energy-minimizing configuration. Understanding how these different configurations organize and emerge is thus of general importance in the study of complex systems.

In magnetism, competing constraints arise when the geometry of bonds creates spin–spin interactions that cannot all be simultaneously satisfied, a phenomenon known as magnetic frustration [1, 2]. Frustrated systems often exhibit unusual low-temperature behavior and complex collective phenomena that are qualitatively distinct from those of ordered matter. For instance, classical spin liquids can host low-energy excitations associated with emergent gauge fields [3, 4]. Beyond their fundamental interest, their quantum mechanical counterparts, quantum spin liquids [5, 6], feature also the possibility for topological quantum computing [7].

When magnetic frustration is combined with disorder, often an unusual magnetic state known as the spin glass phase emerges at low temperatures [8–11]. In this phase, individual spins freeze in a fixed but random orientation below a critical temperature. Experimentally, spin glasses are typically identified by thermomagnetic hysteresis [10, 12] and by slow, history-dependent relaxation phenomena, commonly referred to as aging, memory, and rejuvenation effects [13–15]. This slow relaxation, which in some cases even exceeds a month [12], means that all investigation of the spin glass phase

study out-of-equilibrium physics. Remarkably, they share very similar characteristics despite this. Several theoretical frameworks have been proposed to explain these behaviors. The most influential are the infinite-range replica-symmetry-breaking solution [16] and the droplet model [17, 18], which differ mainly in the prediction of the presence the absence or the absence of the spin glass phase at a finite magnetic field. Apart from their importance for fundamental science, quantum spin glasses have also been proposed as passive quantum memory devices [19].

As matter is typically electrically neutral and magnetic monopoles do not exist, the strongest long-range electric or magnetic interactions naturally realized are dipolar. As a result, dipole-dipole interactions play an important role in several quantum simulation platforms, such as NV centers in diamond [20–22], polar molecules [23–26], and Rydberg atoms [27–30]. In condensed matter systems, an important example of a dipolar interacting system is the diluted rare-earth compound $\mathrm{Li\,Ho}_x\,\mathrm{Y}_{1-x}\mathrm{F}_4$, which realizes a dipolar Ising spin glass [31]. At intermediate dilution ($x = 16.7\,\%$), a spin glass phase is experimentally well established [32]. However, at strong dilution ($x = 4.5\,\%$), the nature of the low-temperature phase remains debated, with evidence pointing either toward a spin glass or a spin liquid-like regime [33–38]. Moreover, the dynamics accelerate drastically in the presence of a transverse magnetic field, raising the question of whether the spin glass phase persists at finite transverse fields [39–41]. Because such a field introduces quantum fluctuations, it is an open challenge to fully understand the interplay of quantum fluctuations and dipolar interaction in putative spin glass systems.

In a related direction, a strongly disordered three dimensional dipolar-interacting Heisenberg XY model, realized on a Rydberg quantum simulation platform, was recently shown to exhibit slow, glassy relaxation [42] and an apparent absence of thermal equilibration on experimental timescales [43]. These findings demonstrate that isolated dipolar-interacting quantum systems can display highly nontrivial dynamics, similar to expectation from spin glasses. This motivates the central question of this thesis

What is the nature of a bond-disordered, long-range interacting isolated spin system?

In this thesis, we address this question from two complementary perspectives. First, we investigate whether the system displays signatures typically associated with spin glass behavior. Motivated by established protocols used to characterize thermomagnetic hysteresis in spin glasses [10, 12], we introduce analogous methods to probe energetic–magnetic hysteresis in an isolated quantum system and implement these protocols on our Rydberg quantum simulation platform. In addition, we develop a theoretical framework based on the Kibble–Zurek mechanism [44] that enables the

extraction of critical behavior using only global magnetization measurements. We validate this framework for one-dimensional spin systems and subsequently apply it to experimentally investigate the three-dimensional dipolar XY model on the possibility of a magnetic-field-dependent spin glass transition.

Second, motivated by numerical studies demonstrating that spin glass phases also feature many-body localization at finite system sizes [45–47], we explore the emergence of localization phenomena in long-range, disordered spin systems. Building upon our recent implementation of a time-reversal protocol on the Rydberg platform [48], we numerically analyze how different time-reversal based protocols can be used to experimentally detect localization in a toy model with power law interactions.

This thesis is structured as follows:

- In *Chapter 2* we review the key concepts, experimental results, and theoretical frameworks relevant to this thesis. This chapter distills the open questions on dipolar spin glasses and many body localization in systems with power law interactions, setting the stage for the research presented in following chapters.

- In *Chapter 3*, we investigate energetic-magnetic hysteresis in a three-dimensional dipolar-interacting Heisenberg XY model. We first explain how this Hamiltonian is realized on a Rydberg platform. We then introduce two new experimental protocols, zero-field annealing and field annealing, and implement them to characterize the system's response to different energy and magnetic field histories.

- In *Chapter 4*, we extend the generalized Kibble-Zurek mechanism to reverse quench protocols and verify it for both uniform and disordered one-dimensional transverse-field Ising models. We then implement the reverse quench protocol on our Rydberg simulation platform to investigate potential critical spin glass behavior in the dipolar-disordered Heisenberg XY model.

- In *Chapter 5*, we first discuss how time can be effectively reversed on our Rydberg quantum simulation platform and how potential experimental imperfections may be further improved. We then study three time-reversal-based protocols, the Loschmidt echo, the fidelity OTOC, and the magnetization OTOC, to characterize localization on a bond-disordered power law interacting toy model. We compare our observed localization properties with those of other known localized systems.

- In *Chapter 6*, we propose two directions to further probe glassy behavior using our Rydberg simulation platform. First, we briefly introduce the concepts of

aging, rejuvenation, and memory effects in spin glasses, and propose experimental protocols to investigate these phenomena in an isolated spin system. In addition, we evaluate wheter such an implementation might benefit from the measurement of ac susceptibilities. Second, we discuss how a dipolar Ising model, rather than the XY model, could be realized on the Rydberg platform, enabling direct comparison with results in $LiHo_xY_{1-x}F_4$.

- In *Chapter 7*, we conclude the work presented in this thesis, organizing the discussion around the open questions introduced in Chapter 2.

If not stated otherwise, all fits in this thesis have been based on the library *LMFIT* [49], and all plots of numerical or experimental data have been producing using the library *matplotlib*. The authors acknowledge support by the state of Baden-Württemberg through bwHPC and the German Research Foundation (DFG) through grant INST 35/1597-1 FUGG, where the cluster Helix was used for the simulations in Chapters 4 and 5. The AI language model ChatGPT (GPT-5, mini) was used occasionally to support textual editing and to improve grammar, clarity, and style. Its use did not affect the scientific content, methodology, analysis, or conclusions of this thesis.

CHAPTER 2

Concepts in Disordered Magnetism

2.1 Phases of frustrated magnetism

Geometric frustration arises when spin interactions are mutually incompatible, preventing the system from settling into a simple ordered ground state. Instead, typically a large number of nearly degenerate low-energy configurations emerge. Understanding the structure and dynamics between these states is an important aim of this thesis, which focuses on a frustrated magnet with long-range interactions.

To provide the necessary theoretical background, this chapter reviews the most relevant frustrated phases: spin liquids, spin ice, the random singlet phase, and spin glasses. While all of these phases lack conventional long-range magnetic order, they differ in their ground state properties and elementary excitations. This diversity poses a significant challenge to developing a unified framework for how microscopic frustration leads to emergent complex macroscopic behavior.

Beyond their fundamental importance, these phases are also of interest for quantum technologies such as topological quantum computing [7] and passive quantum memories [19], because of their potential to host robust and perturbation-resistant quantum states.

This chapter thus sets the stage for the central question of the thesis:

What is the nature of a bond-disordered, long-range interacting isolated spin system?

2.1.1 Spin liquids, spin ice and the random singlet phase

We begin with the simplest case of magnetic frustration: antiferromagnetically interacting classical Ising spins on an equilateral triangle. This small system captures

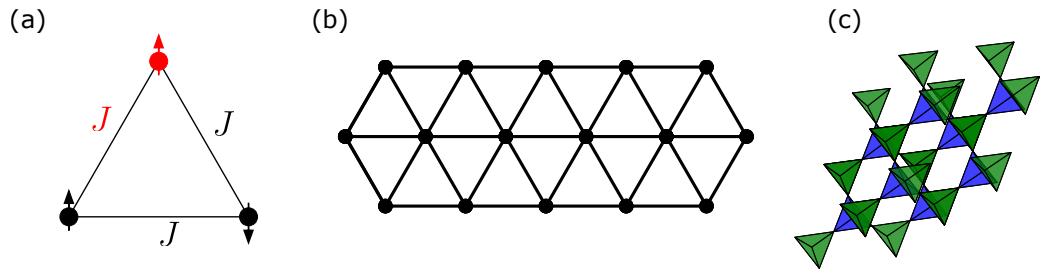

Figure 2.1: *Frustration leading to classical spin liquids.* (a) Ising spins with antiferromagnetic couplings at the vertices of a triangle. The red spin violates the geometric constraints imposed by the two black ones. The violating edge is highlighted by a red coupling constant. (b) Triangular lattice. Edges represent antiferromagnetic coupling, vertices spin positions (c) The pyrochlore lattice. The pyrochlore lattice can be viewed as consisting of two sublattices (blue and green) of tetrahedrons of equal orientation. Spins sit at the vertices of the individual tetrahedrons.

the essential physics of competing interactions. The classical Hamiltonian governing the system is

$$H = J\left(S_1S_2 + S_2S_3 + S_3S_1\right), \tag{2.1}$$

where $J > 0$ is the coupling constant and $S_i = \pm 1$ describes the classical spin state. For every edge of the triangle, the total energy is reduced when the spins on the same edge are antialigned. As can be seen in Fig. 2.1(a), when we choose two spins on one edge to fulfill this condition, the third spin cannot lower the energy on both remaining edges. In this example, the lowest energy constraint is violated on the left edge. The total energy of this state is $-J - J + J = -J$. Of the total $2^3 = 8$ configurations, all 2-up-1-down and 2-down-1-up configurations share this energy. As a consequence, the system hosts a sixfold degenerate ground state.

Classical Spin Liquids

When the single triangle is extended into a two-dimensional triangular lattice, the ground state degeneracy becomes extensive, scaling exponentially in the number of spins. This was first demonstrated by Wannier in 1950 [50] and has since become a textbook example of geometric frustration [1, 2]. Approximately a third of the spins necessarily always violate the local antiferromagnetic constraint, resulting in a macroscopically large set of degenerate ground states. Most of these configurations are highly disordered and lack long-range magnetic order despite strong local (antiferromagnetic) correlations. The continuous fluctuations among these disordered

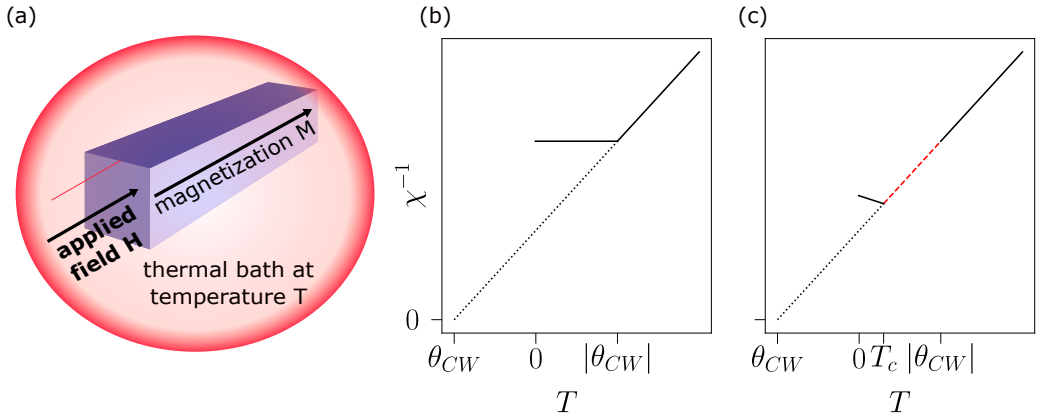

Figure 2.2: *Susceptibility measurements in frustrated systems.* (a) Schematic of a susceptibility measurement. Arrows indicate the applied and measured magnetic fields. The thermal bath surrounding the sample (blue box) is represented by a red sphere. (b) Inverse susceptibility as a function of temperature for an antiferromagnet. The solid line shows the expected susceptibility. The dotted line extends the Curie-Weiss law down to its intersection with the zero inverse-susceptibility line, defining the Curie-Weiss temperature. (c) Inverse susceptibility as a function of temperature for a classical spin liquid. The solid line indicates the expected susceptibility. The dotted line represents the extension of the Curie-Weiss law to the Curie-Weiss temperature. The red dashed line illustrates that the susceptibility continues to follow the Curie-Weiss law below the Curie-Weiss temperature.

states, reminiscent of molecular motion in a liquid, led to the classification of the system as a classical spin liquid (CSL). As a result, the system retains a finite entropy even at zero temperature. This appears to violate Nernst's theorem, which requires entropy to vanish in the zero-temperature limit. In practice, however, such a violation is avoided: real materials inevitably experience small perturbations, such as further-neighbor interactions, that lift the degeneracy and restore consistency with classical thermodynamics.

These classical spin liquids also share an interesting experimental phenomenology. Typically, as depicted in Fig. 2.2 (a), the inverse equilibrium susceptibility χ^{-1} is measured as a function of temperature. The susceptibility describes the build-up of magnetization M in a material as a function of an applied magnetic field H, i.e. $\chi = \frac{dM}{dH}$. For magnetic materials in their paramagnetic regime, mean-field theory

predicts that the susceptibility follows an inverse temperature scaling:

$$\chi = \frac{C}{T - \theta_{CW}}, \tag{2.2}$$

where C is the material-dependent Curie constant, and θ_{CW} is the Curie-Weiss temperature. For antiferromagnetic systems, θ_{CW} is negative. Mean-field theory is expected to fail at temperatures on the order of $|\theta_{CW}|$ [51]. In Figs. 2.2(b) and (c), we compare the susceptibilities between an antiferromagnet and a CSL. In the antiferromagnet, the susceptibilities follow the Curie-Weiss law from high temperatures to $|\theta_{CW}|$, which in this case is also the critical temperature T_c for a phase transition. On the other hand, in the CLS, the system follows the Curie-Weiss law well below $|\theta_{CW}|$, and the eventual critical temperature to an ordered state is $T_c \ll |\theta_{CW}|$. In this intermediate regime $T_c < T < |\theta_{CW}|$, the system still looks like a paramagnet, that is, follows the Curie-Weiss law, but since the temperature is lower than the typical spin-spin interaction energy scales in the system that determine θ_{CW}, local correlations arise. As a consequence, classical spin liquids are sometimes also dubbed cooperative paramagnets. At this point, we want to emphasize that this behavior in the susceptibility is not unique only to classical spin liquids, but commonly found in frustrated magnetic systems. The smoking gun for classical spin liquids lies in the existence of extensively many degenerate ground states. Despite extensive research, classical spin liquids (CSLs) remain difficult to classify and characterize within a single unified theoretical framework. This challenge stems from the broad variety of lattice structures, interaction types, and the discrete nature of classcial spins [3, 4].

Spin Ice

Spin ice is a prominent example of a classical spin liquid realized in the pyrochlore lattice, as illustrated in Fig. 2.1(c) and thoroughly reviewed in Refs. [52, 53]. This lattice geometry is notably the same as that on which protons are arranged in water ice. Unlike lower-dimensional systems, where reduced connectivity enforces stronger local constraints, spin ice is distinguished as one of the rare classical spin liquid phases naturally occurring in three-dimensional materials. Under antiferromagnetic boundary conditions, the energy of each tetrahedron in the pyrochlore lattice is minimized when the spins point either inward toward the center of the tetrahedron or outward. If one spin points inward, the others must point outward to minimize energy, and vice versa. Since it is impossible for all four spins in a tetrahedron to simultaneously satisfy these opposing orientations, the ground state is characterized by the "ice rules": exactly two spins point inward and two outward per tetrahedron. These local constraints give

the system a topological character, giving rise to emergent fractional excitations that manifest in the spin ice as magnetic monopoles. The term "fractionalized" reflects the fact that, although the fundamental physical excitation is a complete magnetic dipole, the lattice constraints enable the emergence of quasiparticles that behave as fractions of this excitation, which are isolated magnetic monopoles in this case. Inspired by these discoveries, so-called artificial spin ice systems have been engineered, both in two and three dimensions, at the nanoscale to implement tailored ice-rule-like constraints. These systems similarly exhibit extensive ground-state degeneracy and support a variety of emergent fractional excitations [54–57]. Importantly, the local constraints that produce these fractional excitations closely resemble the gauge conditions fundamental to lattice gauge theories, establishing a conceptual framework that will be central in the subsequent discussion of quantum spin liquids (QSLs).

Quantum Spin Liquids

Until now, the discussion has remained within the framework of classical mechanics. However, already in 1973, P. W. Anderson posed a pivotal question: What is the effect of quantum fluctuations in frustrated magnetic systems? In his seminal work [58], he proposed that for the antiferromagnetic triangular lattice, the ground state could be a novel quantum state, namely the resonating valence bond (RVB) state, illustrated in Fig. 2.3(a). In this picture, the system forms singlet pairs of spins, referred to as dimers, which locally satisfy the antiferromagnetic exchange constraint. The true ground state, Anderson suggested, is not a static arrangement of dimers, but rather a quantum superposition of many such configurations, giving rise to long-range quantum entanglement.

Analogous to the CSL, where no magnetic ordering occurs even at zero temperature, the RVB state preserves full spin-rotation symmetry and no ordering due to spontaneous symmetry breaking occurs. This absence of conventional order, combined with the long-range entanglement in the ground state, defines a new phase of matter known as a quantum spin liquid (QSL). A rigorous proof for such a state on a triangular lattice was later provided by Moessner and Sondhi in 2001 [59].

The long-range entanglement inherent in QSLs stands in stark contrast to conventional ordered magnetic phases. In the latter, the ground state is typically characterized by a local order parameter which can be calculated from the orientation or magnitude of individual spins. Measurement of such an order parameter thus requires commuting local spin observables, which is incompatible with the long-range entanglement structure of spin liquids. Consequently, QSLs represent a qualitatively distinct class of quantum ground states [5, 6].

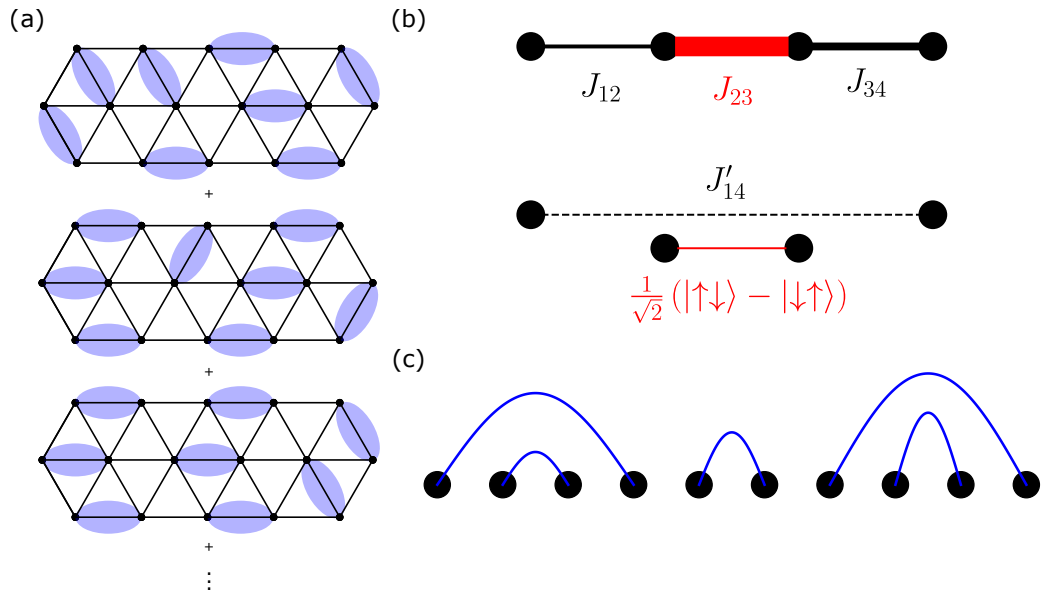

Figure 2.3: *Quantum spin liquid and random singlet phase ground states.* (a) Resonating valence bond state. The triangular lattice is covered by nearest-neighbor spin-singlet bonds (blue shaded ellipses). (b) Sketch of the elimination of a strongly interacting bond to approach the ground state of the random singlet phase. Black circles represent spins, and lines Heisenberg interaction between these spins. Bond thickness correspond to coupling strength. Red color highlights strongest bond $J_{23} \gg J_{12}, J_{23}$. Dotted line represents effective new coupling between spins 1 and 4. Spins 2 and 3 form a spin singlet. (c) Random singlet phase ground state. The system falls into pairs of singlets (pairs marked by blue connecting lines). Note that the lines do not cross.

Nonetheless, as in the case of CSLs, a key challenge remains: how can quantum spin liquids be systematically classified? What physical mechanisms give rise to such highly entangled ground states? Despite the diverse phenomenology of QSLs, including gapped and gapless variants, and the presence or absence of well-defined quasiparticle excitations, many can be described in terms of emergent local gauge fields arising from spin interactions, where local gauge constraints are reminiscent of the "ice rules" in classical spin ice. This emergent gauge structure enables a classification of QSLs based on the symmetry of the associated gauge field [60]. For example, when the effective field is governed by an Ising-like interaction, the emergent gauge symmetry is $\mathbb{Z}_2$, leading to the so-called $\mathbb{Z}_2$ spin liquid. Notably, experimental realization of such a phase was only recently achieved on a Kagome lattice system [7].

Despite all the theoretical advances, it remains an open and active area of research whether QSLs can be reliably identified in natural materials, and more fundamentally, what would be a definitive diagnostic for quantum spin liquids, as most experimental signatures are not unique and can in principle result from extrinsic or unrelated phenomena [61, 62].

Random Singlet Phase

Unto this point, we only discussed the effect of geometric frustration. Another interesting phase can also arise when the system is not frustrated, but only disordered. The initial studies of strongly disordered one-dimensional antiferromagnets were performed by Dasgupta and Ma [63] and Bhatt and Lee [64] in the early 1980s. Fisher later successfully applied these methods to different nearest-neighbor XXZ spin chains [65], and by now the random singlet phase (RSP) and its properties are well known and reviewed [66]. The RSP is often called spin-liquid like, as it shares the partition into singlets from the RVB state known from the QSL.

To get an intuitive picture, we study the random singlet phase in a strongly bond-disordered one-dimensional spin-1/2 Heisenberg antiferromagnet. A subsystem of such a long range 1D chain is depicted in Fig. 2.3(b). This subsystem follows the Hamiltonian

$$H = J_{12}\vec{S_1}\vec{S_2} + J_{23}\vec{S_2}\vec{S_3} + J_{34}\vec{S_3}\vec{S_4}. \tag{2.3}$$

Here, $\vec{S_i}$ denotes the vectorial spin-1/2 operator acting on spin i. We assume that all couplings are positive and that the system is so strongly disordered, such that one coupling is way larger than all the other couplings. In this example, we assume $J_{23} \gg J_{12}, J_{34}$. In this case, we can simplify the Hamiltonian as

$$\begin{aligned} H &= H_0 + H' \\ &= J_{23}\vec{S_2}\vec{S_3} + \left(J_{12}\vec{S_1}\vec{S_2} + J_{34}\vec{S_3}\vec{S_4}\right). \end{aligned} \tag{2.4}$$

The ground state of H_0 is the spin singlet of $\vec{S_2} + \vec{S_3}$ with energy $-3/4J_{23}$, which can be written as

$$|\Psi_{\text{singlet}}\rangle = \frac{|\uparrow\downarrow\rangle - |\downarrow\uparrow\rangle}{\sqrt{2}}, \tag{2.5}$$

where $|ab\rangle$ denotes a state in the product basis such that spin 2 is in the state $|a\rangle$ and spin 3 in the state $|b\rangle$. The states $|\uparrow\rangle$ and $|\downarrow\rangle$ on site i are the eigenstates to the eigenvalues $1/2$ and $-1/2$ of the z-component of $\vec{S_i}$, respectively.

In Eq. 2.3 we can interpret H' as a perturbation to H_0. As a consequence, the ground state energy in second order perturbation theory reads

$$E_{\text{gs}} = -\frac{3}{4}J_{23} + \langle \Psi_{\text{singlet}}|H'|\Psi_{\text{singlet}}\rangle + \sum_{|t\rangle\in\mathcal{T}} \frac{|\langle \Psi_{\text{singlet}}|H'|t\rangle|^2}{\frac{J_{23}}{4} - (-\frac{3J_{23}}{4})}, \tag{2.6}$$

where $\mathcal{T}$ denotes the set of all triplet states of $\vec{S}_2 + \vec{S}_3$. If we treat Eq. 2.6 as an operator equation putting an identity operator on all scalar quantities, we obtain a new form

$$E_{\text{gs}} = -\frac{3}{4}J_{23} - \frac{3}{16}\frac{J_{12}^2 + J_{34}^2}{J_{23}} + J'_{14}\vec{S}_1\vec{S}_4. \tag{2.7}$$

As a consequence, we can assume for the detection of the ground state of the system, that the pair $2 \longleftrightarrow 3$ form a singlet which is now taken out of the chain, and the 1D chain connects know spins 1 and 4 with the new coupling $J'_{14} = \frac{J_{12}J_{34}}{2J_{23}}$, which is still positive. In the limit of strong disorder, this step can now be repeated with the strongest coupling in the remaining chain. As a consequence, the ground state will decompose into non-interacting, fixed singlet pairs [67], as we depict in Fig. 2.3(c). Even though most spins will pair with their nearest neighbor, there are also spins that pair with a spin that can be arbitrarily far away. As such, disorder gives rise to a freezing of the ground state in singlet pairs, without the fluctuations we have reviewed in classical and quantum spin liquids.

2.1.2 Spin glasses

As discussed in the previous section, frustration alone typically induces strong fluctuations and a high degree of degeneracy, whereas disorder alone can lead to the local freezing of spin pairs. When combined, these two ingredients give rise to a new phase: the spin glass, which has recently been reviewed in multiple publications [9–11]. Remarkably, microscopically very different systems exhibit very similar behavior, provided both frustration and disorder are present. This observation motivates the definition of a spin glass phase:

> "A spin glass is a random mixed-interacting system characterized by a random, yet cooperative, freezing of spins at a well-defined temperature T_{f}, below which a highly irreversible metastable frozen state occurs without the usual long-range spatial magnetic order." [8]

While this definition offers a solid theoretical basis, it does not directly translate into measurable observables. We therefore begin this review by briefly reviewing

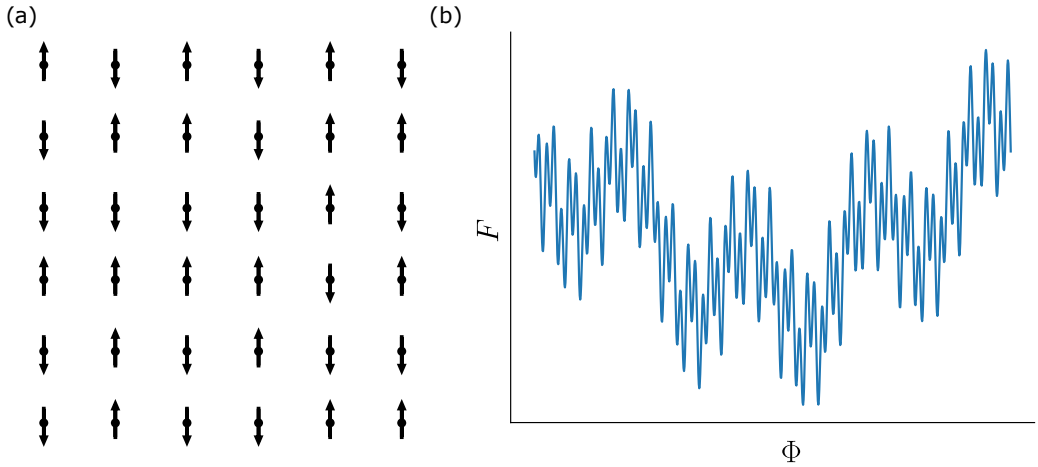

Figure 2.4: *Intuitive picture of a spin glass phase.* (a) Sketch of an Ising spin glass. Each magnetic moment points randomly either upwards or downwards. The position is frozen due to the interaction with neighboring spins. (b) Free energy F as a function of configuration Φ. The free energy landscape is rugged, but a hierarchical structure is visible.

the two leading theoretical frameworks proposed to explain spin glass behavior: the replica symmetry breaking (RSB) mean-field theory [16] and the droplet scaling picture [17, 18]. Subsequently, we summarize the key experimental signatures of spin glasses, which are also nicely reviewed in Ref. [12]. This sets the stage for a central question of this work:

Does a dipolar-interacting, isolated Heisenberg spin system host a spin glass phase?

After that, we consider a dipolar Ising spin glass, which is most closely related to the one studied in this thesis, and which reveals intriguing connections to the quantum spin liquid phase.

Theoretical models

As mentioned earlier, in spin glasses individual magnetic moments are frozen in a certain, fixed direction, but their direction is random, as sketched for the Ising case in Fig. 2.4(a). Intuitively, such a freezing without long-range order should be due to a large energy barrier preventing each single spin from flipping to a possibly energetically better configuration that lowers the total free energy. Thinking in a mean-field picture, this is the idea behind the Parisi mean field solution [16, 68].

In this theory, which is proven exactly for an infinite dimensional system, the free energy landscape is rugged, as sketched in Fig. 2.4(b), but a hierarchy of energy valleys is present, mathematically expressed in the notion of ultrametricity. When the system is falls into a local minimum, it has to overcome very high energy barriers to reach the next minimum, which leads to very slow glassy dynamics. Moreover, in the thermodynamic limit, the Parisi mean-field solution predicts a continuum of multiple equilibrium states, which are separated by infinitely high energy barriers. The upper critical dimension of this solution, defined as the lowest dimension where mean-field theory describes the system accurately up to logarithmic corrections, is $D_u \geq 8$ at zero temperature and $D_u \geq 6$ for finite-temperature models [69]. As such it is even today, more than 50 years after the initial publication, debated to which extent it is applicable to finite dimensional systems.

Fisher and Huse challenged this picture of multiple equilibria, and proposed instead a droplet-scaling model [17, 18]. In their model, the spin glass has only two true equilibria, like the Ising ferromagnet, which are related by the symmetry of the Hamiltonian. When the system falls into one of the two equilibria, its excitations are droplets of spin clusters of size L that flip simultaneously. However, the energy of this excitation scales as a power law in the droplet size L^θ, which makes large droplets very unlikely, and thus the system adapts only slowly to perturbations.

The TNT (trivial non-trivial) model, developed by Krzakala and Martin [70] and Palassini and Young [71] as well as the chaotic pair model [72] try to combine aspects of these models, as is nicely reviewed in Ref. [73]. They all share the idea of only two ground states, but they differ in the nature of the excitations. Even though tremendous numerical progress was established, the question of which model describes the spin glass phase best is still unresolved, as finite size effects persists even up to large system sizes [74]. Even though ultrametricity and replica symmetry breaking have been recently measured in a small cavity system [75], large scale simulations suggest that replica symmetry breaking might be only an effect visible for small system sizes [76]. So far, the most promising experimental signature to distinguish at least the RSB and droplet-scaling picture is a measurement of a spin glass phase in presence of a finite magnetic field.

In quantum systems on expander graphs, properties which are impossible to produce in finite dimensional systems can emerge. Here, it was shown that even in an isolated quantum system, an extensive number of local topologically protected ground states exists, but similar to the droplet scaling picture, excitations from these ground states show a strong scaling in size, relying on a finite energy density to be excited [19, 77]. As a consequence, it is an open question whether the models so far also well suited to describe possible quantum spin glasses at zero temperature, or

whether a change in paradigm will be needed.

Determining the transition temperature

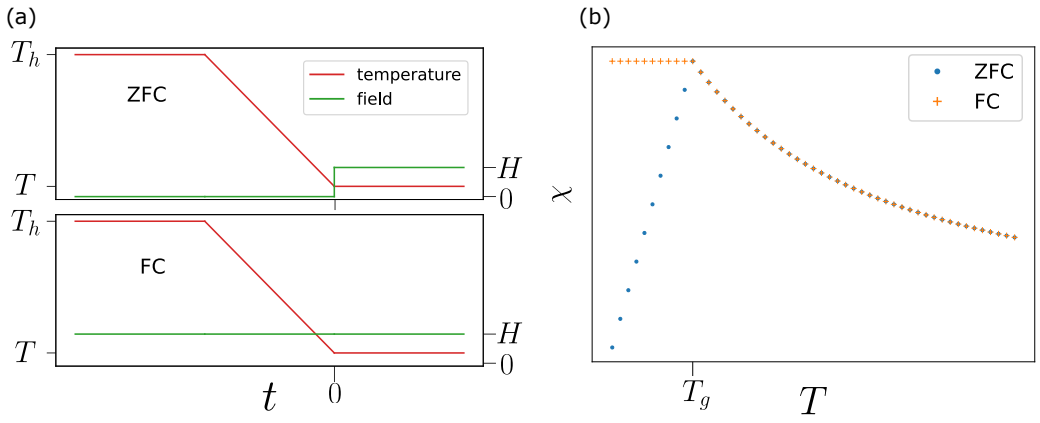

Figure 2.5: *Thermomagnetism in spin glasses.* (a) Time-dependence of the temperature (red, left axis) and magnetic field (green, right axis) curves both in the ZFC (top) and FC(bottom) protocols. The system is always prepared at a high temperature T_h and cooled down to a finite temperature T. Dependent on the protocol, at some time a finite field H is applied. (b) ZFC and FC susceptibilities χ as a function of temperature T. Typically a bifurcation at temperature T_g is observed, which is an estimate of the spin glass transition temperature.

One of the first experiments in spin glass systems was the measurement of susceptibilities [78]. A susceptibility is measured by applying a magnetic field H to a probe, which causes a build-up of a magnetization M. The linear susceptibility χ is defined as the derivative of the build-up magnetization with respect to the applied field $\chi = dM/dH$. An outstanding result was that below the freezing transition temperature T_f, the system shows strong signatures of hysteresis, in the sense that the magnetization M measured at a temperature T in an applied field H depends on the history of the system. Over time, two standard protocols, sketched in Fig. 2.5 developed to characterize thermomagnetic hysteresis in different materials. In both protocols, the material is prepared in its paramagnetic phase at high initial temperature T_h, where no hysteresis effects are present. In the zero-field cooled (ZFC) protocol, the material is cooled down to its final temperature. After that, a magnetic field H is applied, and the magnetization is measured. In the field cooled (FC) case, the field is first applied, and the material is cooled down in the presence of

this field. Dividing the measured magnetizations by the applied field gives the ZFC and FC susceptibilities. A bifurcation between them indicates hysteresis, and the temperature at which they bifurcate gives an upper estimate for the glass transition temperature T_g, and shows the onset of irreversibility in the system [79]. Initially, it was believed that a splitting between the ZFC and FC susceptibilities, as sketched in Fig. 2.5(b) is a hallmark of the spin glass phase [80]. This was even further established as in terms of the Parisi mean field solution of spin glasses [16, 68], this splitting can be related to replica symmetry breaking. However, recent progress in the construction of high precision detectors and nanofabrication techniques showed that such a bifurcation is also observed in ferro- and ferrimagnetic systems [81, 82] as well as in ensembles of nanoparticles [83–85], where this phenomenon is related to coercivity and crystalline anisotropy in the lattice structure. Also in spin glasses, it is still an open question how accurately the onset of bifurcation is estimating the glass transition temperature, which was only recently investigated in comparison with other methods [86]. Nonetheless, the observation of this bifurcation effect remains a necessary condition for spin glass behavior, and one of the most important effects observed in these systems.

Typically, the ZFC magnetization has a strong time dependence, while the FC magnetization is nearly constant [79, 80]. This is usually explained as the ZFC state being quenched to a temperature below the glass transition and thus evolving to its true equilibrium state, while the FC state could already align to the applied field during the cooling procedure, and is thus an equilibrium state. This picture was challenged by recent experiments [87, 88], and thus it is still an open question what exactly is the microscopic reason for this macroscopic bifurcation. Even more so, as cooling is a crucial ingredient in these protocols, the question arises

How can thermomagnetic hysteresis protocols be adapted to isolated quantum systems?

Measuring critical exponents

One of the most important techniques to characterize spin glasses [12], and magnetic systems in general [89], are AC susceptibility measurements, which will be crucial to establish the spin glass as a thermodynamic phase, in the sense that it can be identified by a set of critical exponents. For the measurement of an AC susceptibility at frequency f, the magnetic field H is time dependent, i.e. $H(t) = H\cos(2\pi ft)$. As a consequence, the response of the system at this frequency is $M(t) = M'\cos(2\pi ft) + M''\sin(2\pi ft)$,

so two different susceptibilities can be defined:

$$\chi' = \frac{dM'}{dH} \tag{2.8}$$

is the in-phase susceptibility, and

$$\chi'' = \frac{dM''}{dH} \tag{2.9}$$

is the out-of-phase susceptibility, which in solids is typically related to absorption or dissipation. The first measurement of an AC susceptibility in a spin glass was

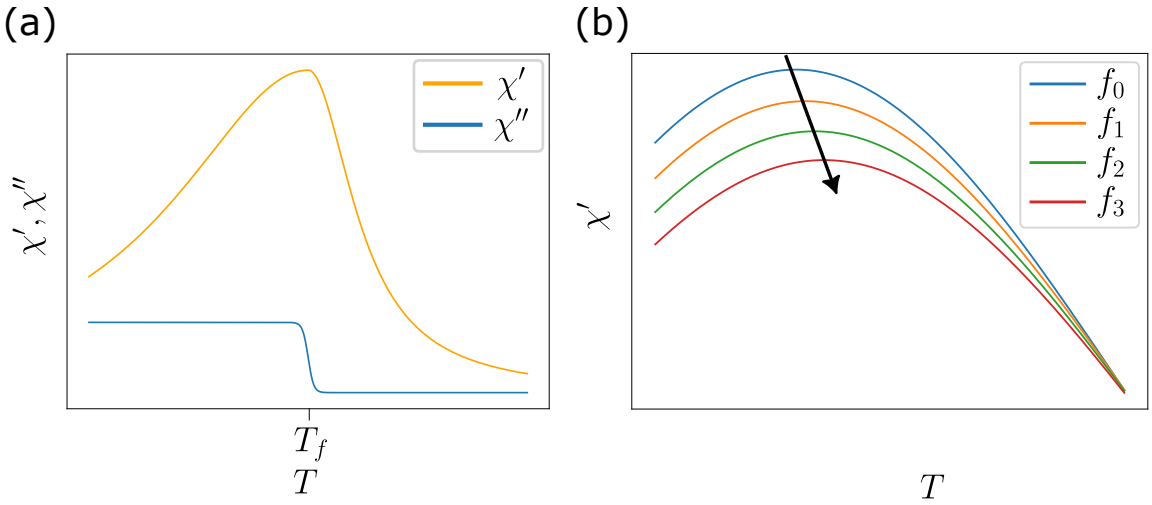

Figure 2.6: *Sketch of AC susceptibility measurements in spin glasses.* (a) In-phase (χ') and out-of phase (χ'') susceptibilities as a function of temperature T. The peak in χ' marks the freezing temperature T_f. (b) Temperature dependence of the in-phase susceptibility χ', measured for for different frequencies $f_0 < f_1 < f_2 < f_3$. Black arrow serves as guide to the eye to indicate that the maximum of χ' moves towards higher temperatures for higher frequencies.

conducted by Cannella and Mydosh in 1972 [90], marking the beginning of the field. As sketched in Fig. 2.6(a), they observed a peak in the in-phase susceptibility χ', accompanied by a sharp increase in the out-of-phase susceptibility χ''. This behavior closely resembles that of a phase transition in an antiferromagnet. However, no evidence of long-range magnetic order was found.

At the time, it was speculated that the sharp peak at the so-called freezing temperature T_f could be an artifact of the measurement protocol, possibly the result

of a sharp many-body resonance excited by the AC drive. In case of a thermodynamic phase transition, T_f is expected to be independent of the drive frequency. This was initially confirmed with high accuracy over five decades of frequency in a 1979 study [91].

However, subsequent and more precise measurements revealed a subtle but measurable dependence of T_f on frequency [92], which later became one of the hallmark signatures of spin glass behavior. This characteristic is now commonly quantified using the Mydosh parameter [93]

$$S = \frac{T_{f_2} - T_{f_1}}{T_{f_2} \log_{10}(f_2/f_1)}, \tag{2.10}$$

which is believed to be the most reliable observable to distinguishing different spin glasses, like the canonical spin glass from the cluster spin glass, and a superparamagnet [94], which are sketched in Fig. 2.7.

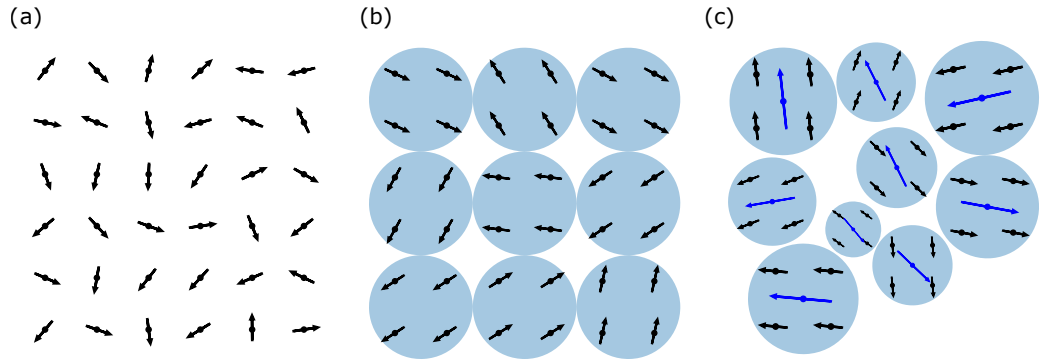

Figure 2.7: *Sketch of different glassy-like systems.* (a) Canonical spin glass. Individual spins (black arrows) are frozen in a random direction. (b) Cluster spin glass. Spins form magnetic clusters (blue circles). Each cluster is frozen into a fixed direction due to random interactions. Cluster spin glasses are believed to be described by the same theory as canonical spin glasses [80]. (c) Superparamagnet. A sample of magnetic nanoparticles with different sizes, where each nanoparticle can host only exactly one magnetic domain. Depending on the size of the particle, either all spins in a single nanoparticle are tight to the crystalline easy axis (blue arrow), which is called blocked, or they can flip collectively to a random direction, like a single spin in a paramagnet, which is referred to as superparamagnetic behavior.

In spin glasses, the temperature dependence of the freezing transition T_f typically follows the behavior illustrated in Fig. 2.6(b). With increasing drive frequency, the

freezing temperature changes to higher values and the peak response decreases. This reflects the fact that only the fastest spin dynamics can follow high-frequency drives. Even above the critical temperature, some spins begin to freeze and thus respond only slowly to external perturbations. As a result, they remain active under slow drives, but cannot follow fast ones, leading to a frequency-dependent shift in T_f. The reduced peak amplitude at higher frequencies arises because fewer spins remain unaffected by the onset of glassy freezing. In systems with long-range order, this behavior is typically not visible, as the ordering due to spontaneous symmetry breaking happens faster than any experimentally observable time scale. As such, in ordered systems like ferro- and antiferromagnets, $S = 0$.

For canonical spin glasses, which are the magnetic alloys initially studied, S is typically between 0.005 and 0.01. Later, so-called cluster spin glasses were studied [95], where spins seem to form ferromagnetic clusters, and the clusters freeze into an individual direction. In these systems, S is typically between 0.01 and 0.08. In superparamagnetic systems, S typically exceeds 0.2. These materials consist of a broad distribution of non-interacting or weakly interacting magnetic nanoparticles. As a result, the system does not exhibit a genuine spin glass phase, as cooperative effects are absent. The Mydosh parameter thus typically serves as a characteristic tool to classify the type of spin glass, and to distinguish it from other phases [96–99].

In addition, the functional form of T_f as a function of frequency can shed further light on the nature of the material. This dependence is typically rewritten in terms of the system response time $\tau = 2\pi/f$. In order to exclude that the system consists of individual non-interacting nanoparticles, the system's response time is typically fitted an Arrhenius law

$$\tau = \tau_0 \exp\left(\frac{U}{k_B T_f}\right), \tag{2.11}$$

where U is the activation energy of a typical nanoparticle, k_B the Boltzmann constant, and τ_0 a microscopic time scale. Both in canonical spin glasses and in cluster spin glasses, fitting the frequency dependence of T_f to this law leads to unphysical parameters, like activation energies $U/k_B \approx 4000\,\mathrm{K}$.

More reasonable values are obtained in cluster glasses from a Vogel-Fulcher law [100, 101] which was initially developed to describe highly viscous fluids

$$\tau = \tau_0 \exp\left(\frac{U}{k_B\,(T_f - T_0)}\right), \tag{2.12}$$

where T_0 corresponds to an interaction strength between the different clusters. In spin glass physics, a finite T_0 at the same order of magnitude as T_f is seen as an

indication of cluster formation and a proof for a cluster spin glass [99].

In addition, the shift in frequency can also be used to determine critical behavior. Close to a phase transition [102] at the critical temperature T_c, the correlation length ξ in a material is expected to diverge with the correlation length critical exponent ν as

$$\xi \sim |T - T_c|^{-\nu} . \tag{2.13}$$

The relaxation time τ of the system diverges with the dynamical critical exponent z as

$$\tau \sim \xi^z. \tag{2.14}$$

In spin glasses, the critical temperature T_c is assumed to be equal to the freezing temperature in the limit of a DC drive, i.e. $T_g = \lim_{f \to 0} T_f$ [80]. This thus leads to a scaling relation of the form

$$\tau = \tau_0 \left(\frac{T_f - T_g}{T_g} \right)^{-zv} , \tag{2.15}$$

where independent of whether the system is a canonical spin glass or a cluster glass, combinations of zv between 4 and 12 have been measured [94].

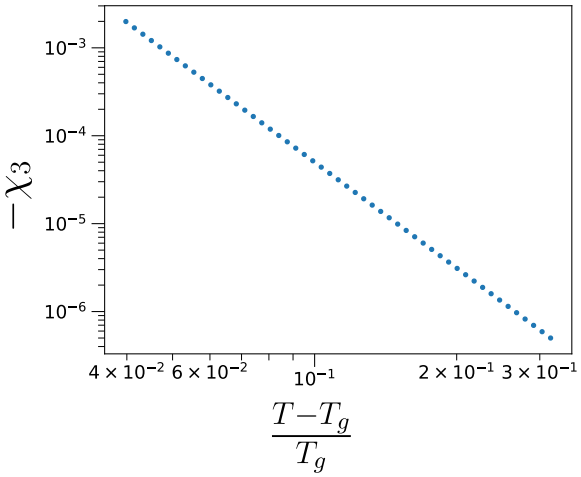

Figure 2.8: *Nonlinear susceptibility in a spin glass.* Sketch of the modulus of the nonlinear susceptibility χ_3 as a function of reduced temperature $(T - T_g)$ above the glass transition temperature T_g. Values estimated from [103]. In the double logarithmic plot, we observe a power law divergence of the nonlinear susceptibility toward the glass transition temperature.

As the dynamical critical exponent is involved, this so far only establishes the spin glass phase as a dynamical phase. In order to show the presence of a static continuous phase transition, the exponent ν need to be estimated independently in an equilibrium setting. This is accomplished by DC susceptibility measurements above the glass transition temperature, where no hysteresis effects are present, and thus an equilibrium state is probed. It is noteworthy that the critical behavior is absent in the linear susceptibility introduced above, but only present in the higher orders of the susceptibility [80, 103, 104]. The magnetization M can be expanded in the applied field H as

$$M(H) = \chi H + \chi_3 H^3 + \chi_5 H^5 + \sum_{l=3}^{\infty} \chi_{2l+1} H^{2l+1}. \tag{2.16}$$

In terms of scaling with reduced temperature $\tau = (T - T_g)/T_g$, we find the scaling laws

$$\begin{aligned} \chi_3 &\sim \tau^{-\gamma}, \\ \chi_5 &\sim \tau^{-2\gamma-\beta}. \end{aligned} \tag{2.17}$$

This behavior was measured initially by Lévy et. al. [104] and improved to high precision by Gunnarson et. al. [103], where we sketched their result in Fig. 2.8. We observe a clear critical behavior of the nonlinear susceptibility following a power law, but we also see that the nonlinear susceptibility is roughly two orders of magnitude smaller than the linear one, and high precision measurements are needed to detect it. Using different relations between the critical exponents, so-called scaling relations, all other statical critical exponents can be inferred from the two exponets β and γ. From the scaling relation for the correlation length critical exponent, they found, using

$$\nu = \frac{2\beta + \gamma}{d}, \tag{2.18}$$

with $d = 3$ as the dimension of the material, $\nu \approx 1.7$, close to the RSB mean field prediction $\nu \approx 1.3$. An open question that arises is

How can the critical exponents of a spin glass be experimentally accessed in an isolated quantum system, where temperature scaling is absent?

2.1.3 Dipolar spin glasses

The experiments discussed so far have been conducted in materials where the magnetic coupling is effectively nearest-neighbor, for the experimental results, or infinite-range,

for the Parisi mean-field solution. However, an interesting question arises how the spin glass phase changes once long-range order is introduced. As the lowest order magnetic moment is a magnetic dipole, dipole-dipole interactions pose the strongest long-range interacting coupling. A system that naturally realizes a dipolar Ising Hamiltonian

$$H = \sum_{i<j} J \frac{1 - 3\cos^2(\theta_{ij})}{r_{ij}^3} S_z^{(i)} S_z^{(j)}, \tag{2.19}$$

where J is a coupling constant, r_{ij} is the distance between magnetic dipoles at positions i and j, θ_{ij} is the angle with respect to a preferred crystalline axis, and $S_z^{(i)}$ denote an Ising spin at position i, is realized in $\mathrm{Li\,Ho}_x\mathrm{Y}_{1-x}\mathrm{F}_4$, where x denotes the impurity concentration of the magnetic Ho^{3+} ions that replace the nonmagnetic Y^{3+} ions in the lattice [31]. It is these Ho^{3+} impurities that give rise to the dipolar spin-spin interaction described in Eq. 2.19. A dilution of the magnetic moments, i.e. a reduction in x, introduces randomness in the couplings, as positions and thus distances r_{ij} obtain a broad distribution. Moreover, frustration arises as the distribution in the angle θ_{ij} also broadens, leading to negative (ferromagnetic) and positive (antiferromagnetic) couplings.

At $x = 16.7\,\%$, spin glass behavior is well established, and it seems to persist at a finite transverse field [39], more in alignment with the droplet scaling picture. However, at very low temperatures, the critical exponents show a rather complicated picture. Close to $T = 0$, the glass phase seems to vanish, and there might not be a quantum phase transition at $T = 0$ [40], as the measured critical exponent γ from the nonlinear susceptibility seems to vanish for decreasing temperature. However, the product $z\nu$ from AC susceptibility measurements seems to be rather temperature independent, and was found initially to be $z\nu = 7.4(6)$ [32], and reconfirmed even at a lower filling of $x = 4.5\,\%$ to be $z\nu = 7.8(2)$ [33].

In the limit of this strong dilution $x = 4.5\,\%$, however, there is an ongoing controversy on the existence of a spin glass phase. From an experimental point of view, initial experiments found that AC susceptibilities are contradicting a broad distribution of relaxation times as found in spin glasses, but instead rather indicate the presence of multiple independent oscillators [34, 35]. Further numerical studies on the build-up of entanglement support the idea of the presence of a quantum spin liquid and no spin glass phase [36].

However, a more recent experiment at the same concentration x contradicted the previous measurements, finding even in the AC susceptibility strong glass behavior and no spin liquid [33]. Even though also numerical simulations come to different conclusions [37], the most recent Monte Carle simulation rather establish the existence of a spin glass phase even in the limit of $x = 0$, both for $\mathrm{Li\,Ho}_x\mathrm{Y}_{1-x}\mathrm{F}_4$ [38], as well

as in a diluted spin ice [105], where a critical exponent $\nu = 1.27(8)$ is predicted.

For dipolar interacting Heisenberg glasses, the existence of a glass phase is so far only established numerically [106], where the correlation length critical exponent is approximated to be $\nu \approx 1.2(1)$ [107]. The open question that arises is thus

Does a spin glass phase exist in the dipolar-interacting Heisenberg XY model, and if so, is it connected to a quantum phase transition driven by an external magnetic field?

In addition, studying the spin glass phase in isolated systems adds another layer of complexity not present in classical systems: the effect of many-body localization, which we will review more detailed in the next section. To conclude this section on frustrated magnetic phases, we want to note that so far, in all numerically studied models that show both a quantum spin glass and a many-body localized regime, the spin glass is always fully localized [46, 47, 108, 109]. So far, one of these models was only recently realized, and effects of both localization and spin glass ordering have been observed on a quantum annealer [110, 111]. However, the detailed interplay between localization and glassiness remains an open question, and it would be interesting to see whether long-range interacting models can show a similar behavior, and whether clustering plays an important role in the measured localization [111].

2.2 Thermalization and localization

As mentioned in the previous section, also in an isolated quantum system, the spin glass phase is typically linked to the phenomenon of many-body localization, a phenomenon closely linked to thermalization. In this chapter, we we will thus set the stage to ask

Does a finite-size dipolar interacting quantum system show indications of many-body localization?

We begin with a brief review of thermalization in isolated quantum systems and its connection to random matrix theory and the spectral properties of the Hamiltonian. We then outline how these concepts relate to many-body localization, with a focus on systems featuring long-range, algebraically decaying interactions, such as the one examined in this thesis. Finally, we discuss how out-of-time-order correlators have been employed to identify localization in NMR platforms dominated by dipolar couplings.

2.2.1 ETH and quantum chaos

The concept of quantum thermalization and the eigenstate thermalization hypothesis (ETH) is reviewed in multiple outstanding reviews [112–116]. If not stated otherwise, we will mainly follow [112] in this introductory chapter.

In a classical system, the thermal equilibrium state is defined by being time-translation invariant, i.e. a system in thermal equilibrium does not know about any of its history, and will stay in the thermal equilibrium state, if not perturbed. A system out of equilibrium is said to thermalize if after some time, the system arrives in the thermal state, where it has lost all of its initial memory.

For a theoretical analysis of this phenomenon, we consider an isolated quantum system that evolves unitarily under a generic Hamiltonian H. This Hamiltonian can be diagonalized with eigenenergies $E_1, E_2, \ldots, E_d$ and corresponding eigenstates $|1\rangle, |2\rangle, \ldots, |d\rangle$, where d is the dimension of the Hamiltonian. The Hamiltonian shall be considered to be generic in the sense that it does not have protected symmetry sectors by a unitary symmetry, and thus no degenerate eigenenergies. An arbitrary state $|\Psi\rangle$ will follow the time evolution

$$|\Psi(t)\rangle = \sum_{m=1}^{d} \langle \Psi|m\rangle \, e^{-iE_m t} = \sum_{m=1}^{d} c_m e^{-iE_m t}. \tag{2.20}$$

Next, we consider a general observable $O = \sum_{m,n=1}^{d} O_{mn} \, |m\rangle\langle n|$ where $O_{mn} = O_{nm}^* \in \mathbb{C}$. The time-dependent expectation value for this observable is as a consequence

$$\begin{aligned} O(t) = \langle \Psi(t)|O|\Psi(t)\rangle &= \sum_{k,m,n,l}^{d} c_k^* O_{mn} c_l \, \langle k|m\rangle \, \langle n|l\rangle \, e^{iE_k t} e^{-iE_l t} \\ &= \sum_{m,n=1}^{d} c_m^* c_n O_{mn} e^{-i(E_n - E_m)t}. \end{aligned} \tag{2.21}$$

Taking the assumption of no accidental degeneracies in the Hamiltonian, the equilibration value of the observable will be

$$\begin{aligned} \overline{O} &= \lim_{t\to\infty} \frac{1}{t} \int_0^t O(t) \\ &= \sum_m |c_m|^2 \, O_{mm}. \end{aligned} \tag{2.22}$$

As is clearly observable, this value strongly depends on the initial state $|\Psi\rangle$ and all its overlaps with the eigenstates of the Hamiltonian c_m. As such, the system

always preserves a memory of the initial state. A system is defined to thermalize with respect to the operator O if this equilibrium value is independent of the initial state, and its value is given by the expectation value from a thermal ensemble, for example the microcanonical ensemble ρ_{mic}:

$$\overline{O} = \lim_{t\to\infty} \frac{1}{t} \int_0^t O(t) \stackrel{!}{=} \text{Tr}\{O\rho_{\text{mic}}\}. \tag{2.23}$$

Other thermodynamic ensembles like the canonical or the grand-canonical are also possible. This cannot be true for all operators O, as for example, all projection operators onto an eigenstate $|m\rangle\langle m|$ will fail Eq. 2.23. As a consequence, an isolated quantum system is defined as thermal, when Eq. 2.23 holds for all local operators O.

Another important aspect of Eq. 2.22, is that the time until the equilibrium value $\overline{O}$ is reached must be large compared to the Heisenberg time $\tau_H = 2\pi/\delta$, where δ is the mean level spacing. As δ is typically exponentially small in the system size, the equilibration time would be at least exponentially large in system size, and thus one would expect to never see equilibrium values in a real experimental setup.

Hence two problems arise: What leads to the thermalization of local operators, and why does equilibration occur on observable timescales? In his seminal paper [117], Deutsch solved the former of these two problems, while Srednicki solved the second one shortly thereafter [118]. They proposed that all local operators O take the form

$$O_{mn} = \mathcal{O}(E)\delta_{mn} + e^{-S(E)/2} f(E,\omega) R_{mn} \tag{2.24}$$

where $\mathcal{O}$ is a smooth function of the mean energy $E = (E_m + E_n)/2$ and equals the equilibrium value of O for initial states with energy E, and f a smooth function of the mean energy and the energy difference $\omega = E_m - E_n$, which determines the time scale of the equilibration process. $S(E)$ is the thermodynamic entropy defined by the logarithm of the number of eigenstates in the energy windows $E \pm \delta E$, i.e. the logarithm of the density of states. R_{mn} is a random Hermitian matrix, where each entry has zero mean, unit variance on off-diagonal entries, and, if the Hamiltonian is time-reversal symmetric, variance 2 on the diagonal. What is the origin of this random matrix?

This is nicely outlined in [114], and we will follow the derivation from there. Consider a system governed by a random Hamiltonian H, with eigenstates $|\alpha\rangle$ and eigenergies E_α, and O as above a Hermitian operator with eigenstates $|i\rangle$ and eigenvalues O_i. Under these assumptions, the eigenstates of O will look like random vectors decomposed in the eigenstate basis of the Hamiltonian. As a consequence, the expectation value of the operator averaged over all possible random Hamiltonians

gives

$$\begin{aligned} \overline{O_{\alpha\alpha}} &= \frac{1}{d}\sum_i O_i = \overline{O}, \\ \overline{O_{\alpha\beta}} &= 0, \\ \overline{O^2_{\alpha\alpha}} - \overline{O_{\alpha\alpha}}^2 &= \frac{3-g}{d}\sum_i {O_i}^2 = \frac{3-g}{d}\overline{O^2}. \end{aligned} \tag{2.25}$$

where the bar denotes an average over different Hamiltonians. In the equation above, $g = 1$ for real-valued Hamiltonians, i.e. the Gaussian Orthogonal Ensemble (GOE), while $g = 2$ for complex-valued Hermitian Hamiltonians, i.e. the Gaussian Unitary Ensemble (GUE). The importance of the GOE in physical systems lies in the fact that a Hamiltonian that is time-reversal symmetric can always be written in a basis where it is completely real, which is why time-reversal symmetric systems are typically captured by the GOE [114]. As a consequence, up to first order in the inverse dimension of the Hilbert space, we obtain for the matrix elements of O

$$O_{\alpha\beta} = \overline{O}\delta_{\alpha\beta} + \sqrt{\frac{3-g}{d}\overline{O^2}}R_{\alpha\beta}. \tag{2.26}$$

Comparing this to the ETH ansatz in Eq. 2.24, a direct connection becomes apparent. Random Matrix Theory (RMT) predicts the same equilibrium value $\overline{O}$ for observables, irrespective of the initial state's energy. This implies that RMT effectively captures the infinite-temperature limit of a physical system, where all energy eigenstates contribute equally. Moreover, RMT reproduces the ETH ansatz when the physical system is restricted to an energy shell narrow enough that both $\mathcal{O}(E)$ and $f(E,\omega)$ can be considered approximately constant. Within such a narrow energy window, ETH gains a clear physical interpretation: the Hamiltonian, projected onto this local subspace of the Hilbert space, behaves like a random matrix. This connection is significant because RMT allows one to compute spectral properties of Hamiltonians. As discussed in Eq. 2.23, ETH is sufficient for thermalization. Therefore, any system that obeys ETH, will exhibit either GOE or GUE level spacing statistics within a constant-energy window, and can thus be characterized by its eigenvalue statistics. In the following section, we examine how this picture changes in the case of many-body localized (MBL) systems, where thermalization fails, and how this gets expressed in their level spacing statistics and other properties.

2.2.2 Many body localization and ergodicity breaking

In his seminal paper [119], Anderson demonstrated that a single particle can become localized in a lattice with random on-site potentials, a phenomenon now known as Anderson localization. This result was later reinforced using scaling theory [120], which showed that in a lattice with random on-site potentials and nearest-neighbor hopping, a single particle cannot propagate arbitrarily far. Specifically, in one and two dimensions, even arbitrarily weak disorder leads to complete localization. In three dimensions, localization occurs when the disorder exceeds a certain threshold. In all these cases, the particle becomes confined within a finite length scale, known as the localization length.

The open question remained how this picture changes in the presence of interactions, and was answered by the proposal of the many-body localized phase [121–123], which was recently thoroughly reviewed in Ref. [45]. It is defined as a phase where thermalization in the sense of Eq. 2.23 is not possible. Such a system might be described by showing emergent integrability upon the introduction of disorder, i.e. an extensive number of quasilocal conserved quantities arise as an effect of disorder which might be absent in the corresponding ordered model. The Hamiltonian that models such a behavior is the so-called l-bit model [124, 125]

$$H_{\mathrm{MBL}} = \sum_i h_i \tau_z^{(i)} + \sum_{i<j} J_{ij} \tau_z^{(i)} \tau_z^{(j)} + \sum_{i<j<k} J_{ijk} \tau_z^{(i)} \tau_z^{(j)} \tau_z^{(k)} + \ldots, \tag{2.27}$$

where the Hamiltonian is written as a sum of quasilocal integrals of motion (LIOMs) $\tau_z^{(i)}$, which commute with each other and with the Hamiltonian. Even though any Hamiltonian might be expressible in terms of such a sum [126], what makes the many-body localization special is that these LIOMs are exponentially localized in real-space operators. For any local observable $A^{(i)}$ at site i, the overlap with a LIOM $\mathrm{Tr}\left\{\tau^{(j)} A^{(i)}\right\} \sim e^{-|i-j|/\xi}$ is exponentially suppressed in their distance, where ξ denotes the localization length. The couplings in the LIOM Hamiltonain thus fulfill $J_{ij} \sim e^{-\frac{|i-j|}{\kappa}}$, $J_{ijk} \sim e^{-\frac{|i-k|}{\kappa}}$, where κ is in general a length scale different from the localization length [125].

In most systems, the LIOMs $\tau^{(i)}$ can be adiabatically connected to number operators onto exponentially localized single-particle orbitals of a corresponding non-interacting Anderson localized model. In such Anderson insulators, the l-bit Hamiltonian contains no interaction terms. This absence of interactions is a key feature distinguishing Anderson localization from the many-body localized (MBL) regime, as these terms give rise to dephasing and a slow growth of entanglement [127].

However, there are cases in which MBL behavior is observed even though the corresponding non-interacting system has fully delocalized single-particle states [128].

This raises the open question of whether all many-body localized systems can truly be described within the framework of local integrals of motion (LIOMs).

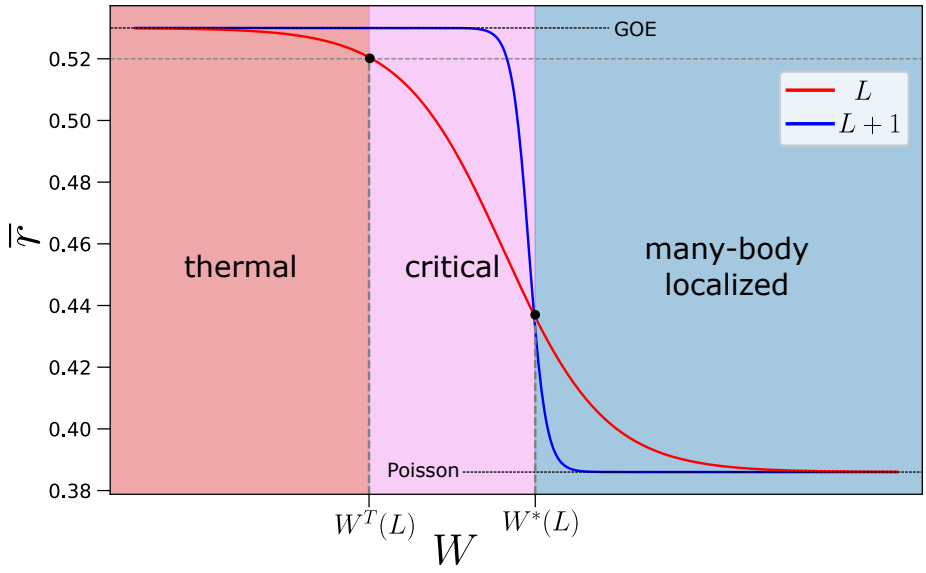

Figure 2.9: *The many-body localization-delocalization transitions (MBLD) in a finite size system of length L.* The mean level spacing ratio $\bar{r}$ is shown as a function of the disorder strength W. Following [45], the system is thermal (red shaded region) for disorder strength below $W^T(L)$ and many-body localized (blue shaded region) for disorder strength above $W^*(L)$. In between, a critical region (pink region) is defined. $W^*(L)$ is defined by the crossing of the curves for system size L (red line) and $L+1$ (blue line). GOE and Poisson level statistic predictions are indicated by dashed black lines.

In order to identify thermal and localized regimes, spectral statistics which are directly related to random matrix theory provide a natural tool. These statistics are typically expressed in the gap ratio introduced by Oganesyan and Huse [123]

$$r_n = \frac{\min(\delta_n, \delta_{n-1})}{\max(\delta_n, \delta_{n-1})}, \tag{2.28}$$

where $\delta_n = E_{n+1} - E_n$ denotes the level spacing between two neighboring energy levels E_{n+1} and E_n of a given Hamiltonian. For a thermal system obeying ETH, where random matrix theory predicts the Hamiltonian to be sampled from the GOE, the value is roughly $\bar{r} \approx 0.531$, while for the localized regime, the energy levels are expected to have uncorrelated eigenenergies as in integrable systems like the LIOM

model. Thus, the Poisson distribution predicts an average gap ratio $\overline{r} \approx 0.386$ for integrable systems.

The typical mean level spacing ratio as a function of disorder W for a model with a localized and thermal ETH regime is sketched for two different system sizes in Fig. 2.9. As long as the mean level statistics is close to the GOE prediction, the system is believed to be thermal, as it can typically be described by ETH. When $\overline{r}(W) < 0.531 - \Delta r$, where $\Delta r \ll 1$, this is no longer fulfilled, which defines the critical disorder strength $W^T(L)$. In case of [45], they chose $\Delta r = 0.01$. In the theory of critical scaling, the crossing point of $\overline{r}(W)$ for different system sizes marks the critical transition point, as beyond this point the level spacing ration decreases as a function of system size. This defines a second critical disorder strength $W^*(L)$. The disorder strengths in between mark the critical region of the localization-delocalization transition. The question of whether the many-body localized region is now a thermodynamic phase, that is, persists in the limit $L \to \infty$, is an open and interesting question, but not in the scope of this thesis. Instead, as this thesis deals with a disordered dipolar interacting model, we want to ask

How can localization and ETH effects be experimentally characterized in a power law interacting, bond-disordered system?

2.2.3 Algebraic localization

For dipolar interacting systems, where the interaction between particles at positions i and j typically scales as $|i-j|^{-\alpha}$, the MBL picture starts changing. In principle, as pointed out very early [129], two different kinds of disorder can arise. Diagonal or on-site disorder means that the particles sit on a lattice and disorder arises due to random on-site potential on top of the algebraic interactions. For this case, it was shown that for dimension $d > \alpha$, no localization can occur, while for $d < \alpha$, localization may occur upon sufficient disorder [130, 131].

Recently, it could be shown that this phase can be described by so-called algebraic LIOMs, where the LIOMs of Eq. 2.27 are now power law or algebraically localized, i.e. for any local observable $A^{(i)}$ at site i, the overlap with a LIOM $\mathrm{Tr}\left\{\tau^{(j)} A^{(i)}\right\} \sim \frac{1}{|i-j|^{\beta}}$ decays in a power law [132, 133]. The idea for this model stems from algebraically localized single-particle eigenstates in a non-interacting model $\phi(x) \sim |x - x_0|^{-\gamma}$, where x_0 is a position in real space and $\gamma > 0$ the power law exponent of the decay. If we think of these wavefunctions as being adiabatically connected to the eigenstates in an interacting picture, we would expect that we arrive at the algebraic LIOM picture. From a dynamic point of view, this algebraically localized phase is qualitatively different from the exponentially localized standard MBL regime. This can be seen

for example in the entanglement entropy, which grows logarithmically in time in exponentially localized MBL, while in this power law system it grows as a power law [132, 133].

Another type of disorder arises when the on-site potential is zero, but the particles are placed in random positions, leading to random coupling strengths [134]. This is typically called bond-disorder or off-diagonal disorder. For this case, it was also established that in the interacting case, single-particle wavefunctions are algebraically localized [135], and thus the algebraic LIOM picture might hold.

However, this picture was recently questioned [136]. Even though the Hamiltonian under investigation

$$H = \sum_{i<j} \frac{J}{|i-j|^{\alpha}} \left(S_x^{(i)} S_x^{(j)} + S_y^{(i)} S_y^{(j)} + \Delta S_z^{(i)} S_z^{(j)} \right) \tag{2.29}$$

is similar in both works [134, 136], very different behavior was observed. In terms of the model, Ref. [136] focus on the zero magnetization sector, considers only nearest-neighbor interactions, and has $\Delta = 0.73$, while Ref. [134] focuses on the sector with magnetization $-L/2+1$, includes long-range hopping, and uses $\Delta = 0$. In terms of observables, Ref. [136] observes subpoissonian level statistics, which it describes as incommensurate with any LIOM picture, while Ref. [134] observes algebraically localized wavefunctions and a power law growth of entanglement entropy, which are consistent with a LIOM picture. As a consequence, the question arises

What is the nature of the localized phase in a bond-disordered power law interacting system?

In this thesis, we address this question from a dynamical point of view, inspired by localization measurements in NMR systems.

2.2.4 Out-of-time-order correlators and localization

So far, we discussed thermalization and localization, i.e. properties of local observables. For thermalization, we assume that two different initial states with the same energy lead to the same expectation value for local observables, and thus they cannot be distinguished locally. However, unitary dynamics implies that quantum states that are orthogonal at initial time will remain orthogonal for all times. Thus, thermalization and unitary dynamics imply that initial local information must spread to non-local highly entangled subspaces of the Hilbert space. This phenomenon is known as information scrambling and is typically measured by out-of-time-order correlators (OTOCs), which have been recently reviewed in Ref. [137].

The OTOC between two observables V and W, which was initially introduced in the context of superconducting materials [138], is given by the expression

$$C = \left\langle [W(t), V]^\dagger [W(t), V] \right\rangle, \tag{2.30}$$

where the angle brackets can denote either an expectation value from a thermal ensemble with regard to a density matrix, or an expectation value with regard to a pure state. The time dependence of operators is understood in the Heisenberg picture. In the case that both V and W are both Hermitian and unitary, the expression above simplifies to

$$C = 2 - 2\left\langle W^\dagger(t) V^\dagger W(t) V \right\rangle = 2 - 2F, \tag{2.31}$$

where F as the only non-trivial part in C is also referred to as an OTOC. Typically, V and W are taken as local operators on different sites that commute at $t = 0$. As can be seen in Eq. 2.30, the OTOC thus measures how the operator W grows over time and begins to overlap with V. As $W(t)$ is highly nonlocal, the OTOC can capture scrambling dynamics even after thermalization and thus provides a finer tool for characterizing non-equilibrium dynamics [137]. For example, OTOCs can detect the onset of chaotic dynamics, as for systems with a semiclassical limit, its initial growth is believed to be related to the Lyapunov exponent of the corresponding classical model [139].

As in this thesis our interest lies in possible localization and thermalization properties, we will focus on a special OTOC known in NMR physics. This OTOC has been used to detect the build-up of spin-spin correlations, and is called multiple quantum coherences (MQC) [140, 141].

State preparation	Forward Evolution	Spin rotation	Backward evolution	Magnetization measurement
$\rho(0) \sim S_z$	$\rho(t) = e^{-iHt}\rho(0)e^{iHt}$	$\rho_\phi(t) = e^{-i\phi S_z}\rho(t)e^{i\phi S_z}$	$\rho_\phi(2t) = e^{iHt}\rho_\phi(t)e^{-iHt}$	$S_\phi(t) = \mathrm{Tr}\{S_z\rho_\phi(2t)\}$

Figure 2.10: *Sketch of the MQC protocol.* Prepraration and measurement are represented by orange blocks, time evolution by blue blocks, and global spin rotation by a violet block.

Following mainly the supplemental material of Ref. [142], the MQC protocol, schematically shown in Fig. 2.10, proceeds according to the steps outlined below:

1. The initial state is prepared by heating the system to a high initial temperature and applying a magnetic field in the z-direction, which is small compared to

the temperature but large compared to spin-spin interactions. The initial state is thus a density matrix, which can be approximated as $\rho(0) = K\mathbb{1} + LS_z$ in the limit of infinite temperature. Here, $\mathbb{1}$ is the identity matrix, S_z is the operator of the global z-magnetization, and K and L are constants depending on the temperature and Zeeman splitting due to the field. As the identity matrix has no time evolution because it commutes with all operators, the initial state can be approximated, up to a proportionality constant, as the S_z operator.

2. After state preparation, the system follows usual Hamiltonian dynamics, where the Hamiltonian can be engineered by pulse sequences. The evolution is thus

$$\rho(t) = e^{-iHt}\rho(0)e^{iHt}. \tag{2.32}$$

3. The density matrix is rotated by an angle ϕ by applying a strong field around the z-axis

$$\rho_\phi(t) = e^{-i\phi S_z}\rho(t)e^{i\phi S_z}. \tag{2.33}$$

In this step, we see why this protocol is able to detect multiple quantum coherences. Suppose that we write down the density matrix in the product basis of single site z-magnetization operators. Then, for every state in the basis, the z-magnetization M_z is well defined. A coherence of order m is defined as an off-diagonal element ρ_{ij} (quantum coherence) in the density matrix that couples product state $|i\rangle$ with product state $|j\rangle$ with magnetization difference $M_z^{(j)} - M_z^{(i)} = \Delta M_z = m/2$, i.e. indicates a quantum coherence of multiple, namely m, spins. As a consequence, we can expand $\rho(t)$ as a sum of terms with equal quantum coherence m, such that we obtain

$$\rho_\phi(t) = e^{-i\phi S_z}\sum_m \rho_m(t)e^{i\phi S_z} = \sum_m \rho_m(t)e^{i\phi m}. \tag{2.34}$$

4. The system is evolved backwards in time, or alternatively forwards in time with a sign-reversed Hamiltonian $-H$. As such, the state after this backwards evolution can be written as

$$\rho_\phi(2t) = e^{iHt}\rho_\phi(t)e^{-iHt}. \tag{2.35}$$

5. The z-magnetization is measured. This leads to

$$S_\phi(t) = \mathrm{Tr}\{S_z\rho_\phi(2t)\}. \tag{2.36}$$

The connection between MQCs and OTOCs becomes apparent by inserting Eqs. 2.32 and 2.33 into Eq. 2.35, together with $\rho(0) \propto S_z$. This yields

$$\begin{aligned} S_\phi(t) &\propto \mathrm{Tr}\Bigg\{ \underbrace{S_z}_{V^\dagger} \underbrace{e^{iHt}e^{-i\phi S_z}e^{-iHt}}_{W_\phi(t)} \underbrace{S_z}_{V} \underbrace{e^{iHt}e^{i\phi S_z}e^{-iHt}}_{W_\phi^\dagger(t)} \Bigg\} \\ &\overset{\text{Tr cycl.}}{=} \mathrm{Tr}\Big\{ W_\phi^\dagger(t) V^\dagger W_\phi(t) V \Big\}, \end{aligned} \tag{2.37}$$

which describes an OTOC between the operators $S_z = V$ and $e^{-i\phi S_z} = W_\phi$. At this point, we want to highlight that this magnetization measurement is equivalent, up to a prefactor, to a fidelity measurement, as the initial density matrix is proportional to the magnetization operator S_z. We now simplify this expression

$$\begin{aligned} S_\phi(t) = \mathrm{Tr}\{S_z \rho_\phi(2t)\} &\propto \mathrm{Tr}\Big\{ \rho(0) e^{iHt} \rho_\phi(t) e^{-iHt} \Big\} \\ &= \mathrm{Tr}\Bigg\{ \rho(0) e^{iHt} \sum_m \rho_m(t) e^{i\phi m} e^{-iHt} \Bigg\} \\ &\overset{\text{Tr cyclic}}{=} \mathrm{Tr}\Bigg\{ e^{-iHt} \rho(0) e^{iHt} \sum_m \rho_m(t) e^{i\phi m} \Bigg\} \\ &= \mathrm{Tr}\Bigg\{ \sum_{m=q} \rho_q(t) \sum_{m=p} \rho_p(t) \Bigg\} e^{i\phi \Delta q} \\ &= \sum_m \mathrm{Tr}\{\rho_m \rho_{-m}\} e^{i\phi m} = \sum_m I(m) e^{i\phi m}. \end{aligned} \tag{2.38}$$

where in the last step we used that $\mathrm{Tr}\{\rho_q(t)\rho_p(t)\} \propto \delta_{p,-q}$, and introduced the multiple quantum coherence intensities $I(m)$.

6. Perform a Fourier transformation of the signal to obtain the multiple quantum intensities $I(m)$. As they are related to the modulus square of the coherences in the density matrix, a nonzero $I(m)$ indicates the presence of at least m correlated spins.

So the MQC gives a lower bound on multiple spin correlations in a system at effectively infinite temperature (this is the assumption for the initial state preparation). In addition, unlike other OTOCs which are harder to interpret because decoherence cannot be typically distinguished from scrambling [143], the MQC spectrum is known to be robust against weak decoherence effects [144]. From here, two different directions

can be followed. Is there more information contained in the distribution of the MQCs, and what happens at finite or even zero temperature?

For the former problem, a combinatorial argument shows that for three-dimensional systems the MQCs are Gaussian distributed, and the width corresponds to the typical size of a cluster of correlated spins [141]. This property was used to show that the extracted cluster size can be used to characterize a localization-delocalization transition [142, 145, 146], where decoherence leads to localization in form of a finite maximal cluster size. In a one-dimensional chain, this argument is not true anymore, but even there the MQC spectrum can be used to extract a localization length for a system with on-site disorder and nearest-neighbor interactions only, and study a localization-delocalization transition [147].

For the latter problem, when changing from infinite temperature density matrices to pure quantum states, the structure of the problem changes fundamentally. In the NMR protocol discussed above, measuring the fidelity or the magnetization is equivalent because the initial state is proportional to the magnetization operator. In isolated quantum systems, however, this is not the case anymore, and it is possible to define a magnetization OTOC and a fidelity OTOC separately [148, 149], which contain different information. We therefore adopt a modified version of the sequence shown in Fig. 2.10.

For the magnetization OTOC, the initial state is a pure state $|\Psi\rangle$ that satisfies $S_z\,|\Psi\rangle = M_z\,|\Psi\rangle$ with $M_z \neq 0$. A magnetization measurement in step 5 of the protocol then yields

$$S_\phi(t) = \frac{1}{M_z}\,\mathrm{Tr}\Big\{W_\phi^\dagger(t)\,S_z\,W_\phi\,S_z\,\rho(0)\Big\} = \frac{1}{M_z}\,\Big\langle W_\phi^\dagger(t)\,S_z\,W_\phi\,S_z\Big\rangle\,. \tag{2.39}$$

Following [148], we thus define the magnetization OTOC as

$$F_\phi(t) = \frac{1}{M_z^2}\,\Big\langle S_z\,W_\phi^\dagger(t)\,S_z\,W_\phi\Big\rangle\,, \tag{2.40}$$

where we recover the definition from Ref. [148] in the case of $|\Psi\rangle$ as the fully polarized state in z-direction. In this case, the Fourier components of $F_\phi(t)$ give the multiple quantum amplitudes A_m. A non-zero A_m signals the presence of at least m-body spin correlations. Furthermore, magnetization OTOCs have been shown to be robust against decoherence at long evolution times [148].

For the fidelity OTOC, the initial density matrix is a pure state $\rho(0) = |\Psi\rangle\langle\Psi|$. In step 5, measuring the fidelity gives

$$\mathcal{F}_\phi(t) = S_\phi(t) = \mathrm{Tr}\{\rho(0)\rho_{2\phi}(t)\} = \mathrm{Tr}\Big\{W_\phi^\dagger(t)\rho(0)W_\phi\,\rho(0)\Big\} = |\langle W_\phi(t)\rangle|^2\,, \tag{2.41}$$

in analogy to [148]. This OTOC contains information about the full density matrix written in terms of z-basis product states. The case $\phi = 0$, which directly yields the state's purity, also corresponds to a Loschmidt echo, which is commonly used to probe localization [150] or decoherence [151]. The Fourier transform of $\mathcal{F}_\phi(t)$ with respect to ϕ yields the multiple quantum intensities I_m, where a non-zero I_m indicates the presence of at least m-body coherences in the density matrix written in terms of product states in z-basis [148].

If instead of a rotation around S_z one considers a rotation generated by an arbitrary operator A in step 3 of the protocol, the multiple quantum intensities obtain an additional interpretation [149]. The width of their distribution satisfies

$$2 \sum_{m=-N}^{N} I_m m^2 = F_Q(\rho(t), A), \tag{2.42}$$

which yields the quantum Fisher information F_Q of the density matrix $\rho(t)$ with respect to the observable A. The quantum Fisher information provides a lower bound on the entanglement entropy, and its temporal scaling has been used to distinguish exponentially localized, algebraically localized, and thermal regimes both numerically [132] and experimentally [152]. In both studies, the observable A was the staggered magnetization and the initial state a Néel state. By contrast, the fidelity MQC protocol employs the total magnetization as the observable A and the fully polarized state as the initial state. This motivates the question:

Can the magnetization and fidelity MQC protocols be used to test a power law interacting isolated spin system for localization effects?

CHAPTER 3

Magnetic Irreversibility in an Isolated Spin System

Parts of this chapter are based on the following publication, from which parts of the text have been taken verbatim and adapted for better readability:

Observation of hysteresis in an isolated quantum system of disordered Heisenberg spins
Moritz Hornung, Eduard J. Braun, Sebastian Geier, Titus Franz, Gerhard Zürn, and Matthias Weidemüller
arXiv:2508.18197 (2025)

In the previous chapter, we introduced several open questions about the behavior of dipolar spin glasses in isolated quantum systems. This chapter addresses two of the central questions raised there:

Does a dipolar-interacting, isolated Heisenberg spin system host a spin glass phase?

How can thermomagnetic hysteresis protocols be adapted to isolated quantum systems?

To address these questions, we introduce two new measurement protocols that we call zero-field annealing (ZFA) and field annealing (FA). These protocols are tailored to characterize energetic-magnetic hysteresis in isolated quantum systems, similar to the way ZFC and FC characterize thermomagnetic hystersis in systems coupled to a thermal bath. While these protocols are platform-independent, we demonstrate

their application using a Rydberg atom quantum simulation platform that realizes a dipolar-interacting Heisenberg XY spin model.

The chapter is structured as follows. We begin by introducing the quantum simulation platform and explaining how it realizes the relevant Hamiltonian in Sec. 3.1. We then introduce the newly devised ZFA and FA protocols in detail and show their implementation on the Rydberg simulation platform in Sec. 3.2. We summarize the findings and outline possible directions for further investigation in Sec. 3.3.

3.1 A Rydberg atom spin simulator

This chapter explores quantum effects on potential spin glass behavior in a dipolar interacting system. While spin glass physics in low-dimensional dipolar systems without thermal fluctuations is of fundamental interest, we focus on a three-dimensional system to draw closer parallels with experiments in $LiHo_xY_{1-x}F_4$ [35, 39, 40], where spin-1/2 degrees of freedom arise naturally. In this thesis, we extend these investigations by studying a spin-1/2 Heisenberg XY model with dipolar interactions. This Hamiltonian is naturally implemented in the Rydberg quantum simulation platform, as demonstrated in previous works from our group [153–157]. Beyond realizing the relevant Hamiltonian, this platform has already been used to observe slow, glassy relaxation dynamics [155] as well as the absence of thermalization signatures on experimentally accessible timescales. It is therefore ideally suited for further exploration of spin glass phenomena. A detailed description of the experimental setup and sequence is provided in Chap. A; here, we briefly summarize the aspects most relevant to the questions addressed in this chapter.

3.1.1 Preparation of a frozen Rydberg gas with positional disorder

To simulate the dynamics of a three-dimensional Heisenberg XY spin model, the experimental platform must satisfy two key criteria:

- It must locally encode a pseudospin-1/2 degree of freedom, with dipolar interactions between the local constituents.
- It must allow control over the spatial distribution of the individual constituents, enabling the study of disorder effects.

The first requirement is fulfilled by encoding the spin-1/2 degree of freedom in two Rydberg states $|r_1\rangle$ and $|r_2\rangle$ of an atom, which act as local constituents carrying

spin and interacting via dipolar couplings. The effective dipolar Heisenberg XY spin model arising from Rydberg interactions in weak electric and magnetic fields was analyzed in previous work [42]. Here, we demonstrate that this mapping remains valid even in the presence of strong magnetic fields. A detailed discussion is provided in Appendix D.

The second requirement is met by preparing a three-dimensional cloud of cold atoms that remain stationary on experimental timescales—a regime known as a frozen Rydberg gas [158–160]. By varying the density of the Rydberg atom cloud, spin Hamiltonians with tunable disorder can be realized. In the following, we describe how such a cloud is prepared experimentally, using the setup shown in Fig. 3.1. We use rubidium as the atomic species. Its large ground-state hyperfine splitting, combined with the presence of an optical clock transition, enables both efficient cooling and trapping, as well as precise preparation of the initial electronic state in individual atoms. Further details are provided in Appendix A.

To reach the frozen Rydberg gas regime, we require an atomic cloud that is both sufficiently cold, such that atomic motion is negligible on experimental timescales, and sufficiently dense, such that Rydberg–Rydberg interactions occur fast on experimental timescales. To achieve rapid cooling of a large number of atoms and to prepare a high-density cloud, we employ a combination of a two-dimensional (2D) and a three-dimensional (3D) magneto-optical trap (MOT).

^{87}Rb atoms are initially loaded and cooled in a 2D-MOT, operating on the 780 nm D2 clock transition between the states $|g\rangle = \left|5S_{1/2}, F = 2, m_F = 2\right\rangle$ and $|e\rangle = \left|5P_{3/2}, F = 3, m_F = 3\right\rangle$. The 2D-MOT slows atoms to velocities below the capture threshold of the 3D-MOT and provides a more compact alternative to a Zeeman slower, allowing for improved optical access in the science chamber. A pusher beam directs the atoms into the science chamber, where approximately 100 000 atoms are collected in a 3D-MOT.

To achieve a deterministic atomic positional distribution, we transfer N_g atoms from the 3D MOT into a crossed beam optical dipole trap (ODT) at a temperature of 12(1) µK. The trap is formed by tightly focused laser beams at a wavelength of 1064 nm, and the crossed-beam geometry provides strong confinement in all spatial directions while maintaining a low atomic temperature. For experiments involving Rydberg atoms, a strong magnetic field is required to induce significant Zeeman splittings in both the ground and Rydberg states. This enables spectral selectivity during Rydberg excitation as well as in subsequent microwave manipulations, which will be discussed below. To generate the high field of 185 G, we employ the MOT coils, which are already equipped with an efficient cooling system. This magnetic field also defines the quantization axis, which we identify with the z-axis, for all

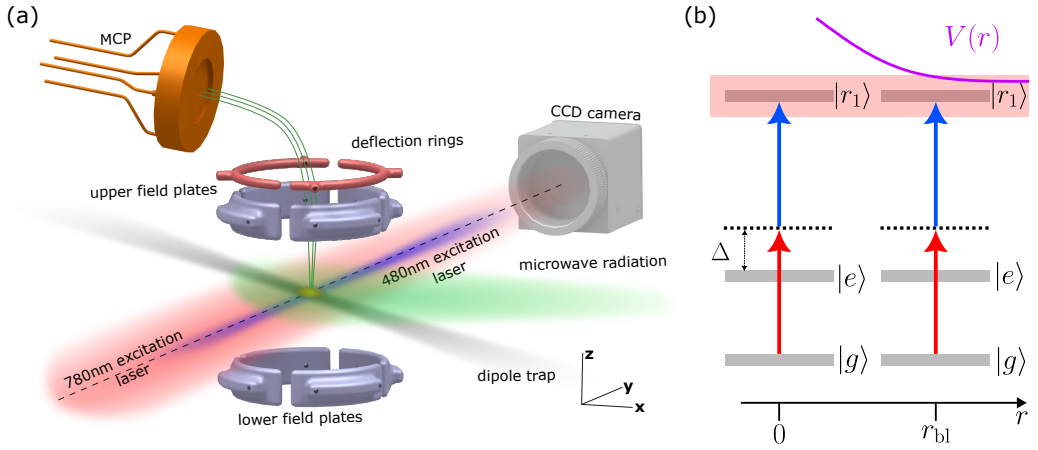

Figure 3.1: *Preparation of a frozen Rydberg gas.* (a) Schematic of the experimental apparatus. Atoms are initially loaded into a three-dimensional magneto-optical trap (3D MOT) and subsequently transferred into a crossed beam optical dipole trap (gray region), where they adopt a Gaussian spatial distribution (yellow ellipsoid). Excitation to Rydberg states is achieved via a two-photon transition using a 780 nm (red) and and 480 nm (blue) excitation laser. Transitions between Rydberg states are driven by microwave radiation (green). A strong electric field is applied using the field plates to ionize the Rydberg atoms and detect them on a microchannel plate (MCP). Figure taken and adapted from [161]. (b) Excitation and the Rydberg Blockade. Gray rectangles represent the atomic energy levels: ground state $|g\rangle$, intermediate state $|e\rangle$, and Rydberg state $|r_1\rangle$. The two-photon excitation pathway is shown by red (780 nm) and blue (480 nm) arrows. The single-photon detuning Δ from the intermediate state $|e\rangle$ is indicated by a black dashed line. The violet solid curve shows the Rydberg interaction potential $V(r)$ as a function of interatomic distance r. At short distances, the interaction-induced energy shift of the doubly excited Rydberg state exceeds the excitation linewidth (red shaded region). Excitation for both atoms is only possible for distances r larger than the blockade radius r_{bl}.

experiments presented in this thesis.

The crossed-beam optical dipole trap confines a cloud of rubidium atoms in the ground state $\left|5S_{1/2}, F = 2, m_F = 2\right\rangle$. The atomic spatial distribution follows a Gaussian profile, with widths determined by the temperature of the trapped cloud and the power and waist of the trapping beams. From this point, we have two options to modify the positional distribution of Rydberg atoms:

(i) We increase the positional disorder in the ground-state atoms by allowing the

atomic cloud to expand freely for a time t_{tof}. After this expansion, the spatial distribution can be approximated by a three-dimensional Gaussian profile with standard deviations σ_x and $\sigma_y = \sigma_z$. Increasing t_{tof} leads to higher values of these standard deviations, which enhances spatial disorder in the atomic cloud prior to Rydberg excitation.

(ii) We reduce the positional disorder of Rydberg atoms by exciting a larger number of atoms within a fixed volume. To this end, we control the Rydberg excitation time t_{exc}. During this time, atoms are excited from the ground state $|g\rangle$ to the Rydberg state $|r_1\rangle = \left|61S_{1/2}, m_J = 1/2\right\rangle$ using a two-photon excitation scheme. A 780 nm coupling beam, blue-detuned by 97 MHz from the $|g\rangle \rightarrow |e\rangle$ transition, and a 480 nm probe beam drive the excitation. The excitation time t_{exc} not only determines the number of excited atoms N_r, but also sets the minimum allowed distance between Rydberg atoms due to the Rydberg blockade effect [162–165], illustrated in Fig. 3.1(b). The blockade radius r_{bl} is defined by the condition that the Rydberg-Rydberg interaction energy is equal to the excitation line width. To ensure precise control over the excitation linewidth, we operate the experiment in a regime where the linewidth is dominated by the Fourier width of the excitation pulse. In this regime, the linewidth decreases with increasing excitation time t_{exc}. Therefore, a longer excitation time leads to a larger blockade radius. The Rydberg blockade introduces short-range positional correlations, as atoms within a blockade radius cannot be simultaneously excited. As a result, a larger r_{bl} reduces positional disorder in the Rydberg ensemble.

In summary, the positional disorder of the Rydberg ensemble can be systematically controlled by adjusting the excitation time t_{exc} and the free expansion duration t_{tof}. To quantify the degree of disorder, we estimate the mean interparticle distance r_{mean} using a depletion imaging technique [166]. The Rydberg blockade radius r_{bl} is obtained by a calibration protocol described in [155]. This protocol involves fitting a model that incorporates theoretical input parameters calculated with the *PairInteraction* package [167], with r_{bl} as the only free parameter in the fit. We create two regimes of different disorder strength by choosing t_{tof} and t_{exc} such that the overall system size is kept approximately constant, allowing us to isolate the role of disorder on the dynamics and exclude possible finite-size effects in the comparison.

We emphasize that, unlike previous experiments on this platform [42, 43, 48, 155, 168], the strong magnetic field applied here induces anisotropy in the Rydberg-Rydberg excitation responsible for the blockade radius. Specifically, the blockade radius is approximately twice as large in the plane perpendicular to the magnetic field compared to the axis aligned with it, as detailed in Appendix D. This leads to

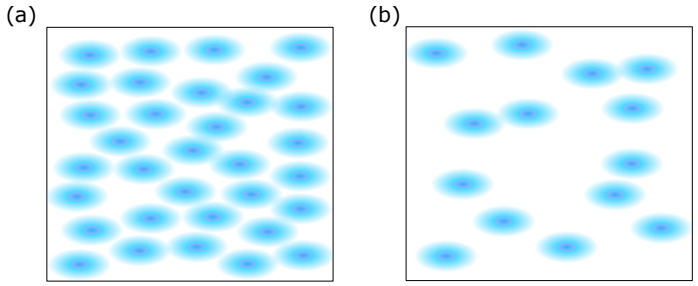

Figure 3.2: *Sketch of different disorder realizations.* Rydberg atoms (dark blue circle) exhibit the blockade effect, preventing the excitation of neighboring atoms within the blockade radius. The extent of the blockade region (light blue ellipses) is anisotropic due to the presence of a strong magnetic field, which is assumed in vertical direction. (a) Weakly disordered regime. (b) Strongly disordered regime. Inspiration taken from [155].

an anisotropic blockade radius. The two realized configurations incorporating this anisotropy are illustrated in Fig. 3.2. The calculated blockade radius, following the method introduced in [155], is derived from a model assuming isotropic interactions. Thus, our value for r_{bl} represents an average over all spatial directions. The ratio $r_{\mathrm{bl}}/r_{\mathrm{mean}}$ serves as a quantitative measure of positional disorder in the Rydberg cloud. The different times controlling the atomic ground state distribution and the parameters characterizing the Rydberg cloud are summarized in Tab. 3.1.

regime	N_g	N_r	t_{exc} [µs]	t_{tof} [µs]	σ_x [µm]	$\sigma_{y,z}$ [µm]	r_{mean} [µm]	r_{bl} [µm]
weak disorder	10300	2250	5	600	140	49	18.7	8.15
strong disorder	9300	2100	1	2000	137	97	26.5	7.85

Table 3.1: Comparison of parameters for the Rydberg excitation for the two different disorder configurations. Table taken and adapted from [169].

3.1.2 Experimental realization of a disordered dipolar Heisenberg XY spin model

To realize an effective Heisenberg XY spin-1/2 Hamiltonian, we exploit the fact that a spin-1/2 system is inherently a two-level system. In our implementation, this pseudospin degree of freedom is encoded in two Rydberg states, $|r_1\rangle$ and $|r_2\rangle$, which are eigenstates of the atomic Hamiltonian in the presence of a magnetic field. These states

are coherently coupled by a microwave field at frequency ω, generated using a Keysight M8195A arbitrary waveform generator (AWG). The choice $|r_1\rangle = \left|61S_{1/2}, m_J = 1/2\right\rangle$ is motivated by practical considerations: transition frequencies between Rydberg states with principal quantum number $n = 61$ remain below 25 GHz, and can thus be directly accessed using the AWG. The exact transition frequencies are listed in Tab. 3.2. As discussed above, a strong external magnetic field of 185 G is applied to energetically isolate the relevant Zeeman sublevels, thereby justifying the validity of the two-level approximation. Within this framework, we identify the states $|r_1\rangle \equiv |\downarrow\rangle$ and $|r_2\rangle \equiv |\uparrow\rangle$ as the eigenstates of the spin-1/2 operator S_z. The dipole-dipole interaction between atoms in these Rydberg states naturally gives rise to an effective Heisenberg XY spin model, as established in previous works [42, 48, 170–174]:

$$H_{\mathrm{dd}} = \sum_{i<j} J_{ij} \left(S_x^{(i)} S_x^{(j)} + S_y^{(i)} S_y^{(j)} \right), \tag{3.1}$$

where $S_\alpha^{(i)}$ denotes the component α of the spin-1/2 operator acting on spin i. These couplings J_{ij} ($\hbar = 1$) follow a dipolar interaction law

$$J_{ij} = \frac{C_3}{r_{ij}^3}(1 - 3\cos(\theta_{ij})^2), \tag{3.2}$$

where C_3 is the dispersion coefficient, r_{ij} the distance between spins i and j, and θ_{ij} the angle between the interparticle axis and the z-axis. The dispersion coefficient C_3 usually depends only on the choice of the Rydberg states $|r_1\rangle$ and $|r_2\rangle$. However, since the magnetic field is strong enough to start mixing states in the Rydberg manifold, $|r_2\rangle$ and thus also the C_3 coefficient depend on the magnetic field as well. The dependence of the dispersion coefficients on strong static electric and magnetic fields, as used in this work, is derived in detail in Appendix D.

The timescale of the system's dynamics is primarily determined by the magnitude of the nearest-neighbor couplings, irrespective of their sign. We therefore define the median coupling strength $J_{\mathrm{med}} \coloneqq \underset{i}{\mathrm{median}} \max_j |J_{ij}|$ as a natural reference scale [42]. The relative standard deviation $\sigma_J/J_{\mathrm{med}}$, with $\sigma_J \coloneqq \underset{i}{\mathrm{std}} \max_j |J_{ij}|$, quantifies the degree of bond disorder, i.e., variations in the interaction strengths across the system. Although both J_{med} and $\sigma_J/J_{\mathrm{med}}$ capture key properties of the Hamiltonian, they are not directly measurable. To estimate these quantities, we numerically sample disorder realizations of Rydberg atom positions using the experimental parameters listed in Tab. 3.1, following the procedure of Ref. [155]. The coefficient C_3, which sets the overall interaction scale and is only dependent on the Rydberg states $|r_1\rangle$ and $|r_2\rangle$, but not on the positional disorder configuration, is computed using the

PairInteraction package. We then evaluate the couplings J_{ij} for all pairs r_i and r_j using Eq. 3.2, and extract J_{med} and σ_J from their distribution. To further characterize the distribution of nearest-neighbor couplings, we define, for each spin i, the index $j^* = \max_j |J_{ij}|$ identifying its strongest coupling, and denote the nearest-neighbor coupling as $J_i := J_{ij^*}$. The values J_i are binned into a histogram with a bin width of 1 MHz, which is smaller but comparable to J_{med}. This ensures the histogram is smooth without over-resolving fine details. The histogram is normalized to unity, thereby estimating a probability density. To obtain a smooth, parameter-free estimation of the probability distribution, we further apply a Gaussian Kernel Density Estimate (KDE) [175, 176], with the kernel bandwidth selected according to Scott's rule [176].

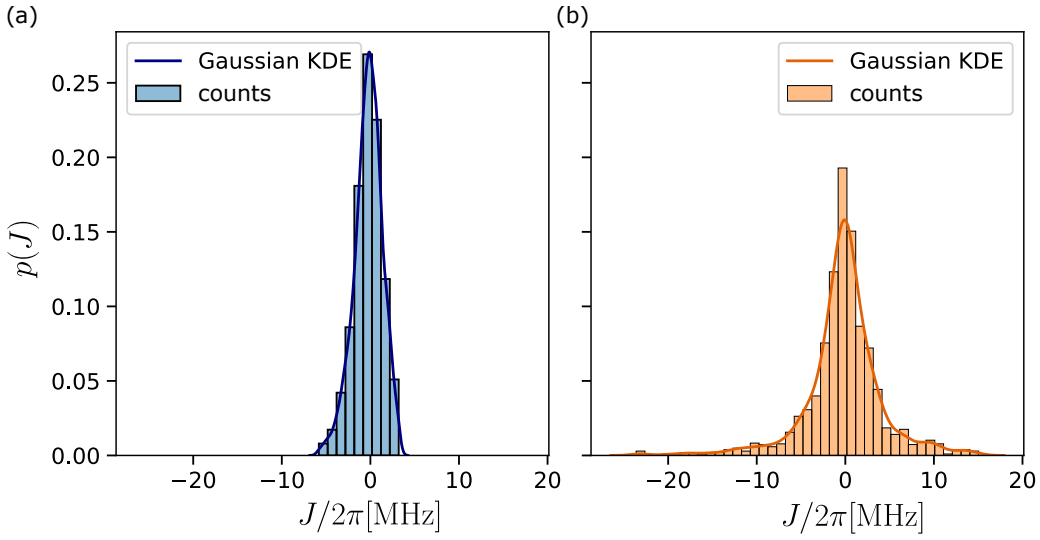

Figure 3.3: *Simulated coupling probability distributions.* Histogram of the coupling strengths calculated from atom positions sampled according to the experimental parameters in Tab. 3.1. The data are binned into histograms (blue and orange bars) with a width of 1 MHz. The solid line shows a Gaussian kernel density estimate (KDE) of the distribution, with the bandwidth chosen according to Scott's rule. Panels (a) and (b) show results for the weakly and strongly disordered regimes, respectively.

To realize two regimes with different disorder strengths while keeping all other parameters fixed, we prepare a similar number of Rydberg atoms in two configurations with different ground-state densities: a dense regime with weak positional disorder, and a dilute regime with strong disorder. In the dense configuration, the reduced mean interparticle distance leads to stronger interactions for a given pair of Rydberg states $|r_1\rangle$ and $|r_2\rangle$, resulting in a larger median coupling strength. To compensate for

this effect and ensure comparable interaction scales in both regimes, we select different Rydberg states $|r_2\rangle$. Specifically, the state $\left|61P_{3/2}, m_J = 1/2\right\rangle$ exhibits a dispersion coefficient C_3 to $|r_1\rangle$ that is approximately twice as large as that of $\left|61P_{1/2}, m_J = 1/2\right\rangle$ to $|r_1\rangle$. Since the mean interparticle distance in the weakly disordered regime is smaller, we choose the state with the weaker dipolar interaction for this case to ensure comparable values of J_{med} in both configurations. This strategy yields two disorder regimes that differ in spatial distribution and interaction anisotropy, yet exhibit similar median coupling strengths. Consequently, their dynamical behavior can be directly compared, isolating the effect of bond disorder. The specific choices of $|r_2\rangle$, along with the resulting values of J_{med} and σ_J/J_{med}, are summarized in Tab. 3.2. The corresponding probability distributions of nearest-neighbor couplings, including their signs, are shown in Fig. 3.3.

	$\lvert r_2\rangle$	$\omega/(2\pi)$ [MHz]	$J_{\text{med}}/(2\pi)$	σ_J/J_{med}
weak disorder	$\left\lvert 61P_{1/2}, m_J = 1/2\right\rangle$	15 791.2	1.01	1.02
strong disorder	$\left\lvert 61P_{3/2}, m_J = 1/2\right\rangle$	16 324.4	1.63	2.24

Table 3.2: Parameters relevant for the microwave drive

For the study of energetic-magnetic hysteresis effects with the simulated spin model, we need to measure the global magnetization. The x- and y-component of the maqnetization can be mapped onto a measuremnt of the z-component via a tomgraophic readout, which we discuss in more detail in Appendix A. The measurement of the z-component, on the other hand, is closely connected to a measurement of the population in the state $|r_2\rangle$, which corresponds to evaluating the operator $\sum_i \left(S_z^{(i)} + \frac{1}{2}\mathbb{1}\right)$. To determine this population, a laser pulse at 480 nm, resonant with the $|e\rangle \to |r_1\rangle$ transition, is applied for a duration of 5 µs. Given the short lifetime of the intermediate state $|e\rangle$ (26.2 ns [177]), this pulse is sufficient to depopulate the occupancy in the state $|r_1\rangle$ through rapid decay [178].

Subsequently, the remaining population in $|r_2\rangle$, as well as any atoms that may have decayed into other Rydberg states, which are above the ionization threshold, is detected via field ionization. A strong electric field is applied using field plates, ionizing all atoms in the Rydberg state above the ionization threshold. The resulting ions are deflected onto a microchannel plate (MCP) detector, where the signal from the impacting ions generates voltage peaks. These peaks are then counted to determine the number of detected ions N.

To extract the z-magnetization for an experimental protocol of duration t, two

reference measurements are performed:

1. **Calibration of the total atom number N_{tot}:** Following Rydberg excitation, the AWG prepares all atoms in the equal superposition state $\frac{1}{\sqrt{2}}(|\uparrow\rangle + |\downarrow\rangle)$. This accounts for the fact that the two Rydberg states $|r_1\rangle$ and $|r_2\rangle$ have different lifetimes. A strong electric field is then applied after time t to ionize all atoms in a Rydberg state. The influence of finite lifetimes on magnetization measurements is further discussed in Chap. 4.

2. **Detection of background atom number N_{dp}:** After excitation to the state $|r_1\rangle$, the system is allowed to evolve for a time t before applying a down-pumping pulse intended to depopulate all Rydberg states. However, due to black-body radiation–induced decay, some atoms populate nearby Rydberg levels that have negligible interaction with the states $|r_1\rangle$ and $|r_2\rangle$. These atoms do not participate in the dynamics governed by the interaction Hamiltonian, but still contribute as background ions upon field ionization.

Assuming that the ion number is proportional to the Rydberg population, we thus obtain for the expectation value of the average z-magnetization, when N ions are measured:

$$\frac{1}{N_r}\sum_{i=1}^{N_r}\left\langle S_z^{(i)}\right\rangle = \frac{2N - N_{\mathrm{tot}} - N_{\mathrm{dp}}}{2\left(N_{\mathrm{tot}} - N_{\mathrm{dp}}\right)}. \tag{3.3}$$

3.1.3 Experimental realization of time-dependent effective magnetic fields

The Hamiltonian in Eq. 3.1 describes a bond-disordered Heisenberg XY spin model with dipolar interactions. This model arises naturally from Rydberg-Rydberg interactions. To investigate magnetic susceptibilities, an external field coupling to individual spins must be implemented experimentally. In this section, we show how resonant microwave radiation can be used to engineer effective magnetic fields acting on the spin degrees of freedom. These fields enable both energetic tuning of the spin system and access to its magnetic response. Throughout the experiments presented in the main text of this thesis, the applied microwave power remains sufficiently weak to justify a perturbative treatment. Under these conditions, the two-level approximation holds. A contrasting regime, characterized by strong microwave driving and involving multiple atomic levels, is discussed in Appendix E. We begin by describing the experimental implementation of the microwave coupling, and then analyze its impact on the effective spin Hamiltonian.

The microwave signal is generated by the AWG and emitted into free space using a horn antenna. A wire grid polarizer ensures that the radiation is vertically polarized, parallel to the external magnetic field. By aligning the polarizer wires perpendicular to the magnetic field created by the MOT coils, the radiation becomes π-polarized relative to the quantization axis. This polarization restricts the set of allowed transitions through dipole selection rules, enabling cleaner state addressing in combination with spectral selectivity. This polarized electromagnetic wave couples to the electric dipole moment of the Rydberg atoms. As a consequence, the Hamiltonian for the interaction of the atom with the microwave radiation at frequency ω reads

$$\begin{aligned} H(t) &= -E_z(t)\hat{d}_z + H_0 \\ &= -(i\frac{E}{2}e^{i\phi}e^{-i\omega t} - i\frac{E}{2}e^{-i\phi}e^{i\omega t})\hat{d}_z + H_0, \end{aligned}$$

where E defines the amplitude and ϕ the phase of the drive frequency, $\hat{d}$ the electric dipole operator of the atom and H_0 the atomic Hamiltonian [179]. Assuming a dipole-allowed transition between two atomic eigenstates $|\uparrow\rangle$ and $|\downarrow\rangle$ that is resonant with the driving field, the system Hamiltonian can be expressed in the basis of these two states. By moving to the rotating frame and applying the rotating wave approximation (RWA), the Hamiltonian can be further simplified to

$$\begin{aligned} H &= \begin{pmatrix} 0 & -i\frac{E}{2}e^{-i\phi}d \\ i\frac{E}{2}e^{i\phi}d & 0 \end{pmatrix} = \frac{1}{2}\begin{pmatrix} 0 & -i\Omega^* \\ i\Omega & 0 \end{pmatrix} \\ &= \frac{1}{2}\begin{pmatrix} 0 & -i\,\mathrm{Re}(\Omega) - \mathrm{Im}(\Omega) \\ i\,\mathrm{Re}(\Omega) - \mathrm{Im}(\Omega) & 0 \end{pmatrix} \\ &= -\,\mathrm{Im}(\Omega)\frac{1}{2}\begin{pmatrix} 0 & 1 \\ 1 & 0 \end{pmatrix} + \mathrm{Re}(\Omega)\frac{1}{2}\begin{pmatrix} 0 & -i \\ i & 0 \end{pmatrix} \\ &= -\,\mathrm{Im}(\Omega)S_x + \mathrm{Re}(\Omega)S_y, \end{aligned}$$

where $d = \langle\uparrow|\hat{d}|\downarrow\rangle \in \mathbb{R}$ is the dipole matrix element between the two atomic eigenstates, and $\Omega = dEe^{i\phi}$ is the complex valued Rabi frequency. By this definition of Ω, we immediately see that the phase ϕ of the drive $E_z(t) = -E\sin(\omega t + \phi)$ is exactly equal to the phase of the Rabi frequency. Identifying $\mathrm{Im}(\Omega) \coloneqq \Omega_x$ and $-\,\mathrm{Re}(\Omega) \coloneqq \Omega_y$ we recover the paramagnetic Hamiltonian

$$H_{\text{para}} = -\Omega_x \sum_i S_x^{(i)} - \Omega_y \sum_i S_y^{(i)}, \tag{3.4}$$

This corresponds to a spin model in which the spins couple only to an external field, with no spin-spin interactions. The external field is effectively realized through resonant microwave driving.

The experiments utilize a Keysight M8195A AWG, featuring an analog bandwidth of 25 GHz and a sampling rate of 65 GSa s^{-1}. This enables phase and amplitude modulation of radiation up to 25 GHz on timescales as short as 16 ps. By controlling both the phase and amplitude of the drive as functions of time t, we can dynamically tune the phase and amplitude of the Rabi frequency, and consequently the direction and magnitude of the effective magnetic field $\begin{pmatrix}\Omega_x(t) & \Omega_y(t)\end{pmatrix}$.

Including the effect of microwave radiation, the total Hamiltonian of the disordered Rydberg cloud reads

$$\begin{aligned} H &= H_{\mathrm{dd}} + H_{\mathrm{para}} \\ &= \sum_{i<j} J_{ij}\left(S_x^{(i)}S_x^{(j)} + S_y^{(i)}S_y^{(j)}\right) - \Omega_x\sum_i S_x^{(i)} - \Omega_y\sum_i S_y^{(i)}. \end{aligned} \tag{3.5}$$

3.2 Measuring energetic-magnetic irreversibility

Drawing an analogy to thermomagnetic hysteresis, we define *energetic-magnetic hysteresis* as a memory effect that depends on both the magnetic field and the energy history of a system. To experimentally create such an energy history in an isolated spin system, it is necessary to devise a method for tuning the system's energy in a controlled manner. For this purpose, we employ an annealing protocol, schematically illustrated in Fig. 3.4(a), which was initially introduced in [156], and further studied in a different direcion in the context of aging in Ref. [180].

3.2.1 Annealing in an isolated dipolar-interacting spin system

The main idea of the annealing protocol is to prepare the ground state of H_{para} and then dynamically change the magnetic field to prepare a low-energy state of H_{dd}. The duration of this change will make the transition more diabatic, thus introducing more energy to the system. In detail, we prepare the fully spin-polarized state in z-direction $|\Psi_z\rangle = |\downarrow\rangle^{\otimes N_r}$ by excitation of N_r atoms into the state $|r_1\rangle$. A subsequent application of a Rabi $\pi/2$-pulse [179] with Rabi frequency Ω rotates this state into the x-basis, yielding the fully spin-polarized state in x-direction $|\Psi_x\rangle = |\rightarrow\rangle^{\otimes N_r}$, where $S_x|\rightarrow\rangle = \frac{1}{2}|\rightarrow\rangle$. In order to achieve a high fidelity in the preparation of $|\Psi_x\rangle$, we choose $\Omega \gg J_{\mathrm{med}}$. By application of a large field with amplitude $\Omega_{x,0} \gg |J_{ij}|\,\forall i,j$ in

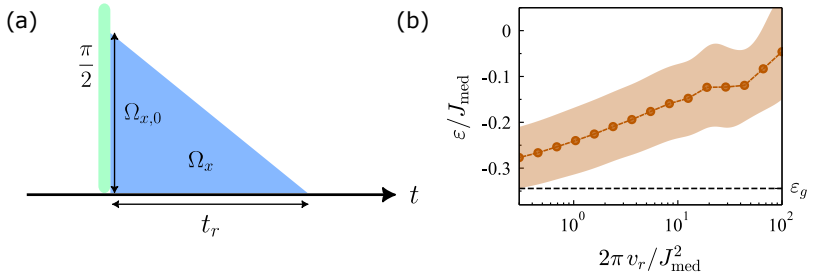

Figure 3.4: *Annealing in an isolated spin system.* (a) Sketch of the annealing protocol. Field strength of the $\pi/2$-pulse (green) and the annealing field (blue) as a function of time. Initial field strength $\Omega_{x,0}$ and ramp time t_r are indicated by arrows. (b) Numerical simulation of mean energy per particle (orange dots) and uncertainty represented by one standard deviation (orange region) for the annealing protocol as a function of ramp speed. The mean and standard deviation of ε is taken performed over different disorder realization of the Hamiltonian. Simulation is performed in a system with $N = 12$ particles, $\Omega_{x,0} = 2.4 J_{\mathrm{med}}$ and disorder $\sigma_J / J_{\mathrm{med}} = 0.33$. A dashed line indicates the average ground state energy ε_g. Figure (b) taken from [169].

the x-direction, this state is effectively the ground state of H_{para} where $\Omega_x = \Omega_{x,0}$ and $\Omega_y = 0$.

To modify the system's energy, we apply a time-dependent annealing field along the x-direction. The field amplitude follows the linear ramp

$$\Omega_x(t) = \Omega_{x,0} - v_r t, \quad 0 \leq t \leq t_r, \tag{3.6}$$

where t_r is the ramp time, and $v_r = \Omega_{x,0}/t_r$ is the ramp speed. In order to express the ramp speed as a dimensionless quantity related to the typical energy scale of the Hamiltonian J_{med}, we rescale the energy of the initial ramp field $\Omega_{x,0}$ by J_{med}, and the ramp time t_r by the duration of a typical interaction cycle $2\pi/J_{\mathrm{med}}$, giving the quantity $\Omega_{x,0}/J_{\mathrm{med}}/\left(t_r/\left(2\pi/J_{\mathrm{med}}\right)\right) = 2\pi v_r/J_{\mathrm{med}}^2$.

As stated above, because $\Omega_{x,0}$ is large compared to all couplings J_{ij}, spin-spin interactions can be neglected at $t = 0$ and the Hamiltonian Eq. 3.5 reduces to the paramagnetic Hamiltonian H_{para}. In this paramagnetic regime, the ground state configuration is the fully polarized state $|\Psi_x\rangle$. The field ramp can be interpreted as an annealing scheme from H_{para} to H_{dd} [181]. Variation of the ramp speed v_r allows one to initialize states at different mean energies per particle ε, as depicted in Fig. 3.4(b). Fast (diabatic) ramps leave the system in the initial polarized state $|\Psi_x\rangle$, corresponding to a high-energy state with $\varepsilon \sim 0$. In contrast, slow (adiabatic) ramps

allow the system to follow the instantaneous eigenstate, and thus prepare it close the ground state of H_{dd} with energy ε_g.

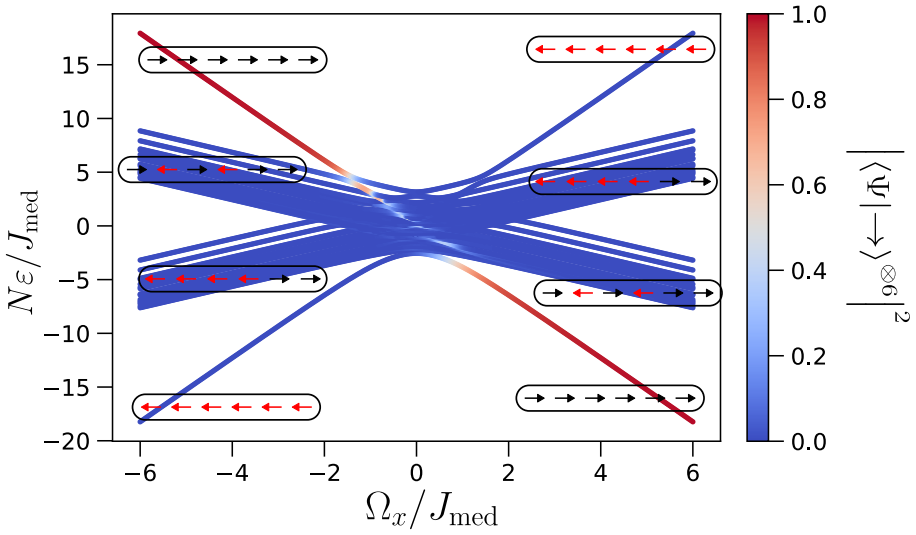

Figure 3.5: *Positive parity spectrum of a disordered Heisenberg XY model.* Eigenenergies $N\varepsilon$ in the positive parity subspace as a function of the applied magnetic field Ω_x for a single disorder realization with $N = 6$ particles. All energies are given in units of J_{med}. The color indicates the overlap of the eigenvector corresponding to that eigenenergy with the fully polarized state $|\rightarrow\rangle^{\otimes 6}$ in x-direction. Arrows indicate asymptotic states for large magnetic fields, where either 0, 2, 4, or all 6 spins are reversed. Aligned spins are depicted in black, while anti-aligned states are depicted in red. Figure and Caption taken and adapted from [169].

To better illustrate the annealing protocol, we analyze the energy spectrum of a disordered Heisenberg XY model with a transverse field along the x-direction. The Hamiltonian conserves the parity operator $P = \prod_{i=1}^{N} S_x^{(i)}$, implying that states of different parity are not interacting. Since the annealing protocol uses the fully polarized state $|\rightarrow\rangle^{\otimes N}$ in $x-$-direction as the initial state, which has even parity for even N, the system evolves entirely within the even-parity subspace. Consequently, we restrict our analysis to this subspace of the Hilbert space.

In Fig. 3.5, we show the energy spectrum of the even-parity eigenstates as a function of the annealing field Ω_x, computed for a single disorder realization with $N = 6$ spins. In the limit of strong transverse fields, $|\Omega_x| \gg J_{\mathrm{med}}$, the spin–spin interactions act as a perturbation to the paramagnetic limit. In this regime, the

eigenenergies vary linearly with Ω_x, and each spin contributes $\pm\frac{1}{2}\Omega_x$ depending on its alignment along x-direction.

Due to the parity constraint, only configurations with an even number of spins aligned along each direction are allowed. The corresponding asymptotic energies are thus given by $-3\Omega_x$, $-\Omega_x$, Ω_x, and $3\Omega_x$, corresponding to spin configurations with 6, 4, 2, or 0 spins anti-aligned with the field, respectively. The asymptotic spin configurations are indicated alongside the eigenstates in Fig. 3.5.

For large positive fields, the ground state exhibits an almost perfect overlap with the fully spin-polarized state $|\Psi_x\rangle$. Infinitely slow adiabatic annealing therefore follows the instantaneous ground state, leading to the preparation of the ground state of H_{dd}. When Ω_x is quenched to zero, the expectation value of the energy with respect to H_{dd} remains close to zero. This results from the disordered couplings J_{ij}, which include both positive and negative values and thus cancel in the energy expectation. An infinitely fast quench consequently populates either eigenstates near zero energy or a superposition of states with positive and negative energies that average to zero. The system is therefore initialized in a high-energy state relative to the ground state of H_{dd}. Due to the $\mathbb{Z}_2$-symmetry of H_{dd}, an energy $\varepsilon = 0$ corresponds, within the microcanonical ensemble, to an infinite-temperature state. By varying the ramp speed between these two limits, states can be prepared with energies continuously ranging from the ground-state energy up to zero energy. Within the microcanonical description, these energies correspond to zero and infinite temperature, respectively, thus spanning the full thermodynamic range of the system. Since faster ramps induce more diabatic transitions between energy levels, the resulting state energy increases monotonically with ramp speed.

3.2.2 Zero-field annealing and field annealing protocols

Based on this annealing scheme, we experimentally implement two protocols designed to study energetic-magnetic hysteresis. While similar protocols have previously been explored numerically in the context of quantum thermalization and aging, and compared to canonical spin glass behavior [180], our work focuses on their experimental realization using a Rydberg quantum simulator. The results are interpreted in light of findings from both canonical and dipolar spin glasses, providing a framework to understand magnetic irreversibility in this system.

In analogy to the well-known ZFC and FC protocols discussed in Chapter 2, we refer to these schemes as zero-field annealing (ZFA) and field annealing (FA). The ZFA protocol is a variant of a similar protocol, which has been proposed and simulated in the context of aging [156]. As illustrated in Fig. 3.6(a), both protocols

employ two time-dependent external fields: an annealing field Ω_x, which controls the system's energy, and a probe field Ω_y, which allows us to measure the magnetization response. The magnetization is measured by the average expectation value of the spin-1/2 operator

$$M_\alpha = \frac{1}{N}\sum_i \left\langle S_\alpha^{(i)} \right\rangle = \langle S_\alpha \rangle \,, \tag{3.7}$$

where M_α denotes the α-component of the magnetization, and S_α without superscript denotes the average spin operator of the N spins in the system.

In both protocols, the annealing ramp is applied at the beginning of the sequence. After that, in case of the ZFA protocol, the system is let to equilibrate at $\Omega_x = 0$ for a waiting time t_w, during which any remanent magnetization relaxes towards zero. Subsequently, a small probe field Ω_y is applied and the steady-state magnetization M_y is measured in y-direction. The relaxation prior to field application ensures that the application of the probe field does not introduce additional energy to the system, thus allowing to study magnetic response at constant energy conditions. For the FA protocol, the probe field Ω_y is permanently applied from the start of the annealing ramp. After the ramp, the system equilibrates at finite Ω_y. The probe field is chosen orthogonal to the annealing field, thus ensuring that the build-up of the measured magnetization is caused by the probe field alone, and not by the annealing field.

Both protocols are implemented on the Rydberg simulation platform in the two disorder regimes. For clarity, we first discuss the time evolution in the weakly disordered regime. To account for possible experimental imperfections, we measure not only the y-magnetization, but all magnetization components using a tomographic readout technique[155, 157], described in detail in Appendix A. The time-dependent magnetization components are shown in Fig. 3.6(b), and the corresponding experimental parameters are provided in the figure caption.

In the ZFA protocol, both M_x and M_z relax to zero by the end of the waiting time. Since t_w is on the order of $2\pi/J_{\text{med}} \approx 0.99\,\mu\text{s}$, we infer that only a few interaction cycles among the more strongly coupled spins are sufficient to equilibrate the magnetization. This behavior was also shown in previous work in our group [42, 43], and is consistent with results from dipolar spin glasses [39–41], where enhanced coherent quantum tunneling dynamics were found to accelerate otherwise slow glassy relaxation.

$2\,\mu\text{s}$ after application of the probe field in the ZFA protocol ($3\,\mu\text{s}$ after the end of the ramp in the FA protocol) M_y reaches an equilibrium value, which does not change over several interaction cycles and we call the ZFA (FA) magnetization. As a consequence, for the following measurements, we fix $t_\text{w} = 1\,\mu\text{s}$ and measure the ZFA/FA magnetization $3\,\mu\text{s}$ after the annealing ramp.

We also observe two unexpected phenomena arising from experimental imperfec-

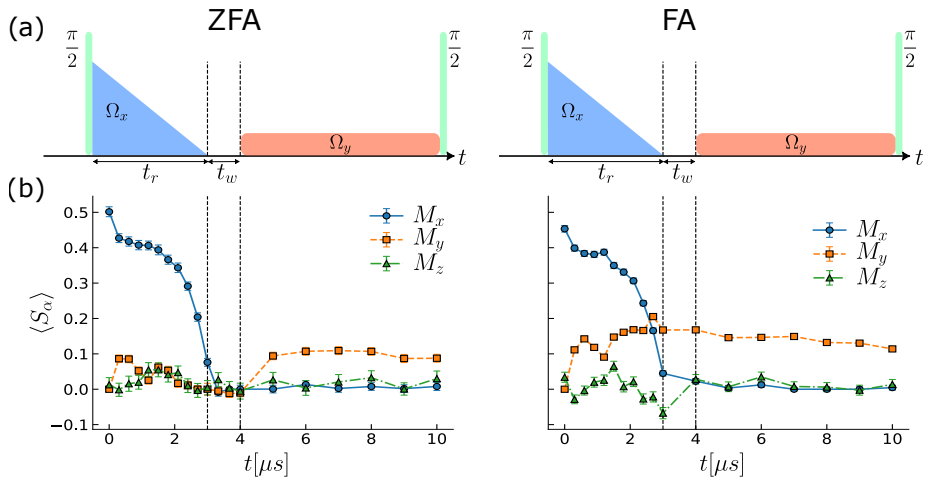

Figure 3.6: *Time evolution of the ZFA and FA protocols.* (a) Sketches of applied fields in different direction in the ZFA (left) and FA (right) protocls. Black lines indicate waiting time in the ZFA protocol. Green rectangles depict Rabi $\pi/2-$pulses. Blue triangle and orange rectangle depict time-dependence of the annealing and probe field, respectively. Waiting time t_w and ramp time t_r are indicate by black arrows. (b) Experimental realization ($\Omega/2\pi = 12.18\,\text{MHz}$, $\Omega_x/2\pi = 3.65\,\text{MHz}$, $\Omega_y/2\pi = 0.49\,\text{MHz}$, $t_r = 3\,\mu\text{s}$, $t_w = 1\,\mu\text{s}$) of the ZFA (left) and FA (right) protocols. Magnetization components M_x (blue), M_y (orange) and M_z (green) measured as a function of evolution time t in µs. Figure created from data in [169]. Capture taken and adapted from [169].

tions, which we believe do not significantly affect the resulting ZFA or FA magnetizations.

1. In the ZFA protocol, oscillations in M_y and M_z are observed during the annealing ramp, despite theoretical predictions that these components should remain zero throughout the protocol [42].

2. In the FA protocol, we note that M_x is less than 0.5 for the initial state and has non-zero y- and z- components.

A possible explanation for the first observation is a time-dependent light shift induced by the annealing ramp. As the microwave drive power decreases over time, light shifts to nearby Rydberg states may also decrease, thereby modifying the transition frequency between $|r_1\rangle$ and $|r_2\rangle$, calibrated at Rabi frequency $\Omega_{x,0}$. Consequently, the microwave drive becomes slightly detuned from resonance. Within

the rotating-wave approximation, this detuning acts as an effective magnetic field along the z-direction in the spin model, producing a time-dependent longitudinal field component. The resulting field induces a rotation of the global magnetization in the $x-y$ plane, which can account for the observed build-up of y-magnetization. The build-up of z-magnetization may be explained by a small deviation of the microwave phase from $\pi/2$, which introduces a y-component to the annealing field, shifting it away from the intended orientation along the x-axis. A weak global field along y then drives a rotation of the magnetization in the $x-z$ plane. The second observation, on the other hand, may be explained by power fluctuations in the microwave drive after calibration, thus leading to an imperfect $\pi/2$-pulse, which causes the reduction in initial x-magnetization.

For both effects, we assume that their impact on the measured ZFA and FA magnetizations is negligible. Since $M_x \gg M_{y,z}$ throughout the annealing ramp, the prepared energy at the end of the protocol is expected to be robust against small oscillations of the M_y and M_z components. Moreover, in the ZFA protocol, both transverse components relax during the waiting time, such that their influence on the final magnetization after the probe field is applied is minimal. Even if the initial state is not perfectly polarized in x-direction, a spin-polarized configuration with a large x-magnetization still has substantial overlap with the ground state. Consequently, imperfections in the initial state preparation are expected to have only minor effects on both the ZFA and FA magnetizations.

3.2.3 Excursus: zero-field annealing of an isolated paramagnet

Before discussing the dependence of ZFA and FA magnetizations on the annealing ramp time, it is worth noting that the magnetic response in the ZFA protocol is unexpected. For a single spin initially aligned along x, a magnetic field along y induces rotation in the $x-z$ plane but does not generate a y-component. To build further intuition, we consider a system without spin-spin interactions, defined as a paramagnet, in which spins couple only to an external magnetic field. We study its magnetic response under constant energy conditions. Energy conservation is justified because, in the ZFA protocol, the probe field is quenched when $M_y = 0$, so no additional energy is injected. Moreover, since the Hamiltonian remains time-independent after the probe is applied, the total energy is conserved throughout the subsequent evolution. We first analyze the linear response from a thermal equilibrium state with zero magnetization using the Kubo formula [182]. This choice is to better compare the result to the ZFA protocol, where the magnetization is let to equilibrate

prior to application of the probe field, even though this equilibrium state must not necessarily be a thermal equilibrium state. We then compare these results to thermodynamic predictions, where we employ the Legendre transform of the entropy with respect to the magnetic field as the thermodynamic potential. This choice allows us to determine equilibrium values at fixed energy and external magnetic field, conditions that are precisely realized in the ZFA protocol under the assumption of a quasi-static process.

Since a paramagnet is defined as an ensemble of non-interacting spins coupled only to an external magnetic field, its dynamics can be fully captured by analyzing a single spin. Accordingly, we perform our analysis for a single spin-$\frac{1}{2}$ particle. The results can be straightforwardly generalized to a paramagnet consisting of N spins by interpreting the single-particle spin operators S_α as collective spin operators, i.e., sums over the individual spins in the ensemble. We consider the Hamiltonian of a single spin subject to a magnetic field Ω oriented along the x-direction, given by $H_0 = -\Omega S_x$. We assume that the spin reaches thermal equilibrium under this Hamiltonian, with the system initialized at zero total energy. To probe the system's response, we examine the y-component of the magnetization, $M_y = \langle S_y \rangle$, under the influence of a perturbation $H_{\text{pert}} = -\Omega_y S_y$, which simulates the effect of an external probe field applied along the y-direction.

In the interaction picture, the time evolution of the operator S_y is given as

$$\begin{aligned} S_y(t) &= e^{iH_0 t} S_y e^{-iH_0 t} = e^{-i\Omega t S_x} S_y e^{i\Omega t S_x} \\ &= S_y + \frac{(-i\Omega t)^1}{1!}[S_x, S_y] + \frac{(-i\Omega t)^2}{2!}[S_x, [S_x, S_y]] + \dots \\ &= S_y + \frac{(\Omega t)^1}{1!} S_z - \frac{(\Omega t)^2}{2!} S_y + \dots = \cos(\Omega t) S_y + \sin(\Omega t) S_z, \end{aligned} \tag{3.8}$$

where we made use of the Hadamard formula in the first line and the spin algebra commutation relation $[S_\alpha, S_\beta] = i\epsilon_{\alpha\beta\gamma} S_\gamma$ in the second line. We insert these relations into the Kubo formula:

$$\begin{aligned} \langle S_y \rangle (t) &= -i \int_0^t \langle [S_y(t), H_{\text{pert}}(t')] \rangle \, dt' \\ &= i\Omega_y \int_0^t \langle [\cos(\Omega t) S_y + \sin(\Omega t) S_z, \cos(\Omega t') S_y + \sin(\Omega t') S_z] \rangle \, dt' \\ &= -i\Omega_y \int_0^t (\sin(\Omega t)\cos(\Omega t') - \sin(\Omega t')\cos(\Omega t)) i \langle S_x \rangle \\ &= \Omega_y \langle S_x \rangle \int_0^t \sin(\Omega(t-t'))dt' = \Omega_y \langle S_x \rangle \frac{1-\cos(\Omega t)}{\Omega}. \end{aligned} \tag{3.9}$$

We observe that for a state with no equilibrium magnetization, i.e. where $\langle S_x \rangle$ is zero, the Kubo formula yields no response. In the limit of negligible fields in x-direction, which is the limit at the end of the annealing ramp, we obtain $\lim_{\Omega \to 0} \frac{1-\cos(\Omega t)}{\Omega} = 0$ and also no response. Thus, for a paramagnet, we expect no ZFA response at all.

This behavior can be understood thermodynamically by using a potential with magnetic field Ω and energy E as natural variables. In the absence of thermal fluctuations, the temperature and, by the third law, the entropy are zero. In this regime, $E = -M\Omega$, where M is the magnetization. This thermodynamic potential allows access to the linear susceptibility at constant energy: $\chi_{\text{mag}} = \left(\frac{\partial M}{\partial \Omega}\right)_E$. For zero magnetic field, $E = 0$, and in a constant-energy process, E remains zero. Hence, $M\Omega = E = 0$ implies $M = 0$ also for finite Ω. Since $M = \chi_{\text{mag}}\Omega$ for small but finite Ω, we find $\chi_{\text{mag}} = 0$. Thus, due to the restricted phase space at zero energy, no magnetic response is expected.

In spin systems that thermalize according to the eigenstate thermalization hypothesis (ETH) [117, 118], high-energy eigenstates are expected to exhibit paramagnetic behavior. Consequently, the observation of a finite magnetic ZFA response indicates a deviation from paramagnetic behavior, suggesting that the system may instead reside in a distinct low-energy regime.

3.2.4 Susceptibilities and the onset of hysteresis

We aim to investigate energetic-magnetic hysteresis by comparing the magnetization response of many-body states that share the same final energy and applied magnetic field, but originate from different dynamical protocols, each encoding a distinct history. In the limit $M_y \to 0$, the ZFA and FA protocols become effectively equivalent, preparing final states that are nearly indistinguishable in terms of both energy and probe field. This regime enables a direct comparison of the magnetic response as a function of the system's history. To quantify this response, we measure the transverse magnetization M_y as a function of the applied probe field Ω_y. Linearizing this relation around $\Omega_y = 0$ allows us to extract the linear magnetic susceptibility for each protocol:

$$\chi_{\text{mag}} := \left(\frac{\partial M_y}{\partial \Omega_y}\right)\Big|_{\Omega_y = 0}. \tag{3.10}$$

The experimental realizations of the ZFA and FA protocols for the two disorder configurations sketched in Fig. 3.2 are presented in Fig. 3.7. The insets display the measured magnetization as a function of the probe field Ω_y for a fixed ramp time of 3 µs, revealing a linear response regime at small probe amplitudes. In the weakly disordered configuration, the ZFA and FA magnetization curves exhibit

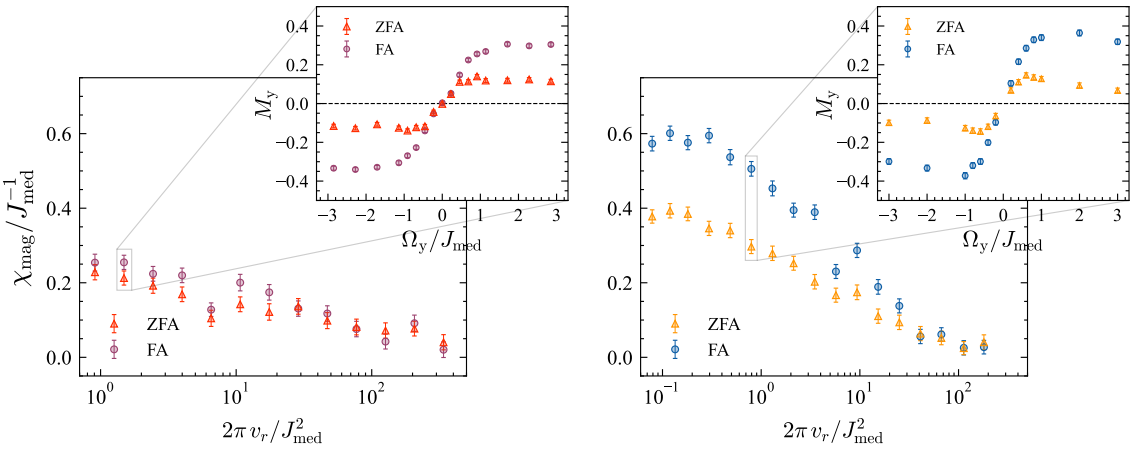

Figure 3.7: *Measurements of ZFA and FA susceptibilities in two disorder configurations.* (a) Linear susceptibility χ_{mag} in units of J_{med} as a function of the ramp speed v_r rescaled by $J_{\mathrm{med}} = 2\pi \times 1.01\,\mathrm{MHz}$ for the ZFA (red) and FA (violet) magnetization in the weakly disordered regime. Inset shows response measurements of y-magnetization as a function of the dimensionless probe field $\Omega_y/J_{\mathrm{med}}$. Magnetization is measured 3 µs after the end of the annealing ramp, corresponding to 5 interaction cycles of the median interaction. In both cases the equilibration time is chosen such that both protocols have the same absolute duration when magnetization in y-direction. A linear fit to the 5 data points centered around zero is used to extract the susceptibility and its errorbar. (b) Linear susceptibility χ_{mag} in units of J_{med} as a function of the ramp speed v_r rescaled by $J_{\mathrm{med}} = 2\pi \times 1.63\,\mathrm{MHz}$ for the ZFA (yellow) and FA (blue) magnetization in the strongly disordered regime. Inset shows response measurements of y-magnetization as a function of the dimensionless probe field $\Omega_y/J_{\mathrm{med}}$. A linear fit to the 5 data points centered around zero is used to extract the susceptibility and its errorbar. Figure and caption taken and adapted from [169].

nearly identical slopes, indicating similar magnetic susceptibilities. In contrast, for the strongly disordered configuration, the slopes differ substantially, suggesting a history-dependent magnetic response. As discussed above, the probe field in the ZFA protocol does not change the energy of the system, whereas in the FA protocol it does: since a finite y-magnetization already builds up during the annealing along the direction of the applied field, the product $M_y\Omega_y$ is nonzero, leading to a slight reduction in the energy of the FA state. This behavior was also observed in Ref. [180], where a 12-particle numerical simulation showed that for slow ramps, the FA energy lies below the ZFA energy. Moreover, the magnetization difference between

the two states was found to vary nonlinearly with their energy difference, inconsistent with a paramagnetic description where energy and magnetization are negatively correlated. This was interpreted as evidence that the splitting between ZFA and FA magnetizations originates from history effects rather than from energy differences. While we agree that the system is no longer in a paramagnetic regime, consistent with the finite ZFA response, the strong nonlinear behavior inherent to the dipolar Heisenberg-XY model does not exclude a nonlinear dependence of magnetization on energy. Therefore, we cannot fully exclude the possibility that the observed splitting stems from an energy difference between the ZFA and FA states. However, the fact that the largest splitting between ZFA and FA susceptibilities in the strongly disordered regime is almost an order of magnitude larger than the largest splitting observed in the weakly disordered regime, makes this scenario rather unlikely.

The magnetic susceptibilities for both protocols are extracted from a linear fit of the magnetization for small probe fields, and are shown as a function of ramp speed in Fig. 3.7. We find a common behavior of the susceptibilities independent of the disorder configuration and the protocol: At very fast ramps, corresponding to final states at high energy, the susceptibilities approach zero for both disorder configurations, consistent with the paramagnetic behavior discussed previously. As the ramp speed decreases and the system's energy approaches the ground state energy, the susceptibilities increase monotonically for both ZFA and FA protocols. This trend mirrors the behavior of thermal magnetic systems at low temperatures, where the fluctuation-dissipation theorem links enhanced susceptibility to the emergence of spin correlations [183].

We observe a clear distinction between the two disorder configurations. In the weakly disordered regime, the ZFA and FA susceptibilities coincide within experimental uncertainty, whereas in the strongly disordered case a bifurcation emerges already at comparatively fast ramps, $2\pi v_r/J_{\mathrm{med}} \approx 15$. In the latter regime, the difference between the two susceptibilities increases as the system energy decreases, indicating pronounced hysteresis and, consequently, irreversible behavior. Irreversibility can be understood in analogy with irreversible quasistatic thermodynamic processes, where the system's state depends on its history, such that a closed loop in the natural variable space leads to a different final state. Using entropy as a thermodynamic potential, the divergence between the ZFA and FA susceptibilities therefore serves as a signature of thermodyamic irreversibility. In thermal equilibrium, the magnetic susceptibility should depend solely on the system's energy and not on its history, i.e., it should be identical for both protocols. The observed deviation thus implies that at least one of the two final states realized in the protocols does not represent a thermal equilibrium state. The non-thermal nature of this bifurcation may indicate

the emergence of a new phase at low energies.

3.3 Conclusion

In this chapter, we initiated our experimental investigation of the low-energy dynamics in a disordered, dipolar-interacting Heisenberg XY spin model in three dimensions. We first outlined how this model is realized on a Rydberg atom quantum simulation platform, and then introduced an annealing protocol that allows controlled tuning of an isolated system's energy.

The capability to control the energy of an isolated quantum system enables the exploration of non-equilibrium phenomena that are typically studied in thermally equilibrated settings. In this context, we adapted the well-established zero-field-cooled (ZFC) and field-cooled (FC) protocols to the regime of isolated quantum dynamics. Specifically, we introduced and implemented quantum analogues of these procedures, referred to as zero-field annealing (ZFA) and field annealing (FA), on our quantum simulation platform.

In the high-energy regime, the system exhibits behavior reminiscent of the paramagnetic phase in canonical spin glasses. In contrast, the low-energy regime, characterized by a bifurcation between the zero-field-annealed (ZFA) and field-annealed (FA) susceptibilities, remains to be fully understood. The observed energy-dependent magnetic hysteresis qualitatively resembles thermomagnetic hysteresis phenomena reported in canonical spin glasses [83, 184, 185], suggesting the possible emergence of a quantum spin glass phase. This interpretation is supported by earlier observations of anomalously slow relaxation and incomplete thermalization in our system [42, 43]. Moreover, the bifurcation appears already at fast ramps, with relaxation dynamics occurring on timescales comparable to the median interaction cycle. This is consistent with findings in dipolar spin glasses, where unitary evolution has been shown to facilitate the formation of a spin glass phase through quantum tunneling, more efficiently than classical thermal fluctuations [35, 41].

Previous work has shown that the magnetization dynamics of strongly disordered, isolated dipolar spin systems can be effectively described by the evolution of interacting pairs of spins [42, 186]. In the limiting case of purely antiferromagnetic couplings, such a pair-based description reproduces the random singlet phase [63, 64, 66, 187, 188]. Conversely, when ferromagnetic couplings dominate, the model exhibits similarities to a cluster glass or superspin glass [84], for which a bifurcation between zero-field-cooled (ZFC) and field-cooled (FC) susceptibilities has also been observed in systems coupled to a thermal bath, as we discussed in Chapter 2.

Given that our Heisenberg system incorporates both ferromagnetic and antiferromagnetic interactions, future studies may aim to explore potential connections between these two distinct phases. In particular, time-reversal protocols, which have recently been demonstrated in our platform [48], offer a promising tool: While the random singlet phase preserves time-reversal symmetry, the spin glass phase is characterized by spontaneous breaking of this symmetry.

The bifurcation between ZFA and FA susceptibilities suggests a spin glass phase, motivating several potential research directions.

1. In the mean-field Parisi picture of spin glasses, the field-cooled (FA) state is generally considered a metastable configuration that corresponds to the thermal equilibrium expectation value [68]. However, this interpretation has been challenged by recent experimental results [87, 88]. A deeper characterization of the FA state, particularly through the study of time-dependent self-similarity in the form of aging [189], could provide new insights into the nature of the FA state and address fundamental questions about the spin glass phase. The phenomenon of aging, along with a proposed experimental realization, is discussed further in Chapter 6.

2. As discussed in Chapter 2, two hallmarks of the spin glass phase are the divergence of the nonlinear susceptibility, as well as a weak frequency dependence of the ac-susceptibility as a function of temperature. These phenomena allow to test whether critical behavior, establishing the glass as an equilibrium phase, are present. We propose an experimental realization in Chapter 6.

3. In the introduction, we noted that it is an open question, related to the long-standing question of replica symmetry breaking [16] or droplet scaling model [17, 18], whether a spin glass phase can persist at finite magnetic fields, and whether there is a second order phase transition. This was also questioned specifically for dipolar spin glasses [190]. In the next chapter, Chapter 4, we devise a protocol based on the Kibble-Zurek mechanism [191–193] to study exactly this question.

As a final remark, we note that the presented ZFA and FA protocols are interaction-agnostic and applicable to arbitrary spin models with $\mathbb{Z}_2$ parity symmetry, as this symmetry ensures that $|\Psi_x\rangle$ corresponds to a high-energy state. Thus, they provide a robust framework for probing thermalization in quantum systems beyond the dipolar model studied above. In addition to advancing understanding of spin glass physics, the protocols also offer practical relevance for benchmarking adiabaticity and performance in annealing-based quantum computing platforms [110, 194–196].

CHAPTER 4

Characterizing Critical Behavior with a Global Protocol

As discussed in the previous chapter, the onset of hysteresis constitutes a necessary, but not sufficient condition for the emergence of a spin glass phase. A natural progression from this observation is to investigate whether a second-order phase transition occurs between the paramagnetic phase and the proposed spin glass phase. As established in Chapter 2, the existence of such a transition is well supported for known spin glasses as a function of temperature. However, whether this transition persists down to zero temperature, as a quantum phase transition where the magnetic field serves as a control parameter, remains a topic of significant debate.

In this chapter, we aim to contribute to the resolution of the following question:

Does a spin glass phase exist in the dipolar-interacting Heisenberg XY model, and if so, is it connected to a quantum phase transition driven by an external magnetic field?

Given that quantum phase transitions are characterized by critical exponents, we also address a complementary question:

How can the critical exponents of a spin glass be experimentally accessed in an isolated quantum system, where temperature scaling is absent?

As the experimental platform introduced in the previous chapter has only access to global observables, we seek a protocol that characterizes the critical exponents of a second-order quantum phase transition by global measurements only. Therefore, we develop a theory, based on an extension of the Kibble-Zurek mechanism (KZM).

The Kibble-Zurek mechanism (KZM) originates from studies by Kibble on defect formation in the early universe [191], and was later adapted by Zurek for quantum systems [192, 193]. It is a general concept which relates the dynamical formation of topological defects to the equilibrium critical exponents of a continuous phase transition. In so called *forward quenches* where the control parameter is ramped once across the critical point, the KZM predicts scaling laws for defect density and correlation lengths based on critical exponents and the quench rate. Its validity in the quantum realm is astonishing, as for a many-body quantum system, it couples the physics of quantum phase transitions to the complex nonlinear dynamics of highly correlated systems. The validity of the KZM goes far beyond the initial prediction on equilibrium second order phase transitions, reaching from non-equilibrium transitions [197–203] over topological phase transitions [44] to transitions through a critical surface [204] and transitions with an inhomogenous drive [205–207].

This chapter, which further builds upon the KZM, is organized as follows. We begin with a review of the generalized Kibble-Zurek mechanism (gKZM) in Sec. 4.1, introduced by Adolfo del Campo [208–213]. While the KZM makes predictions about the expected number of defects after a forward quench, the gKZM predicts the full counting statistics including all higher order cumulants of the defects. Its main result is that the measurement of these higher order cumulants as a function of the quench time allows for a measurement of the KZM critical exponent, which quantifies the phase transition. We then extend the gKZM to *reverse quenches* [214–217] in Sec. 4.2, where the system is driven twice across a quantum critical point. This allows us to derive the main result of this chapter, which is a general relation between the variance of the defect density after a forward quench and the defect density after a reverse quench protocol for quantum spin systems. We benchmark the validity of our extension in two model systems. First, we study the transverse field Ising model (TFIM) in Sec. 4.3 using both analytical and numerical methods. Parts of the numerical implementation and, in particular, the analysis of the Stückelberg oscillations were carried out under the supervision of the author by Daniel Rubin and were included in his Bachelor's thesis [218]. Second, we apply the protocol to the bond-disordered TFIM in Sec. 4.4, focusing on numerical simulations.

Next, for quantum phase transitions involving a paramagnetic phase, we show in Sec. 4.5 that global magnetization measurements can serve as a reliable approximation for the defect density, thus eliminating the need for local measurements We also discuss the limitations and qualitative implications of this approach. The idea of using global reverse quenches to identify a possible spin glass critical point was originally proposed in the author's Master's thesis [219]. Finally, we implement the reverse quench protocol on our experimental platform, using the two disorder configurations

introduced in the previous chapter. We present and analyze the resulting data in Sec. 4.6 and conclude with a summary of the main findings and their broader significance in Sec. 4.7.

4.1 The generalized Kibble-Zurek mechanism

We outline the physics of the KZM and the gKZM on the example of a spin system that undergoes a continuous phase transition as a function of the magnetic field h at the critical point h_c. For the derivations in this section, we only rely on the universal behavior of the system at the critical point. As such, the derivations are both valid for a classical system in thermal equilibrium undergoing a thermal phase transition as well as for an isolated quantum system undergoing a quantum phase transition. Close to the critical point, the correlation length ξ of the system diverges as a power law

$$\xi(h) = \xi_0 \left| \frac{h - h_c}{h_c} \right|^{-\nu}, \tag{4.1}$$

where ν is the correlation length critical exponent, and ξ_0 the correlation length at $h = 0$. The typical timescale of the system τ, for example a relaxation time, also diverges close to criticality

$$\tau(h) = \tau_0 \left| \frac{h - h_c}{h_c} \right|^{-z\nu}, \tag{4.2}$$

where z is the dynamical critical exponent and τ_0 the typical timescale at $h = 0$ [44, 102].

We now review the system's behavior when the field h is quenched across a phase transition, a process known as the forward quench protocol, illustrated in Fig. 4.1(a). Our derivation mainly follows [209], which presents KZM and gKZM for systems of arbitrary dimension. In this protocol, the system is initially prepared in equilibrium far from the critical point at a field $h_0 \gg h_c$. For spin systems in the large-field limit, the system is paramagnetic, with the equilibrium state fully polarized along the initial field. The control parameter h is then varied linearly in time, driving the system across the critical point

$$h(t) = -h_0 \frac{t}{\tau_Q}, \quad -\tau_Q \leq t \leq 0, \tag{4.3}$$

where τ_Q is the quench time and t the instantaneous time. Let $\Delta t(t)$ denote the remaining time to reach the critical point at a given time t. As the control parameter

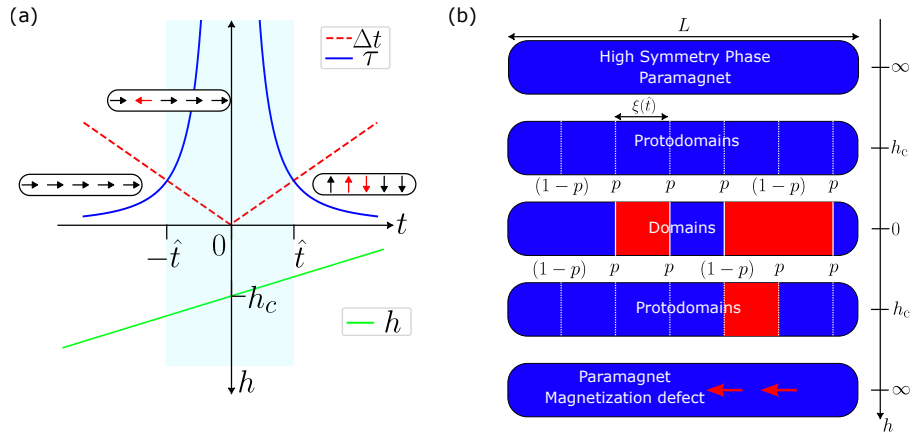

Figure 4.1: *Schematic of the generalized and the standard Kibble-Zurek mechanism.* (a) Adiabatic impulse approximation in an Ising ferromagnet. The system is driven from the paramagnetic phase through the critical field h_c. The figure features two anti-aligned vertical axes. The green line (lower axis) shows the linear variation of the field $h(t)$, with time t defined so that $h(t = 0) = h_c$. The red dashed and blue solid lines (top axis) represent the remaining time Δt to the critical point and the system's response time τ, respectively. The cyan shaded region marks the freeze-out interval between $-\hat{t}$ and $\hat{t}$, during which the system's dynamics effectively freeze. The inset arrows illustrate spin configurations, with defects highlighted in red. (b) Reverse quench protocol in the gKZM framework for an Ising ferromagnet. The system of size L evolves through successive stages of the reverse quench, each at a different magnetic field h. Initially, it is in a defect-free paramagnetic phase (blue). As h decreases past the critical value h_c, protodomains of size ξ form, separated by white dashed boundaries. At $h = 0$, deep in the ferromagnetic phase, these boundaries become domain walls (black lines) separating domains with distinct magnetizations (red and blue). When the field increases and crosses h_c again, the protodomain pattern reappears. In the final paramagnetic phase, residual domain walls adiabatically transform into localized spin-flip defects (red arrows).

$h(t)$ approaches the critical value h_c, the correlation length ξ and relaxation time τ diverge according to equations 4.1 and 4.2, while $\Delta t(t)$ decreases linearly. This leads to the definition of the freeze-out time $\hat{t}$, determined by the condition $\tau(-\hat{t}) = \Delta t(-\hat{t})$. Since Δt depends on the quench time τ_Q, the freeze-out time $\hat{t}$ is likewise a function of τ_Q.

At $-\hat{t}$, the system can no longer evolve adiabatically and falls out of equilibrium.

The correlation length becomes effectively frozen at $\xi = \xi(-\hat{t})$. This behavior is described by the adiabatic impulse approximation [44], which has been experimentally observed across various platforms [220–223].

As a result, domains form with an average size $\xi(-\hat{t})$, separated by domain walls that arise as non-equilibrium excitations, i.e., defects. After the time $\hat{t}$, as the system moves further away from the critical point, adiabatic evolution resumes. According to the KZM, the domain walls generated at the freeze-out time become adiabatically connected to the defects in the final phase. For this reason, we use the terms *domain wall* and *defect* interchangeably in the following discussion.

For a d-dimensional defect in a D-dimensional system, the KZM predicts that the defect density after a forward quench scales as

$$n_{\text{def}} \sim \frac{\xi(-\hat{t})^d}{\xi(-\hat{t})^D} \sim \tau_Q^{\frac{(d-D)\nu}{1+z\nu}} = \tau_Q^{-\mu}, \tag{4.4}$$

where μ is the KZM critical exponent, which can be used to distinguish different universality classes [44].

Equation 4.4 predicts the expected number of defects n_{def} as a function of the quench time τ_Q. Intuitively, it implies that faster quenches drive the system further out of equilibrium, resulting in a higher number of elementary excitations. However, this prediction concerns only the expectation value of the defect density and provides no information about the statistical properties of the defects, such as their variance or higher-order cumulants. To access these quantities, a microscopic probabilistic model of defect formation is required, which is precisely what the gKZM provides.

For pedagogical clarity, we introduce the gKZM in the context of a one-dimensional system ($D = 1$) with point-like defects ($d = 0$). As shown in Fig. 4.1(b), the gKZM offers a stochastic reinterpretation of the scaling behavior presented in Eq. 4.4, previously derived from adiabatic and diabatic dynamics in the standard KZM. In this formulation, the system at the critical point is divided into protodomains [212] of fixed length $\xi(-\hat{t})$, corresponding to the frozen correlation length. For a system of length L, the number of protodomains N is thus $\frac{L}{\xi(-\hat{t}(\tau_Q))}$. Unlike KZM domains, which have a distribution of sizes and correspond to observable structures, protodomains are a conceptual tool: they partition the system into equal segments of length $\xi(-\hat{t})$, within which no domain wall can arise by construction.

After the system traverses the critical point, a domain wall may form between any two adjacent protodomains with a probability p, which depends on the microscopic details of the system. Physical domains are then defined as regions consisting of contiguous protodomains bounded by two domain walls.

The generalized Kibble-Zurek mechanism (gKZM) extends the classical KZM by modeling domain wall formation probabilistically. The simplest assumption is that domain walls form independently at each boundary between adjacent protodomains, with a uniform probability p. This corresponds to a Bernoulli process for defect formation [208, 209]. Each of the N protodomain boundaries represents an independent trial where a domain wall appears with probability p. In one-dimensional systems, the number of boundaries equals the number of protodomains. In higher dimensions, the number of boundaries is proportional to the number of protodomains by a factor $1/f$, where f reflects the typical number of protodomains meeting at a boundary.

Within this stochastic framework, the average defect density at the end of the quench follows

$$n_{\mathrm{def}}(\tau_Q) = \frac{1}{L}Np = \frac{1}{L}p\frac{L}{\xi\left(-\hat{t}(\tau_Q)\right)} = \frac{p}{\xi_0}\left(\frac{\tau_Q}{\tau_0}\right)^{-\mu} \sim \tau_Q^{-\mu}. \tag{4.5}$$

As noted by Ref. [208], the scaling predicted by the gKZM matches exactly the classical KZM scaling given in Eq. 4.4, including the correct critical exponent μ. Moreover, interpreting defect formation as a Bernoulli process enables calculation of higher-order cumulants of the defect density. In particular, the variance of the average defect density, $\mathrm{Var}\left(n_{\mathrm{def}}\right)$, is given by

$$\mathrm{Var}\left(n_{\mathrm{def}}\right) = \frac{1}{L}Np(1-p) = \frac{1}{L}p\left(1-p\right)\frac{L}{\xi\left(-\hat{t}(\tau_Q)\right)} = \frac{p\left(1-p\right)}{\xi_0}\left(\frac{\tau_Q}{\tau_0}\right)^{-\mu}. \tag{4.6}$$

Thus, the defect variance also scales with the KZM exponent μ as a function of the quench time τ_Q. Furthermore, the Bernoulli-process formulation allows calculation of higher-order cumulants of the defect distribution, which is not possible in the classical KZM framework. This approach has been extended to higher-dimensional systems [209, 224] and recently also to systems with long-range interactions [225].

4.2 Extending the generalized Kibble-Zurek mechanism to reverse quenches

Here, we extend the gKZM to analyze the dynamics along reverse quenches, which is sketched in Fig. 4.1(b). In the reverse quench protocol, the magnetic field is quenched forth and back over the critical field with the same speed, i.e.

$$h(t) = h_0|t|/\tau_Q, \quad -\tau_Q \leq t \leq \tau_Q. \tag{4.7}$$

We analyze the protocol regarding it as a sequence of two distinct forward quenches: the first occurring in the time $-\tau_Q \leq t \leq 0$ and the second one in $0 \leq t \leq \tau_Q$. Each of these can be viewed as a distinct forward quench originating from a different original phase. In case of the first quench, at time $-\hat{t}$ the standard gKZM applies. The correlation length is frozen and the system can be divided in protodomains, where the boundaries between adjacent protodomains form a domain wall with probability p. After crossing the critical point, the domain walls adiabatically transform into the defects of the respective phase, but the number of defects remains constant. This follows from the adiabatic impulse approximation.

In the second quench, we use the adiabatic impulse approximation again. The system follows the drive adiabatically, keeping the number of defects constant, until the correlation length freezes again. Assuming equal critical components on both sides approaching the phase transition, this correlation length will be equal to the freezing length of the first quench $\xi\left(-\hat{t}(\tau_Q)\right) = \xi\left(\hat{t}(\tau_Q)\right)$. As such, the system can be divided again into the same protodomains. However, unlike in the first quench, the system is at the beginning of the second quench not in equilibrium. As a result, domain walls, which were formed during the first quench, are already present at the boundaries between adjacent protodomains. For each boundary, a domain wall already exists with probability p.

At this point, we introduce the key assumption for applying the gKZM to reverse quenches. If a domain wall is absent (present) at a given boundary, the reverse quench creates (annihilates) a domain wall with probability p. Consequently, after the second quench, a domain wall remains either if it was formed during the second quench or if it was initially present and survived, in both cases with probability $1-p$. The combined probability to find a domain wall is $2p(1-p)$. This result agrees with [226], where a single forward quench crosses two identical critical points, a scenario mathematically equivalent to a reverse quench across a single critical point.

Using the stochastic framework of an N-trial Bernoulli process, we calculate the expected defect density following a reverse quench:

$$n_{\text{def}}^{\text{rev}} = \frac{1}{L} 2p\,(1-p)\,N = \frac{1}{L} 2p\,(1-p)\,\frac{L}{\xi(\hat{t})} = 2\frac{p\,(1-p)}{\xi_0}\left(\frac{\tau_Q}{\tau_0}\right)^{-\mu}. \tag{4.8}$$

At this point, we find that the reverse quench defect density shows the same scaling behavior with the very same critical exponent μ as the forward quench. This is consistent with studies on reverse quenches from microscopic dynamics in different 1D systems [214–217], where the gKZM was not used. In addition, a comparison to Eq. 4.6 yields

$$n_{\text{def}}^{\text{rev}} = 2\text{Var}\left(n_{\text{def}}\right), \tag{4.9}$$

which is our main prediction of the gKZM on reverse quench defect densities:

The variation of the defect density after a forward quench equals half of the defect density after a reverse quench protocol.

Our extension of the gKZM thus allows fluctuations (the variance of the defect density after a forward quench) to be inferred from an average macroscopic observable (the average defect density). In addition, a comparison to Eq. 4.5 yields

$$n_{\mathrm{def}}^{\mathrm{rev}} = 2\,(1-p)\,n_{\mathrm{def}}, \tag{4.10}$$

which allows for a direct calculation of the probability p. This is also consistent with the other studies mentioned previously [214–217]. A second method to obtain p results from equating equations 4.9 and 4.10,

$$\mathrm{Var}\,(n_{\mathrm{def}}) = (1-p)\,n_{\mathrm{def}}. \tag{4.11}$$

Comparing the values for p obtained by Eq. 4.10 and Eq. 4.11 allows to validate our extension of the gKZM.

4.3 The uniform transverse field Ising model

We benchmark our findings of the gKZM on two different paradigmatic models. We start with reviewing the results of the 1D uniform transverse field Ising model (TFIM), which belongs to the class of quasifree fermion models, together with others like the 1D XY, the 1D Heisenberg and the 1D Kitaev model. For these models, the gKZM is predicted to hold for forward quenches [208, 212]. In this section, we will derive the defect density in the forward and reverse quenches and the defect density variance in the forward quench scenario from a microscopic picture. The results are then compared to our gKZM predictions. In order to simplify the mathematical and numerical treatment, we study the dimensionless model Hamiltonian

$$H = -\sum_{i=1}^{N} J_i \sigma_i^z \sigma_{i+1}^z - h \sum_{i=1}^{N} \sigma_i^x, \tag{4.12}$$

where N is the number of spins, σ_i^α a Pauli-α operator acting on spin i, $J_i > 0$ the coupling constant between spins i and $i+1$, and h an external magnetic field. Throughout this article, we apply periodic boundary conditions, i.e. $\vec{\sigma}_{N+1} = \vec{\sigma}_1$. For $J_i = 1$, i.e. the TFIM with uniform couplings, which we call the uniform TFIM, this model shows a quantum phase transition at $h_c = 1$ with critical exponents $z = \nu = 1$ and $\mu = 1/2$ [102]. For simplicity, we will restrict without loss of generality to the case of an even particle number [227, 228].

Forward quench defect density

The forward quench protocol was initially studied in [227], and recently again in [229]. We shortly review the most important steps. The basic idea is to perform a Jordan-Wigner transform on the the Ising Hamiltonian and describe the Pauli operators by spinless fermionic creation and annihilation operators

$$\sigma_i^z = -\prod_{j<i}(1-2c_j^\dagger c_j)(c_i + c_i^\dagger) \tag{4.13}$$

$$\sigma_i^x = 1 - 2c_i^\dagger c_i \tag{4.14}$$

Without loss of generality, we assume an equal number of particles. The periodic boundary conditions of the spin Hamiltonian then translate into anti-periodic boundary conditions for the fermionic annihilation operators, $c_{N+1} = -c_1$. For an odd number of spins, the treatment is analogous. The resulting Hamiltonian is:

$$H = \sum_{i=1}^{N}(c_i - c_i^\dagger)(c_{i+1} + c_{i+1}^\dagger) + h(2c_i^\dagger c_i - 1). \tag{4.15}$$

This Hamiltonian can be Fourier-transformed into momentum space to yield

$$H = \sum_k 2(h - \cos(k))c_k^\dagger c_k + \sin(k)(c_k^\dagger c_{-k}^\dagger + c_{-k}c_k) - h. \tag{4.16}$$

In momentum space, with modes

$$k \in \left\{\pm\frac{\pi}{N}, \pm\frac{3\pi}{N}, \ldots, \pm\frac{(N-1)\pi}{N}\right\},$$

the Hamiltonian decomposes into N independent two-level systems. Each pair of modes $\pm k$ undergoes a Landau-Zener crossing with gap $\Delta_k = (4\tau_Q \sin^2 k)^{-1}$. For an odd number of spins, the modes are the same, but an additional non-interacting mode $k = \pi$ requires separate treatment; the Landau-Zener picture still applies to all other modes.

A defect corresponds to an excitation of a Landau-Zener system, with the excitation probability for each mode k given by

$$p_k = e^{-\frac{\pi}{2\Delta_k}}. \tag{4.17}$$

For slow quenches, only the long wavelength modes get excited, such that p_k has a relevant support only close to zero [229], and can be approximated for $k \approx 0$ as a Gaussian

$$p_k \approx e^{-2\pi\tau_Q k^2}. \tag{4.18}$$

In the thermodynamic limit $N \to \infty$, the defect density is given by

$$\begin{aligned} n_{\text{def}} &= \lim_{N\to\infty} \frac{1}{N} \sum_k p_k = \frac{1}{2\pi} \int_{-\pi}^{\pi} p_k dk \\ &\approx \frac{1}{2\pi} \int_{-\infty}^{\infty} p_k dk = \frac{1}{2\pi} \frac{1}{\sqrt{2\tau_Q}}. \end{aligned} \tag{4.19}$$

This approximation is valid as long as the width of the Gaussian integral is way smaller than 2π. As p_k is a Gaussian function centered around 0, if the width of the Gaussian function is way less than 2π, extending the integration boundaries from $(-\pi, \pi)$ to $(-\infty, \infty)$ will leave the integral almost unchanged. This condition is fulfilled for $\frac{1}{\sqrt{4\pi\tau_Q}} \ll \pi$, which is true for long quench times.

We also read off $\mu = \frac{1}{2}$ from Eq. 4.19, as predicted both from the KZM and the gKZM.

Reverse quench defect density

For the uniform TFIM, the reverse quench protocol was solved exactly for arbitrary quench times in [217]. Unlike in the forward quench, interference arises between paths where a defect forms in the first or second forward quench. This effect produces oscillations in the defect density as a function of the quench time, known as Stückelberg oscillations [217, 230–232]. An approach neglecting these oscillations is discussed in [214]. Here, we adopt an alternative approach that incorporates Stückelberg oscillations to approximate the defect density in the limit of large quench times.

For the treatment of the Stückelberg oscillations, we follow mainly [232]. For a single k-mode, the reverse quench protocol is equivalent to a double passage of a Landau-Zener crossing. In this double passage, an interference effect occurs when measuring the excitation probability. The path in which an excitation occurs in the first crossing but not in the second one interferes with the path in which an excitation occurs in the second crossing but not in the first one. The phase difference between these two paths is the Stückelberg phase Φ_{St}

$$\Phi_{\text{St}} = \zeta_1 + \phi_S, \tag{4.20}$$

where ζ_1 is the phase acquired during an adiabatic evolution and ϕ_S is the Stokes phase which is acquired due to the non-adiabatic nature of a forward quench. ζ_1 can

be calculated from the energy difference between the two Landau-Zener crossings, i.e.

$$\begin{aligned}\zeta_1(k) &= \frac{1}{2}\int_{t_1}^{t_2} \Delta E_k(t) dt \\ &= 2\int_{t_1}^{t_2} \sqrt{\left(\frac{t}{\tau_Q}\right)^2 - 2\frac{|t|}{\tau_Q}\cos(k) + 1} dt,\end{aligned} \tag{4.21}$$

where $t_1 = -\tau_Q \cos(k)$ and $t_2 = \tau_Q \cos(k)$ are the times at which the gap is minimal. For small $k \ll \frac{\pi}{4}$ which are excited for long enough quench times, $\cos(k) \approx 1$. Making the substitution $u = \frac{t}{\tau_Q}$, the phase ζ_1 can be approximated by

$$\zeta_1(k) \approx 2\tau_Q \int_{-1}^{1} \sqrt{u^2 - 2|u| + 1} du = 2\tau_Q, \tag{4.22}$$

which for small k is nearly k-independent [218]. On the other hand, for large quench times, the Stokes phase ϕ_S is known to be approximately zero [232]. As such, the Stückelberg phase for large quench times is nearly $2\tau_Q$. Hence, averaging the Stückelberg oscillations over one time period of $\pi/2$, one obtains

$$\begin{aligned}\overline{p_k} &= 4e^{-\frac{\pi}{2\Delta_k}}\left(1 - e^{-\frac{\pi}{2\Delta_k}}\right)\frac{2}{\pi}\int_0^{\frac{\pi}{2}} \sin^2(2\tau_Q) \\ &= 2e^{-\frac{\pi}{2\Delta_k}}\left(1 - e^{-\frac{\pi}{2\Delta_k}}\right)\end{aligned} \tag{4.23}$$

for the average excitation probability $\overline{p_k}$. As such, the defect density after the reverse quench $\overline{n_{\text{def}}^{\text{rev}}}$ averaged over one oscillation cycle in the limit of large τ, where only the long wavelength modes are excited, is

$$\begin{aligned}\overline{n_{\text{def}}^{\text{rev}}} &= \frac{1}{2\pi}\int_{-\pi}^{\pi} \overline{p_k} dk \\ &= \frac{1}{2\pi}\int_{-\pi}^{\pi} 2e^{-\frac{\pi}{2\Delta_k}}\left(1 - e^{-\frac{\pi}{2\Delta_k}}\right) dk \\ &\approx \frac{1}{2\pi}\int_{-\infty}^{\infty} 2e^{-2\pi\tau_Q k^2}\left(1 - e^{-2\pi\tau_Q k^2}\right) dk \\ &= \frac{1}{2\pi} 2\left(\frac{1}{\sqrt{2\tau_Q}} - \frac{1}{\sqrt{4\tau_Q}}\right) \\ &= \left(2 - \sqrt{2}\right)\frac{1}{2\pi}\frac{1}{\sqrt{2\tau_Q}} = \left(2 - \sqrt{2}\right) n_{\text{def}}.\end{aligned} \tag{4.24}$$

A comparison to Eq. 4.10 shows that the gKZM applies with the domain wall formation probability $p = 1/\sqrt{2}$. The scaling exponent is $\mu = 1/2$ as predicted from the critical exponents of the model via the KZM and gKZM.

Forward quench variance

A detailed derivation of the defect variance after a forward quench using the moment generating functional is given in [208, 211]. Here, we adopt a different approach, starting from Eq. 4.16. Since the system decomposes into N independent subsystems of modes $\pm k$, higher-order cumulants of the defect density can be computed from the cumulants of the individual subsystems. Consequently, the defect number variance is the sum of the variances of each subsystem, eliminating the need to compute the moment generating functional for the entire system.

Each subsystem labeled by its mode k comprises a 2-level system undergoing a Landau-Zener transition. We assume that the subsystem is initialized in its ground state $|g\rangle$ and undergoes a time evolution to its final state $|g(t_{\text{final}})\rangle$. The number operator that counts the amount of excitations is represented by the operator $\hat{n} = |e\rangle\langle e|$. As already stated in Eq. 4.17, according to the Landau-Zener-formula, we obtain that the expectation value of the number operator gives the excitation probability

$$\langle g(t)|\hat{n}|g(t)\rangle = p_k = \langle g(t)|e\rangle \langle e|g(t)\rangle \,. \tag{4.25}$$

In addition, since $|e\rangle\langle e|$ is a projection operator, it fulfills $\hat{n}^m = |e\rangle\langle e|^m = |e\rangle\langle e| = \hat{n}, \quad \forall m \in \mathbb{N}$. As a consequence, the expectation value of higher powers of the number operator is equal to the excitation probability

$$\langle g(t)|\hat{n}^m|g(t)\rangle = \langle g(t)|\hat{n}|g(t)\rangle = p_k, \quad \forall m \in \mathbb{N}. \tag{4.26}$$

As a consequence, the number variance for a single mode k is given by

$$\text{Var}(n_{\text{def}}(k)) = \left\langle n_{\text{def}}(k)^2 \right\rangle - \langle n_{\text{def}}(k)\rangle^2 = p_k - p_k^2. \tag{4.27}$$

In the continuum limit and in the limit of large quench times, such that only long wavelength modes get excited, the variance of the number of defects in the system normalized by the system size is thus given by

$$\begin{aligned}
\text{Var}(n_{\text{def}}) &= \frac{1}{2\pi}\int_{-\pi}^{\pi} \left(p_k - p_k^2\right) dk \\
&\overset{4.17}{=} \frac{1}{2\pi}\int_{-\pi}^{\pi} \left(e^{-\frac{\pi}{2\Delta_k}} - e^{-\frac{\pi}{\Delta k}}\right) dk \\
&\overset{4.18}{=} \frac{1}{2\pi}\int_{-\infty}^{\infty} \left(e^{-2\pi\tau_Q k^2} - e^{-4\pi\tau_Q k^2}\right) dk \\
&= \frac{1}{2\pi}\left(\frac{1}{\sqrt{2\tau_Q}} - \frac{1}{\sqrt{4\tau_Q}}\right) \\
&= \left(1 - \frac{1}{\sqrt{2}}\right) n_{\text{def}}.
\end{aligned} \tag{4.28}$$

A comparison with Eq. 4.24 shows that indeed $2\mathrm{Var}(n_{\mathrm{def}}) = \overline{n_{\mathrm{def}}^{\mathrm{rev}}}$ in agreement with the gKZM prediction in Eq. 4.9. Moreover, comparing to Eq. 4.11, we can read $p = 1/\sqrt{2}$, demonstrating the applicability of the gKZM framework to the reverse quench.

Numerical simulation

We compare the analytic results which we derived for large quench times with a numerically exact simulation with $N = 1 \times 10^4$ particles using periodic boundary conditions. For the forward quench protocol, we choose to start in the ground state at $h = 0$ and apply the quench protocol

$$h(t) = h_0 \frac{t}{\tau_Q}, \quad 0 \leq t \leq \tau_Q \tag{4.29}$$

as the defect density is independent of the quench direction [227]. The reverse quench protocol is as above. For better readability, we denote for both quench protocols the initial time as t_{init} and the final time as t_{final}. Conversely, the magnetic field h at initial time is h_{init} and at final time h_{final}. For the numerical implementation of the forward and reverse quenches, we extend the techniques described in [227].

As a starting point, we seek to bring the Hamiltonian in Eq. 4.16 into the form

$$H = \sum_k \epsilon_k \left(\gamma_k^\dagger \gamma_k - \frac{1}{2} \right), \tag{4.30}$$

where γ_k is the annihilation of a fermionic quasiparticle, and ϵ_k the energy associated to it. This can be achieved by applying the Bogoliubov transformation

$$c_k = u_k \gamma_k + v_{-k}^* \gamma_{-k}^\dagger, \tag{4.31}$$

where the prefactors u_k and v_k must fulfill

$$\epsilon_k \begin{pmatrix} u_k \\ v_k \end{pmatrix} = \begin{pmatrix} 2(h - \cos(k)) & 2\sin(k) \\ 2\sin(k) & -2(h - \cos(k)) \end{pmatrix} \begin{pmatrix} u_k \\ v_k \end{pmatrix}. \tag{4.32}$$

This equation has a positive and a negative solution with energy $\pm\epsilon_k$. While the positive energy eigenvector is associated with the creation operator of the quasiparticle $\gamma_k^\dagger$, the negative solution is associated with the creation operator of a hole, equivalent to the annihilation of a quasiparticle γ_{-k}.

We now change to the Heisenberg picture, where operators are time-evolving and quantum mechanical states are time-independent. In this picture, the ground state

of the Hamiltonian is the quasiparticle vacuum $|0\rangle$, defined by $\gamma_k |0\rangle = 0$ for all k, where the γ_k that annihilate the vacuum are given by the positive solution of Eq. 4.32. In the limit $h \to \infty$, the ground state is the fully polarized state $|{\to}\rangle^{\otimes N}$, and the γ_k are obtained from $(u_k, v_k) = (1, 0)$.

A time evolution can be achieved using the Heisenberg equation of motion

$$i\frac{dc_k}{dt} = [c_k, H(t)] \tag{4.33}$$

together with the constraint $\frac{d\gamma_k}{dt} = 0$. This constraint essentially defines the γ_k and $\gamma_k^\dagger$ obtained at initial time as generators of the fermionic algebra. Applying Eq. 4.31 and thus taking all the time-dependence into the u_k and v_k, we obtain the time-dependent Bogoliubov-de Gennes equations

$$i\frac{d}{dt}\begin{pmatrix} u_k(t) \\ v_k(t) \end{pmatrix} = \begin{pmatrix} 2(h(t) - \cos(k)) & 2\sin(k) \\ 2\sin(k) & -2(h(t) - \cos(k)) \end{pmatrix} \begin{pmatrix} u_k(t) \\ v_k(t) \end{pmatrix}. \tag{4.34}$$

Equations 4.32 and 4.34 allow us to perform all calculations in terms of the Bogoliubov coefficients u_k and v_k. We first use Eq. 4.32 at $h = h_{\text{init}}$ to determine the initial values of the negative energy eigenvectors $u_k^-(h_{\text{init}})$ and $v_k^-(h_{\text{init}})$, as well as the positive energy eigenvectors $u_k(h_{\text{init}})$ and $v_k(h_{\text{init}})$. The positive energy eigenvectors serve as initial values of Eq. 4.34 when the system is initialized in the ground state. Subsequently, we evolve these coefficients using Eq. 4.34 to obtain the final values $u_k(t_{\text{final}}) \equiv \tilde{u}_k$ and $v_k(t_{\text{final}}) \equiv \tilde{v}_k$. Additionally, equation 4.32 is employed to compute the negative eigenmode $u_k^-(h_{\text{final}}) \equiv \bar{u}_k$ and $v_k^-(h_{\text{final}}) \equiv \bar{v}_k$, corresponding to a quasiparticle excitation at $h = h_{\text{final}}$. The time evolution governed by the differential equations is solved using the *DifferentialEquations.jl* package [233]. The total number of defects is given by the total number of quasiparticles, which corresponds to the overlap between the final states $(\tilde{u}_k, \tilde{v}_k)$ and the negative eigenstates $(\bar{u}_k, \bar{v}_k)$.

$$\begin{aligned} n_{\text{def}} &= \frac{1}{N}\sum_k \left| \begin{pmatrix} \bar{u}_k^* & \bar{v}_k^* \end{pmatrix} \begin{pmatrix} \tilde{u}_k \\ \tilde{v}_k \end{pmatrix} \right|^2 \\ &= \frac{1}{N}\sum_k \begin{pmatrix} \tilde{u}_k^* & \tilde{v_k}^* \end{pmatrix} \begin{pmatrix} \bar{u}_k\bar{u}_k^* & \bar{u}_k\bar{v}_k^* \\ \bar{v}_k\bar{u}_k^* & \bar{v}_k\bar{v}_k^* \end{pmatrix} \begin{pmatrix} \tilde{u}_k \\ \tilde{v}_k \end{pmatrix} \\ &= \frac{1}{N}\sum_k \begin{pmatrix} \tilde{u}_k^* & \tilde{v_k}^* \end{pmatrix} \hat{O}_k \begin{pmatrix} \tilde{u}_k \\ \tilde{v}_k \end{pmatrix} \\ &= \frac{1}{N}\sum_k p_k, \end{aligned} \tag{4.35}$$

where $\hat{O}_k$ represents the operator that measures the number of defects in mode k at the field h_0, and p_k thus corresponds to the expectation value of a defect creation in mode k. To calculate the defect density variance we exploit that each k-mode, as defined in Eq. 4.34, is independent of the other k-modes. As such, the variance of the whole system is the sum of the variances of the individual modes. Thus, the variance of the defect density can be calculated from the variance of the operator $\hat{O}_k$. Note that due to the fermionic nature of both c_k and γ_k, $|\bar{u}_k|^2 + |\bar{v}_k|^2 = 1$, which leads to $\hat{O}_k^2 = \hat{O}_k$. Thus, the defect variance is given by

$$\begin{aligned}
&\mathrm{Var}(n_{\mathrm{def}}) \\
&= \frac{1}{N}\sum_k \left[\begin{pmatrix} \tilde{u}_k^* & \tilde{v_k}^* \end{pmatrix} \hat{O}_k^2 \begin{pmatrix} \tilde{u}_k \\ \tilde{v}_k \end{pmatrix} - \left(\begin{pmatrix} \tilde{u}_k^* & \tilde{v_k}^* \end{pmatrix} \hat{O}_k \begin{pmatrix} \tilde{u}_k \\ \tilde{v}_k \end{pmatrix} \right)^2 \right] \\
&= \frac{1}{N}\sum_k \left(p_k - p_k^2 \right).
\end{aligned} \tag{4.36}$$

The results of the numerical analysis are presented in Fig. 4.2. For quench times much longer than unity, corresponding to the inverse spin-spin interaction, all three observables follow a power law dependence with the KZM exponent $\mu = 1/2$. This behavior agrees with the predictions of the KZM, the gKZM, and our extended gKZM framework for reverse quenches. Furthermore, for quench times slightly above unity, Stückelberg oscillations emerge in the reverse-quench defect density. To extract the overall trend of the oscillations for $\tau_Q > 10$, we average the defect density over two oscillation periods, as detailed in the caption of Fig. 4.2. The resulting averaged behavior closely follows the power law scaling predicted by our extension of the gKZM.

To assess how accurately the dynamics of the one-dimensional uniform TFIM are described by the gKZM and its extension, we solve Eq. 4.10 for the gKZM domain-wall formation probability p

$$p = 1 - \frac{n_{\mathrm{def}}^{\mathrm{rev}}}{2n_{\mathrm{def}}}. \tag{4.37}$$

The same can be done for Eq. 4.11 to yield

$$p = 1 - \frac{\mathrm{Var}\left(n_{\mathrm{def}}\right)}{n_{\mathrm{def}}} \tag{4.38}$$

to show the validity of the gKZM. The gKZM is valid if in long quench time limit p is independent of the quench time τ_Q and the formula used to calculate it.

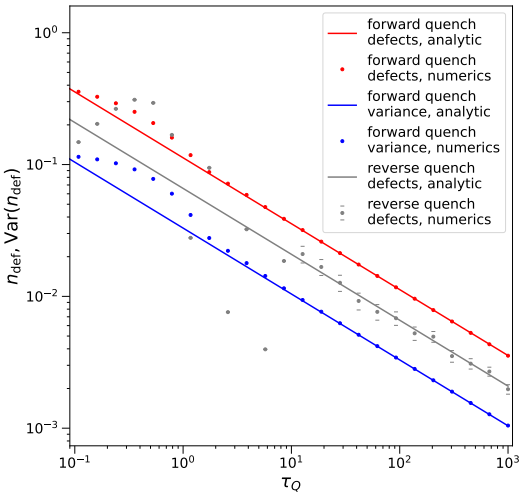

Figure 4.2: *Numerically exact simulation of different quenches in the uniform transverse field Ising model.* Defect density in the forward quench (red) and reverse quench (gray) protocols as well as the variance of the defect density after a forward quench (blue) are shown as a function of the quench time τ_Q on a double-logarithmic scale. The analytic power law predictions from equations 4.19, 4.24 and 4.28 (solid lines) are shown as solid lines. Error bars for the defect density after the reverse quench for $\tau_Q > 10$ stems from averaging the defect density simulated for 11 points equally spaced in the interval $[\tau_Q - \pi/2, \tau_Q + \pi/2]$, i.e. over two Stückelberg oscillations. The error is defined as the standard deviation of the mean.

The numerical results for the probability as a function of the quench time τ_Q, obtained from the defect densities, are shown in Fig. 4.3. For short quench times, where the KZM scaling with exponent μ does not yet hold in the defect densities, the probability p exhibits a strong dependence on τ_Q, independent of the calculation method. In contrast, for long quench times, where all three observables in Fig. 4.2 display the expected KZM power law scaling, the probability p converges to the analytically predicted value $1/\sqrt{2}$ when evaluated using both equations 4.37 and 4.38. This agreement confirms the validity of the gKZM and its extension.

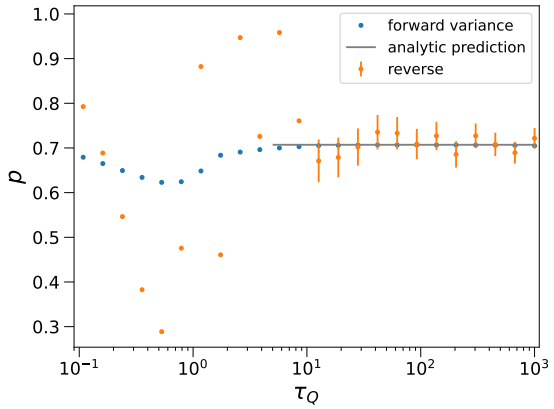

Figure 4.3: *Numerically exact calculation of the gKZM domain wall formation probability in the uniform transverse field Ising model.* Calculated domain wall formation probability p in the gKZM as a function of the quench time τ_Q. The probability is estimated both from a comparison between forward quench defect density and forward quench variance (blue dots, Eq. 4.38) as well as from a comparison between the reverse quench defect density and the forward quench defect density (orange dots, Eq. 4.37). In the latter case, error bars are propagated from the reverse quench defect density. The gray line shows the analytic prediction $p = 1/\sqrt{2}$.

4.4 The bond-disordered transverse field Ising model

Using the uniform Ising model, we tested the predictions of the gKZM in a system that decomposes into pairs of non-interacting fermions. During a forward quench, each fermion pair undergoes an effective Landau–Zener transition. For such quasi-free fermionic systems, the derivations developed for the uniform Ising model can be straightforwardly generalized. Consequently, the gKZM is expected to apply to other related quasi-free fermion models, such as the one-dimensional Kitaev chain [215] and the one-dimensional XY model [214], in the case of reverse quenches. In this section, we want to test whether the predictions of the gKZM, i.e. the scaling with the KZM exponent μ and the time-independent domain wall formation probability p, can also be found in qualitatively different system. We test these predictions for a bond-disordered 1D TFIM. There are three reasons to use this model as a benchmark:

1. It is an integrable model that can be calculated in polynomial time as a function of the particle number. As such, phase transition effects which are usually quite prone to finite size effects and only exact in the thermodynamic limit, can be

calculated efficiently on a classical computer.

2. It is a paradigmatic model that possesses an infinite randomness fixed point (IRFP) $z = \infty$, such that the power law predicted by the KZM only holds for rather short times, while larger times show logarithmic corrections. It is an open question whether these corrections are also subject to the gKZM. In addition, it is governed by the same physics as other IRFP models, like Hubbard models showing random singlet phases [63, 66].

3. This model does not fractionalize into subspaces of dimension two that can be mapped onto Landau-Zener crossings. As such, it is a priori not clear whether the gKZM predictions, even for the forward quench protocol, hold.

The model is chosen according to Eq. 4.12, where the J_i are drawn from a uniform distribution $J_i \in (0, 2)$, leading to a critical field of $h_c = 2/e$, and critical exponents $\nu = 2$ and $z = \infty$ [234, 235], and thus $\mu = 0$.

For this system, we solve the time-dependent Bogoliubov-deGennes equations following [236] to simulate the system's dynamics numerically exactly for a system size of $N = 128$ particles.

As the J_i are disordered, there is no discrete translation symmetry in this model, and hence the Hamiltonian will not fragment into subspaces that conserve the modulus of the momentum k. Instead, we use the most general form of the Bogoliubov transformation, involving all possible operators

$$\gamma_m = u^*_{mn} c_n + v^*_{mn} c^\dagger_n, \tag{4.39}$$

where the prefactors u_{nm} and v_{nm} are complex prefactors, and we used Einstein summation convention. In order that the γ_m fulfill the fermionic commutation relations, the prefactors are subject to the constraints

$$\begin{cases} u_{mn} v_{ln} + v_{mn} u_{ln} = 0 \\ u_{nl} u^*_{nm} + v_{nl} v^*_{nm} = \delta_{lm}. \end{cases} \tag{4.40}$$

Using these constraints, the reverse transformation reads

$$c_n = u_{mn} \gamma_m + v^*_{mn} \gamma^\dagger_m. \tag{4.41}$$

We insert this transformation into Eq. 4.15 and demand that the Hamiltonian can be represented by noninteracting Bogoliubov quasiparticles

$$H = \sum_m \epsilon_m \left(\gamma^\dagger_m \gamma_m - \frac{1}{2} \right), \tag{4.42}$$

where ϵ_m is the energy related to the creation of quasiparticle m. We rewrite Eq. 4.15 into the form

$$H = \frac{1}{2}\begin{pmatrix} c_1^\dagger & \dots & c_N^\dagger & c_1 & \dots & c_N \end{pmatrix} \begin{pmatrix} a & b \\ -b^* & -a^* \end{pmatrix} \begin{pmatrix} c_1 \\ \vdots \\ c_N \\ c_1^\dagger \\ \vdots \\ c_N^\dagger \end{pmatrix}, \tag{4.43}$$

where a is a Hermitian and b an antisymmetric $N \times N$ matrix. In order for the transformation Eq. 4.41 to yield the Hamiltonian Eq. 4.42, we arrive at the Bogoliubov-de Gennes equations

$$\epsilon_m \begin{pmatrix} u_{mn} \\ v_{mn} \end{pmatrix} = \begin{pmatrix} a & b \\ -b^* & -a^* \end{pmatrix} \begin{pmatrix} u_{mn} \\ v_{mn} \end{pmatrix}. \tag{4.44}$$

We observe that the $\begin{pmatrix} u_{mn} & v_{mn} \end{pmatrix}$ are eigenvectors of a Hermitian matrix, and as such immediately fulfill Eq. 4.40. In addition, we observe another symmetry: If $\begin{pmatrix} u_{mn} & v_{mn} \end{pmatrix}$ is an eigenvector with positive energy ϵ_m, $\begin{pmatrix} v_{mn}^* & u_{mn}^* \end{pmatrix}$ is a solution with the negated energy $-\epsilon_m$. From Eq. 4.39, this process corresponds to the annihilation of particle m and is therefore associated with the energy of a quasihole. Hence, positive-energy quasiparticles represent the creation of excitations, while negative-energy quasiparticles correspond to their annihilation. This symmetry is consequently referred to as particle-hole symmetry.

As in the case for the uniform Ising model, we can obtain the time-dependent Bogoliubov-de Gennes equation by applying the Heisenberg equation of motion

$$i\frac{dc_n}{dt} = [c_n, H] \tag{4.45}$$

and applying the transformation Eq. 4.41. Assuming the initial state in the Heisenberg picture was the vacuum state annhiliated by all γ_m, and using the γ_m as a time-independent generator of the fermion algebra, i.e. $\frac{d\gamma_m}{dt} = 0$, the time-dependent Bogoliubov-de Gennes equations read

$$i\frac{d}{dt}\begin{pmatrix} u_{mn}(t) \\ v_{mn}(t) \end{pmatrix} = \begin{pmatrix} a(t) & b \\ -b^* & -a^*(t) \end{pmatrix} \begin{pmatrix} u_{mn}(t) \\ v_{mn}(t) \end{pmatrix}. \tag{4.46}$$

As only the matrix a has a dependence on the magnetic field h, only a is time dependent.

Like in the case of the TFIM model with identical couplings discussed in the previous section, we use Eq. 4.39 to get the initial values $u_{mn}(h_{\text{init}})$ and $v_{mn}(h_{\text{init}})$ as the positive eigenenergy solutions at $h = \text{h}_{\text{init}}$ We insert these initial conditions into Eq. 4.46 to obtain the time-evolved values $u_{mn}(t_{\text{final}}) := \tilde{u}_{mn}$ and $v_{mn}(t_{\text{final}}) := \tilde{v}_{mn}$. We solved this differential equation using the *QuantumOptics.jl* package [237].

Using equations 4.39 and 4.44, we can rewrite the quasiparticle annihilation operator at the field h_{final} as

$$\bar{\gamma}_m = \bar{u}^*_{mn} c_n + \bar{v}^*_{mn} c^\dagger_n, \tag{4.47}$$

where the $\bar{u}_{mn}$ and $\bar{v}_{mn}$ are obtained from solving Eq. 4.44 restricting the solutions to positive energy eigenstates at $h = h_{\text{final}}$. In the Heisenberg picture, the operator $\bar{\gamma}_m$ has a time-dependence, which can be expressed through the time-dependence of the fermionic operators c_n by equation 4.45. Their time-dependence can be calculated using Eq. 4.41, where now the time-dependence lies only in $u_{mn}(t)$ and $v_{mn}(t)$, which are given by Eq. 4.46.

Thus, the quasiparticle defect density after the quench reads:

$$\begin{aligned} n_{\text{def}} &= \frac{1}{N} \sum_{m=1}^{N} \bar{\gamma}^\dagger_m(t_{\text{final}}) \bar{\gamma}_m(t_{\text{final}}) \\ &= \frac{1}{N} \sum_m \begin{pmatrix} \tilde{u}^*_{ml} & \tilde{v}^*_{ml} \end{pmatrix} \begin{pmatrix} \bar{v}^*_{ql} \bar{v}_{qn} & \bar{v}^*_{ql} \bar{u}_{qn} \\ \bar{u}^*_{ql} \bar{v}_{qn} & \bar{u}^*_{ql} \bar{u}_{qn} \end{pmatrix} \begin{pmatrix} \tilde{u}_{mn} \\ \tilde{v}_{mn} \end{pmatrix}. \end{aligned} \tag{4.48}$$

In order to calculate the variance of the defect density, we calculate the expectation value of the squared number of quasiparticles

$$\begin{aligned} \left\langle N^2_{\text{def}} \right\rangle &= \langle 0 | \, \bar{\gamma}^\dagger_m(t_{\text{final}}) \bar{\gamma}_m(t_{\text{final}}) \bar{\gamma}^\dagger_n(t_{\text{final}}) \bar{\gamma}_n(t_{\text{final}}) \, | 0 \rangle \\ &= (\bar{u}_{mq} \tilde{v}_{aq} + \bar{v}_{mq} \tilde{u}_{aq}) \, (\bar{u}^*_{mk} \tilde{v}^*_{ak} + \bar{v}^*_{mk} \tilde{u}^*_{ak}) \\ &\quad (\bar{u}_{nl} \tilde{v}_{cl} + \bar{v}_{nl} \tilde{u}_{cl}) \left(\bar{u}^*_{np} \tilde{v}^*_{cp} + \bar{v}^*_{np} \tilde{u}^*_{cp} \right) \\ &\quad + (\bar{u}_{mq} \tilde{v}_{aq} + \bar{v}_{mq} \tilde{u}_{aq}) \left(\bar{u}^*_{np} \tilde{v}^*_{ap} + \bar{v}^*_{np} \tilde{u}^*_{ap} \right) \\ &\quad (\bar{u}^*_{mk} \tilde{u}_{bk} + \bar{v}^*_{mk} \tilde{v}_{bk}) \, (\bar{u}_{nl} \tilde{u}^*_{bl} + \bar{v}_{nl} \tilde{v}^*_{bl}) \\ &\quad - (\bar{u}_{mq} \tilde{v}_{aq} + \bar{v}_{mq} \tilde{u}_{aq}) \, (\bar{u}_{nl} \tilde{u}^*_{al} + \bar{v}_{nl} \tilde{v}^*_{al}) \\ &\quad (\bar{u}^*_{mk} \tilde{u}_{bk} + \bar{v}^*_{mk} \tilde{v}_{bk}) \left(\bar{u}^*_{np} \tilde{v}^*_{bp} + \bar{v}^*_{np} \tilde{u}^*_{bp} \right). \end{aligned} \tag{4.49}$$

Using Eq. 4.48, we thus find for the variance of the defect number

$$\begin{aligned}\mathrm{Var}\left(N_{\mathrm{def}}\right) &= \left\langle N_{\mathrm{def}}^2 \right\rangle - \langle N_{\mathrm{def}} \rangle^2 \\ &= \left(\bar{u}_{mq}\tilde{v}_{aq} + \bar{v}_{mq}\tilde{u}_{aq}\right)\left(\bar{u}_{np}^*\tilde{v}_{ap}^* + \bar{v}_{np}^*\tilde{u}_{ap}^*\right) \\ &\quad \left(\bar{u}_{mk}^*\tilde{u}_{bk} + \bar{v}_{mk}^*\tilde{v}_{bk}\right)\left(\bar{u}_{nl}\tilde{u}_{bl}^* + \bar{v}_{nl}\tilde{v}_{bl}^*\right) \\ &\quad - \left(\bar{u}_{mq}\tilde{v}_{aq} + \bar{v}_{mq}\tilde{u}_{aq}\right)\left(\bar{u}_{nl}\tilde{u}_{al}^* + \bar{v}_{nl}\tilde{v}_{al}^*\right) \\ &\quad \left(\bar{u}_{mk}^*\tilde{u}_{bk} + \bar{v}_{mk}^*\tilde{v}_{bk}\right)\left(\bar{u}_{np}^*\tilde{v}_{bp}^* + \bar{v}_{np}^*\tilde{u}_{bp}^*\right).\end{aligned} \tag{4.50}$$

We now define the matrices $\bar{\mathbf{u}} \coloneqq \bar{u}_{mn}$, $\bar{\mathbf{v}} \coloneqq \bar{v}_{mn}$, $\tilde{\mathbf{u}} \coloneqq \tilde{u}_{mn}$ and $\tilde{\mathbf{v}} \coloneqq \tilde{v}_{mn}$. Using a single product of the matrices, we construct the matrices $\mathbf{A} \coloneqq \tilde{\mathbf{v}}\bar{\mathbf{u}}^\top + \tilde{\mathbf{u}}\bar{\mathbf{v}}^\top$ and $\mathbf{B} \coloneqq \bar{\mathbf{u}}^*\tilde{\mathbf{u}}^\top + \bar{\mathbf{v}}^*\tilde{\mathbf{v}}^\top$ and their product $\mathbf{C} \coloneqq \mathbf{AB}$. With this definition, we find for defect density variance

$$\mathrm{Var}\left(n_{\mathrm{def}}\right) = \frac{\mathrm{Var}\left(N_{\mathrm{def}}\right)}{N} = \frac{\mathrm{Tr}\left\{\mathbf{CC}^\dagger\right\} - \mathrm{Tr}\{\mathbf{CC}^*\}}{N}. \tag{4.51}$$

This matrix calculation allows for a more efficient implementation than a direct implementation of Eq. 4.50 using for-loops. In addition, we can also recast Eq. 4.48 into the form

$$n_{\mathrm{def}} = \frac{\mathrm{Tr}\left\{A^\dagger A\right\}}{N}. \tag{4.52}$$

Figure 4.4 shows the numerical results. The data were obtained by solving Eq. 4.46 for 20 different realizations of the J_i, which were sampled from a uniform distribution of the interval $[0, 2]$ using the *Statistics.jl* core library of the Julia programming language [238]. For each disorder realization, the defect density and its variance were computed for both forward and reverse quench protocols using equations 4.51 and 4.52. For the forward quench protocol, we choose the initial and final fields as $h_{\mathrm{init}} = 0$ and $h_{\mathrm{final}} = 10$, while for the reverse quench, $h_{\mathrm{init}} = h_{\mathrm{final}} = 10$, like we also did in the uniform 1D TFIM. The resulting observables were then averaged over all 20 realizations. To quantify the associated uncertainty, the standard error of the mean was also calculated for each observable.

For the forward quench, the defect density agrees with the findings of [236]. In the intermediate quench time regime ($2 \leq \tau_Q \leq 20$), the scaling follows a power law, $\sim \tau_Q^{-1/2}$, consistent with an exponent $\mu = 1/2$, which is the KZM critical exponent of the uniform TFIM discussed above. This agreement arises because, at short time scales, the disorder acts as a weak perturbation. It does not have enough time to significantly influence the dynamics. Consequently, the $z = \infty$ characteristic of the bond-disordered system does not yet manifest.

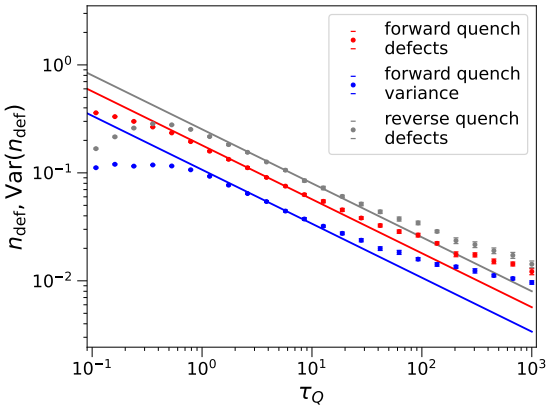

Figure 4.4: *Numerically exact simulation of different quenches in the bond-disordered transverse field Ising model.* Defect density in the forward quench (red) and reverse quench (gray) protocols as well as the variance of the defect density after a forward quench (blue) are presented as a function of the quench time τ_Q on a double-logarithmic scale. Solid lines serve as guide to the eye depicting a power law dependence $n_{\text{def}} = \frac{C}{2\pi\sqrt{2\tau_Q}}$. The constant C is 1.6, 0.95 and 2.25 for the forward quench defect density (red), the forward quench defect variance (blue), and the reverse quench defect density (gray), respectively.

For longer quench times, the defect density decays more slowly. It may approach a constant value, consistent with an effective exponent $\mu = 0$. This behavior is attributed to logarithmic corrections, as discussed in [236].

Furthermore, we observe also for the large quench times the same scaling behavior in the variance of the defect density after the forward quench and in the defect density from the reverse quench. These findings provide preliminary evidence that the gKZM remains valid in bond-disordered systems. In particular, it appears to capture the IRFP behavior associated with $z = \infty$.

To validate the probabilistic interpretation of the gKZM, we compute the domain wall formation probability p using equations 4.37 and 4.38. These expressions relate p to the simulated defect densities and the variance obtained from the forward quench. The results are shown in Fig. 4.5. For large quench times, we find $p \approx 35\%$, consistent across both regimes: the intermediate regime governed by the $z = 1$ fixed point, and the asymptotic regime where logarithmic corrections dominate and the system flows to the $z = \infty$ fixed point. At large quench times, the defect density becomes very low, often approaching a single defect. This leads to enhanced fluctuations across

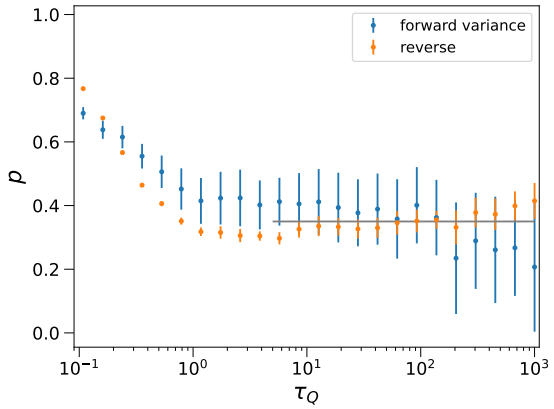

Figure 4.5: *Numerically exact calculation of the gKZM domain wall formation probability in the bond-disordered transverse field Ising model.* Domain wall formation probability p is presented as a function of the quench time τ_Q. Estimates are obtained from two approaches: comparing defect density and variance after a forward quench (blue dots, Eq. 4.38), and comparing defect densities between reverse and forward quenches (orange dots, Eq. 4.37). Error bars reflect propagated uncertainties from the defect densities and its variance. The horizontal gray line at $p = 0.35$ serves as a guide to the eye.

disorder realizations as we approach finite size effects, resulting in larger statistical uncertainties.

For the bond-disordered TFIM, we want to highlight that the reverse quench defect density is significantly larger than both mean defect density and defect density variance in the forward quench protocol. This is an effect of $p < 1/2$, which leads according to equations 4.10 and 4.11 to $n_{\mathrm{def}}^{\mathrm{rev}} > n_{\mathrm{def}} > \mathrm{Var}\,(n_{\mathrm{def}})$. In an experimental setup, this effect can be used to obtain a stronger signal, i.e. a higher number of defects, to determine the gKZM coefficient μ more accurately.

4.5 Excursus: Influence of paramagnetic approximations

As discussed at the beginning of this chapter, one objective is to develop a method to characterize a potential spin glass–to–paramagnet quantum phase transition using our experimental platform. The apparatus described in Chap. 3 and detailed in Appendix A, however, provides access only to global observables and therefore cannot

directly resolve individual defects. We show that, in a system undergoing a continuous transition to a paramagnetic phase, measurements of the global magnetization can nonetheless be used to quantify the defect density. In the regime of a strong magnetic field, the ground state is well approximated by the fully polarized state, which can be prepared through a global pulse. In this section, we demonstrate that our extension of the gKZM for reverse quenches enables the characterization of critical scaling that relies only on global access to a system exhibiting a continuous quantum phase transition to a paramagnetic phase.

As a starting point, we observe that both previously discussed models deal with a phase transition between a paramagnetic and a different phase, and thus serve as paradigmatic models to test our claim. In the paradigmatic limit $h \to \infty$ the spin-spin interaction is negligible. Here, Eq. 4.41 essentially simplifies to $\gamma_m = c_m$, thus showing that a defect corresponds to a local flip of a single spin. This also shows that in the limit $h \to \infty$, the ground state is given by the fully polarized aligned to h. As a consequence, the defect density can be approximated for large fields and is exactly given for $h = \infty$ by

$$n_{\text{def}} = 1/2 - \langle S_x \rangle \,, \tag{4.53}$$

where S_x denotes the average magnetization operator. This is precisely the magnetization deviation from full magnetization. Taking the square of the previous equation, one can also show for the variances

$$\text{Var}\,(n_{\text{def}}) = \text{Var}\,(S_x)\,. \tag{4.54}$$

Thus, in the limit where the applied field is large compared to the strongest spin-spin interaction, both the defect density and the defect density variance can be well approximated by a global measurement of the magnetization only, rendering an experimental implementation with only global system access possible.

To estimate the validity of this approximation, we simulate again the quench dynamics, both in the uniform and bond-disordered TFIM. Here, we evaluate the defect density from the global magnetization using Eq. 4.53 after forward and reverse quenches. The defect density variance after a forward quench is approximated by the magnetization variance, as shown in Eq. 4.54. In both forward and reverse quenches, the final magnetic field h_{final} is chosen to exceed all couplings,

$$h_{\text{final}} \gg 2 \geq J_i \geq 0, \quad \forall i \in \{1, \ldots, N\},$$

ensuring that the system is initialized deep in the paramagnetic phase, where these approximations are expected to hold.

For the numerical simulation of the uniform TFIM, we employ the same Bogoliubov–de Gennes equations used to obtain the coefficients $\tilde{u}_k$ and $\tilde{v}_k$, as discussed in Sec. 4.3. To compute $1/2 - \langle S_x \rangle$ from these values, we note that measuring the x-magnetization corresponds to quenching the transverse field h to infinity and evaluating the resulting number of excitations in this limit. Mathematically, this quench is equivalent to setting all couplings $J_i = 0$ for all i. From Eq. 4.32, this limit yields $\bar{u}_k = 1$ and $\bar{v}_k = 0$ for all k, independent of the specific finite positive value we may choose for h. Inserting this into Eq. 4.35 yields thus

$$1/2 - \langle S_x \rangle = \frac{1}{N} \sum_k |\tilde{v}_k|^2 . \tag{4.55}$$

The variance of the magnetization yields

$$\mathrm{Var}(S_x) = \frac{1}{N} \sum_k |\tilde{v}_k|^2 - |\tilde{v}_k|^4 . \tag{4.56}$$

For the bond-disordered TFIM with all couplings set to zero, we compute the matrices $\tilde{\mathbf{u}}$ and $\tilde{\mathbf{v}}$ by solving the time-dependent Bogoliubov–de Gennes equations derived in Sec. 4.4. Following the same approach as for the uniform TFIM, a measurement of the magnetization is represented by quenching the Hamiltonian to $h = \infty$. In this limit, we obtain $\bar{\mathbf{u}} = \mathbb{1}_{N\times N}$ and $\bar{\mathbf{v}} = 0$. Consequently, the expressions for $\mathbf{A}$ and $\mathbf{B}$ introduced in Sec. 4.4 simplify to $\mathbf{A} = \tilde{\mathbf{v}}$ and $\mathbf{B} = \tilde{\mathbf{u}}^\top$. Substituting these into equations 4.51 and 4.52 yields the expressions for the magnetization and its average fluctuation:

$$\langle S_x \rangle = \frac{1}{2} - \frac{1}{N} \mathrm{Tr}\left\{\tilde{\mathbf{v}}^\dagger \tilde{\mathbf{v}}\right\}, \tag{4.57}$$

$$\mathrm{Var}\,(S_x) = \frac{\mathrm{Tr}\left\{\tilde{\mathbf{v}}\tilde{\mathbf{u}}^\top \tilde{\mathbf{u}}^* \tilde{\mathbf{v}}^\dagger\right\} - \mathrm{Tr}\left\{\tilde{\mathbf{v}}\tilde{\mathbf{u}}^\top \tilde{\mathbf{v}}^* \tilde{\mathbf{u}}^\dagger\right\}}{N}. \tag{4.58}$$

The simulation results are shown in Fig. 4.6(a) for the uniform TFIM and in Fig. 4.6(b) for the bond-disordered TFIM. As described above, in the uniform TFIM, the estimated defect density after a reverse quench is averaged over two Stückelberg oscillation periods for quench times $\tau_Q > 10$. For the bond-disordered TFIM, each data point represents an average over 20 independent disorder realizations.

We observe that in the uniform TFIM, the defect density for both forward and reverse quenches can be accurately estimated from a magnetization measurement at the final field $h = 10$ for $\tau_Q < 1 \times 10^2$. In contrast, the magnetization variance already overestimates the defect variance for $\tau_Q > 1 \times 10^1$, indicating that it is more sensitive

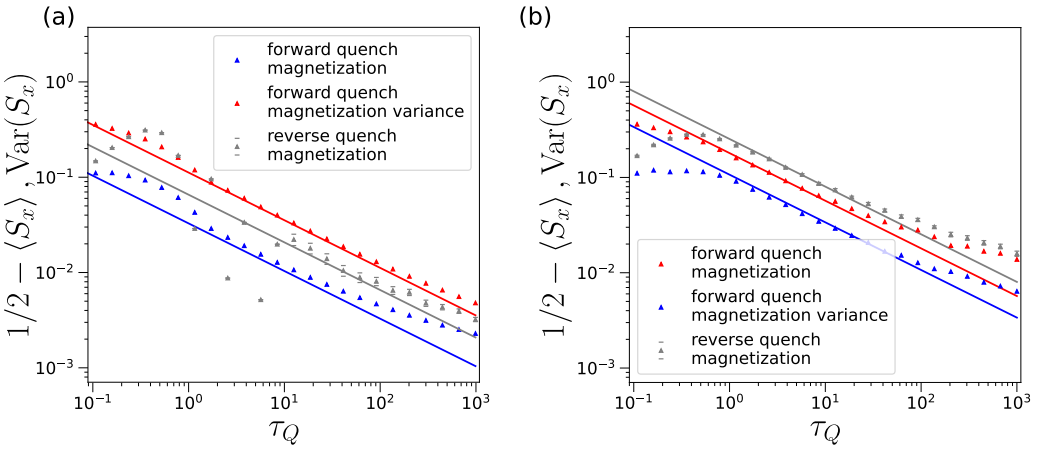

Figure 4.6: *Numerically exact calculation of the deviation from full magnetization and its variance.* The deviation from full magnetization is shown for the uniform (a) and bond-disordered (b) TFIM under forward (red) and reverse (gray) quench protocols, together with the magnetization variance following a forward quench (blue), all as functions of the quench time τ_Q. In panel (a), solid lines represent the analytical predictions for the uniform TFIM, corresponding to those shown in Fig. 4.2. Error bars of the reverse-quench magnetization for $\tau_Q > 10$ denote the standard error of the mean, obtained by averaging over 11 uniformly spaced data points in the interval $[\tau_Q - \pi/2, \tau_Q + \pi/2]$. In panel (b), solid lines serve as visual guides, identical to those in Fig. 4.4. Error bars indicate the standard error of the mean, calculated from averages over 20 disorder realizations.

to finite final-field effects. Consequently, the reverse-quench magnetization provides a more robust means of extracting the defect-density variance after a forward quench, using our extension of the gKZM. However, we note that the discrepancy between the exact defect density and the estimate obtained from magnetization measurements decreases for larger final fields h, vanishing in the limit $h \to \infty$. Consequently, this limitation can, in principle, be overcome in experiments where a sufficiently strong magnetic field can be applied and the coherence time of the platform is long enough to maintain a constant ratio $h_{\mathrm{final}}/\tau_Q$ for the largest τ_Q considered.

We emphasize that, qualitatively, all curves obtained from magnetization estimates in the uniform Ising model exhibit the same behavior: a slower decay than a power law, similar to the exact defect density curves in the bond-disordered Ising model, which features a $z = \infty$ IRFP. Consequently, deviations from power law behavior may arise from finite final fields, and one should exercise caution when inferring $z = \infty$

from magnetization measurements. Nevertheless, on intermediate timescales, all curves follow a power law with $\mu = 1/2$, allowing the KZM exponent of the uniform model to be directly extracted from the data.

In the bond-disordered TFIM, the magnetization and defect density measurements, both in the forward and reverse quench, lie essentially on top of each other for all times, such that the KZM exponent $\mu = 0$ for late times, and $\mu = 1/2$ for intermediate times can be read off. Surprisingly, in the bond-disordered model, the magnetization variance follows a power law scaling over a wider range of quench times than the exact defect density variance and underestimates it. This indicates that estimating the reverse quench defect density from magnetization measurements is more reliable than inferring the defect density variance after a forward quench from the magnetization variance. Although both quantities would coincide in the limit of an infinitely large final magnetic field $h_{\text{final}} = \infty$, at finite final fields the magnetization variance deviates more significantly from the defect density variance than the magnetization does from the defect density.

In summary, approximating the defect density via magnetization measurements introduces only small errors at late times, which can be controlled by increasing the final magnetic field. As long as a power law scaling is observed, the Kibble-Zurek exponent μ can be reliably determined. Deviations from a power law should be interpreted with caution, since both experimental imperfections and the approximation itself can produce behavior resembling that of an infinite-randomness fixed point.

4.6 Experimental implementation on a disordered dipolar Heisenberg XY model

In Chap. 3, we demonstrated energetic-magnetic hysteresis in a disordered dipolar XY model. This raises the question of whether a quantum phase transition is associated with this phenomenon, analogous to the spin glass transition, which is linked to thermomagnetic hysteresis effects [86]. To investigate this, we present complementary measurements performed in the same weakly and strongly disordered regimes as the experiments in Chap. 3.

The aim is to test for a continuous quantum phase transition as a function of a transverse magnetic field. Studying such a transition is crucial for understanding the dipolar spin glass phase:

- The Parisi mean-field solution for Ising spins predicts no spin glass transition under a transverse field, while the droplet-scaling model by Fisher and Huse

predicts a second-order phase transition. Establishing the presence or absence of such a transition is therefore critical for developing theoretical models of spin glasses.

- Experimental evidence for a prospective dipolar Ising spin glass under a finite transverse field is inconclusive [40, 239, 240]. Because the transverse field does not commute with the Ising spins, it induces strong quantum fluctuations, leaving the nature of a dipolar quantum spin glass an open question.

A continuous phase transition is characterized by a set of critical exponents. In $\mathrm{Li\,Ho}_x\mathrm{Y}_{1-x}\mathrm{F}_4$, typical measurements of these exponents rely on either the nonlinear susceptibility, which yields weak signals, particularly at finite transverse fields [40], or ac-susceptibility analysis, which provides inconclusive results in strongly disordered systems [33, 35].

Here, we apply our extension of the generalized Kibble-Zurek mechanism (gKZM) to a system that may host a spin glass phase: a bond-disordered Heisenberg XY model. To our knowledge, no Kibble-Zurek experiment has previously been performed on spin glasses due to the absence of locally characterizable defects. However, dynamical finite-size scaling of relaxation times, based on the KZM, has been studied numerically [241] and on a quantum annealing platform [110]. Complementing these approaches, we present the first Kibble-Zurek-based analysis at fixed system size in an isolated system with potential spin glass behavior.

Experimental Protocols

We experimentally implement the reverse quench protocol introduced above, as illustrated in Fig. 4.7. First, we prepare the system in the ground state of the putative paramagnetic phase. This is achieved by initializing the fully spin-polarized state $|\Psi_x\rangle$ along the x-direction and applying a strong initial magnetic field $\Omega_{x,0}$ that exceeds all spin-spin interactions. We prepare the fully spin-polarized state in negative z-direction for the weakly and strongly disordered regimes exactly as described in Chap. 3. From there, $|\Psi_x\rangle$ is prepared using a Rabi $\pi/2$-pulse with Rabi frequencies $2\pi \times 12.18(4)\,\mathrm{MHz}$ and $2\pi \times 15.71(4)\,\mathrm{MHz}$ in the weakly and strongly disordered regimes, respectively. These values are significantly larger than the median interaction energy $J_{\mathrm{med}} < 2\pi \times 1.7\,\mathrm{MHz}$, ensuring high-fidelity state preparation of $|\Psi_x\rangle$.

To realize the reverse quench, resonant microwave radiation with initial amplitude $\Omega_{x,0}$ is applied. The amplitude is linearly decreased to zero over a time τ_Q and then linearly increased back to $\Omega_{x,0}$ using an arbitrary waveform generator. The initial

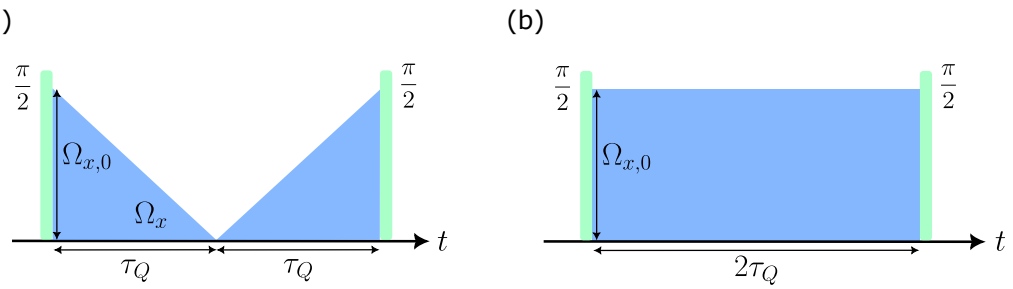

Figure 4.7: *Sketch of the experimental implementation of the reverse quench and spinlock protocol.* (a) Reverse quench protocol. Rabi $\pi/2$-pulses are indicated by green bars, while the microwave Rabi frequency Ω_x corresponding to the linear quench is indicated by the blue area as a function of evolution time t. Initial field $\Omega_{x,0}$ and quench time τ_Q are indicated by arrows. (b) Spinlock protocol. Colored regions have the same correspondence as in (a). The microwave drive is applied with constant Rabi frequency Ω_x for time $2\tau_Q$.

amplitudes are $\Omega_{x,0} = 2\pi \times 4.872(16)\,\mathrm{MHz}$ and $\Omega_{x,0} = 2\pi \times 4.713(12)\,\mathrm{MHz}$ for the weakly and strongly disordered regimes, respectively. The choice of $\Omega_{x,0} \approx 5J_{\mathrm{med}}$ in the weakly disordered regime and $\Omega_{x,0} \approx 3J_{\mathrm{med}}$ in the strongly disordered regime is motivated by two considerations. First, the ramp slope, $\Omega_{x,0}/\tau_Q$, should be small so that the system spends sufficient time near $h = 0$, allowing the adiabatic-impulse approximation to hold. This is limited by the condition that $2\tau_Q$ should be small compared to the Rydberg lifetime of the states encoding the spin, in order to observe isolated dynamics. Second, $\Omega_{x,0}$ must exceed J_{med} to ensure significant overlap of the initial state with the ground state. A final Rabi $\pi/2$-pulse with adjustable phase enables tomographic readout of the magnetization.

We experimentally quantify how close the ground state of the Hamiltonian is described by $|\Psi_x\rangle$ by the use of a *spinlock* protocol [43, 156, 242]. In the spinlock protocol, we prepare the system in $|\Psi_x\rangle$. In contrast to the reverse quench protocol, we keep the microwave drive at constant amplitude, resulting into a constant Rabi frequency $\Omega(t) = \Omega_{x,0}$. A final $\pi/2$-pulse with adjustable phase is applied for tomographic magnetization readout. If the field $\Omega_{x,0}$ is stronger than almost all spin-spin couplings J_{ij}, the fully polarized state $|\Psi_x\rangle$ is effectively the ground state of the Hamiltonian and no dynamics is expected. Conversely, a strong magnetization decay over time signals that spin-spin interactions, as perturbations to the interaction with the drive field, gain importance.

Measurements

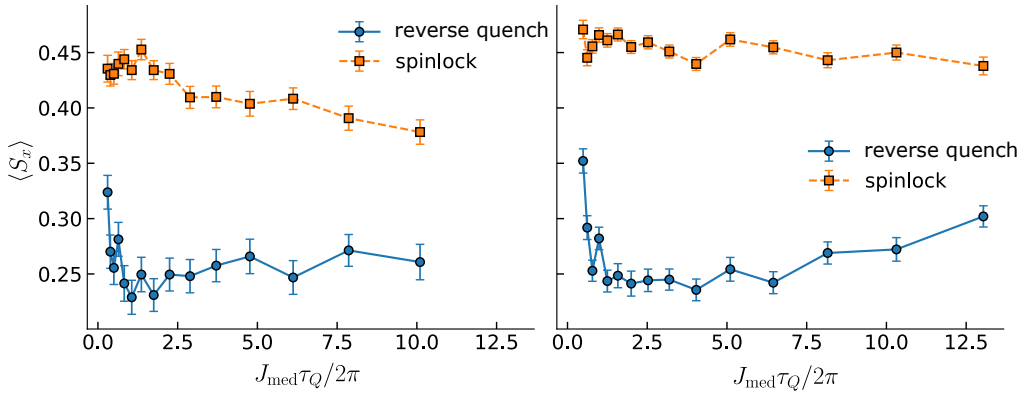

Figure 4.8: *Magnetization measurements for the reverse quench protocol.* Magnetization measurements for the reverse quench (blue) and spinlock protocol (orange) for the weakly (left) and strongly (right) disordered regime as a function of quench time τ_Q, rescaled with the median interaction strength J_{med} to show median interaction cycles. Error bars are calculated as standard deviation of the mean from averaging over repeated measurements.

We measure both spinlock and reverse-quench magnetizations as functions of the quench time τ_Q. In the weakly disordered regime, τ_Q ranges from 300 ns to 10 µs, while in the strongly disordered regime it ranges from 300 ns to 8 µs. The lower limit lies below the interaction cycle of the median interaction strength, allowing us to probe the fastest system dynamics. The upper limit is set below the Rydberg lifetime, such that black-body radiation effects remain perturbative. The experimental results are presented in Fig. 4.8. We emphasize that, despite Fig. 4.8 suggesting a longer experimental duration in the strongly disordered regime, the experiment was in fact performed on shorter absolute timescales compared to the weakly disordered regime. A comparison of the two experiments as a function of evolution time in microseconds is provided in Appendix B.

We find that, despite a larger ratio $\Omega_{x,0}/J_{\mathrm{med}}$ in the weakly disordered regime the spinlock magnetization decreases from approximately 0.45 to below 0.35. In contrast, it remains nearly constant around 0.45 in the strongly disordered regime. This behavior is attributed to the higher connectivity of spins in the weakly disordered regime, which enhances spin-spin interactions relative to the strongly disordered case. For the reverse quench protocol, in both regimes the magnetization first decreases to a minimal value close to 0.25. Although in the weakly disordered regime, this

value remains largely constant, it increases significantly above 0.3 in the strongly disordered regime, which may indicate the presence of KZM defects.

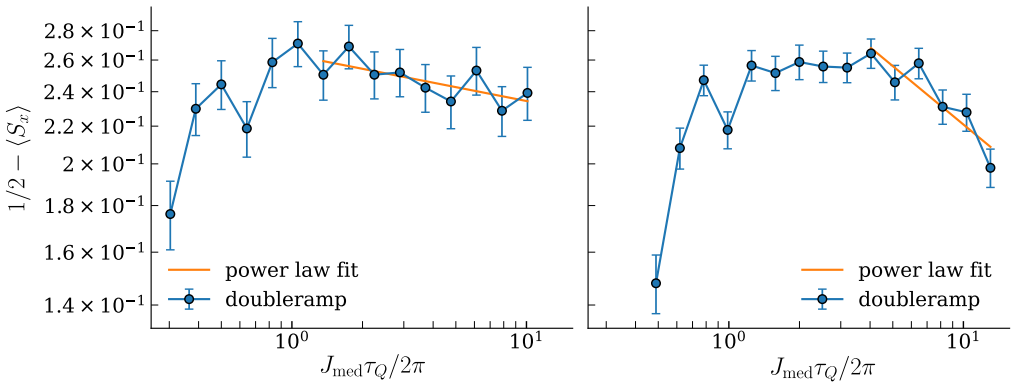

Figure 4.9: *Power law fit to the estimated defect density.* The deviation from full magnetization (blue) is plotted as a function of the quench time τ_Q, with both axes displayed on a logarithmic scale. A corresponding plot using linear axes, which more clearly reveals the nonlinearity of the fit function, is provided in Appendix B. The error bars result from the propagation of uncertainties in the measured magnetization. In the weakly disordered regime (left), the last nine data points are fitted with a power law (orange), whereas in the strongly disordered regime (right), the fit includes only the last six points.

To quantify the increase, we calculate the deviation from full magnetization, $\frac{1}{2} - \langle S_x \rangle$, from the measured magnetization. This quantity serves as an approximation of the reverse-quench defect density and is expected, according to our extension of the gKZM, to follow a power law:

$$\frac{1}{2} - \langle S_x \rangle = A\, \tau_Q^{-\mu},$$

with A and μ as free parameters. We fit this power law to the calculated deviation using a least-squares method. The resulting fits are shown in Fig. 4.9. In the weakly disordered regime, we include the last nine data points, while in the strongly disordered regime, we use the last six, corresponding to the region where power law scaling becomes apparent.

To assess the stability of the fitted Kibble-Zurek exponent μ, we vary the number of data points included in the fit and compute μ as a function of this number. In the weakly disordered regime, μ is indistinguishable from zero when only the last few

points are considered. Including more points yields a small finite value, reflecting a slight increase of magnetization over time. As shown in the next section, this increase is not due to critical dynamics but arises from black-body radiation effects. In contrast, in the strongly disordered regime, μ remains significantly different from zero across all fitting ranges, which may indicate the presence of critical behavior. This will be analyzed in section following the discussion on black-body radiation effects.

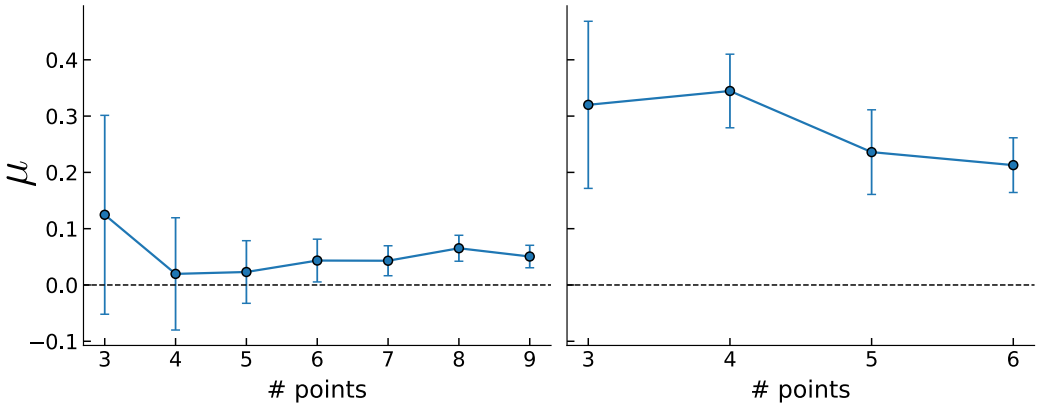

Figure 4.10: *Fitted KZM exponent μ.* Power law fit to of the KZM exponent μ for the weakly (left) and strongly (right) disordered regimes fitted with a least-square fit using the last "# points" from the latest times in the experiment for the fit. Error bars indicate standard deviation of the mean calculated from the covariance matrix. Value zero, marking either the absence of criticality or an infinite randomness fixed point, is indicated by a gray dashed line.

Black-body radiation

Using the *ARC* package [243], we calculate the lifetime of the state $\left|61S_{1/2}, m_J = 1/2\right\rangle$ as $\tau_s = 103.6\,\mu s$, and of the states $\left|61P_{1/2}, m_J = 1/2\right\rangle$ and $\left|61P_{3/2}, m_J = 1/2\right\rangle$ as $\tau_p = 138.4\,\mu s$. These correspond to decay rates on the order of 10 kHz, which is two orders of magnitude smaller than the median interaction strength J_{med}. Consequently, due to separation of timescales, black-body radiation effects may be treated independently from the unitary evolution. This approximation is further supported by the experimental timescale. For the weakly disordered regime, the total experimental duration, comprising the Rydberg excitation time plus twice the maximal quench time, is $5\,\mu s + 2 \times 10\,\mu s = 25\,\mu s$. For the strongly disordered regime, the corresponding

time is $1\,\mu s + 2 \times 8\,\mu s = 17\,\mu s$. Therefore, the maximum time an atom remains in the Rydberg state is at most $t_{max} = 25\,\mu s$, which is small compared to the lifetimes.

We now examine the impact of black-body radiation-induced decay on the magnetization dynamics. For clarity, we begin with the z-component before addressing the experimentally measured x-component. The z-component is determined by the population imbalance between atoms in the p- and s-states. Since the p-states exhibit longer lifetimes than the s-states, this imbalance gradually shifts toward an excess of atoms in the p-state. Let N_p and N_s denote the number of atoms in the p- and s-states, respectively, and define the population ratio as $x = N_s/N_p$. The corresponding magnetization is then given by

$$\langle S_z \rangle = \frac{1}{2}\frac{1-x}{1+x}. \tag{4.59}$$

This equation can be inverted to estimate the population ratio from the magnetization

$$x = \frac{1 - 2\langle S_z \rangle}{1 + 2\langle S_z \rangle}. \tag{4.60}$$

As can be seen from Eq. 4.59, any time dependence of the Rydberg population ratio will eventually affect all magnetization measurements. We will show that this time dependence can lead to an effective increase in magnetization. The ratio x decays as

$$x(t) = N_s(t)/N_p(t) = N_s(0)e^{-t/\tau_s}/(N_p(0)e^{-t/\tau_p} = x(0)e^{-t/\tau_x}, \tag{4.61}$$

where we define the lifetime of the population ratio $x = N_s/N_p$ as

$$\tau_x = \frac{1}{\frac{1}{\tau_s} - \frac{1}{\tau_p}} = 412\,\mu s.$$

This ratio, and consequently the inferred magnetization, is generally more robust than the individual population measurements of N_s and N_p. Experimentally, $x(t)$ is determined by measuring the spin imbalance $N_p(t) - N_s(t)$ via tomographic readout and normalizing it to the total population $N_{tot}(t) = N_s(t) + N_p(t)$.

The evolution of the z-component of the magnetization due to black-body-induced decay is then given by

$$\langle S_z(t) \rangle = \frac{1}{2}\frac{1 - x(0)e^{-t/\tau_x}}{1 + x(0)e^{-t/\tau_x}} = \frac{1}{2}\tanh\left(\frac{t/\tau_x - \ln x(0)}{2}\right). \tag{4.62}$$

The tanh function exhibits its steepest positive slope near zero. Thus, the effect of black-body radiation is strongest at short times when $\ln x(0) = 0$, corresponding to

$x(0) = 1$ or $N_s(0) = N_p(0)$, i.e., vanishing initial magnetization. This condition is met in our experiment, where the initial state is $|\Psi_x\rangle$. In this regime, the magnetization evolves as

$$\langle S_z(t_{\max})\rangle = \frac{1}{2}\tanh\frac{t_{\max}}{2\tau_x} = 0.015\,16\ldots \tag{4.63}$$

As the z-component of the magnetization builds up in the presence of a constant effective magnetic field along the x-direction, generated by the microwave drive during the reverse qeunch or the spin lock protocol, it undergoes coherent rotation in the y-z plane over time. Our tomographic readout accurately captures the modulus of the magnetization in the x-y plane, but has limited sensitivity in distinguishing small y-components from the x-component. As a result, an emerging y-component may be partially misinterpreted as an apparent increase in the measured x-component. As shown in Fig. 4.8, this increase is approximately 0.01, which is smaller than the value expected from black-body radiation alone and can therefore be attributed to it. Moreover, this estimate represents a worst-case scenario. In practice, black-body radiation also introduces dephasing, which drives the system toward thermalization and reduces the magnetization. Additionally, the y-magnetization of the system under the pure dipolar XY Hamiltonian naturally relaxes toward zero [155]. This effect counteracts the increase in y-magnetization and further supports the interpretation that the observed rise is x-magnetization may not be related to critical dynamics.

Comparison to spin glass exponents

In the strongly disordered regime, the observed increase in magnetization is approximately 0.05, about three times larger than our worst-case estimate based on black-body radiation decay. This suggests that the effect cannot be attributed solely to this experimental imperfection. Additionally, the total experimental timescale in this regime is shorter: the maximum quench time is limited to 8 µs, compared to 10 µs in the weakly disordered case. This difference is further reinforced by the shorter Rydberg excitation time, which is only 1 µs in the strongly disordered regime, as opposed to 5 µs in the weakly disordered one.

For all tested numbers of fitting points, the KZM exponent μ remains larger than 0.15 within one standard deviation. Moreover, all values of μ obtained for different numbers of fitting points agree within one sigma, suggesting that μ converges toward a stable value. The most accurate estimate, derived from the fit using six data points, is $\mu = 0.21(5)$. From the definition of the Kibble-Zurek critical exponent, we know

$$\mu = K\frac{\nu}{1+z\nu}. \tag{4.64}$$

We define $K = D - d$ as the difference between the physical dimension of the system, D, and the topological dimension of the defect, d. In the droplet model, these defects correspond to localized excitations, or "droplets", which are expected to have an effective dimension $d = 0$ in the thermodynamic limit, yielding $K = 3$. In contrast, according to the TNT model [71] and the chaotic pair model [72], domain-wall-like excitations may occur, corresponding to $K = 1$. To compare our result for the KZM exponent μ with previous experimental studies of critical spin glass behavior, where the product $z\nu$ is typically extracted from ac-susceptibility measurements [94], we determine $z\nu$ for different assumed values of K. For comparison, we also perform this analysis in the weakly disordered regime, using the most accurately fitted value $\mu = 0.05(2)$, calculated from nine data points.

We use literature values for the correlation-length critical exponent ν. Specifically, we take $\nu_{\text{Ising}} = 1.27(8)$ from recent simulations of a three-dimensional dipolar Ising spin glass [105] and $\nu_{\text{Heisenberg}} = 1.2(1)$ from simulations of a three-dimensional dipolar Heisenberg spin glass [107]. Due to the extremely long relaxation times characteristic of spin glasses [240], the exponent ν has not yet been experimentally determined for the dipolar spin glass $LiHo_xY_{1-x}F_4$. A Monte Carlo study of a possible dipolar XY spin glass, which is still lacking, would be of particular interest for a comparison with our experimentally obtained values of μ. The literature values of ν are used to extract the dynamical critical exponent

$$z = \frac{K}{\mu} - \frac{1}{\nu} \tag{4.65}$$

first. A direct calculation of $z\nu$ from μ and ν using Gaussian error propagation is not applicable, as ν and $z\nu$ are statistically correlated. The error dz is given via Gaussian error propagation as

$$dz = \sqrt{\left(\frac{d\nu}{\nu^2}\right)^2 + \left(\frac{Kd\mu}{\mu^2}\right)^2}. \tag{4.66}$$

We use these values to calculate the product $z\nu$ and its error

$$d(z\nu) = \sqrt{\left(\frac{dz}{z}\right)^2 + \left(\frac{d\nu}{\nu}\right)^2}. \tag{4.67}$$

The results are summarized in Table 4.1. We first note that the choice of the critical exponent ν, whether taken from the dipolar Ising or Heisenberg spin glass

K	Model	Disorder Regime	
		Weakly Disordered	**Strongly Disordered**
1	Ising	$z = 19(8)$, $z\nu = 24(10)$	$z = 3.9(11)$, $z\nu = 5.0(11)$
	Heisenberg	$z = 19(8)$, $z\nu = 23(10)$	$z = 3.9(11)$, $z\nu = 4.6(13)$
2	Ising	$z = 39(16)$, $z\nu = 49(20)$	$z = 8.6(21)$, $z\nu = 10.9(28)$
	Heisenberg	$z = 39(16)$, $z\nu = 47(19)$	$z = 8.6(21)$, $z\nu = 10.3(27)$
3	Ising	$z = 59(24)$, $z\nu = 74(30)$	$z = 13(3)$, $z\nu = 17(4)$
	Heisenberg	$z = 59(24)$, $z\nu = 70(29)$	$z = 13(3)$, $z\nu = 16(4)$

Table 4.1: *Critical exponent calculations.* Exponents z and $z\nu$ are extracted, using the measured exponent μ in both disordered regimes as a function of K. The exponent ν is taken from literature values for both a dipolar Heisenberg [107] and Ising spin glass [105].

universality class, has negligible impact on the outcome. This is expected, as both values agree within their respective uncertainties.

In the weakly disordered regime, for defect dimensions $d = 1$ or $d = 0$ corresponding to $K = 2$ and $K = 3$, the extracted values of z and $z\nu$ significantly exceed those observed in known spin glass systems. To our knowledge, the highest reported value of $z\nu = 19.2$ to date was found in $LiFeSnO_4$–LT [94]. Such a large dynamical exponent could suggest the presence of an infinite-randomness fixed point. However, this scenario is typically associated with systems at strong disorder, where the dynamics slow down dramatically. It is therefore unphysical to attribute such behavior to a weakly disordered system, where the value of z does not increase towards ∞, but instead decreases at stronger disorder. The only seemingly reasonable values of z and $z\nu$ occur for $K = 1$. Yet even here, the mean value of $z\nu \approx 24$ remains unphysically large. Furthermore, the large uncertainty renders this value statistically insignificant within a three-sigma confidence interval.

These findings further support our earlier conclusion: the observed slight increase in magnetization over time is better explained by black-body radiation effects rather than critical slowing down. No evidence of genuine critical behavior is found.

In contrast, in the strongly disordered regime the extracted values of $z\nu$ are significantly greater than zero, with confidence intervals exceeding three standard deviations. Furthermore, the estimated values are consistent with those reported in other glassy systems [94]. Notably, the value $z\nu = 7.8(2)$ measured in the dipolar Ising spin glass $LiHo_{0.045}Y_{0.955}F_4$ [33] lies within one standard deviation of our results for both $K = 1$ and $K = 2$.

This consistency supports the interpretation that the observed increase in magnetization may be linked to critical dynamics characteristic of a spin glass phase. The large dynamical cricital exponents z extracted from the data are in line with values typically found in spin glasses and are uncommon in other ordered magnetic systems. However, this interpretation is constrained by the uncertainties in the magnetization measurements, which permit alternative functional interpretations beyond a simple power law scaling, for example exponential or logarithmic scaling. However, from a physical perspective, the increase in magnetization for large quench times after an initial loss from magnetization is most easily explained by the onset of critical dynamics. Another constraint is that at late times, the system can no longer be treated fully isolated. This raises the possibility that the observed behavior does not reflect a true quantum phase transition, but rather a finite-energy or finite-energy-density crossover.

Several approaches may be pursued to improve the present results. One possibility is to ensure that the system remains effectively isolated for longer quench times, for example by exciting to higher Rydberg states. The state $\left|76S_{1/2}, m_J = 1/2\right\rangle$ has a lifetime of $\tau_s = 179\,\mu\text{s}$, nearly twice that of the state used in the previous experiment. Based on the ratio of dipole matrix elements, the interaction strength between $\left|76S_{1/2}, m_J = 1/2\right\rangle$ and $\left|76P_{1/2}, m_J = 1/2\right\rangle$ is expected to increase by a factor of approximately 2.5 relative to the J_{med} in the current experiment, extending $J_{\text{med}}\tau_Q$ by about half a decade. However, caution is required, as achieving spectral selectivity with the microwave drive becomes more challenging for higher-lying Rydberg states, particularly under strong driving conditions. An additional improvement would be to reduce the standard deviation of the magnetization measurements, thereby strengthening the evidence for a power law dependence of the magnetization on the quench time. This could be achieved by increasing the number of measurements, for example, by extending the measurement time from 10 hours to one week, or by reducing detection noise. Implementing fluorescence detection with high-resolution imaging capabilities would be a promising approach in this direction.

This experiment is also well suited for other platforms, such as NV centers in diamond. In white diamonds, the product of the median interaction strength and the coherence time can reach $J_{\text{med}}\tau_Q \sim 10^4$ [244]. Furthermore, the weak coupling of these systems to a phonon bath allows the study of potential spin glass transitions at small finite temperatures in the presence of a transverse field.

4.7 Conclusion

This chapter began with the question of whether a disordered dipolar XY model can host a spin glass phase transition, typically characterized by a set of critical exponents. Our goal was to detect this critical behavior using only global access to the system, since accurately measuring spin–spin correlations in a three-dimensional system is experimentally challenging. Additionally, we explored the possibility of a quantum phase transition in the absence of thermal fluctuations. This regime is of particular interest for two reasons. First, in Ising spin glasses, the presence of a phase transition as a function of a transverse magnetic field can help distinguish between different paradigmatic models, such as the Parisi mean-field solution [16] and the droplet scaling model by Fisher and Huse [17, 18]. Second, in dipolar Ising spin glasses, the existence of a spin glass phase under a transverse magnetic field remains debated [40, 239, 240]. To address these questions, we developed an extension of the generalized Kibble-Zurek mechanism (gKZM) that enables the observation of critical behavior via global magnetization measurements. Our extension treats defect formation as a stochastic process during reverse quenches. Building on the work of [227], we derived analytical expressions for the defect density after both forward and reverse quenches, as well as for the defect density variance following a forward quench, in the uniform transverse-field Ising model in the limit of large quench times. These predictions were confirmed through exact numerical simulations with $N = 10{,}000$ spins, validating our extension of the gKZM and accurately reproducing the predicted probability of domain-wall formation, $p = 1/\sqrt{2}$.

We then extended our analysis to the bond-disordered transverse field Ising model, building on [236]. Using numerically exact simulations with $N = 128$ spins, we computed the defect density and its variance after both forward and reverse quenches. This model, governed by an infinite-randomness fixed point with dynamical exponent $z = \infty$, presents a regime where critical scaling is controlled by logarithmic corrections and the applicability of the gKZM had remained an open question. Our numerical results demonstrate that the gKZM and our extension accurately describes the behavior in this disordered regime as well, with a domain wall formation probability of $p \approx 0.35$.

In both the uniform and the bond-disordered model, we showed numerically that the defect density can be closely approximated by a measurement of global magnetization in the paramagnetic phase. This observation enables direct experimental implementation. We therefore applied the reverse quench protocol on the Rydberg platform introduced in Chapter 3 to study putative critical behavior in a disordered dipolar XY model. The experiments were performed complementary to

the experiments in Chap. 3 to test whether the observation of energetic-magnetic hysteresis may be connected to the presence of a new magnetic phase. In the weakly disordered regime, were no energetic-magnetic hysteresis was found, we also observed no signatures of critical behavior. In contrast, in the strongly disordered regime, where energetic-magnetic hysteresis effects are strong, we extracted a finite Kibble-Zurek exponent $\mu = 0.21(5)$. Assuming the droplet picture of Fisher and Huse and that the system shares the same correlation length exponent as dipolar Ising spin glasses, we obtained an estimate $z\nu = 17(4)$, consistent with values reported for different spin glass materials [94]. The fact that such scaling behavior is observable on short experimental timescales supports previous predictions that quantum fluctuations can significantly accelerate spin glass dynamics [39–41].

These results establish the reverse quench protocol as a robust, versatile, and experimentally accessible method for dynamically probing criticality using only global control and measurements. This is particularly significant for disordered systems such as spin glasses, where local observables are difficult to access and no practical protocol has previously existed to extract dynamical critical exponents for large system sizes in the absence of thermal fluctuations, where temperature scaling is not available. By enabling such measurements through simple and scalable means, our method addresses a long-standing gap in the experimental toolkit for spin glass physics.

Moreover, the protocol is readily adaptable to a wide range of systems. In experimental realizations of the Edwards–Anderson model [110, 245], it enables the extraction of $z\nu$ from a static magnetization measurement following a reverse quench. This allows a direct comparison with dynamic finite-size scaling estimates on the same platform, providing further validation of the protocol, whose exact applicability has so far only been proven for quasi-free fermion systems. However, as for the KZM and gKZM, we expect our extension to be applicable to a broader class of systems [44, 224, 225]. Additionally, ac-susceptibility measurements, discussed in Chapter 6, offer a complementary probe of spin glass criticality on the same platform and may be used to corroborate this initial signature of critical scaling.

In the strongly disordered regime of the dipolar XY model, we observed both energetic–magnetic hysteresis and signatures of possible critical scaling. As discussed in Chapter 2, theoretical studies of systems exhibiting both many-body localization and spin glass behavior indicate that the spin glass phase is also many-body localized. This observation motivates a detailed investigation of potential many-body localization effects in disordered dipolar systems, which will be addressed in the next chapter.

CHAPTER 5

Probing Localization Effects with Time-Reversal Based Protocols

Parts of this chapter are based on the following publication

Time-reversal in a dipolar quantum many-body spin system[a]
Sebastian Geier, Adrian Braemer, Eduard Braun, Maximilian Müllenbach, Titus Franz, Martin Gärttner, Gerhard Zürn, and Matthias Weidemüller
Phys. Rev. Research **6**, 033197 (2024)

[a]Parts of this manuscript also appear in the dissertation of Sebastian Geier [157]. While Geier concentrates on the experimental realization within a specific set of spin states and on imperfections arising from atomic motion, this chapter focuses on identifying state configurations that enable an accurate experimental implementation. In addition, it examines how higher-order terms in the Rydberg interaction contribute to residual imperfections and how the time-reversal protocol may be extended to characterize localization effects.

In the previous chapters, we have shown that a three-dimensional disordered dipolar Heisenberg XY model exhibits energetic magnetic hysteresis and, assuming the applicability of our extension of the generalized Kibble-Zurek mechanism, a dynamical critical exponent consistent with glassy behavior. Together, these results indicate that the system displays characteristic signatures of a spin glass. Numerical studies of models with both a spin glass phase and a many-body localized phase suggest that the spin glass phase is typically fully localized [46, 47, 108, 109, 111]. This motivates the following question:

Does a finite-size dipolar-interacting quantum system show indications of many-body localization?

Dipolar-interacting systems naturally feature long-range power law couplings. For such systems, recent numerical work suggests that the mechanisms leading to localization may differ from the established picture of exponentially localized many-body localization [132, 133]. Instead, an alternative form of localization, algebraic localization, has been proposed. Moreover, in bond-disordered systems with power law interactions, the localized phase appears to differ qualitatively from all previously studied cases [136]. This leads us to a second question addressed in this chapter:

What is the nature of the localized phase in a bond-disordered, power law interacting system?

While the spectral methods discussed in Chap. 2 provide a robust framework for probing localization, we also seek protocols that can be implemented on the experimental platform described in Appendix A. As outlined in Chap. 2, multiple quantum coherence (MQC) protocols have proven to be effective tools for detecting localization effects, and rely only on global system access. This motivates us to ask:

Can the magnetization and fidelity MQC protocols be used to test a power law interacting isolated spin system for localization effects?

However, these protocols rely on the possibility to accurately revert the arrow of time, or equivalently, to change the sign of the Hamiltonian. As a consequence, this chapter is structured as follows:

In Sec. 5.1, we describe the time-reversal protocol from Ref. [48], with particular attention to experimental imperfections inherent to the platform and possible optimizations. In Sec. 5.2, we then study localization in a one-dimensional bond-disordered, power law interacting toy model, where numerically accessible system sizes allow for larger bulk-to-boundary ratios than in three dimensions, enabling a clearer observation of intrinsic bulk dynamics. In this section, we focus on the time-dependent behavior of the Loschmidt echo, as well as fidelity and magnetization MQCs, in both thermalizing and localized regimes of the model. Finally, Sec. 5.3 summarizes our main findings and proposes directions for further investigation.

5.1 Time-Reversal in a Rydberg quantum simulator

5.1.1 Experimental realization of a time-reversal protocol

In this section, we discuss a protocol designed to reverse the time evolution of an effective spin Hamiltonian employing the experimental platform described in the

previous chapters. To outline this protocol, we will follow mainly [48]. The Rydberg platform realizes a dipolar Heisenberg XY Hamiltonian

$$H_{\text{int}} = \sum_{i<j} J_{ij} \left(S_x^{(i)} S_x^{(j)} + S_y^{(i)} S_y^{(j)} \right), \tag{5.1}$$

where $S_\alpha^{(i)}$ denotes the α-component of the spin-$\frac{1}{2}$ operator acting on site i, and J_{ij} are the interaction coefficients. We seek to invert the global sign of this Hamiltonian, which is mathematically equivalent to time-reversal. This Hamiltonian is implemented by encoding a pseudospin degree of freedom in two Rydberg states, $|\downarrow\rangle_1$ and $|\uparrow\rangle_1$, which feature a dipole-allowed transition. The coupling strengths thus obey a dipolar interaction law,

$$J_{ij} = \frac{C_3^{(1)} \left(1 - 3\cos^2\theta_{ij}\right)}{r_{ij}^3}, \tag{5.2}$$

as detailed in Appendix D. Here, θ_{ij} is the angle between the interatomic axis and the quantization axis set by the applied magnetic field, and r_{ij} is the distance between atoms i and j. In Ref. [48], a different convention is used, with $J_{ij} = C_3^{(1)} \left(1 - 3\cos^2\theta_{ij}\right) / \left(2r_{ij}^3\right)$. As a result, the C_3-coefficients reported in that work is twice as large as the values used here. The convention in this chapter is, however, consistent with the other chapters of this thesis.

This description holds when the atomic separation is large enough that dipole-dipole interactions dominate, and the magnetic field lifts the degeneracy of other atomic eigenstates. Under these conditions, the only resonant pair state coupled to $|\uparrow\rangle_1 \otimes |\downarrow\rangle_1$ is $|\downarrow\rangle_1 \otimes |\uparrow\rangle_1$. The coupling coefficient $C_3^{(1)}$ is then determined by the choice of Rydberg states and reads

$$C_3^{(1)} = \frac{1}{8\pi\epsilon_0} \left\langle 2d_0^{(i)} d_0^{(j)} + d_+^{(i)} d_-^{(j)} + d_-^{(i)} d_+^{(j)} \right\rangle, \tag{5.3}$$

where the angle brackets denote the matrix element evaluated between $|\uparrow\rangle_1 \otimes |\downarrow\rangle_1$ and $|\downarrow\rangle_1 \otimes |\uparrow\rangle_1$, and $d_q^{(i)}$ denotes the q-th component of the dipole operator acting on atom i in the spherical basis. Since the spin degree of freedom is encoded identically for all atoms, the coefficient $C_3^{(1)}$ is uniform across all spin pairs. Consequently, the interaction Hamiltonian is proportional to $C_3^{(1)}$, i.e.

$$H_{\text{int}} \propto C_3^{(1)}. \tag{5.4}$$

To realize effective time reversal, it suffices to invert the sign of the C_3-coefficient, as this consequently also inverts the sign of the Hamiltonian. Because C_3 depends

only on the choice of Rydberg states defining the pseudospin, this inversion can be achieved by encoding the spin degree of freedom in an alternative pair of Rydberg states, $|\downarrow\rangle_2$ and $|\uparrow\rangle_2$. We will show that the sign of the coefficient C_3 depends only on the difference Δm_J between the states encoding the spin. For a dipole-allowed transition, the change in the magnetic quantum number satisfies $\Delta m_J \in \{0, \pm 1\}$. When the states $|\uparrow\rangle_1$ and $|\downarrow\rangle_1$ differ by $\Delta m_J = 0$, Eq. 5.3 gives

$$C_3^{(1)} = \frac{1}{4\pi\epsilon_0} \left| \langle\uparrow|_1 \, d_0 \, |\downarrow\rangle_1 \right|^2 > 0, \tag{5.5}$$

where we used $\langle\uparrow|_1 \, d_0 \, |\downarrow\rangle_1^* = \langle\downarrow|_1 \, d_0 \, |\uparrow\rangle_1$. Here, d_q (without an upper index) denotes the dipole operator acting on a single Rydberg atom.

Conversely, if $\Delta m_J = \pm 1$, Eq. 5.3 yields

$$C_3^{(1)} = -\frac{1}{8\pi\epsilon_0} \left| \langle\uparrow|_1 \, d_\pm \, |\downarrow\rangle_1 \right|^2 < 0, \tag{5.6}$$

where we used $\langle\uparrow|_1 \, d_\pm \, |\downarrow\rangle_1^* = -\langle\downarrow|_1 \, d_\mp \, |\uparrow\rangle_1$.

In summary, the C_3-coefficient is positive when the spin is encoded in states with identical magnetic quantum numbers, and negative otherwise. Since a magnetic field does not mix states with different magnetic quantum numbers when the quantization axis is aligned with the field, this conclusion remains valid for atomic eigenstates in the presence of a magnetic field.

Therefore, time-reversal may be achieved as sketched in Fig. 5.1(a). Without loss of generality, we choose an initial spin encoding where $|\uparrow\rangle_1$ and $|\downarrow\rangle_1$ have identical magnetic quantum numbers. Thus, they realize the Hamiltonian H_{int} with $C_3^{(1)} > 0$. Then, applying coherent Rabi π-pulses, state $|\uparrow\rangle_1$ is transferred to state $|\uparrow\rangle_2$ and $|\downarrow\rangle_1$ to state $|\downarrow\rangle_2$. The states are chosen such that $|\uparrow\rangle_2$ and $|\downarrow\rangle_2$ differ in their magnetic quantum number. Therefore, the interaction is now described by the dipolar Hamiltonian with $C_3^{(2)} < 0$. The inverse encoding, leading to $C_3^{(1)} < 0$ and $C_3^{(2)} > 0$ is also possible. In both cases, according to equations 5.2 and 5.1, after the coherent transfer pusles, the system evolves under the Hamiltonian $-kH_{\text{int}}$, where

$$k = \left| \frac{C_3^{(2)}}{C_3^{(1)}} \right|. \tag{5.7}$$

Note that in Ref. [48], k was defined as the inverse of this quantity, emphasizing the relative duration required in the second encoding step to achieve full time reversal. In this thesis, we instead define k as the proportionality factor of the reverted Hamiltonian, as illustrated in Fig. 5.1. This choice ensures a consistent and

unambiguous definition of k throughout the thesis. We now seek to interpret the rescaling of H_{int} by a dimensionless factor of $-k$. For a time-independent Hamiltonian H_{int}, the time evolution operator is $U(t) = e^{-iH_{\text{int}}t}$. After the coherent transfer pulses, the evolution can be expressed as $U(t) = e^{ikH_{\text{int}}t} = e^{-iH_{\text{int}}(-kt)}$. This describes a time evolution with reversed time, where the effective time scale is multiplied by k: it proceeds faster for $k > 1$ and slower for $k < 1$. Consequently, if the system evolves first under H_{int} for a time t, and then under $-kH_{\text{int}}$ for a time t/k, it should return to its initial state. Consequently, even very small deviations from the ideal evolution become quickly visible by comparing the final state to the initial state. This high sensitivity to imperfections is precisely what makes time-reversal based protocols powerful tools for metrology and quantum sensing [246–248].

To evaluate the accuracy of the time-reversal protocol, we employ the experimental sequence shown in Fig. 5.1(b). The system is first initialized in the spin encoding $|\downarrow\rangle_1$ and $|\uparrow\rangle_1$, and prepared in the fully polarized state along the x-direction, $|\Psi\rangle_x$. It then evolves under the interaction Hamiltonian H_{int} for a duration t_1. Next, two coherent transfer pulses convert the spin encoding to the states $|\downarrow\rangle_2$ and $|\uparrow\rangle_2$. In this basis, the system evolves under the reversed Hamiltonian $-kH_{\text{int}}$ for a time t_2. The sequence concludes with a tomographic magnetization readout, as described in the previous chapters. If the reversal is ideal and $t_2 = t_1/k$, the evolution should perfectly retrace its trajectory, restoring the initial fully polarized state $|\Psi\rangle_x$ with full magnetization along x. However, the derivation of H_{int} and the state transfer rely on several approximations. Consequently, we expect deviations from perfect reversal in the experimental realization of this protocol:

- The two-level approximation assumes that the system dynamics are restricted to the pair states $|\uparrow\rangle_1 \otimes |\downarrow\rangle_1$ and $|\downarrow\rangle_1 \otimes |\uparrow\rangle_1$ in the first spin encoding, and to $|\uparrow\rangle_2 \otimes |\downarrow\rangle_2$ and $|\downarrow\rangle_2 \otimes |\uparrow\rangle_2$ in the second. This assumption neglects off-resonant couplings to other pair states induced by the dipole-dipole interaction, which generate higher-order effects like van-der-Waals interactions which are not time-reverted. Moreover, higher-order multipole interactions, like dipole-quadrupole interactions, are disregarded. The approximation is valid only for dilute Rydberg ensembles, where the interatomic separation is large enough that observable dynamics on experimental timescales arise only from resonant dipole-dipole interactions.

- The preparation of the fully polarized state $|\Psi\rangle_x$ is achieved by driving a resonant transition between $|\uparrow\rangle_1$ and $|\downarrow\rangle_1$ at frequency f_1. The subsequent state transfer employs two Rabi π-pulses: one resonant with the transition $|\downarrow\rangle_1 \leftrightarrow |\downarrow\rangle_2$ at frequency f_2, and another resonant with $|\uparrow\rangle_1 \leftrightarrow |\uparrow\rangle_2$ at frequency f_3. For the

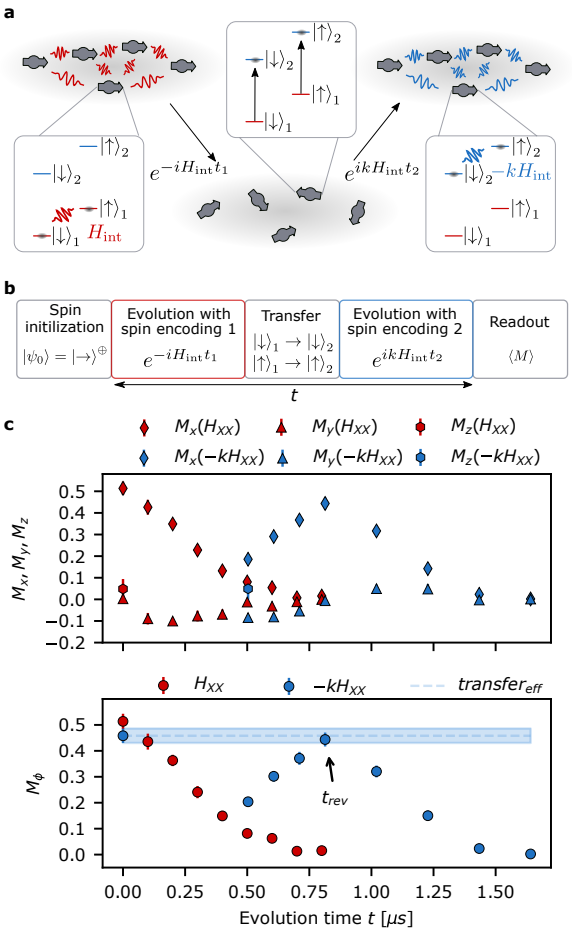

Figure 5.1: *Time reversal in a dipolar Rydberg spin system.* (a) Time reversal protocol. The spin (gray arrow) is initially encoded in the states $|\uparrow\rangle_1$ and $|\downarrow\rangle_1$, evolving under H_{int} (red lines). Coherent transfer to the states $|\uparrow\rangle_2$ and $|\downarrow\rangle_2$ reverses the interaction to $-kH_{\text{int}}$ (blue lines). (b) Experimental protocol used to characterize the time-reversal efficiency. Different steps are indicated by colored boxes. (c) Top: Measurements of the x- (diamond), y- (triangle), and z-magnetization (hexagon) in the first spin encoding (red) and after transfer to the second spin encoding (blue) as a function of evolution time t. Bottom: Measurement of magnetization in the equatorial plane M_ϕ as a function of evolution time t. The blue dashed line indicates the transfer efficiency. Figure taken from [48] with permission.

tomographic readout, Rabi oscillations are driven on the transition $|\downarrow\rangle_2 \leftrightarrow |\uparrow\rangle_2$ at frequency f_4. The selected states $|\uparrow\rangle_1$, $|\downarrow\rangle_1$, $|\uparrow\rangle_2$, and $|\downarrow\rangle_2$, together with the

applied magnetic field, must be chosen such that no near-resonant transitions occur close to the driving frequencies f_1, f_2, f_3, f_4. This condition enables fast driving without unwanted population transfer to other states. A short drive duration also ensures that Rydberg-Rydberg interactions remain negligible during the pulses, thus maximizing pulse fidelity.

We experimentally realize this protocol on the Rydberg quantum simulation platform described in the previous chapters, at a magnetic field of 78 G, with the state encoding defined as $|\downarrow\rangle_1 = \left|61S_{1/2}, m_J = 1/2\right\rangle$, $|\uparrow\rangle_1 = \left|61P_{1/2}, m_J = 1/2\right\rangle$, $|\downarrow\rangle_2 = \left|61P_{1/2}, m_J = -1/2\right\rangle$, and $|\uparrow\rangle_2 = \left|62S_{1/2}, m_J = 1/2\right\rangle$. For clarity, we first present the experimental sequence and the results obtained with this configuration, and subsequently discuss the rationale for selecting these specific states and conditions.

First, a cloud of 332 Rydberg atoms with a median nearest-neighbor distance of $r_{\text{med}} = 8.1\,\mu\text{m}$ is prepared in the Rydberg state $|\uparrow\rangle_1$. A subsequent Rabi $\pi/2$-pulse initializes the system in the fully polarized state $|\Psi\rangle_x$. The state then evolves under the interaction Hamiltonian H_{int}, during which a slow relaxation of the magnetization is observed. The top panel of Fig. 5.1(c) shows the time evolution of all magnetization components, while the lower panel presents the magnetization $M_\phi = \sqrt{M_x^2 + M_y^2}$ in the equatorial plane. We use M_ϕ as a robust measure of the x-magnetization, since phase errors in the tomographic readout can misidentify x-magnetization as y-magnetization. As expected, the magnetization decays over approximately 0.7 µs, consistent with previous observations [42].

To test the time-reversal protocol, a state transfer is applied after 0.4 µs. We observe a subsequent increase of the magnetization, reaching a maximum at 0.81 µs. From this measurement, we estimate $k = 0.97(2)$. In Ref. [48], the interaction coefficients were estimated as $C_3^{(1)} = 1.6\,\text{GHz}\,\mu\text{m}^3$ and $C_3^{(2)} = -1.4\,\text{GHz}\,\mu\text{m}^3$, corresponding to $k = 0.88$. This calculation assumed a negligible effect of the 78 G magnetic field. Using the perturbative code we developed in Appendix D, we recalculate the coefficients including the magnetic field and obtain $C_3^{(1)} = 1.200\,\text{GHz}\,\mu\text{m}^3$ and $C_3^{(2)} = -1.148\,\text{GHz}\,\mu\text{m}^3$, yielding $k = 0.96$, in excellent agreement with the experiment.

The maximal magnetization M_ϕ observed after reversal, defined as the reversal efficiency, is slightly below the expected value of 1/2 for a fully polarized state, indicating imperfect time reversal. A likely cause is the finite Rydberg interaction during the transfer pulses. To quantify this effect, we define the state transfer efficiency as the magnetization measured when the transfer pulses are applied immediately after preparing $|\Psi\rangle_x$. The reversal efficiency matches this transfer efficiency, suggesting that finite interactions during the transfer pulses primarily limit the reversal efficiency.

Additional experiments, presented in Fig. 2a) of Ref. [48], show that the reversal efficiency decreases when the reversal pulses are applied later. A likely explanation, discussed in Ref. [48], is that atomic motion gradually changes the interatomic distances, which in turn modifies H_{int} over time. As a result, the system's evolution cannot be described simply by time-independent Hamiltonians H_{int} in the first encoding and $-kH_{\text{int}}$ in the second. Instead, the evolution follows $H_{\text{int}}(t)$ in the first encoding and $-kH'_{\text{int}}(t')$ in the second, with $H_{\text{int}}(t_1) = H'_{\text{int}}(0)$, reflecting that the atomic positions are approximately the same before and after the transfer pulses. Consequently, the Hamiltonian governing the reversed evolution is not identical to that of the unreversed evolution, even up to a global prefactor, so the system does not retrace its original trajectory perfectly. In the next section, we show that even for static atoms, higher-order terms in the Rydberg–Rydberg interaction generate contributions that are not inverted by the time-reversal protocol, further reducing the reversal efficiency, and we discuss how experimental parameters may be chosen to improve it.

5.1.2 Imperfections in the time-reversal protocol

For short evolution times, the reversal efficiency is primarily limited by the transfer efficiency. We therefore seek two pairs of Rydberg states in which Rabi oscillations can be driven several orders of magnitude faster than the corresponding Rydberg interaction timescale, while ensuring that no non-targeted Rydberg states are populated during the drive. In the following, we justify why, for a magnetic field of 78 G, the experimental choice of states is optimal.

As detailed in Appendix A, the experimental apparatus is designed to excite Rydberg states with quantum numbers $L = 0$, $J = 1/2$ and $m_J = 1/2$. Dipole-allowed transitions between states with principal quantum numbers $48 \lesssim n \lesssim 70$ are accessible with our microwave setup, and the corresponding states exhibit lifetimes of $80\,\mu\text{s} \lesssim \tau \lesssim 200\,\mu\text{s}$. To observe significant dynamics on timescales well below these lifetimes, we encode the spin in the $|61S\rangle$, $|61P\rangle$, and $|62S\rangle$ manifolds. In this regime, microwave-driven state transfer is readily achievable with our Keysight M8195a arbitrary waveform generator without requiring frequency up-conversion, and Rydberg interactions in a dilute system occur on MHz timescales.

For this magnetic field of 78 G, the level diagram within the specified manifolds is shown in Fig. 5.2, with the transitions used in the previous experimental implementation indicated. The magnetic sublevels of $\left|61P_{3/2}\right\rangle$ are not evenly spaced with the magnetic quantum number, as expected from a linear Zeeman effect. This arises because, even at this modest magnetic field, the eigenstate adiabatically con-

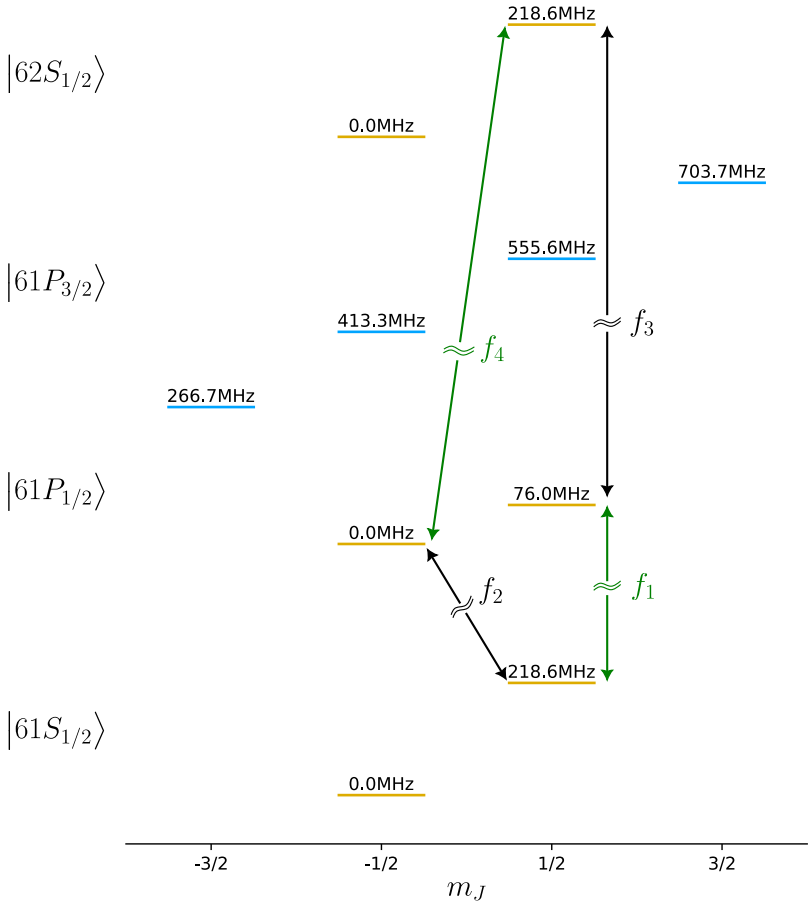

Figure 5.2: *Level diagram of the relevant Rydberg states for the time-reversal protocol.* Energy levels of atomic eigenstates in a magnetic field of 78 G along the quantization axis are shown as horizontal lines, sorted by their magnetic quantum numbers m_J. Levels with total angular momentum $J = 1/2$ are shown in yellow, and those with $J = 3/2$ in blue. Energies ($h = 1$) are indicated above each level relative to a reference. Within each $|nL\rangle$ submanifold, the same energy scale is used. For Rydberg $|nS\rangle$ states, the reference is the energy of the state adiabatically connected to $\left|nS_{1/2}, m_J = -1/2\right\rangle$; for $|nP\rangle$ states, it is the energy of the state adiabatically connected to $\left|nP_{1/2}, m_J = -1/2\right\rangle$. Black arrows indicate the transfer pulse transitions, while green arrows represent the transitions used for spin rotations in each encoding.

nected to $\left|61P_{3/2}, m_J = 1/2\right\rangle$ contains a 1 % admixture of $\left|61P_{1/2}, m_J = 1/2\right\rangle$, and $\left|61P_{3/2}, m_J = -1/2\right\rangle$ includes a 2 % admixture of $\left|61P_{1/2}, m_J = -1/2\right\rangle$. Consequently,

the expected Rabi frequencies are modified at the percent level compared to the zero-field values. Within this diagram, we aim to identify four states suitable for implementing the time-reversal protocol described in the previous section. Therefore, we first focus on identifying four states that allow fast driving while avoiding off-resonant coupling to other, non-targeted states.

To recall, for a two-level system driven with an on-resonant Rabi frequency Ω and detuned by Δ from resonance, the population $p_e(t)$ in the excited state $|\uparrow\rangle$, assuming the system is initially in $|\downarrow\rangle$, is given by

$$p_e(t) = \frac{\Omega^2}{\Omega^2 + \Delta^2} \sin^2\left(\frac{1}{2}\sqrt{\Omega^2 + \Delta^2}\, t\right). \tag{5.8}$$

The time-averaged population exhibits a Lorentzian dependence on the detuning, with a resonance linewidth of Ω [179]. Accordingly, we demand any non-targeted transition with an on-resonant Rabi frequency Ω to be detuned by at least $\Delta = 5\Omega$ to remain effectively off-resonant. As the Rydberg lifetime is small compared to the drive Rabi frequency, it can be neglected.

In addition, the polarization of the microwave drive must be considered. In one spin encoding, the two states have the same magnetic quantum number, whereas in the other encoding, they differ in magnetic quantum number. Consequently, one encoding requires π-polarized radiation, while the other requires circularly polarized radiation with respect to the quantization axis.

In the current setup, the horn antenna produces only linearly polarized light. To generate all required polarization components, a wire grid polarizer is placed at an angle of 135° with respect to the quantization axis. This ensures that a linearly polarized field of amplitude E enters the vacuum chamber at 45° relative to the quantization axis. The resulting field can be decomposed into two components: a field of amplitude $E_0 = E/\sqrt{2}$ linearly polarized along the quantization axis, and a field of amplitude $E_\perp = E/\sqrt{2}$ linearly polarized in the plane perpendicular to it. The latter can be further decomposed into an equal superposition of σ^+ and σ^- components, each with amplitude $E_\pm = E/2$.

Since the Rabi frequency for a drive with amplitude E_d is given by $\Omega = -dE_d$, where d denotes the dipole matrix element, the effective field driving the $\sigma^\pm$ transitions is reduced by a factor of $1/\sqrt{2}$ compared to that driving a π-transition for the same input electric field E. To enable a direct comparison of on-resonant Rabi frequencies across different transitions, we define a weighted dipole matrix element d_w, which equals d_0 for a π-transition and $d_\pm/\sqrt{2}$ for a $\sigma^\pm$-transition. This definition allows a unified comparison of transition strengths independent of the magnetic quantum number change, as d_w accounts for the different field amplitudes associated with each

$\lvert r_1\rangle$	$\lvert r_2\rangle$	d_w $\left[\frac{\text{GHz}}{\text{V cm}^{-1}}\right]$	$\Delta_{f_1}/2\pi$ [MHz]	$\Delta_{f_2}/2\pi$ [MHz]	$\Delta_{f_3}/2\pi$ [MHz]	$\Delta_{f_4}/2\pi$ [MHz]
$\lvert 61S_{1/2}, -1/2\rangle$	$\lvert 61P_{1/2}, -1/2\rangle$	1.65	143	219	-1159	-1235
	$\lvert 61P_{1/2}, 1/2\rangle$	1.65	219	295	-1083	-1159
	$\lvert 61P_{3/2}, -3/2\rangle$	1.99	409	485	-892	-968
	$\lvert 61P_{3/2}, -1/2\rangle$	2.3	556	632	-745	-821
	$\lvert 61P_{3/2}, 1/2\rangle$	1.15	698	774	-603	-679
$\lvert 61S_{1/2}, 1/2\rangle$	$\lvert 61P_{1/2}, -1/2\rangle$	1.65	-76	0	-1377	-1453
	$\lvert 61P_{1/2}, 1/2\rangle$	1.65	0	76	-1301	-1377
	$\lvert 61P_{3/2}, -1/2\rangle$	1.15	337	413	-964	-1040
	$\lvert 61P_{3/2}, 1/2\rangle$	2.3	480	556	-822	-898
	$\lvert 61P_{3/2}, 3/2\rangle$	1.99	628	704	-674	-750
$\lvert 62S_{1/2}, -1/2\rangle$	$\lvert 61P_{1/2}, -1/2\rangle$	1.56	1159	1235	-143	-219
	$\lvert 61P_{1/2}, 1/2\rangle$	1.56	1083	1159	-219	-295
	$\lvert 61P_{3/2}, -3/2\rangle$	1.94	892	968	-409	-485
	$\lvert 61P_{3/2}, -1/2\rangle$	2.24	745	821	-556	-632
	$\lvert 61P_{3/2}, 1/2\rangle$	1.12	603	679	-698	-774
$\lvert 62S_{1/2}, 1/2\rangle$	$\lvert 61P_{1/2}, -1/2\rangle$	1.56	1377	1453	76	0
	$\lvert 61P_{1/2}, 1/2\rangle$	1.56	1301	1377	0	-76
	$\lvert 61P_{3/2}, -1/2\rangle$	1.12	964	1040	-337	-413
	$\lvert 61P_{3/2}, 1/2\rangle$	2.24	822	898	-480	-556
	$\lvert 61P_{3/2}, 3/2\rangle$	1.94	674	750	-628	-704

Table 5.1: *Dipole-allowed transitions in the time-reversal protocol.* The weighted dipole matrix element d_w and the detunings Δ_{f_i} for each drive frequency f_i are presented for all combinations of Rydberg states $|r_1\rangle$ and $|r_2\rangle$. Eigenstates of the Hamiltonian are labeled using the shorthand $|nL_J, m_J\rangle$. Transitions of the 1/2-system and the 3/2-system are highlighted in yellow and orange, respectively.

polarization component in the drive. For all dipole-allowed transitions within the relevant Rydberg manifolds, Table 5.1 lists the corresponding weighted dipole matrix

elements d_w and the detunings from the four transitions used in the experimental implementation.

Experimentally, the system is initialized in a state with magnetic quantum number $m_J = 1/2$. We therefore choose $|\downarrow\rangle_1 = \left|61S_{1/2}, m_J = 1/2\right\rangle$ as the initial state, eliminating the need for additional microwave pulses for state preparation and reducing pulse-induced errors. In order to choose other states, they must satisfy the following requirements:

1. Transfer pulses should have a large d_w, enabling high Rabi frequencies with the experimental microwave setup. Ideally, the Rabi frequency is orders of magnitude larger than the typical Rydberg-Rydberg interaction strength.

2. To maintain the validity of the two-level approximation while driving the system rapidly, transfer pulses must be far detuned from all other nearby transitions.

From this analysis, the states used in the experiment appear suboptimal. Both the transfer pulses and the pulses within each spin-encoding manifold are detuned from nearby resonances by only $\Delta = 2\pi \times 76\,\mathrm{MHz}$, corresponding to the Zeeman splitting in the $\left|61P_{1/2}\right\rangle$ manifold. Requiring clean pulses with $\Omega/\Delta < 1/5$ limits the Rabi frequency to $\Omega < 2\pi \times 15\,\mathrm{MHz}$, only about an order of magnitude larger than the median interaction $J_{\mathrm{med}} = 2\pi \times 0.86\,\mathrm{MHz}$.

A better choice is the encoding $|\downarrow\rangle_1 = \left|61S_{1/2}, m_J = 1/2\right\rangle$, $|\uparrow\rangle_1 = \left|61P_{3/2}, m_J = 1/2\right\rangle$, $|\uparrow\rangle_2 = \left|62S_{1/2}, m_J = 1/2\right\rangle$, $|\downarrow\rangle_2 = \left|61P_{3/2}, m_J = -1/2\right\rangle$, which omits the small splitting in the $\left|61P_{1/2}\right\rangle$ manifold. We refer to this as the 3/2-system, since all P-states lie in the $P_{3/2}$ manifold, in contrast to the 1/2-system used in the experiment. In addition to a larger minimum detuning of $2\pi \times 140\,\mathrm{MHz}$, the 3/2-system also features larger d_w for the transfer pulses, making it an optimal choice.

However, so far we neglected the effects of higher-order terms in the Rydberg-Rydberg interaction. Apart from the direct dipole-dipole interaction, which scales as $\sim 1/r^3$ for a distance r between two Rydberg states, treating the dipole-dipole interaction up to second order in perturbation theory leads to additional terms scaling as $1/r^6$. Including these additional terms within the two-level approximation, the effective Hamiltonian reads

$$H_{\mathrm{int}} = \sum_{i<j} {J_x}^{(ij)} \left(S_x^{(i)} S_x^{(j)} + S_y^{(i)} S_y^{(j)}\right) + {J_z}^{(ij)} S_z^{(i)} S_z^{(j)} + {h_z}^{(ij)} \left(S_z^{(i)} + S_z^{(j)}\right), \qquad (5.9)$$

where the coupling constants fulfill

$$J_z^{(ij)} = \frac{C_6(\theta_{ij}, |\uparrow\uparrow\rangle) + C_6(\theta_{ij}, |\downarrow\downarrow\rangle) - 2C_6(\theta_{ij}, |\uparrow\downarrow\rangle)}{r_{ij}^6}, \tag{5.10}$$

$$J_x^{(ij)} = C_3 \frac{1 - 3\cos^2(\theta_{ij})}{r_{ij}^3}, \tag{5.11}$$

$$h_z^{(ij)} = \frac{C_6(\theta_{ij}, |\uparrow\uparrow\rangle) - C_6(\theta_{ij}, |\downarrow\downarrow\rangle)}{2r_{ij}^6}. \tag{5.12}$$

Here, we introduce $C_6(|ab\rangle)$ as the energy shift that the pair state $|ab\rangle$ experiences due to off-resonant coupling of the dipole-dipole interaction to other pair states, as detailed in Appendix D.

A detailed analysis of the C_6 coefficients for the 1/2-system was previously carried out in the Bachelor's thesis of Matthias Lotze [249] under the supervision of the author. In that work, an early implementation of the code described in Appendix D was provided, and the study concentrated on the angular dependence for the terms in the two distinct spin encodings. In the following, we extend this analysis by comparing the 1/2- and 3/2-systems. We further demonstrate why, when the initial encoding is defined as $|\downarrow\rangle_1 = |nS\rangle$ and $|\uparrow\rangle_1 = |n'P\rangle$, the corresponding reversed encoding should take the form $|\downarrow\rangle_2 = |n''P\rangle$ and $|\uparrow\rangle_2 = |n'''S\rangle$, which we will denote as a parity flip encoding, rather than $|\downarrow\rangle_2 = |n''S\rangle$ and $|\uparrow\rangle_2 = |n'''P\rangle$.

Therefore, we start by calculating the terms J_x, J_z and h_z for two Rydberg atoms at a distance $r = 16\,\mu\text{m}$ as a function of the angle θ between the interatomic axis and the quantization axis set by the applied magnetic field of 78 G. The distance is chosen at 16 µm, as this is often a typical median atom-atom distance realized with the Rydberg platform. We begin by discussing the results for the 1/2-system, where these terms are depicted in Fig. 5.4.

We first note the characteristic $1 - 3\cos^2(\theta)$ dependence in the J_x terms. From this, we extract $C_3^{(1)} = 1.2\,\text{GHz}\,\mu\text{m}^3$ and $C_3^{(2)} = -1.148\,\text{GHz}\,\mu\text{m}^3$, yielding $k = 0.96 \approx 1$. Consequently, for complete time reversal, the system must evolve for approximately the same duration in both spin encodings. The mean local fields are $h_z^{(1)} = 2\pi \times -0.004\,\text{MHz}$ and $h_z^{(2)} = 2\pi \times 0.008\,\text{MHz}$, resulting in an average field over a time-reversal protocol

$$\frac{h_z^{(1)} + (1/k)h_z^{(2)}}{1 + 1/k} = 2\pi \times 0.002\,\text{MHz}.$$

Here, the superscript indicates the spin encoding used. As will be shown later, the suppression of the h_z terms arises directly from the parity flip encoding. The main

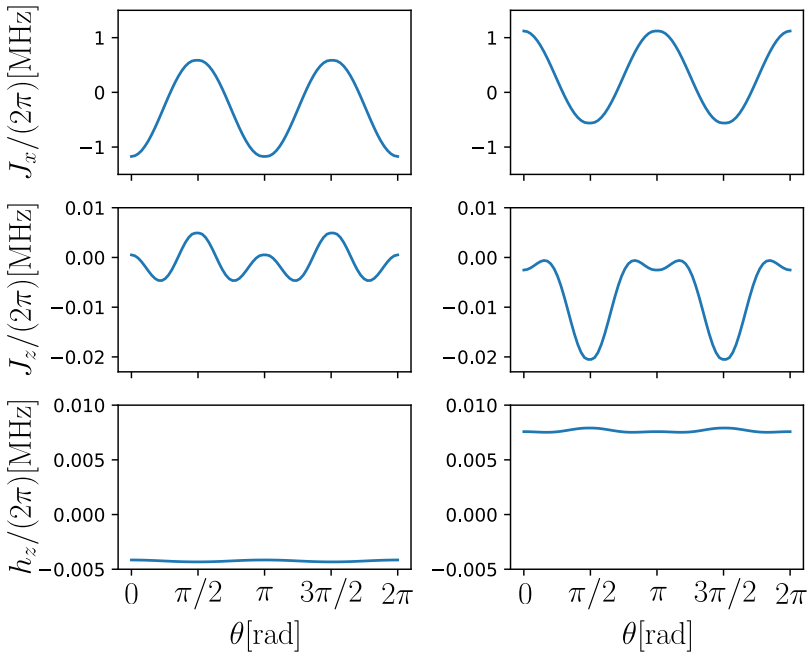

Figure 5.3: *Angular dependence of interaction terms in the* 1/2*-system.* From top to bottom, the Hamiltonian coupling terms J_x, J_z, and h_z are plotted as functions of the angle θ between the interatomic axis and the magnetic field defining the quantization axis. Results are shown for the spin encoding $|\downarrow\rangle_1$, $|\uparrow\rangle_1$ on the left, and for $|\downarrow\rangle_2$, $|\uparrow\rangle_2$ on the right. The interatomic distance is fixed at $r = 16\,\mu\text{m}$.

limitation of the 1/2-encoding is the relatively large Ising interaction term, with $J_z^{(2)} = 2\pi \times -0.007\,\text{MHz}$ and a maximum strength of $J_z^{(2)} = 2\pi \times -0.02\,\text{MHz}$, while $\left|J_z^{(1)}(\theta)\right| \leq 2\pi \times 0.005\,\text{MHz}$. This residual Ising contribution is the dominant source of time-dependent imperfections in the time-reversal protocol in the 1/2-system.

The results for the 3/2-system are shown in Fig. 5.4. As in the 1/2-system, we observe the characteristic $1 - 3\cos^2(\theta)$ dependence of J_x. From this, we determine $C_3^{(1)} = 3.574\,\text{GHz}\,\mu\text{m}^3$ and $C_3^{(2)} = -1.048\,\text{GHz}\,\mu\text{m}^3$, yielding $k = 0.293$. Consequently, to reverse the dynamics driven by direct dipole-dipole interactions, the system must evolve for approximately three times longer in the second spin encoding than in the first. However, the higher-order correction terms J_z and h_z are substantially larger in the second encoding, where the system evolves for a longer time, than in the first encoding. Averaging the Ising interaction over all directions, we obtain $J_z^{(1)} = 2\pi \times -0.009\,\text{MHz}$ and $J_z^{(2)} = 2\pi \times -0.011\,\text{MHz}$, thus resulting in an Ising interaction which is about twice as large in the first encoding compared to the

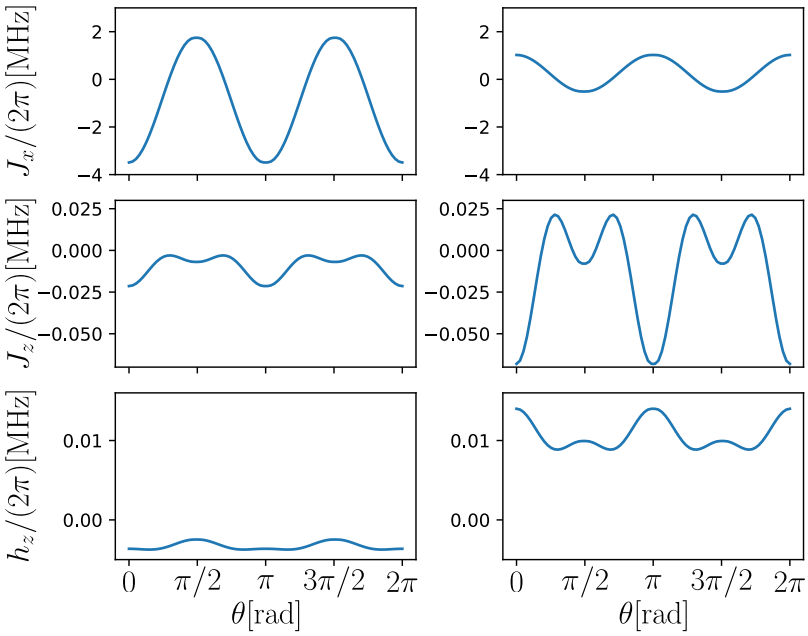

Figure 5.4: *Angular dependence of interaction terms in the* 3/2*-system.* From top to bottom, the Hamiltonian coupling terms J_x, J_z, and h_z are plotted as functions of the angle θ between the interatomic axis and the magnetic field defining the quantization axis. Results are shown for the spin encoding $|{\downarrow}\rangle_1$, $|{\uparrow}\rangle_1$ on the left, and for $|{\downarrow}\rangle_2$, $|{\uparrow}\rangle_2$ on the right. The interatomic distance is fixed at $r = 16\,\mu\text{m}$.

1/2-system, and by a factor of 1.6 larger in the second encoding. As far as the h_z terms are regarded, even though the sign of the meadian interaction is reversed, i.e. $h_z^{(1)} = 2\pi \times -0.003\,\text{MHz}$ and $h_z^{(2)} = 2\pi \times 0.01\,\text{MHz}$, yielding to an average h_z over the duration of a reversal protocol of

$$\frac{h_z^{(1)} + (1/k)h_z^{(2)}}{1 + 1/k} = 2\pi \times 0.007\,\text{MHz},$$

which is three times larger than in the 1/2-system. As a result of the larger J_z and h_z terms, the 3/2-system exhibits stronger time-dependent deviations from an ideal time-reversal protocol. These become especially for the angles where the dipolar interaction almost vanishes, and for pairs with a short distance close to the blockade radius. Consequently, the 1/2-system is less affected by errors arising from van der Waals correction terms, making it better suited for high-precision time-reversal protocols.

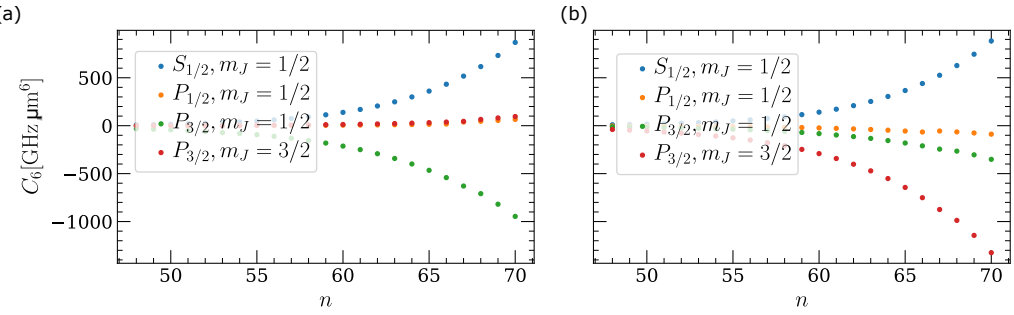

Figure 5.5: *Dependence of the C_6 coefficients on the principal quantum number n.* The C_6 coefficient at zero magnetic field is shown as a function of the principal quantum number n for the pair states $\left|nS_{1/2}, m_J = 1/2\right\rangle \otimes \left|nS_{1/2}, m_J = 1/2\right\rangle$ (blue), $\left|nP_{1/2}, m_J = 1/2\right\rangle \otimes \left|nP_{1/2}, m_J = 1/2\right\rangle$ (orange), $\left|nP_{3/2}, m_J = 1/2\right\rangle \otimes \left|nP_{3/2}, m_J = 1/2\right\rangle$ (green), and $\left|nP_{3/2}, m_J = 3/2\right\rangle \otimes \left|nP_{3/2}, m_J = 3/2\right\rangle$ (red). To account for the slight angular dependence of the C_6 coefficient, results are shown for two orientations of the interatomic axis with respect to the quantization axis: (a) $\theta = 0$ and (b) $\theta = \pi/2$. States with negative m_J are omitted, as the C_6 coefficients are identical to those for positive m_J. The simulation was performed using the *ARC* package [243], where we took into account that *ARC* uses a different sign convention than this thesis.

So far, we have excluded spin encodings which are not parity flip encodings, i.e. spin encodings in which both $|\downarrow\rangle_1$ and $|\downarrow\rangle_2$ correspond to a Rydberg S or a Rydberg P-state, respectively. For one such encoding, Ref. [249] showed that the h_z term does not change sign and is therefore enhanced. In the following, we briefly show that the sign inversion of h_z is a general feature of parity flip encodings.

We recall from Eq. 5.12 that h_z is proportional to the difference between the C_6 coefficients of the two encoding states. Figure 5.5 shows that, in the absence of a magnetic field, the C_6 coefficient of Rydberg nP states is always smaller than that of Rydberg nS states. Consequently, we obtain $h_z < 0$ for $|\downarrow\rangle = |nS\rangle$ and $|\uparrow\rangle = |n'P\rangle$, and $h_z > 0$ for $|\downarrow\rangle = |nP\rangle$ and $|\uparrow\rangle = |n'S\rangle$. Since the C_6 coefficient depends only weakly on the magnetic field below 100 G, this relation also holds for finite fields, consistent with our findings for the 1/2- and 3/2-systems.

To summarize, we have shown that the 1/2-encoding at a magnetic field of 78 G provides optimal conditions for implementing a time-reversal protocol with high reversal efficiency. The main limitation arises from the residual Rydberg interaction during the transfer pulses, whose minimal duration is constrained by the small Zeeman splitting of $\Delta = 2\pi \times 76$ MHz in the $\left|61P_{1/2}\right\rangle$ manifold.

Two strategies can be employed to further enhance the reversal efficiency. Increasing the magnetic field to 185 G would raise the Zeeman splitting to $\Delta = 2\pi \times 180\,\mathrm{MHz}$, enabling the use of transfer pulses with Rabi frequencies up to $\Omega = 2\pi \times 30\,\mathrm{MHz}$ without populating unwanted Rydberg states.

Alternatively, even higher Rabi frequencies could be achieved by employing a quadrupole horn antenna, as described in Appendix E. This setup generates radiation with the correct polarization only, thereby exploiting additional selection rules. Under these conditions, and even at a magnetic field of 78 G, the nearest transition remains detuned by approximately $\Delta \approx 2\pi \times 480\,\mathrm{MHz}$, allowing Rabi cycles at $\Omega = 2\pi \times 80\,\mathrm{MHz}$ without populating neighboring states.

5.2 Studying Localization effects through time-reversal protocols

So far, we have introduced a protocol to invert the dipole-dipole interactions between Rydberg atoms and discussed its limitations. We now address whether this protocol can be used to probe potential localization effects. This question is also motivated by numerical studies of models in which both spin glass behavior and many-body localization occur in isolated quantum systems. In these models, the spin glass phase also exhibits, at finite sizes, a many-body localized regime [46, 47, 108, 109, 111]. As we found glassy behavior in a three dimensional disordered dipolar interacting spin model, we also seek to test whether it exhibits signatures of localization. As discussed in Chap. 2, the Hamiltonian spectral statistics provide a reliable method for detecting localization effects in finite system sizes. However, the properties are typically not experimentally measurable. Therefore, we want to test whether time-reversal based methods might also provide a promising tool to distinguish localized regimes in a power law interacting system. In detail, we will numerically analyze whether Loschmidt echos and multiple quantum coherence (MQC) protocols allow to characterize localization effects in a power law interacting model. The simulation code for generating Hamiltonian spectral statistics, as well as for the time evolution underlying the Loschmidt echo and multiple quantum coherence protocols, was implemented by Matthias Lotze under the supervision of the author, building upon the *SpinModels.jl* library by Adrian Braemer [250].

5.2.1 Spectral statistics of a bond-disordered Heisenberg model with power law interactions

Here, we will further examine a toy model which was shown to feature both a thermalizing and a localized regime [136, 186]. The model is described by the Hamiltonian

$$H_0 = \sum_{i=1}^{N} \sum_{j=1}^{i-1} \frac{1}{|x_i - x_j|^\alpha} \left(S_x^{(i)} S_x^{(j)} + S_y^{(i)} S_y^{(j)} + \Delta S_z^{(i)} S_z^{(j)} \right), \tag{5.13}$$

which corresponds to an anisotropic spin-1/2 Heisenberg XXZ model with N spins located on positions x_i. The interaction has a long range and decays with a power law with exponent α. Additionally, the spin-spin interaction in the z-direction is anisotropic and described with an anisotropy parameter $\Delta \neq 1$. To compare our results to Refs. [136, 186] we choose $\alpha = 6$ and $\Delta = -0.73$, a regime which in three spatial dimensions was also realized with our Rydberg simulation platform [155, 168], and may in principle be realized in one dimension in Rydberg tweezer arrays.

The spin-spin couplings $J_{ij} = 1/|x_i - x_j|^\alpha$ depend on the distance between spins. Thus, we quantify disorder in the model through positional disorder, similar to Ref. [136]. The N spins are assumed to occupy a one-dimensional line of length $L-(N+1)/2$, and we define the ratio $\rho = N/L$. Disorder is introduced by imposing a minimal distance of $1/2$ between spins, generating positional correlations. For $\rho = 1$, the spins are forced onto a uniform lattice with spacing $1/2$, leaving only a single configuration. In contrast, for small ρ (large L), multiple positional configurations become possible, leading to significant disorder. Following [136], we introduce the disorder

$$W = \frac{1}{\rho} - 1. \tag{5.14}$$

Different disorder realizations can be generated following the scheme introduced in Ref. [186]. For a given disorder strength W, the corresponding density ρ is obtained from Eq. 5.14, which in turn yields L for a fixed system size N. The particle positions x_i are then drawn from a uniform distribution within the interval $x_i \in [0, L-(N+1)/2]$. To ensure that $W = 0$ corresponds to a perfect lattice configuration, only configurations where all particles are separated by at least $1/2$ are retained. However, as pointed out in Ref. [186], this procedure becomes highly inefficient for $W \ll 1$ due to the constraints imposed by the Rényi parking constant [251]. To overcome this limitation, we employ the sampling method devised in Ref. [136], which also efficiently generates nearly ordered positional configurations. The key idea is to enforce the distance constraints directly during sampling, thereby avoiding probabilistic post-selection.

For this purpose, we introduce a reduced length $\tilde{L} = L - N$ and draw N sorted positions x_i $(1 \leq i \leq N)$ from a uniform distribution within $[0, \tilde{L}]$. The subsequent mapping $x_i \to x_i + i/2 - 1/2$ ensures that all distance constraints are satisfied. As an illustrative example, for $W = 0$ and $\rho = 1$, we have $L = N$, which implies $\tilde{L} = 0$. In this case, $x_i = 0$ for all i, and the mapping yields $x_1 = 0$, $x_2 = 1/2$, $x_3 = 2/2$, ..., $x_N = (N-1)/2$, corresponding to a perfect lattice configuration with spacing $1/2$.

To minimize finite-size effects, we implement the periodic boundary conditions introduced in Ref. [186]. Since power law interactions are, in principle, infinite-ranged, each spin would interact with every other spin an infinite number of times. To avoid this, we truncate the periodic boundary conditions by retaining, for each pair of spins (i, j), only the strongest interaction. Consequently, the distance $|x_i - x_j|$ is replaced by the distance function

$$d(x_i, x_j) = \begin{cases} |x_i - x_j| & |x_i - x_j| \leq L/2 \\ L/2 - |x_i - x_j| & |x_i - x_j| > L/2. \end{cases} \tag{5.15}$$

Using this model, we first analyze typical signatures of many-body localization to characterize the system as a function of the disorder W. Therefore, we employ two common methods: The mean level spacing ratio $\overline{r}$, which we discussed in detail in Chap. 2, and the Thouless parameter $\overline{\mathcal{G}}$ [252]. The mean level spacing ratio quantifies how closely a Hamiltonian follows random matrix statistics. In contrast, the Thouless parameter measures the sensitivity of eigenstates to a local perturbation V. It is defined as

$$\overline{\mathcal{G}} = \ln \overline{\frac{\langle n|V|n+1\rangle}{E'_{n+1} - E'_n}}, \tag{5.16}$$

where $|n\rangle$ denotes an eigenstate of the unperturbed Hamiltonian H_0 with eigenenergy E_n, and $E'_n = E_n + \langle n|V|n\rangle$ is the corrected energy of $|n\rangle$ in first order perturbation theory. The overline indicates an average within a symmetry sector, since symmetries partition the spectrum into independent sectors and modify the spectral statistics.

Within the framework of the eigenstate thermalization hypothesis (ETH), eigenstates behave as random vectors. A local perturbation V then couples each eigenstate to an extensive number of others at a similar energy, resulting in $\overline{\mathcal{G}} \propto L$. Conversely, for an l-bit Hamiltonian, where the eigenstates of the local integrals of motion $\tau^{(i)}$ are exponentially localized, the coupling between distinct eigenstates of H_0 with similar energy is exponentially suppressed with system size, leading to $\overline{\mathcal{G}} \propto -L$. Hence, in a thermalizing (ETH) regime, $\overline{\mathcal{G}}$ increases with system size, whereas in a localized regime it decreases [252].

The Hamiltonian defined in Eq. 5.13 features two symmetries: A continuous $U(1)$ symmetry considering rotations of the spins around the z-axis, and a discrete

$\mathbb{Z}_2$ spin-flip symmetry $|\downarrow\rangle \leftrightarrow |\uparrow\rangle$. The $U(1)$ symmetry leads to a conserved total z-magnetization, and thus the different symmetry sectors can be labeled by the total z-magnetization M_z. As the $\mathbb{Z}_2$ spin-flip symmetry couples only states with magnetization $+M_z$ to those with magnetization $-M_z$, it is explicitly broken in a sector of $M_z \neq 0$, and thus we may apply Hamiltonian spectral statistics methods. To calculate $\overline{r}$ and $\overline{\mathcal{G}}$, we thus choose for even N the sector with $M_z = 1$ and for odd N the sector with $M_z = 1/2$. For even N, this is the magnetization sector containing the largest number of states and $M_z \neq 0$, and for odd N, it is the sector containing the largest number of states.

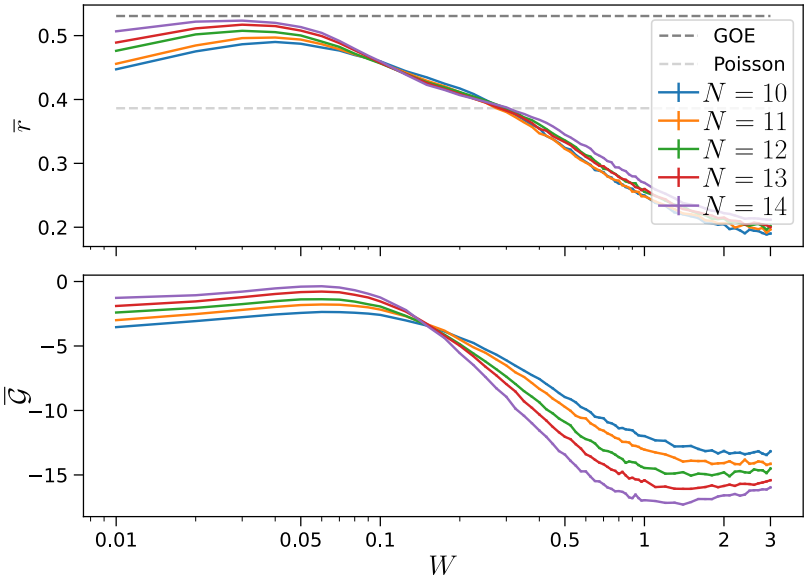

Figure 5.6: *Spectral statistics indicating localization.* For different system sizes, we present the mean level spacing ratio $\overline{r}$ (top) and Thouless parameter $\overline{\mathcal{G}}$ (bottom) as a function of disorder W. A logarithmic scale is used for the disorder axis to resolve the rapid crossover at small W values, which would appear compressed on a linear scale. The values are calculated from averaging over 2000 disorder samples. Error bars indicate the standard deviation of the mean. For the mean level spacing ratio, the values expected for a Gaussian orthogonal ensemble (GOE, dark gray) and for a Poisson level distribution (Poisson, light gray) are indicated as dashed lines.

The results for the numerical simulation of $\overline{r}$ and $\overline{\mathcal{G}}$ are presented in Fig. 5.6. For each particle number N from 10 to 14, we sample for 66 disorder strengths W from 0.01 to 3 two thousand different positional distributions. For each positional distribution, we construct the Hamiltonian according to Eq. 5.13, and project it

onto the magnetization sector with magnetization $M_z = 1$ ($M_z = 1/2$) for even (odd) N. In this subspace, we diagonalize the Hamiltonian, which allows us to immediately calculate $\overline{r}$. To calculate the Thouless parameter, we choose as our perturbation a local magnetic field of $V = gS_z^{(1)}$, where $g = 10$ denotes the strength of the perturbation.

For weak disorder $W < 0.01$, the mean level spacing ration $\overline{r}$ increases as a function N, approaching the GOE prediction of approximately 0.53, indicating an ETH thermalizing regime. On the other hand, for intermediate disorder strengths $0.1 \leq W \leq 0.3$, the level spacing ratio decreases as a function of particle number, and for strong disorder $W > 0.3$ reaches values lower than expected for Poissonian level statistics. This sub-Poissonian behavior, also reported in Refs. [136, 186], suggests a non-thermalizing regime distinct from the integrable l-bit scenarios typically associated with Poissonian statistics [136], and thus might present a distinct type of localization.

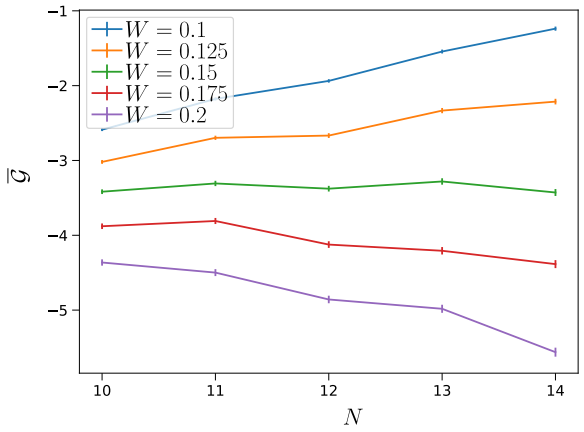

Figure 5.7: *Critical disorder from the Thouless parameter.* The Thouless parameter is shown as a function of system size N for 5 different disorder strengths. Error bars represent the standard error from the mean, taken over 2000 disorder realizations. Connecting lines serve as guide to the eye.

On the other hand, the Thouless parameter behaves similarly to what is known from exponentially localized MBL models. For small disorder, it increases with system size, while for large disorder, it decreases with system size. Following [252], we may determine a critical disorder W_c by presenting the Thouless parameter as a function of system size N for different fixed disorder W, shown in Fig. 5.7. We observe that for $W < 0.15$, the Thouless parameter decreases linearly with N, while for $W > 0.15$, it increases linearly with N. For the simulated system sizes, at $W = 0.15$, we observe no significant change in $\overline{\mathcal{G}}$, thus determining a critical disorder strength $W_c = 0.150(25)$.

Taking the behavior of both the mean level spacing ratio, as well as the Thouless parameter into account, we arrive at the conclusion that for $W = 0.03$, the system is in an ETH thermalizing regime, while for $W = 2.0$, it is a localized, but not exponentially many-body localized regime, for system sizes $N \leq 14$. Therefore, in the following, we will analyze dynamical properties at these two disorder strengths.

5.2.2 Loschmidt Echo

For the considered finite system sizes, we aim to test whether dynamical observables, which may be experimentally accessible, also capture localization properties. Ref. [150] demonstrated that the time-dependent scaling of Loschmidt echoes provides a reliable probe for distinguishing exponentially localized from thermalizing behavior in finite systems. The Loschmidt echo, intrinsically linked to time-reversal protocols, has been discussed from a general perspective in Refs. [253, 254]. It consists of preparing an initial state $|\Psi_0\rangle$, evolving it forward in time under a Hamiltonian H_0, and subsequently backward in time under a perturbed Hamiltonian $H_1 = H_0 + \Sigma$. The fidelity with respect to the initial state defines the Loschmidt echo

$$\mathcal{F}_{\mathrm{LE}}(t) = \left| \langle \Psi_0 | e^{iH_1 t} e^{-iH_0 t} | \Psi_0 \rangle \right|^2 , \tag{5.17}$$

which is highly sensitive to the perturbation Σ. Because of this sensitivity, Loschmidt echoes have been employed for characterizing decoherence in many-body systems [151], and as probes of dynamical phase transitions [255].

Following Ref. [150], we analyze the Loschmidt echo through the overlap function

$$S(t) = \langle \Psi_0 | e^{i(H_0 + V/2)t} e^{-i(H_0 - V/2)t} | \Psi_0 \rangle , \tag{5.18}$$

where the perturbation $V = gS_z^{(1)}$ acts symmetrically during forward and backward evolution. We choose $g = 20$ to study the effect of a strong but local perturbation on the system. Since the operator V here is proportional to the one used in the Thouless parameter analysis, spectral properties can be directly linked to the dynamical behavior discussed below.

Comparing Eq. 5.17 and Eq. 5.18 shows that the Loschmidt echo can be written as the modulus squared of the overlap function $\mathcal{F}_{\mathrm{LE}}(t) = |S(t)|^2$. In thermalizing systems, the Loschmidt echo typically decays exponentially in time toward the equilibrium value, whereas in many-body localized systems it follows a power law decay, $|S(t)|^2 \sim t^{-\delta}$ with $\delta > 0$. Nevertheless, exceptions to the exponential decay in thermalizing systems exists. For example, a decay of the form $|S(t)|^2 = 1 - at^{\gamma}$ with $\gamma, a > 0$ has been reported for an ordered, non-integrable spin system [256]. Thus,

to our knowledge, a power law decay $|S(t)|^2 \sim t^{-\delta}$ is a characteristic signature of a many-body localized phase and can be derived from the assumption of exponentially localized LIOMs [150].

As a bond-disordered localized model differs in many characteristics both from an exponentially localized MBL system, as well as from an ergodic ETH system [136], we examine whether the Loschmidt echo also behaves uniquely in such a system. Therefore, we simulate the overlap $S(t)$ defined in Eq. 5.18 for a perturbation $V = 20S_z^{(1)}$ and two disorder strengths, $W = 0.03$ and $W = 2.0$. For the initial state $|\Psi_0\rangle$, we choose the Néel state $|\uparrow\downarrow\uparrow\ldots\rangle$, which allows first of all for a direct comparison with Ref. [150], where the Loschmidt echo for a Néel state was determined for an exponentially localized model. Furthermore, for spin models with $\mathbb{Z}_2$ spin-flip symmetry, the Loschmidt echo initiated from a Néel state is believed to reflect the high-energy dynamics of the Hamiltonian itself. This means it captures the generic behavior dictated by the Hamiltonian rather than the peculiar dynamics that might arise from a very specific or fine-tuned initial state [257]. For each value of W, we generate 2000 spatial disorder configurations and construct the corresponding Hamiltonian H_0 according to Eq. 5.13. For each realization (l), we compute the median interaction strength

$$J_{\text{med}}^{(l)} = 2\pi \times \underset{j}{\text{median}}\left(\max_i \left|x_i^{(l)} - x_j^{(l)}\right|^{-6}\right).$$

We then rescale the Hamiltonian using the average value $J_{\text{med}} = \underset{(l)}{\text{mean}}\, J_{\text{med}}^{(l)}$ obtained by averaging over all sampled disorder realizations at fixed W.

This normalization enables a meaningful comparison across different disorder strengths, as strong disorder lowers the particle density and thereby weakens the typical interaction scale. The rescaling compensates for this density-dependent effect. After computing $S(t)$ for each Hamiltonian, we average its modulus squared over all disorder realizations, obtaining $\overline{|S(t)|^2}$, which represents the mean Loschmidt echo. The results are shown in Fig. 5.8.

We first analyze the weakly disordered thermalizing regime ($W = 0.03$). For early times with $tJ_{\text{med}}/(2\pi) \ll 1$, we find a decay

$$|S(t)|^2 \approx 1 - 150\left(\frac{tJ_{\text{med}}}{2\pi}\right)^4. \tag{5.19}$$

A detailed discussion of the fit is provided in Appendix C. This quartic decay in time is in contrast to theoretical predictions that the Loschmidt echo typically shows a quadratic decay for short times [253]. We conjecture that the dominant t^2-term

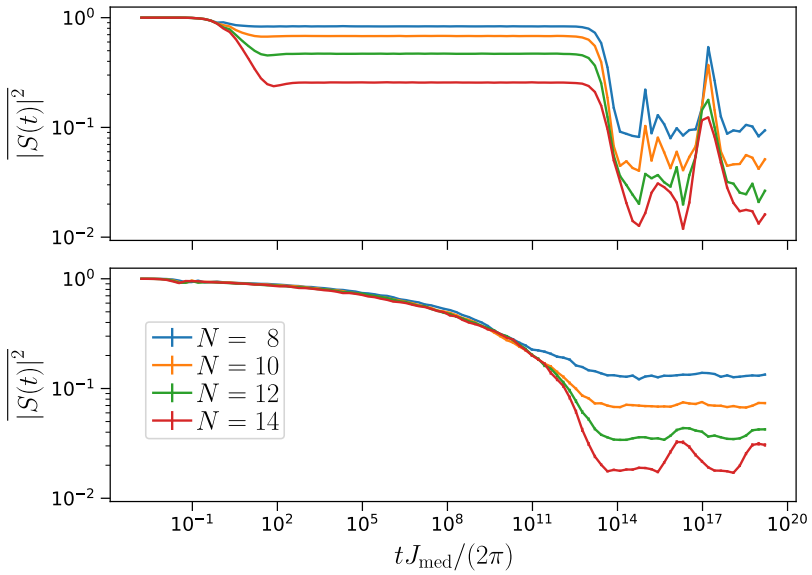

Figure 5.8: *Loschmidt echo in a thermalizing and in a localized regime.* The Loschmidt echo is shown as a function of evolution time for system sizes $N = 8, 10, 12, 14$ on a double-logarithmic scale. The upper panel corresponds to the thermalizing regime ($W = 0.03$), while the lower panel depicts the localized regime ($W = 2.0$). For $t > 1 \times 10^{14}$, the thermalizing case displays strong oscillations after reaching a plateau. We attribute this behavior to finite numerical precision. Because the calculation involves the time-evolution operator e^{-iHt}, numerical errors in the product $J_{\mathrm{med}}t$ on the order of 2π generate random phases, which then lead to large numerical deviations in the calculation of $S(t)$ and consequently $|S(t)|^2$.

vanishes in the ordered model ($W = 0$) due to our specific choice of V. A systematic analysis of this behavior is left for future work. For intermediate times, $tJ_{\mathrm{med}}/(2\pi) > 2$, the weakly disordered system exhibits an exponential relaxation, as shown in Appendix C. After a transient drop below the equilibrium value, the Loschmidt echo reaches a size-dependent plateau that remains stable over several decades in interaction cycles. This behavior indicates that the weakly disorder thermalizing regime shows the same dynamics as ETH thermal systems in the Loschmidt echo.

In contrast, the strongly disordered localized regime ($W = 2.0$) does not reach a plateau equilibrium before numerical errors become significant, and thus from our numerical analysis, the Loschmidt echo does not seem to equilibrate at all. In addition, over 11 different orders of magnitude, we observe no significant finite size effects, and the system dynamics seems to be independent of the system size. To

further investigate this unexpected behavior, we will separately analyze the early transient dynamics and the long-time behavior. For very early times $tJ_{\text{med}}/(2\pi) \ll 1$, we find a quadratic decrease of the Loschmidt echo

$$|S(t)|^2 \approx 1 - 340 \left(\frac{tJ_{\text{med}}}{2\pi}\right)^2 \tag{5.20}$$

in agreement with general expectations for a Loschmidt echo at short times [253]. A power law fit for early times is provided in Appendix C. For long times, unlike the behavior in the exponentially many-body localized regime discussed in Ref. [150], the Loschmidt echo does not decay according to a power law, which would manifest as a linear trend on a double logarithmic plot. Instead, the decay appears faster than exponential and is almost independent of system size N. This behavior is reminiscent of the disorder-averaged modulus of the Loschmidt echo $\overline{|S(t)|}$ for an exponentially localized model, which can be explained by dephasing of exponentially localized integrals of motion [150]. In this case, the modulus follows

$$\overline{|S(t)|} = \prod_{i=1}^{2} \frac{e^{-\frac{\mathrm{W}^2(t\sigma_i^2\langle c_i\rangle + 2\mathrm{W}(t\sigma_i^2\langle c_i\rangle))}{2\sigma_1^2}}}{\sqrt{1+\mathrm{W}(t\sigma_i^2\,\langle c_i\rangle)}}, \tag{5.21}$$

where W denotes the Lambert W function, and $\langle c_i\rangle$ and σ_i are related to the energy distribution of different LIOMs. We will test whether the averaged Loschmidt echo $\overline{|S(t)|^2}$ in the bond-disordered Hamiltonian of Eq. 5.13 follows this dependency. Additionally, we propose an alternative model for the decay of the Loschmidt echo: a stretched exponential function. This model, often used to describe relaxation dynamics in glassy systems, was also applied to magnetization relaxation in a power law interacting 3D Heisenberg spin system [155]. In detail, we will fit the data the stretched exponential function

$$|S(t)|^2 = Ae^{-(t/t_0)^\beta}, \tag{5.22}$$

where A is the amplitude of the function, t_0 describes the typical decay timescale, and β is the stretched exponent. For $\beta = 0$, an exponential decay is recovered, while for $\beta \to 0$, the decay becomes significantly slower than exponential. We analyze the long-time interval $5 \times 10^2 \leq tJ_{\text{med}}/(2\pi) \leq 1 \times 10^{10}$. The lower bound ensures that we are examining data far from any transient initial dynamics, while the upper bound is chosen to be at least one order of magnitude smaller than $tJ_{\text{med}}/(2\pi) \leq 1 \times 10^{11}$, where finite-size effects in the $N = 8$ data become visible. To further minimize these effects, we focus on fitting the dependence of the $N = 14$ data in this interval.

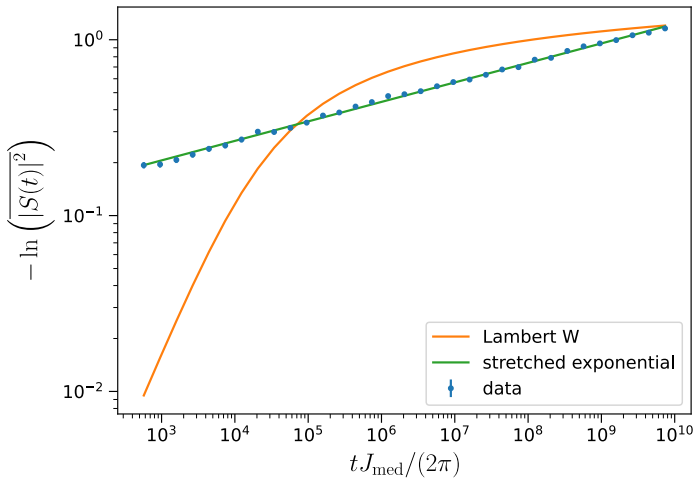

Figure 5.9: *Loschmidt echo as a function of evolution time.* The negative logarithm of the Loschmidt echo (blue dots) is shown as a function of evolution time in a double logarithmic graph. Error bars are calculated from the standard error of the mean of the disorder average. A stretched exponential function (green solid line), as well as the l-bit expectation value involving the Lambert W function (orange solid line) are fitted to the data using a least square fit method.

To reveal a possible stretched exponential behavior, we assume that the data follows a stretched exponential function with amplitude $A \approx 1$, consistent with $|S(t=0)|^2 = 1$. Taking the negative logarithm of both sides of Eq. 5.22 yields

$$-\ln\left(|S(t)|^2\right) = \underbrace{-\ln(A)}_{\approx 0} + \left(\frac{t}{t_0}\right)^{\beta} \sim t^{\beta}. \tag{5.23}$$

Hence, plotting $-\ln\left(|S(t)|^2\right)$ versus t on a double logarithmic plot will yield a straight line, where the slope corresponds to the stretched exponent β.

We present the Loschmidt echo data for $N = 14$ and $W = 2.0$ in a double-logarithmic plot in Fig. 5.9, where a linear behavior is observed, strongly suggesting a stretched exponential decay. A fit based on Lambert W functions according to Eq. 5.21 results in dynamics faster than a stretched exponential, and thus cannot accurately describe the observed data. In contrast, a stretched exponential fit yields the following parameters: $A = 1.05(2)$, $t_0 = 1.01(15) \times 10^9$, and $\beta = 0.100(3)$. This stretched exponential has a reduced $\chi^2 = 0.47 < 1$, thus indicating that the simulated Loschmidt echo data is well described by the fit.

In summary, the observed stretched exponential behavior represents a new scaling

regime that is incompatible with the Loschmidt echo decay observed in both thermalizing and exponentially many-body localized regimes, where the decay follows either exponential or power law forms. This discrepancy is consistent with the findings of Ref. [136], which also suggested that bond-disordered, power law interacting systems introduce a qualitatively new localization mechanism. For future studies, it would be intriguing to explore how the stretched exponent β depends on the strength of disorder and the power law exponent α, further establishing these systems as a distinct class of localization. In the following section, we aim to test whether such an anomalous behavior can also be found by analyzing out-of-time-order correlators (OTOCs).

5.2.3 Multiple Quantum Coherences

As discussed in Chap. 2, OTOCs provide a tool that is sensitive not only to thermalization dynamics but also to operator scrambling [137]. However, OTOCs are typically formulated in terms of local observables, which are not accessible in the experimental apparatus described in Appendix A. A notable exception, where global OTOCs are directly interpretable, is provided by multiple quantum coherence (MQC) protocols, as outlined in Chap. 2.

In this section, we study the time-dependent scaling of the fidelity OTOC $\mathcal{F}_\phi(t)$ and the magnetization OTOC $F_\phi(t)$ for the power law interacting Hamiltonian H_0 of Eq. 5.13. In detail, we will look at their MQC spectrum, characterized by the multiple quantum intensities I_m and the multiple quantum amplitudes A_m. We compare their time evolution in a thermalizing regime at weak disorder $W = 0.04$ and in a localized regime at strong disorder $W = 2.0$. Our aim is to identify qualitative differences in their scaling that reflect the respective localization properties.

Magnetization dynamics of a Heisenberg XXZ model

Before presenting the results for the OTOC and MQC protocols, we briefly justify the choice of the initial state used in both cases and outline the dynamical behavior that can be expected from this choice. As detailed in Chap. 2, the magnetization and fidelity MQCs provide information on the emergence of spin correlations and on coherences between product states in the z-basis with $\Delta M_z \neq 0$ during the evolution of an initial state $|\Psi\rangle$ under the Hamiltonian H_0. If we choose, as in the previous chapters, the fully polarized state in the x-direction $|\Psi_x\rangle$ as the initial state, the fidelity MQC attains its maximal values, since $|\Psi_x\rangle$ is an equal superposition of all product states in the z-basis. As a result, the MQC width is already maximal and cannot increase further. In contrast, if we select the fully polarized state in the z-direction $|\Psi_z\rangle$, then $|\Psi_z\rangle$ is an eigenstate of H_0, and no MQC dynamics is expected.

To generate nontrivial MQC dynamics, we rotate the coordinate system such that the x-axis maps onto the z-axis of H_0. In this rotated frame, $|\Psi_z\rangle$ is no longer an eigenstate of the Hamiltonian. As it is a product state in the z-basis, both the fidelity and magnetization MQCs initially exhibit vanishing width, as we will see later. This initial state thus allows to extract meaningful information on the dynamical properties of H_0.

In the following, we derive the form of H_0 in this rotated basis. As the coordinate system can be viewed by being rotated by $\pi/2$ around the y-axis, the Hamiltonian thus can be viewed as transformed by the rotation matrix

$$R = e^{-i\frac{\pi}{2}S_y} \tag{5.24}$$

As a consequence, we obtain for the rotated Hamiltonian

$$H' = RHR^\dagger = \sum_{i<j} J_{ij}\left(S_z^{(i)}S_z^{(j)} + S_y^{(i)}S_y^{(j)} + \Delta S_x^{(i)}S_x^{(j)}\right) \tag{5.25}$$

For the following simulations in this chapter, we will use this form of the Hamiltonian.

In order to further understand the dynamics on the z-magnetization that this Hamiltonian induces, we rewrite the S_x and S_y operators in terms of spherical basis ladder operators

$$S_\pm^{(i)} = S_x^{(i)} \pm iS_y^{(i)} \tag{5.26}$$

as defined in standard textbooks [258]. Rewriting the Hamiltonian in terms of these operators yields

$$\begin{aligned} H' &= \sum_{i<j} J_{ij}\left(S_z^{(i)}S_z^{(j)} + \frac{S_+^{(i)} - S_-^{(i)}}{2i}\frac{S_+^{(j)} - S_-^{(j)}}{2i} + \Delta\frac{S_+^{(i)} + S_-^{(i)}}{2}\frac{S_+^{(j)} + S_-^{(j)}}{2}\right) \\ &= \sum_{i<j} J_{ij}\left(S_z^{(i)}S_z^{(j)} + \frac{\Delta-1}{4}\left(S_+^{(i)}S_+^{(j)} + S_-^{(i)}S_-^{(j)}\right) + \frac{\Delta+1}{4}\left(S_+^{(i)}S_-^{(j)} + S_-^{(i)}S_+^{(j)}\right)\right) \\ &= H_{\mathrm{XXZ}} + \frac{\Delta-1}{2}H_{\mathrm{DQ}}, \end{aligned} \tag{5.27}$$

where we immediately identify a different XXZ Hamiltonian

$$H_{\mathrm{XXZ}} = \sum_{i<j}\frac{(\Delta+1)J_{ij}}{2}\left(\frac{1}{2}\left(S_+^{(i)}S_-^{(j)} + S_-^{(i)}S_+^{(j)}\right) + \frac{2}{\Delta+1}S_z^{(i)}S_z^{(j)}\right), \tag{5.28}$$

which couples only states with $\Delta M_z = 0$, and the double quantum Hamiltonian

$$H_{\mathrm{DQ}} = \sum_{i<j}\frac{J_{ij}}{2}\left(S_+^{(i)}S_+^{(j)} + S_-^{(i)}S_-^{(j)}\right), \tag{5.29}$$

which couples only states with $\Delta M_z = \pm 1$. Therefore, the MQC protocols yield non-zero amplitudes A_m or intensities I_m only for even m, as $|\Psi_z\rangle$ is a product state in z-basis, H_{XXZ} couples only states with the same total z-magnetization, and H_{DQ} couples only states where exactly two spins are flipped, thus preserving the parity of the number of flipped spins. Moreover, magnetization changes only when spin pairs flip simultaneously, consistent with the observation that magnetization relaxation for short time-scales in Heisenberg XXZ models can be effectively described by the dynamics of pairs of spins [42].

Density matrix OTOC

We begin by simulating the fidelity OTOC $\mathcal{F}_\phi(t)$ for H' in Eq. 5.25. As shown in Chap. 2, this quantity allows for a direct calculation of the quantum Fisher information of the magnetization. The quantum Fisher information of staggered magnetization has previously been used to probe localization in a power law interacting system [132], which motivates examining whether the fidelity OTOC can also serve as an indicator of localization behavior.

For the numerical implementation, we choose a system size of $N = 12$, which allows for a sufficient fast calculation of the required time evolution of the Hamiltonian. We take 2000 disorder realizations, where in each disorder realization, positions are drawn for disorders $W = 0.04$ and $W = 2.0$, corresponding to a thermalizing and a localized regime, respectively. From the positions, we calculate the corresponding couplings J_{ij} as discussed above. For each disorder realization, we evaluate

$$\mathcal{F}_\phi(t) = \left| \langle \Psi_z | e^{iH't} e^{-i\phi S_z} e^{-iH't} | \Psi_z \rangle \right|^2, \tag{5.30}$$

as a function of the rotation angle ϕ applied in the MQC protocol and the evolution time t. Like in our implementation of the Loschmidt echo, evolution times for a given W are specified in units of mean median interaction cycles, $tJ_{\mathrm{med}}/(2\pi)$. Here, the rescaled evolution times are logarithmically spaced between $1 \times 10^{-5}/(2\pi)$ and $1 \times 10^{5}/(2\pi)$. Using a logarithmic spacing of time over several orders of magnitude allows us to identify whether MQC-related quantities may exhibit a slow, logarithmic growth. The rotation angles are sampled uniformly over one period, $\phi_i = 0,\ 2\pi/40,\ 4\pi/40,\ \ldots,\ 2\pi \cdot 39/40$, which allows for an accurate discrete Fourier transformation.

In a system of N spins, at most N spins may flip, implying that the multiple quantum intensities I_m may occupy the full range $m \in [-N, N]$. Consequently, at least $2N + 1 = 25$ sampling angles are required to resolve the MQC spectrum.

Our choice of 40 angles satisfies this requirement and provides additional spectral resolution.

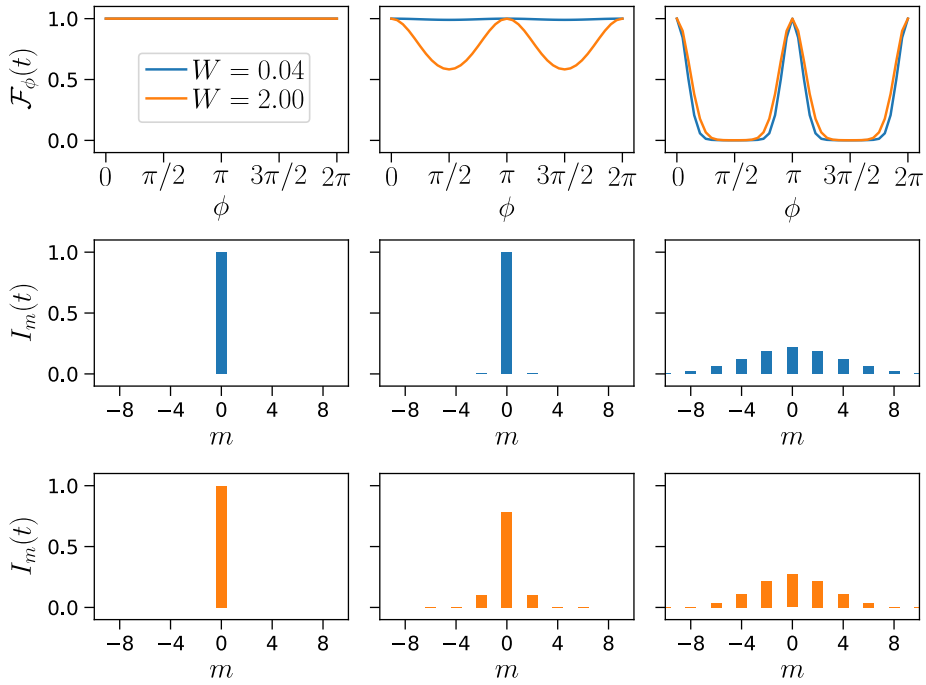

Figure 5.10: *Fidelity OTOC and multiple quantum intensitities.* The plot in each column represents data taken at time $tJ_{\text{med}}/(2\pi)$ equal to 1.59×10^{-6} (left), 1.59×10^{-3}(center) and 1.59×10^{4} (right). The top row presents the fidelity OTOC $\mathcal{F}_\phi(t)$ as a function of the angle ϕ for the thermalizing (blue, $W = 0.04$) and localized (orange, $W = 2$) regimes. The center and bottom row present the multiple quantum intensities for the thermalizing and localized regime, respectively.

The MQC spectrum is obtained by applying a fast Fourier transformation (FFT) to $\mathcal{F}_\phi(t)$ with respect to the rotation angle ϕ. The multiple quantum intensities are therefore given by

$$I_m(t) = \frac{1}{N_\phi} \sum_{\phi_i} \mathcal{F}_{\phi_i}(t) e^{-im\phi_i}, \tag{5.31}$$

where $N_\phi = 40$ denotes the number of different angles ϕ. Because uncertainty propagation through an FFT is nontrivial and remains an active research topic [259], we compute $I_m(t)$ for each disorder realization individually and perform the disorder averaging only afterwards. This procedure allows us to estimate the uncertainty of $I_m(t)$ via the standard error of the mean over all disorder realizations.

The simulation results are shown in Fig. 5.10. At times much shorter than tJ_{med}, $\mathcal{F}_\phi(t)$ remains essentially constant. Consequently, the MQC spectrum contains only a single nonzero multiple quantum intensity $I_{m=0}$, consistent with the expectations outlined above.

For short times, the thermalizing regime exhibits almost no visible dynamics, whereas the localized regime develops pair correlations rapidly. We attribute this behavior to the strong disorder strength in the localized regime: the largest couplings J_{ij} can exceed J_{med} by up to an order of magnitude, producing dynamics on time scales shorter than a median interaction cycle. Such strong couplings are absent in the thermalizing regime, where the positional disorder is weak and the couplings J_{ij} are approximately uniform for equal distances $|i-j|$.

At long times, the situation reverses. The thermalizing regime evolves more rapidly, which is reflected in the broader distribution of I_m at the latest simulated time. In order to further quantify the width of the I_m as a function of the evolution time, we compute the quantum Fisher information of the magnetization operator following [149], which reads

$$F_Q(\rho(t), S_z) = 2\sum_m I_m(t) m^2. \tag{5.32}$$

Figure 5.11 shows the quantum Fisher information F_Q. In the thermalizing regime, F_Q increases slowly at short times and then rapidly reaches an equilibrium plateau around $tJ_{\mathrm{med}}/(2\pi) \approx 0.1$. Since F_Q also serves as an entanglement witness for k-partite entanglement [260–262], the minimal k-partite entanglement can be inferred from its equilibrium value. Here, $F_Q^{\mathrm{eq}} \approx 27.4 > 24$, indicating that the thermalizing system exhibits at least two-body entanglement.

In the localized regime, the quantum Fisher information initially grows logarithmically for times $1 \times 10^{-3} \leq tJ_{\mathrm{med}}/(2\pi) \leq 5 \times 10^2$, appearing as a straight line when plotted against a logarithmic time axis. A least-squares fit within this interval yields

$$F_Q(t) = A \ln\left(\frac{tJ_{\mathrm{med}}}{2\pi b}\right), \tag{5.33}$$

with $A = 1.107(10)$, $b = (2.82 \pm 0.22) \times 10^{-4}$, and a reduced $\chi^2 = 1 \times 10^{-2} \ll 1$, indicating that the data is well captured by a logarithmic growth.

For longer times, $tJ_{\mathrm{med}}/(2\pi) \gtrsim 1 \times 10^3$, the growth slows below logarithmic. Fitting the last four data points with a double-logarithmic function

$$F_Q(t) = f_0 + A \ln\ln\left(\frac{tJ_{\mathrm{med}}}{2\pi b}\right) \tag{5.34}$$

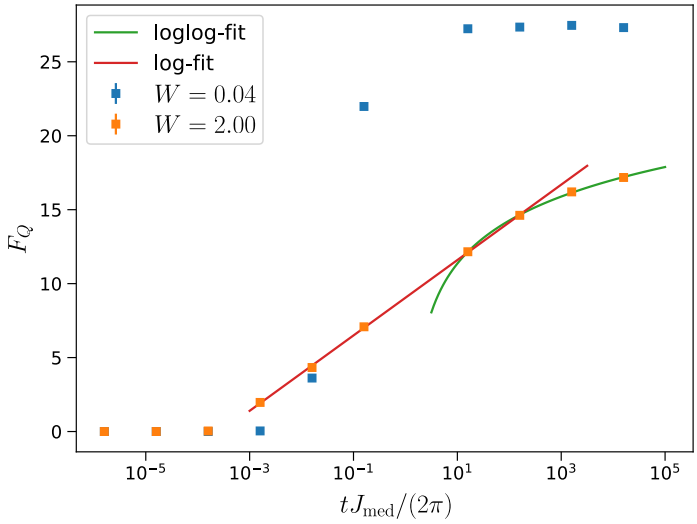

Figure 5.11: *Quantum Fisher information of the magnetization.* The quantum Fisher information of the time-evolved density matrix of the fully polarized state is shown as a function of evolution time. The scale of the abscissa axis is logarithmic, such that a logarithmic growth will be visible as a straight line. Data is shown both in a thermalizing (blue) and a localized (orange) regime. In the localized regimes, the times $1e-3 \leq tJ_{\mathrm{med}}/(2\pi) \leq 5e2$ are fitted a logarithmic behavior (red line). The last four data points are fitted a loglog growth behavior (green line). Error bars, which are smaller than the marker size, are calculated as the standard deviation from the mean over 2000 disorder samples.

using least-squares regression gives $A = 3.7 \pm 0.4$, $b = 1.4 \pm 0.7$, and $f_0 = 8.8 \pm 1.1$, with a reduced $\chi^2 = 5 \times 10^{-3} \ll 1$, showing that the double-logarithmic function provides a good description of the late time behavior.

This behavior is striking compared to that reported in Ref. [132]. In that work, a bond-disordered XY model was shown to exhibit algebraically localized single-particle wavefunctions [134], and it is generally expected that power law interacting models displaying localization cannot support exponentially localized single-particle states, but instead feature algebraically localized wavefunctions [132]. The same reasoning would apply to the XXZ model of Eq. 5.25. In Ref. [132], the quantum Fisher information of the staggered magnetization grows logarithmically for algebraically localized systems, in contrast to double-logarithmic growth for exponentially localized ones.

In the bond-disordered XXZ model studied here, F_Q shows logarithmic growth

at intermediate times, consistent with algebraic localization, but crosses over to double-logarithmic growth at long times, suggesting a tendency toward exponential localization. This behavior reinforces the conclusions drawn from the Loschmidt echo, indicating that bond-disordered, power law interacting systems may exhibit a qualitatively distinct form of localization.

However, this interpretation should be considered with caution. First, the slow double-logarithmic growth may be a finite-size effect that reflects an eventual saturation of F_Q. Examining F_Q for different system sizes, such as $N = 10$ and $N = 14$, and extending the simulations to $tJ_{\text{med}}/(2\pi) = 1 \times 10^{12}$, as in Ref. [132], would help to clarify the nature of this apparent double-logarithmic behavior. Furthermore, since the multiple quantum intensities provide access only to the quantum Fisher information of the magnetization, it would be valuable to compare the quantum Fisher information of the staggered magnetization directly with the scaling behaviors reported in Ref. [132].

Magnetization OTOC

Both the Loschmidt echo and the fidelity OTOC rely on measuring a many-body wavefunction fidelity, which remains experimentally challenging on current quantum simulation platforms for system sizes exceeding roughly ten particles, as full state tomography scales exponentially with system size [148]. For this reason, we focus here on the scaling of a magnetization OTOC and the corresponding MQC protocol in the disorder regimes discussed above. These quantities can be easily accessed experimentally, both on trapped-ion platforms [148] and, using the time-reversal protocol of Ref. [48] discussed in Sec. 5.1, on our Rydberg platform described in Appendix A.

To numerically simulate the magnetization OTOC, we evaluate

$$F_\phi(t) = \frac{4}{N^2} \langle \Psi_z | e^{iH't} e^{i\phi S_z} e^{-iH't} S_z e^{iH't} e^{-i\phi S_z} e^{-iH't} S_z | \Psi_z \rangle \tag{5.35}$$

using the same system size $N = 12$, discrete time steps t, rotation angles ϕ_i, and disorder strengths $W = 0.04$ and $W = 2.0$ as in the fidelity OTOC simulations. Again, the two disorder strengths correspond to a thermalizing and a localized regime, respectively. We sample 2000 disorder realizations of H' and compute the disorder-averaged $F_\phi(t)$, with the standard error of the mean across realizations used as an estimate of the uncertainty.

In addition, for each disorder realization of H', we compute the multiple quantum

amplitudes applying a fast Fourier transform algorithm

$$A_m = \frac{1}{N_\phi} \sum_{\phi_i} F_{\phi_i}(t) e^{-im\phi_i}, \tag{5.36}$$

in analogy to the calculation of the I_m. Again, we first perform the Fourier transform for every disorder realization, and take the disorder average in a second step to omit error propagation through a Fourier transform.

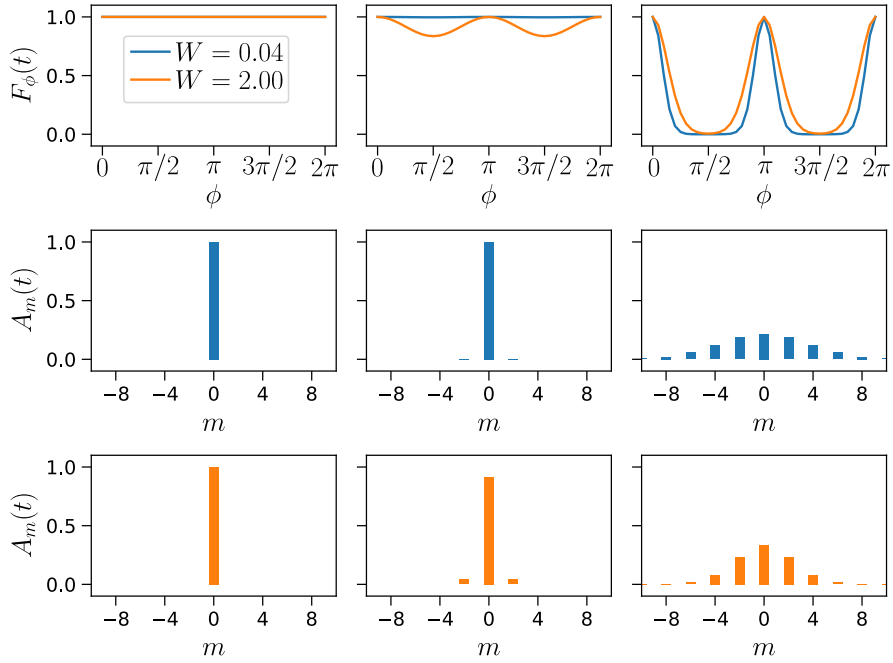

Figure 5.12: *Magnetization OTOC and multiple quantum amplitudes.* The plot in each column represents data taken at time $tJ_{\text{med}}/(2\pi)$ equal to 1.59×10^{-6} (left), 1.59×10^{-3}(center) and 1.59×10^{4} (right). The top row presents the magnetization OTOC $F_\phi(t)$ as a function of the angle ϕ for the thermalizing (blue, $W = 0.04$) and localized (orange, $W = 2$) regimes. The center and bottom row present the multiple quantum amplitudes for the thermalizing and localized regime, respectively.

We present the results of this simulation in Fig. 5.12. By definition, the I_m correspond to the sum of the squared moduli of all matrix elements of $\rho(t)$ connecting z-basis states that differ in z-magnetization by $\Delta M_z = m/2$ [148], and are therefore always real and non-negative. In contrast, the A_m are not necessarily real or positive.

Following Ref. [148], we plot $|A_m|$ to represent the MQC spectrum. We observe qualitatively the same dynamics as in the fidelity OTOC depicted in Fig. 5.10. At times much shorter than tJ_{med}, $F_\phi(t)$ remains essentially constant. Consequently, the MQC spectrum contains only a single nonzero multiple quantum amplitude $A_{m=0}$, consistent with the expectations outlined above.

For short times, the thermalizing regime exhibits almost no visible dynamics, whereas the localized regime develops spin-spin magnetization correlations rapidly. Again, we attribute this behavior to the strong disorder strength in the localized regime. At long times, the situation reverses. The thermalizing regime evolves more rapidly, which is reflected in the broader distribution of A_m at the latest simulated time. To compare with the quantum Fisher information, we aim to further quantify the width of the A_m. However, the A_m lack a second property that is guaranteed for the I_m. For a given density matrix $\rho(t)$, summing over all I_m is equivalent to summing over all entries of $\rho(t)$, yielding

$$\sum_m I_m(t) = \sum_{i,j} |\rho_{ij}|^2 = \mathrm{Tr}\Big\{\rho(t)^\dagger \rho(t)\Big\} \overset{\rho(t)\,\text{pure}}{=} 1, \tag{5.37}$$

so that the quantum Fisher information corresponds to the doubled width of a normalized distribution I_m. This normalization does not necessarily hold for the A_m.

For the A_m, we can define the doubled variance in analogy to Eq. 5.32 as

$$2\mathrm{Var}(A_m) = 2\frac{\sum_m g(A_m) m^2}{\sum_m g(A_m)}, \tag{5.38}$$

where g denotes either the modulus or the real part of A_m. The imaginary part cannot be used, since A_m is the Fourier transform of a real-valued function and thus satisfies $\mathrm{Im}(A_m) = -\mathrm{Im}(A_{-m})$. Using the imaginary part would make Eq. 5.38 ill-defined, as both the numerator and denominator on the left side would vanish.

We present the doubled variance of both the real part and the modulus of the A_m, in Fig. 5.13. Qualitatively, the doubled variance is largely insensitive to this choice. In the thermalizing regime, the doubled variance shows a rapid increase at $tJ_{\text{med}}/(2\pi) \approx 0.1$, saturating at 27.7 when g is taken as the modulus and 27.3 when g is taken as the real part, in close agreement with the equilibrium value of the quantum Fisher information. This indicates that, in the thermalizing regime, the late-time doubled variance of A_m provides a reliable estimate of the equilibrium F_Q.

In the localized regime, we observe that the doubled variance of the A_m increases more slowly than F_Q. In addition, we do not find a logarithmic or a double-logarithmic growth, but instead, at late times we find the data is well described by a power law model

$$2\mathrm{Var}(A_m) = At^\gamma, \tag{5.39}$$

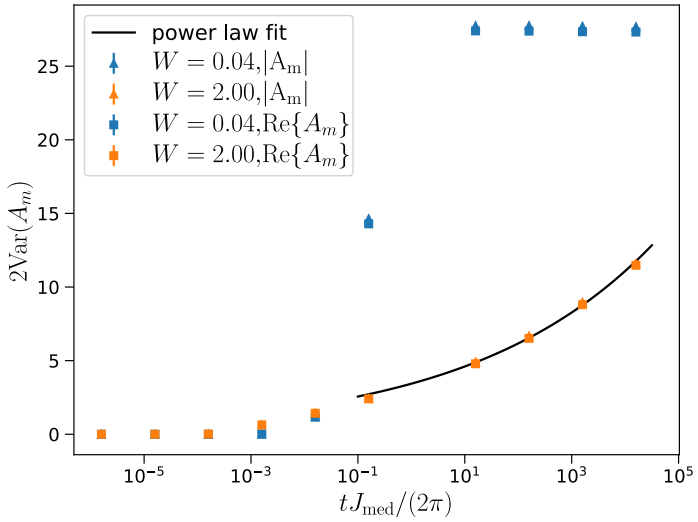

Figure 5.13: *Doubled variance of the multiple quantum amplitudes.* Doubled variance of the multiple quantum amplitudes is presented as a function of evolution time. The scale of the abscissa axis is logarithmic, such that a logarithmic growth will be visible as a straight line. The doubled variance is calculated both for the modulus (triangles) as well as for the real part (squares) of the multiple quantum amplitudes. Data is shown both in a thermalizing (blue) and a localized (orange) regime. For the last 5 data points in the localized regime, a power law model (black line) is fitted to the values obtained from the amplitude.

for which a least-squares fit yields $A = 3.50(14)$ and $\gamma = 0.128(5)$. The reduced $\chi^2 = 0.05 \ll 1$ indicates that this model provides an accurate description of the data in this regime.

This power law behavior differs qualitatively from the dynamics of F_Q. Nonetheless, the evolution is substantially slower than in the thermalizing regime, suggesting the presence of two distinct dynamical regimes. For future work, it would be instructive to compute the doubled variance of the A_m also for exponentially localized models to determine whether they exhibit similar or qualitatively different behavior. We further note that the observed power law scaling may represent a slow, transient regime that eventually crosses over to logarithmic or double-logarithmic growth. Again, examining the doubled variance of the A_m for different system sizes, such as $N = 10$ and $N = 14$, and extending the simulations to $tJ_{\mathrm{med}}/(2\pi) = 1 \times 10^{12}$ would help to clarify the nature of this apparent power law behavior.

5.3 Conclusion

In this chapter, we started by asking whether localization properties could appear in an isolated three-dimensional dipolar-interacting Heisenberg XY model, and whether such behavior could, in principle, be observed with the experimental platform described in Appendix A. To address this question, we proposed using Loschmidt echo and multiple quantum coherence (MQC) protocols, which only require global access to the system. A key challenge, however, is that these protocols rely on the ability to effectively reverse the system's time evolution.

To implement a time-reversal protocol on the Rydberg simulation platform, we explored how coherent transfer pulses between different spin-encoding Rydberg states can be used to effectively reverse dipole–dipole interactions between atoms. Two candidate encodings were considered, both robust against unwanted population of non-targeted Rydberg states during the transfer. The experimentally chosen encoding further minimizes errors from van-der-Waals interactions in the time-reversed Hamiltonian. Increasing the magnetic field strength enables faster spin-state transfer, reducing the dominant errors caused by Rydberg interactions during the pulses. Overall, this provides a practical route to improve the efficiency of the protocol. Additionally, our analysis emphasized that flipping the parity of the spin-encoding states is crucial to suppress effective local magnetic fields in the realized spin Hamiltonian.

This protocol enables the implementation of time reversal in an isolated dipolar spin system, while allowing the imperfections of the reversal to be quantified. It therefore provides a framework for exploring localization effects in such systems. To build intuition for how localization might manifest in time-reversal based protocols in a disordered model with power law interactions, we first analyze representative time-reversal based protocols in a simplified toy model. This model has previously been shown to host both thermalizing and localized regimes [136, 186].

In this toy model, we analyzed the time evolution of the Loschmidt echo. As expected, in the thermalizing regime it relaxes rapidly and exponentially toward equilibrium. In contrast, in the strongly disordered regime we identify a novel behavior: the Loschmidt echo decays as a stretched exponential with a small exponent, $\beta \approx 1/10$. This behavior is distinct from the exponential relaxation typical of thermal systems and the power law decay characteristic of conventional many-body localized systems. The observation of stretched exponential decay reveals a distinctive dynamical feature of strongly bond-disordered, power law interacting systems, consistent with Ref. [136], where such systems were also shown to exhibit behavior different from conventional many-body localized systems. For an experimental implementation, it would be valuable to test whether the Loschmidt echo scales also as a stretched exponential if

instead of a fidelity, a global magnetization is measured.

In addition, we numerically investigated two different MQC protocols. First, we analyzed the time-dependent behavior of the fidelity MQC, which provides a direct measure of the quantum Fisher information of the magnetization. We find that the observed dynamics are incompatible with thermalizing, exponential, or algebraically localized behavior. Specifically, at short times, the quantum Fisher information grows logarithmically, consistent with algebraically localized systems, whereas at late times, it exhibits double-logarithmic growth, as expected for exponentially localized systems. This crossover behavior further supports the finding in Ref. [136] that bond-disordered localized systems display dynamics distinct from both conventional algebraic and exponential localization. It should be noted, however, that these simulations were performed for a single system size and for timescales up to approximately 1×10^5 interaction cycles; future studies should extend these analyses to larger systems and longer times to fully characterize the observed behavior.

Since measuring the fidelity required for the fidelity MQC is experimentally challenging in large many-body systems, we also investigated the time dependence of the magnetization MQC and the variance of the multiple quantum amplitudes, as magnetization measurements are experimentally more accessible. In the thermalizing regime, this variance rapidly reaches an equilibrium value that closely approximates the equilibrium quantum Fisher information. In contrast, in the localized regime, the variance grows significantly more slowly, following a power law with an exponent $\gamma \approx 0.12$. This suggests that the main distinction between thermalizing and localized dynamics lies in the timescale required to reach equilibrium. These findings raise intriguing questions for future studies, including how the exponent γ depends on the disorder strength W or the system size, and whether it exhibits universal behavior. Moreover, it would be valuable to compare these results to exponentially many-body localized systems, as the variance of multiple quantum amplitudes could potentially be measured in both trapped ion experiments [148] and in our Rydberg atom quantum simulator. However, just like the fidelity OTOC, the simulations were performed for a single system size and for timescales up to approximately 1×10^5 interaction cycles; future studies should extend these analyses to larger systems and longer times to fully characterize the observed behavior.

To summarize, the results of this chapter demonstrate that bond-disordered, power law interacting systems exhibit an unconventional dynamical behavior under time-reversal based protocols, which is distinct from both thermalizing and conventional exponentially many-body localized systems. The observation of stretched exponential decay in the Loschmidt echo, alongside the nontrivial time dependence of the fidelity and magnetization MQCs, points to new forms of localization dynamics that merit

further investigation. Future studies exploring different system sizes, longer timescales, and different disorder strengths will be essential to fully characterize the emergent dynamics and to determine whether universal features govern these bond-disordered localized phases. In addition, we have shown that a magnetization OTOC, which is experimentally implementable in current quantum simulation platforms, can at least quantitatively distinguish a localized from a thermal regime. This study thus opens new avenues for identifying localized regimes in finite-size systems.

CHAPTER 6

Perspectives in Disordered Dipolar Quantum Simulators

In the preceding chapters, we investigated spin glass and localization phenomena in a three-dimensional dipolar XY model. In Chap. 3, we studied energetic-magnetic hysteresis, characterized via protocol-dependent steady-state DC magnetization measurements. In Chap. 4, we developed and implemented a protocol to determine putative critical exponents. In both cases, we analyzed equilibrium properties, including linear response from metastable quasi-equilibrium states and the measurement of a combination of equilibrium critical exponents.

However, the spin glass phase is typically out-of-equilibrium and exhibits rich dynamical behavior. Therefore, in Sec. 6.1, we propose methods to characterize dynamical effects typical of spin glasses using the experimental platform described above. We also outline approaches to measure AC susceptibilities, which typically exhibit faster dynamics [12].

As noted, all previous experiments were conducted in a three-dimensional XY spin model, for which no complete theoretical description currently exists. In Sec. 6.2, we demonstrate how the experimental platform can be used to study three-dimensional dipolar Ising models, enabling direct comparison with state-of-the-art theoretical predictions [105].

6.1 Aging, rejuvenation, and memory

Spin glasses are generally considered to remain out-of-equilibrium, which gives rise to rich non-equilibrium dynamics. This section briefly reviews the main out-of-equilibrium phenomena observed in spin glasses and discusses how these may be

probed using the previously discussed Rydberg platform.

Due to their intrinsically slow dynamics, spin glasses provide a convenient setting for studying non-equilibrium processes in the time domain. Since formulating universal predictions for non-equilibrium systems is challenging, it is often instructive to examine situations close to equilibrium. In equilibrium, fluctuations can be related to the dissipation resulting from small perturbations. This relationship is formalized by the fluctuation–dissipation theorem (FDT), which has also been examined in the context of a characteristic non-equilibrium phenomenon in spin glasses, namely aging [263].

The fluctuation-dissipation theorem is typically studied in terms of the two-time autocorrelator $C(t_w, t)$ and the two-time linear response function $R(t_w, t)$, which are for arbitrary spin models given as

$$C(t_w + t, t_w) = \langle M(t_w + t)M(t)\rangle \tag{6.1}$$

$$R(t_w + t, t_w) = \frac{dM(t_w + t)}{dH(t_w)} \tag{6.2}$$

where the two-time autocorrelator $C(t_w, t)$ studies the correlation of the global magnetization M of a system after an observation time t after the waiting time t_w, while the linear response function $R(t_w, t)$ studies how the system's magnetization M responds to a field H applied at an observation time t after it has been prepared in equilibrium for a waiting time t_w. $C(t, t_w)$ is typically hard to measure, as very sensitive noise measurements are required in spin glasses to determine this value [79]. The linear response function, on the other hand, is straight forward to measure by the so-called thermoremanent magnetization, which was initially determined in spin glasses in Ref. [189]. To that end, the system is cooled down in the already introduced field-cooled protocol, sketched in Fig. 2.5(a). After the cooling is finished, the system is left for a waiting time t_w in the field cooled state. After t_w, the magnetization is quenched to zero, and the magnetization is observed as a function of the observation time t. If the system were in equilibrium in the FC state, the magnetization and thus the susceptibility should only depend on the time difference $t + t_w - t_w = t$, i.e.

$$R(t_w + t, t_w) = R(t) \tag{6.3}$$

as the thermal equilibrium state is defined by being time-translation invariant, i.e. it has no time-dependence. If this time-translation symmetry is fulfilled, the FDT holds:

$$R(t) = \frac{1}{T}\frac{\partial C(t)}{\partial t} \tag{6.4}$$

i.e. the linear response is proportional to the change of the fluctuations in a system with time. The higher the temperature, the smaller the response.

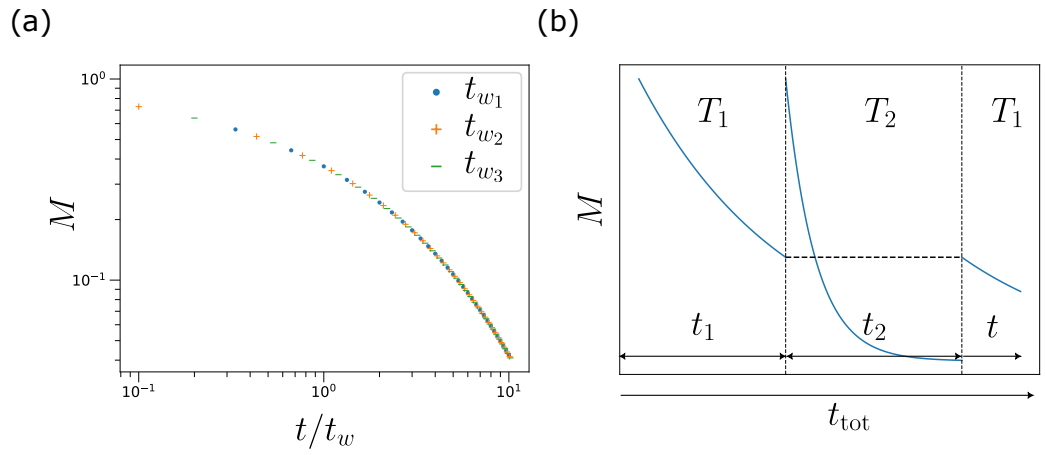

Figure 6.1: *Aging, rejuvenation and memory effects in spin glasses.* (a) Sketch of full aging. The magnetization M is plotted as a function of the ratio t/t_w for different waiting times t_w. By plotting M as a function of the ratio, all curves collapse onto a single curve. (b) Rejuvenation and memory effects. The magnetization M (blue solid line) is plotted as a function of time. The system is first aged at temperature T_1 for time t_1, during which M slowly decays. The temperature is then lowered to $T_2 < T_1$, and a renewed decay of M is observed, indicating rejuvenation. The system appears to "reset" and starts aging as if it was quenched to T_2 from the high temperature paramagnetic phase. After time t_2, the temperature is returned to T_1, and the system resumes its previous aging trajectory, demonstrating memory. It recalls its prior state at T_1 as though there was no time evolution in the temperature bath at T_2 (black dashed line).

In spin glasses, however, below the glass transition temperature, it is believed that the equilibrium is never reached on experimentally accessible timescales. As a consequence, a more generalized FDT is introduced

$$R(t, t_w) = \frac{X(t, t_w)}{T} \frac{\partial C(t, t_w)}{\partial t_w} \tag{6.5}$$

where $X(t, t_w)$ is the fluctuation-dissipation ratio (FDR)[264, 265], which defines an effective temperature $T_{\text{eff}} = T/X(t, t_w)$. Spin glasses are of special interest, as from a mean-field prediction, it is expected that the FDR is only a function of the two-time correlator $X(t, t_w) = f(C(t, t_w))$ and has no other explicit time-dependence on t or t_w, which is a consequence of the famous Cugliandolo-Kurchan equations[264, 266].

In addition, in spin glasses, but also in other systems featuring a continuous phase transition, already the response function or the correlation function alone show an

unexpected behavior: They do not scale with the time difference, but rather with the ratio of the observation and waiting times

$$C(t, t_w) \sim f\left(\frac{t}{t_w}\right) \tag{6.6}$$

$$R(t, t_w) \sim g\left(\frac{t}{t_w}\right) \tag{6.7}$$

where f and g are scaling functions, which is called full aging. For continuous phase transitions, aging is expected when a system is quenched across its critical point. Below the critical temperature, domains form whose typical size depends on the waiting time t_w through the critical exponents ν and z we introduced in Chap. 2. Energy barriers arise between these domains, with heights determined by the domain sizes. Aging is therefore governed by thermal activation of these barriers.

As a result, such systems exhibit full aging, characterized by scale invariance and the absence of an intrinsic time scale [267–271]. In the two-time functions, this manifests as dependence only on the ratio t/t_w, rather than on absolute times such as t, $t + t_w$, or t_w.

However, most spin glasses show subaging, which was initially proposed in studies on amorphous polymers [272]. In subaging, the two-time functions introduced above scale as

$$C(t, t_w) \sim f\left(\frac{t}{t_w^{\mu}}\right) \tag{6.8}$$

$$R(t, t_w) \sim g\left(\frac{t}{t_w^{\mu}}\right) \tag{6.9}$$

where $\mu < 1$, and typical values are $\mu \approx 0.97$[13, 79]. Even though multiple explanations have been considered, so far the mechanism leading to subaging in spin glasses is still an unresolved problem [273, 274].

Two important observations were made in spin glasses which are, unlike the ZFC/FC bifurcation and aging, absent in ordered systems. These effects are rejuvenation and memory[10, 79, 80], which are sketched in Fig. 6.1(b). We will briefly review them, following mainly [12].

The system is first quenched from a temperature well above the glass transition T_g to $T_1 < T_g$ and allowed to age for a time t_1. It is then quenched to a second temperature $T_2 < T_g$, which can be either significantly higher or lower than T_1. The magnetic response is measured after a time t_2. If T_2 differs substantially from T_1, the response after t_2 resembles that of a system quenched directly from the initial

high temperature to T_2, appearing as an additional rise in magnetization. This is the rejuvenation effect. If T_1 and T_2 are close together, the aging process continues without interruption, a behavior called cumulative aging [275, 276].

Alternatively, after aging at T_2 for a time t_2, the system can be quenched back to T_1. In this case, the magnetic response at T_1, measured at a time t after the last quench, appears as if no dynamics occurred at T_2. Specifically, it matches the magnetization observed in a reference measurement where the system is quenched directly from above T_g to T_1 and allowed to age for a time $t_1 + t$. The system thus retains the memory of its prior aging at T_1, a phenomenon referred to as the memory effect.

So far, we described protocols for measuring rejuvenation and memory using DC magnetization. However, aging is typically slow in DC measurements. To accelerate experiments, especially for aging and rejuvenation studies, the out-of-phase component χ'' of the AC susceptibility is measured. This quantity exhibits the fastest time-dependent decay, allowing for shorter experimental durations. Consequently, rejuvenation and memory effects are typically probed using AC susceptibility protocols [12].

The mechanisms underlying rejuvenation and memory effects remain unresolved. Interestingly, such effects can also emerge, depending on the experimental protocol, in superparamagnetic systems of noninteracting nanoparticles with a broad distribution of activation energies [277]. In contrast, memory effects in zero-field-cooled magnetization appear only in interacting nanoparticle assemblies, referred to as superspin glasses [277, 278]. Their behavior aligns well with the droplet model of spin glasses, where each nanoparticle acts as a droplet of characteristic size, and larger droplets require higher thermal activation energies. In conventional spin glasses, however, both memory and rejuvenation phenomena can also be described by a hierarchy of energy scales rather than by droplet or cluster formation alone [12]. This raises an open question about the interplay between droplet or cluster dynamics and hierarchical energy landscapes. Numerical simulations further suggest that temperature chaos [14] and multiscale dynamical processes play a central role in the emergence of memory and aging effects [15, 279].

We now briefly discuss how these protocols can be implemented in our quantum simulation platform. Similar to the ZFC and FC protocols described in Chap. 3, direct temperature control in an isolated quantum system following unitary dynamics is not feasible. Instead, an annealing scheme is employed to tune the system's energy, allowing the investigation of rejuvenation and memory effects as a function of energy. Consequently, these protocols may probe energy-dependent dynamics possibly acting across different length scales.

As outlined in Chap. 3, the system is initially prepared in the fully polarized z-state. A Rabi $\pi/2$-pulse then rotates the state into full polarization along x. An annealing ramp $\Omega_x(t)$ is subsequently applied to reach a low-energy state. For aging studies, it is advantageous to ramp the annealing down to zero field, while the ramp velocity controls the final energy. This also eliminates any remanent x-field, allowing the Heisenberg spin model to be probed without external magnetic fields.

Once the final field is reached, two protocols are considered:

Aging Protocols

1. **FA magnetization protocol**: A small probe field Ω_y is applied throughout the annealing ramp. After reaching the final field, the system ages for a waiting time t_1 in the presence of Ω_y. The probe field is then turned off, and the resulting magnetization M_y is measured after an additional time t.

2. **ZFA magnetization protocol**: After the annealing ramp reaches the final field, the system ages for a waiting time t_1 without a probe field. The small probe field Ω_y is applied afterward, and M_y is measured after a time t. This protocol was studied in [180], however on experimental timescales, no significant aging effect was found.

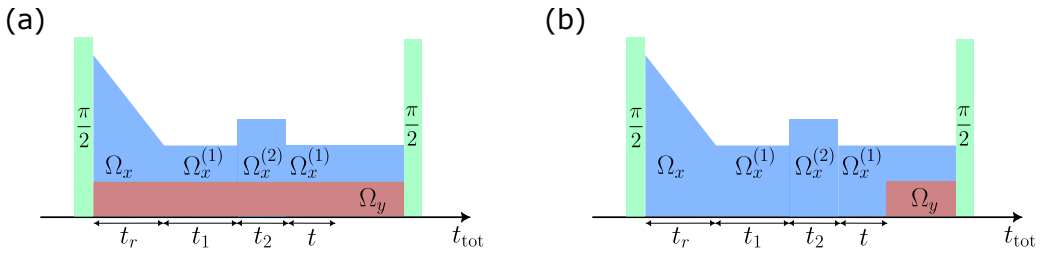

Figure 6.2: *Sketch of the protocol for probing memory effects.* Initialization and detection pulses (green), the annealing field (blue), and the probe field (brown) are shown against time. Field amplitudes are represented by height (not to scale). Time intervals are indicated by black arrows. The protocols are sketched both for the measurement of an FA magnetization (a) and a ZFA magnetization (b). See main text for details.

Although this protocol allows the study of aging, a challenge arises: the energy of the system must be tuned for the second time in a controlled manner to investigate rejuvenation and memory effects. To address this, we propose ending the annealing ramp at a finite field $\Omega_x^{(1)} \neq 0$, as sketched in Fig. 6.2. Although this introduces a

finite x-field during application of the probe field, it ensures that the system always exhibits a nonzero x-magnetization $M_x^{(1)}$. When $\Omega_x^{(1)}$ is subsequently changed to a new value $\Omega_x^{(2)}$, the system is subject to an energy change

$$\Delta E_1 = M_x^{(1)} \left(\Omega_x^{(1)} - \Omega_x^{(2)} \right), \tag{6.10}$$

providing controlled tunability of the energy. This tunability of the energy thus enables us to devise the following protocols to study rejuvenation, based on either ZFA or FA magnetization measurements:

Rejuvenation Protocols

1. **FA magnetization protocol**: A small probe field Ω_y is applied during the entire annealing ramp and maintained afterward. Once the finite field $\Omega_x^{(1)}$ is reached, the system ages for a time t_1. The annealing field is then changed to a new value $\Omega_x^{(2)}$. If $\Omega_x^{(2)} > \Omega_x^{(1)}$, the system's energy decreases; otherwise, it increases. The system then ages for a time t_2, after which the resulting magnetization is measured.

2. **ZFA magnetization protocol**: The system is first annealed down to a finite field $\Omega_x^{(1)}$ and ages there for a time t_1. The annealing field is then changed to $\Omega_x^{(2)}$, where the system ages for a time t_2. Finally, the probe field Ω_y is applied, and the resulting y-magnetization is measured.

These protocols exhibit a limitation compared to studies on magnetic alloys, superparamagnetic nanoparticles, and superspin glasses: the magnetic field and the system's energy are intrinsically coupled. For a meaningful comparison between the described rejuvenation protocol, and an aging protocol where the annealing ramp ends immediately at $\Omega_x^{(2)}$, the system energies at the end of protocols must be similar. Consequently, $\Omega_x^{(1)}$ and $\Omega_x^{(2)}$ should not differ substantially. At the same time, they must be significantly distinct to prevent cumulative aging. Whether these analogies from canonical spin glasses remain valid in an isolated system where the energy can be directly tuned is an open question.

We now focus on the study of memory effects by extending the rejuvenation protocol introduced above. A discussed above, after an initial aging period of duration t_1 under an annealing field $\Omega_x^{(1)}$, the field is quenched to a new value $\Omega_x^{(2)}$. This quench changes the system's energy by $\Delta E_1 = M_x^{(1)}(\Omega_x^{(1)} - \Omega_x^{(2)})$. The system then continues aging under $\Omega_x^{(2)}$ for a time t_2. To probe memory, the energy must subsequently be restored to its value corresponding to the field $\Omega_x^{(1)}$ after t_1. For nearly identical fields, $\Omega_x^{(1)} \approx \Omega_x^{(2)}$, the steady-state magnetizations $M_x^{(1)}$ and $M_x^{(2)}$ are

expected to be comparable. Previous work on the disordered dipolar Heisenberg spin model [43] showed that, for small external fields Ω_x, the steady-state magnetization scales linearly with the field, $M_x \propto \Omega_x$. Consequently, a small variation in Ω_x induces a proportional change in M_x.

Under this assumption, the corresponding energy variation after the second quench is

$$\Delta E_2 = M_x^{(2)} \left(\Omega_x^{(2)} - \Omega_x^{(1)}\right) \overset{M_x \propto \Omega_x}{=} \frac{\Omega_x^{(2)}}{\Omega_x^{(1)}} M_x^{(1)} \left(\Omega_x^{(2)} - \Omega_x^{(1)}\right) = -\frac{\Omega_x^{(2)}}{\Omega_x^{(1)}} \Delta E_1. \tag{6.11}$$

Restoring the annealing field to its initial value $\Omega_x^{(1)}$ after t_2 prepares the system in a state subjected to the same field and nearly the same energy as after t_1, immediately before the quench to $\Omega_x^{(2)}$.

Alternatively, after t_2, the field can be quenched to

$$\Omega_x^{(3)} = \Omega_x^{(2)} - \Omega_x^{(1)} + \frac{{\Omega_x^{(1)}}^2}{\Omega_x^{(2)}}, \tag{6.12}$$

which guarantees that the system's energies at $\Omega_x^{(1)}$ (after t_1) and at $\Omega_x^{(3)}$ (after t_2) are identical, although the corresponding external fields differ. For experimental simplicity, and under the assumption $\Omega_x^{(3)} \sim \Omega_x^{(1)}$, the following protocols to study memory effects, sketched in Fig. 6.2, consider quenches where the magnetic field is returned to its initial value $\Omega_x^{(1)}$:

Memory protocols

1. **FA magnetization protocol**: A small probe field Ω_y is applied continuously throughout the annealing ramp and maintained afterward, as illustrated in Fig. 6.2(a). When the annealing field reaches $\Omega_x^{(1)}$, the system is allowed to age for a duration t_1. The field is then changed to $\Omega_x^{(2)}$, where it ages for an additional time t_2. Subsequently, the annealing field is restored to its initial value $\Omega_x^{(1)}$, and the magnetization in direction of the probe field is measured after a waiting time t.

2. **ZFA magnetization protocol**: The system is first annealed to a finite field $\Omega_x^{(1)}$ and aged for a time t_1, as shown in Fig. 6.2(b). The annealing field is then changed to $\Omega_x^{(2)}$, where the system ages for t_2. The field is subsequently quenched back to $\Omega_x^{(1)}$. After a time t, a small probe field Ω_y is applied, and the resulting y-component of the magnetization is recorded.

The measured magnetization is compared with that obtained from a reference protocol in which the annealing ramp ends at $\Omega_x^{(1)}$ and the system ages there for a total duration $t_1 + t$. A memory effect is identified when the magnetization curves as functions of t coincide for both protocols.

The total duration of the proposed protocol for probing memory effects is $t_r + t_1 + t_2 + t$, where t_r denotes the ramp time. Following the ZFA and FA protocols discussed in Chap. 3, t_r should be at least 0.75 µs to ensure a measurable splitting between the ZFA and FA magnetizations. In a putative spin-glass state, memory and rejuvenation effects are not expected to emerge unless such a splitting is observed. To reach a regime where this separation becomes significant, indicating dynamics deep within the putative spin-glass phase, the ramp time should exceed 3 µs.

The times t_1, t_2, and t need to exceed a typical interaction cycle, ensuring that measurements reflect slow, quasi-steady-state dynamics rather than transient behavior. For $J_{\text{med}} = 2\pi \times 1.64\,\text{MHz}$, which was experimentally realized in the experiments in Chaps. 3 and 4, this requires $t_1, t_2, t \gg 0.6\,\mu\text{s}$. Since aging processes occur over several interaction cycles, it is advisable to probe at least five such cycles, corresponding to about 3 µs. This choice leads to a total experimental duration of approximately $t_r + t_1 + t_2 + t = 12\,\mu\text{s}$.

After applying the probe field, we aim to extract an approximate steady-state magnetization value, similar to the procedure used for the ZFA and FA protocols in Chap. 3. In ZFA-based protocols, the additional probe duration before the tomographic readout pulse extends the total protocol time by 3 µs, bringing the total protocol duration to about 10 % of the lifetime of the Rydberg states encoding the pseudospin degree of freedom.

Even on longer timescales, where black-body radiation leads to noticeable decay, previous experiments reported negligible influence on the observed ZFA aging behavior [180]. Therefore, exploring AC susceptibilities instead of DC susceptibilities may be advantageous, as dynamical effects are enhanced compared to DC susceptibility based protocols [12]. When studying AC susceptibilities, as discussed in Chap. 2, two components must be distinguished: the in-phase susceptibility χ' and the out-of-phase susceptibility χ''. In this work, we focus on measuring χ'', as it exhibits a pronounced acceleration of aging, rejuvenation, and memory dynamics. The choice of drive frequency is constrained by two opposing requirements. It must be low enough to encompass several interaction cycles, ensuring that the response reflects slow rather than transient dynamics. At the same time, it must be high enough to allow accurate measurements of the magnetic response of the system within the finite lifetime of the constituent elements. For a system interacting with $J_{\text{med}} = 2\pi \times 1.64\,\text{MHz}$, the drive frequency should not exceed 1 MHz. On the other

hand, given the Rydberg lifetime of at most 100 µs, the drive frequency should be larger than 100 kHz. Therefore, we suggest using AC susceptibility measurements with a drive frequency of 1 MHz. This drive frequency of an AC magnetic field can be implemented using the arbitrary waveform generator (AWG), by employing an amplitude modulation of 1 MHz frequency. In order to study the linear regime of the AC susceptibility, the drive amplitude needs to be small. The drive amplitude can be accurately tuned to very low amplitudes owing to the 8-bit modulation resolution of the Keysight M8195A AWG.

Next, we assess the precision required for AC magnetization measurements. In Ref. [180], the aging ZFA magnetization signal decreased by only 0.06 over two decades in t_1. Resolving such small changes requires a measurement uncertainty below 0.02. However, as discussed in previous chapters and detailed in Appendix A, each measurement probes a Rydberg population, of which only about 10 % is detected. This limited detection efficiency introduces significant shot-to-shot fluctuations, yielding a standard deviation of the mean of approximately 0.03 for a single measurement, as observed in the ZFA and FA data of Chap. 3, obtained by averaging 50 outcomes per data point. Maintaining this precision, a faster decay of the out-of-phase magnetization would produce a stronger signal decrease over the same t_1 interval, allowing a more reliable characterization of aging dynamics.

We focus on the AC magnetization and its associated uncertainty. To evaluate the expected accuracy of data processing, we numerically sample two representative datasets, recording the magnetization at discrete time steps. Fitting the data then allows extraction of the in-phase and out-of-phase components of the susceptibility. We assume a sinusoidal drive at 2 MHz and consider two scenarios. According to the Kubo formula [182], within the linear-response regime the system responds at the same frequency as the applied drive, so the magnetization can be treated as a sinusoidal function at this frequency.

In the first, idealized case, the system undergoes a full magnetization oscillation that remains in phase with the drive. The magnetization is then described by

$$M(t) = \frac{1}{2}\sin(2\pi \times 2\,\mathrm{MHz} \cdot t). \tag{6.13}$$

This scenario is used to assess the sensitivity of the measurement to a purely in-phase response, corresponding to a vanishing out-of-phase component.

In the second case, we test the ability to measure an AC magnetization with a reduced amplitude $3/10 \lesssim 1/2$ compared to a full amplitude oscillation, as we expect for small drive amplitudes. We also assume a nonzero out-of-phase component, which may occur in a putative spin glass. For this purpose, we model the sample's

magnetization

$$\begin{aligned} M(t) &= \frac{3}{10}\sin(2\pi \times 2\,\mathrm{MHz} \cdot t + \pi/6) \\ &= \frac{3\sqrt{3}}{20}\sin(2\pi \times 2\,\mathrm{MHz} \cdot t) + \frac{3}{20}\cos(2\pi \times 2\,\mathrm{MHz} \cdot t) \\ &= 0.260\sin(2\pi \times 2\,\mathrm{MHz} \cdot t) + 0.15\cos(2\pi \times 2\,\mathrm{MHz} \cdot t) \end{aligned} \tag{6.14}$$

such that the out-of-phase magnetization has approximately half the amplitude of the in-phase magnetization. To emulate experimental conditions, we sample 30 data points linearly spaced from 0 µs to 0.5 µs. For each time step, a simulated measurement value is generated by drawing from a Gaussian distribution with a mean given by the expressions above and a standard deviation of 0.06, which would be readily achievable with the current experimental platform. For each data point, we assume an uncertainty of 0.06. The sampled data is presented in Fig. 6.3.

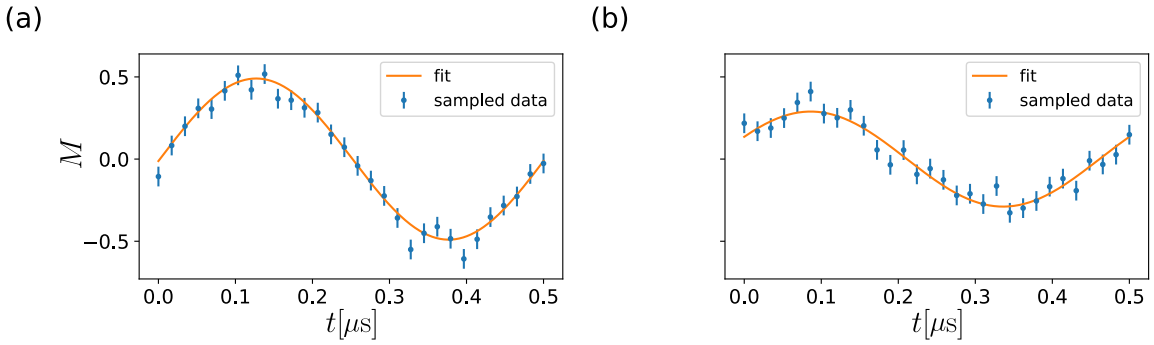

Figure 6.3: *Numerically sampled magnetization data for a simulated AC response measurement.* (a) Pure high-amplitude in-phase response. (b) Response including an additional smaller out-of-phase component. Error bars indicate statistical uncertainties. The orange line represents the best-fit curve obtained via a least-squares fit. Further details are provided in the main text.

To extract the in-phase and out-of-phase components, we fit the simulated data using a least-squares method to the function

$$M(t) = M'\sin(2\pi \times 2\,\mathrm{MHz} \cdot t) + M''\cos(2\pi \times 2\,\mathrm{MHz} \cdot t), \tag{6.15}$$

where M' and M'' are free fit parameters.

For the pure in-phase scenario, the fit yields $M' = 0.490(14)$ and $M'' = -0.012(14)$, which are consistent with the corresponding ground-truth values within one standard

deviation. Similarly, for the scenario including a small out-of-phase component, we obtain $M' = 0.255(15)$ and $M'' = 0.135(15)$. Notably, the uncertainty, which is independent of the amplitude, remains approximately 0.015 in all cases. We will show that this value may be immediately obtained from the number of sampled data points and the uncertainty of a single magnetization measurement.

Therefore, we will make use of the discrete Fourier transformation [280]. We assume we have a dataset of N points, equally spaced by a time interval Δt. The magnetization signal is a discrete function $M(m\Delta t)$ for $0 \leq m < N$. The discrete Fourier transformation is then defined as

$$M(f_k) = \sum_{j=0}^{N-1} M(m\Delta t) e^{-2\pi i (m\Delta t) f_k}, \tag{6.16}$$

where $f_k = k/(N\Delta t)$ are the discrete Fourier frequencies. For simplicity, we will restrict to even N, such that $-N/2 < k \leq N/2$. The inverse Fourier transformation yields

$$M(m\Delta t) = \frac{1}{N} \sum_{k=-N/2+1}^{N/2} M(f_k) e^{2\pi i (m\Delta t) f_k}. \tag{6.17}$$

As $M(m\Delta t)$ as a sampled magnetization is real valued, $M(f_{-k}) = M(f_k)^*$ for $-N/2 < k < N/2$, and $M(f_{N/2}) = \sum_m (-1)^m M(m\Delta t)$ is as an alternating sum of real values and therefore real by construction, we may thus rewrite

$$\begin{aligned} M(m\Delta t) = & \frac{2}{N} \sum_{k=0}^{N/2-1} \mathrm{Re}(M(f_k)) \,\mathrm{Re}\left(e^{2\pi i (m\Delta t) f_k}\right) - \mathrm{Im}(M(f_k)) \,\mathrm{Im}\left(e^{2\pi i (m\Delta t) f_k}\right) \\ & + M(f_{N/2}) \cos(\pi m) \\ = & \sum_{k=0}^{N/2-1} \frac{2\,\mathrm{Re}(M(f_k))}{N} \cos\left(2\pi i (m\Delta t) f_k\right) - \frac{2\,\mathrm{Im}(M(f_k))}{N} \sin\left(2\pi i (m\Delta t) f_k\right) \\ & + M(f_{N/2}) \cos(\pi m). \end{aligned} \tag{6.18}$$

Assuming $M(m\Delta t)$ is a noisy signal which follows a drive of frequency $f = 1/(N\Delta t)$, i.e. assuming that the data points are sampled within one oscillation period, we find for the in-phase and out-of-phase response at frequency f:

$$M' = -\frac{2}{N} \mathrm{Im}\left((M(f_1)\right), \tag{6.19}$$

$$M'' = \frac{2}{N} Re\left((M(f_1)\right). \tag{6.20}$$

We are now interested in the standard deviation of the mean of these quantities. We now assume that each data point $M(\Delta t)$ shows the same uncertainty σ_M, and that these uncertainties are statistically uncorrelated. As a consequence, we may use Gaussian error propagation to estimate the uncertainty of $\mathrm{Re}\,(M(f_1))$ and $\mathrm{Im}\,(M(f_1))$:

$$\begin{aligned}\sigma(\mathrm{Re}\,(M(f_1))) &= \sqrt{\sum_{m=0}^{N-1}\left|\frac{\partial\,\mathrm{Re}\,(M(f_1))}{\partial M(\Delta t)}\sigma_M\right|^2} \\ &= \sigma_M\sqrt{\sum_{m=0}^{N-1}|\cos(2\pi m/N)|^2} \\ &= \sqrt{\frac{N}{2}}\sigma_M,\end{aligned} \tag{6.21}$$

and similarly

$$\begin{aligned}\sigma(Im\,(M(f_1))) &= \sqrt{\sum_{m=0}^{N-1}\left|\frac{\partial\,\mathrm{Im}\,(M(f_1))}{\partial M(\Delta t)}\sigma_M\right|^2} \\ &= \sigma_M\sqrt{\sum_{m=0}^{N-1}|\sin(2\pi m/N)|^2} \\ &= \sqrt{\frac{N}{2}}\sigma_M.\end{aligned} \tag{6.22}$$

As a consequence, we obtain for the uncertainties of the in-phase and out-of-phase magnetizations

$$\sigma(M') = \sigma(M'') = \sqrt{\frac{2}{N}}\sigma_M. \tag{6.23}$$

In the data simulated in Fig. 6.3, we used $N = 30$ and $\sigma_M = 0.06$, resulting to an error of approximately 0.015 for the AC magnetization components. Thus, this represents the reliable lower bound that may be obtained for a given realization of a measured magnetization curve. Thus, AC susceptibilities with an amplitude above 0.045 may be correctly distinguished from zero within a three sigma confidence interval.

We now compare the measurement time between AC and DC susceptibility experiments. In the DC experiment, four magnetization data points were recorded as a function of the probe field amplitude Ω_y. The magnetization for each point in time was averaged over 50 repeated measurements, resulting in a magnetization uncertainty below 0.03. A linear fit using a least-squares method was then performed to extract

the linear susceptibility. For a linear fit, the least-squares method is equivalent to linear regression, where the error of the slope scales as $1/\sqrt{N-2} = 1/\sqrt{2}$ with $N = 4$ points [281]. Therefore, the error of the slope is approximately

$$\frac{0.03}{\sqrt{2}\,\Omega_y}.$$

The total duration required to obtain a DC susceptibility value is $4 \times 50 = 200$ experimental cycles. For the experiments described in Chap. 3, the probe fielded needs to be applied for 3 µs.

In an AC magnetization experiment, we propose measuring the magnetization at $N = 16$ equally spaced time points over one oscillation period. Each magnetization value for each point in time is averaged over 10 repeated measurements, resulting in a magnetization uncertainty of 0.06. From the Fourier transform estimate, the corresponding uncertainty in the AC susceptibilities is

$$\sqrt{\frac{2}{N}}\,\frac{0.06}{\Omega_y} = \frac{0.03}{\sqrt{2}\,\Omega_y},$$

which is identical to the uncertainty obtained in the DC susceptibility measurement. However, only $16 \times 10 = 160$ measurement cycles are required, reducing the total experimental time by 20 %.

Moreover, the probe field needs to be applied for only 2 µs, corresponding to two oscillation periods for a 1 MHz drive. We expect transient effects to decay within one period, since the drive frequency is lower than the typical interaction strength. The validity of the linear-response approximation can be verified by computing the Fourier transform of the measured data and confirming that only the drive frequency exhibits a significant amplitude in the Fourier spectrum.

To summarize, AC susceptibilities can be measured with comparable precision and in even less experimental time than DC susceptibilities. Consequently, AC susceptibility–based protocols may provide an efficient approach to study aging, rejuvenation, and memory effects. Furthermore, they could reinforce the interpretation of our ZFA and FA measurements if the in-phase susceptibility exhibits a peak at the energy where the ZFA and FA susceptibilities diverge. In addition, measuring the AC susceptibility as a function of frequency may enable a direct determination of the dynamical critical exponent z, as discussed in Chap. 2.

6.2 Studying a dipolar Ising Hamiltonian in a Rydberg platform

As discussed in Chap. 2, several open questions concern the nature of a possible Ising spin glass [35, 39, 40, 240], where experimental results can be directly compared with theoretical predictions [105, 282, 283]. The purpose of this section is to demonstrate that the experiments presented and proposed in Chaps. 3, 4, and 5 for the XY model can be straightforwardly extended to a dipolar Ising model, using the very same platform detailed in Appendix A. To this end, we combine the Hamiltonian microwave engineering method previously developed in our group [168] with the time-reversal technique described in Chap. 5.

The realization of various XYZ-Heisenberg spin Hamiltonians with Rydberg atoms, based on an extension of the well-known WaHuHa sequence [284], was first explored in Ref. [168], which we briefly review here. The starting point is the dipolar XY Hamiltonian,

$$H_{XY} = \sum_{i<j} J_{ij} \left(S_x^{(i)} S_x^{(j)} + S_y^{(i)} S_y^{(j)} \right), \tag{6.24}$$

where the coupling coefficients $J_{ij} = (1 - 3\cos^2(\theta_{ij}))\, C_3/r_{ij}^3$ arise from the dipolar interactions between Rydberg atoms, discussed in previous chapters and detailed in Appendix D.

The proposed sequence employs a series of $\pi/2$-pulses to rotate the spin frame during the system's evolution. In each rotated frame, the Hamiltonian H_{XY} transforms into

$$H_{\alpha\beta} = \sum_{i<j} J_{ij} \left(S_\alpha^{(i)} S_\alpha^{(j)} + S_\beta^{(i)} S_\beta^{(j)} \right), \tag{6.25}$$

where $\alpha, \beta \in \{X, Y, Z\}$ depend on the applied pulse sequence. If the pulse duration is negligible compared to an interaction cycle $2\pi/J_{ij}$, the dynamics can be described by a piecewise constant Hamiltonian. In the following, the operator $e^{-i\pi/2S_\alpha}$ represents a Rabi $\pi/2$-pulse around the α-axis, while $e^{i\pi/2S_\alpha}$ corresponds to a rotation around $-\alpha$.

Ref. [168] introduces the following sequence:

1. Evolve under H_{XY} for τ_1.
2. Apply a $\pi/2$-pulse around x to obtain H_{XZ}.
3. Evolve under H_{XZ} for τ_2.
4. Apply a $\pi/2$-pulse around $-y$ to obtain H_{YZ}.

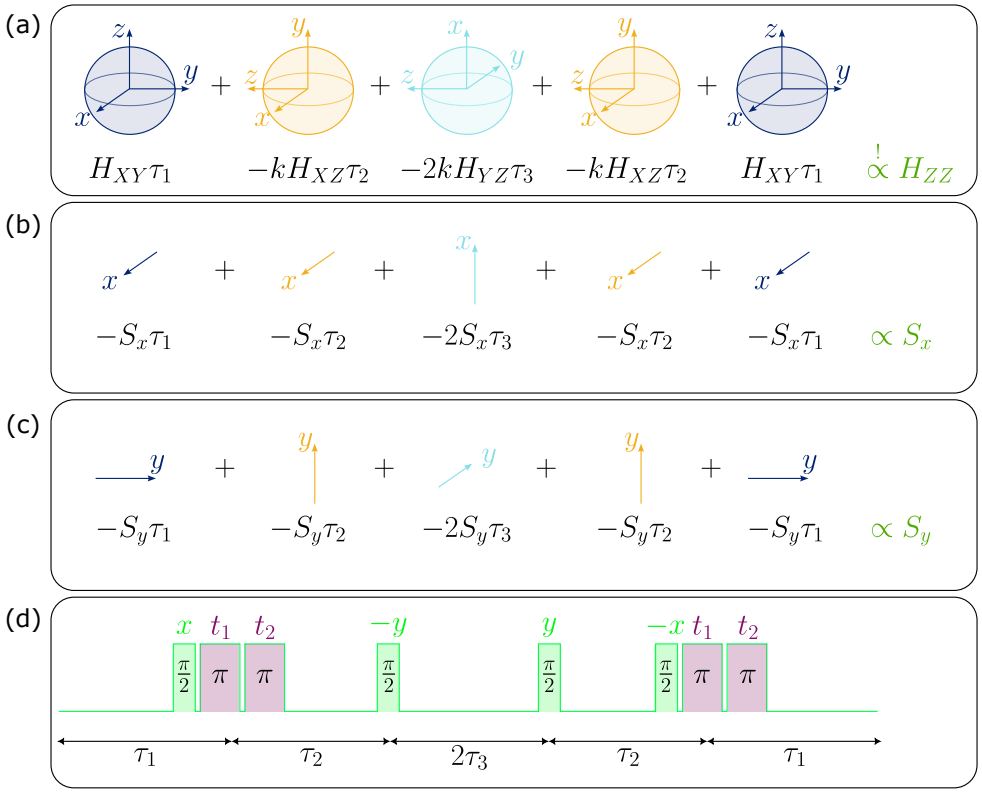

Figure 6.4: *Floquet cycle for the experimental realization of a dipolar Ising model with Rydberg atoms.* (a) Illustration of individual spins on the Bloch sphere. The coordinate system in each sphere represents the current spin frame, while the dark blue sphere also depicts the laboratory frame, which coincides with the spin frame in this case. The expressions below the Bloch spheres denote the product of the instantaneous Hamiltonian and the corresponding evolution time in the spin frame. (b, c) Protocols for applying magnetic fields along the x- and y-axes, respectively. The fields are shown as arrows in the laboratory frame, while the corresponding effective fields in the spin frame are indicated below. We propose to vary the field directions in the laboratory frame, such that the resulting Hamiltonians in the spin frame always align with the x- and y-axes, respectively. (d) Pulse sequence used to implement the averaged Hamiltonians. Green pulses represent the WaHuHa sequence, and violet pulses indicate the transfers required for the time-reversal protocol.

5. Evolve under H_{YZ} for $2\tau_3$.

6. Apply a $\pi/2$-pulse around y to return to H_{XZ}.

7. Evolve under H_{XZ} for τ_2.

8. Apply a $\pi/2$-pulse around $-x$ to return to H_{XY}.

9. Evolve under H_{XY} for τ_1.

The total duration of this sequence is the cycle time $t_c = 2(\tau_1 + \tau_2 + \tau_3)$. Using average Hamiltonian theory [285] in the limit $J_{ij}\tau_c \ll 2\pi$, this sequence effectively realizes the Hamiltonian

$$\sum_{i<j} J_{ij} \left(\delta_x S_x^{(i)} S_x^{(j)} + \delta_y S_y^{(i)} S_y^{(j)} + \delta_z S_z^{(i)} S_z^{(j)} \right), \tag{6.26}$$

with coefficients $\delta_x = 2(\tau_1 + \tau_2)/t_c$, $\delta_y = 2(\tau_1 + \tau_3)/t_c$, and $\delta_z = 2(\tau_2 + \tau_3)/t_c$. An ideal Ising model would correspond to $\delta_x = \delta_y = 0$ and $\delta_z \neq 0$. However, since all evolution times must be positive, the condition $\delta_x = \delta_y = 0$ implies $\tau_1 = \tau_2 = \tau_3 = 0$, leading to the absence of dynamics.

To achieve a dipolar Ising model, we extend the previous scheme by introducing additional time-reversal pulses, as discussed in Chap. 5. The spin states are initially encoded in $|{\downarrow}\rangle_1$ and $|{\uparrow}\rangle_1$, for which the C_3-coefficient determining the couplings J_{ij} is positive. Two coherent pulses, labeled t_1 and t_2, transfer $|{\downarrow}\rangle_1 \to |{\downarrow}\rangle_2$ and $|{\uparrow}\rangle_1 \to |{\uparrow}\rangle_2$. In the second encoding, with spins in $|{\downarrow}\rangle_2$ and $|{\uparrow}\rangle_2$, the C_3-coefficient is rescaled by a factor $-k$. This sign change in the Hamiltonian effectively implements a time-reversal. Using this technique, we devise the following protocol to realize an effective Ising model:

1. Evolve under H_{XY} for τ_1.

2. Apply a $\pi/2$-pulse around x to obtain H_{XZ}, followed by the transfer pulses to realize $-kH_{XZ}$.

3. Evolve under $-kH_{XZ}$ for τ_2.

4. Apply a $\pi/2$-pulse around $-y$ to obtain $-kH_{YZ}$.

5. Evolve under $-kH_{YZ}$ for $2\tau_3$.

6. Apply a $\pi/2$-pulse around y to return to $-kH_{XZ}$.

7. Evolve under $-kH_{XZ}$ for τ_2.

8. Apply a $\pi/2$-pulse around $-x$ to obtain $-kH_{XY}$, followed by the transfer pulses to return to H_{XZ} .

9. Evolve under H_{XY} for τ_1.

This modified scheme also realizes the Hamiltonian 6.26, but with coefficients $\delta_x = 2(\tau_1 - k\tau_2)/t_c$, $\delta_y = 2(\tau_1 - k\tau_3)/t_c$, and $\delta_z = -2k(\tau_2 + \tau_3)/t_c$. Imposing the condition $\delta_x = \delta_y = 0$ yields $\tau_2 = \tau_3 = \tau_1/k$. The resulting effective Hamiltonian is therefore

$$H_{\text{Ising}} = -\frac{2}{1+\frac{2}{k}} \sum_{i<j} J_{ij} S_z^{(i)} S_z^{(j)}. \tag{6.27}$$

For the system realized in Ref. [48], $k \approx 1$ leads to a reduction of the effective median interaction strength in the Ising model by a factor of 2/3, thus still realizing a strongly interacting dipolar Ising model.

To extend this model also to the application of external fields, as indicated in Fig. 6.4 (b) and (c), different fields in the lab frame need to be realized in order to achieve a field in the desired direction in the x- or y-direction in the spin frame. The fields in the lab frame are realized by adjusting the microwave drive coupling the states $|\downarrow\rangle_{(i)}$ and $|\uparrow\rangle_{(i)}$ for $i \in \{1, 2\}$. As we have shown in Chap. 3, different fields in x- and y-directions in the lab frame may be realized by applying a resonant microwave drive, where the phase is adjusted according to the targeted field direction. The same derivation we applied there for resonant microwave drive can also be extended to near-resonant drives. Here, the detuning Δ from resonance realizes an effective field in the z-direction, i.e. a term $-\Delta \sum_i S_z^{(i)}$ in the Hamiltonian. Table 6.1 summarizes the detunings and phases of the microwave drive to realize the fields $\Omega_x S_x$ and $\Omega_y S_y$ in the spin frame.

To experimentally realize the dipolar Ising model, we may employ the same Rydberg states where time-reversal was initially demonstrated [48]. For a system of $N = 332$ spins, the median interaction strength J_{med}, defined as in Chap. 3, was reported to be $J_{\text{med}} = 2\pi \times 0.86\,\text{MHz}$. As discussed in Chap. 5, this weakly interacting regime was chosen because all Rabi frequencies must remain below $2\pi \times 10\,\text{MHz}$ to avoid populating near-resonant, non-targeted Rydberg states. Consequently, the pulse duration of four $\pi/2$- and two π-pulses is bounded from below by 200 ns.

According to the supplemental material of Ref. [168], the pulse duration should remain small compared to the cycle time t_c, since the leading correction due to finite-duration pulses scales with the ratio of the pulse duration to t_c. Importantly, t_c is defined assuming infinitely fast pulses. In addition, corrections arising from higher-order terms in the Rydberg-Rydberg interactions, which are discussed in Chap. 5, are negligible in this Floquet scheme. The median coupling of the average Hamiltonian assuming only resonant dipole-dipole approximation remains comparable to its value in the absence of Floquet driving, while higher-order contributions do not

Evolution time		τ_1	τ_2	$2\tau_3$
Ω_x	Detuning Δ	0	0	Ω_x
	Amplitude Ω	Ω_x	Ω_x	0
	Phase ϕ	0	0	0
Ω_y	Detuning Δ	0	Ω_y	0
	Amplitude Ω	Ω_y	0	Ω_y
	Phase ϕ	$\pi/2$	0	π

Table 6.1: *Experimental parameters for the microwave drive used in the Floquet sequence.* For the transition between the states $|\downarrow\rangle_{(i)}$ and $|\uparrow\rangle_{(i)}$ with $i \in \{1, 2\}$, a microwave field is applied with resonant Rabi frequency $\Omega e^{i\phi}$, where Ω and ϕ denote the amplitude and phase of the drive, respectively. The field is detuned from the resonance by Δ. The parameters listed for each evolution time τ_j for $j \in \{1, 2, 3\}$, shown in Fig. 6.4(d), are chosen to generate effective fields Ω_x along x and Ω_y along y in the spin frame.

increase by orders of magnitude, and thus remain small compared to the dipole-dipole interaction term. Furthermore, the total cycle duration, i.e., the sum of t_c and the pulse duration, should remain small compared to a typical interaction cycle duration, $2\pi/J_{\text{med}} = 1.16\,\mu\text{s}$, to ensure the validity of average Hamiltonian theory. For a total cycle duration of 600 ns, this corresponds to $t_c = 400\,\text{ns}$ and $\tau_1 = 65\,\text{ns}$. Pulses on these timescales can be readily generated with the AWG used in our setup. While the pulse duration is small compared to t_c, it should be noted that t_c is approaching the same order of magnitude as $2\pi/J_{\text{med}}$.

The accuracy of the engineered Hamiltonian can be further improved by reducing the pulse durations. This requires increasing the Rabi frequencies while avoiding population of non-targeted Rydberg states. One approach is to shift these other Rydberg states out of resonance by increasing the magnetic field, as implemented in the experiments described in Chapters 3 and 4. In addition, specific transitions can be selectively addressed using a quadrupole horn antenna, as described in Appendix E, which allows circularly polarized light to illuminate the atoms. This ensures that only σ^+ or σ^- transitions are driven, while the currently used horn antenna remains suitable for driving π-transitions. In this configuration, only one of the σ^+, σ^-, or π transitions can be driven at a time, with the other two being forbidden by dipole selection rules.

Repeating this cycle enables the study of long-time dynamics of a dipolar Ising model. To perform the hysteresis experiments described in Chap. 3 or the reverse quench protocol detailed in Chap. 4, it is necessary to implement time-dependent effective magnetic fields along the x- and y-directions. These fields are generated using the parameters listed in Tab. 6.1 for the microwave drive. The AWG allows precise tuning of the microwave amplitude, frequency, and phase on picosecond timescales, enabling Ω_x and Ω_y to be made time-dependent at each stage of the sequence. To implement time-reversal-based protocols, the effective Ising model can be reversed by applying the transfer pulses t_1 and t_2 prior to a cycle and adjusting the pulse durations τ_1, τ_2, τ_3 according to the transformation $k \to 1/k$.

CHAPTER 7

Conclusion

Central to the field of disordered quantum spin systems with power law interactions, we have based this thesis on the question

> *What is the nature of a bond-disordered, long-range interacting isolated spin system?*

To that end, we started addressing the following questions: Does a dipolar-interacting, isolated Heisenberg spin system host a spin glass phase? How can thermomagnetic hysteresis protocols be adapted to isolated quantum systems? To investigate these questions, we introduced the zero-field annealing (ZFA) and field annealing (FA) protocols, in analogy to the commonly used ZFC and FC protocols in spin glass physics [12, 80], and implemented them in our Rydberg quantum simulation [169]. We studied energetic-magnetic hysteresis in a disordered dipolar XY model under two disorder configurations. At high energies, the system showed no response, consistent with the linear response of an isolated paramagnet at constant energy. In the weakly disordered configuration, ZFA and FA responses were indistinguishable within experimental uncertainties. In contrast, the strongly disordered regime displayed a pronounced bifurcation at low energies, resembling the magnetic irreversibility observed in canonical spin glasses. This splitting, which grows at lower energies, demonstrates a strong dependence on magnetic and energetic history, indicating the absence of thermalization on experimental timescales. Importantly, the ZFA and FA protocols are interaction-agnostic and applicable to arbitrary spin models with $\mathbb{Z}_2$ parity symmetry. They thus provide a versatile framework for probing thermalization in quantum systems beyond the dipolar model studied here. Future investigations could explore whether the energy at which ZFA and FA susceptibilities split corresponds to a glass transition. Numerical studies in one-dimensional toy models suggest that spin glass order is energy-dependent [46]. It would therefore be

valuable to test experimentally and numerically whether the onset of hysteresis we observe is generally linked to the emergence of a spin glass phase. On other quantum simulation platforms, where spin glass order can be directly measured in systems with all-to-all interactions [75, 110, 245], our protocols could be applied to test whether hysteresis indeed signals the emergence of a spin glass phase, complementing our analysis of the putative dipolar glass.

To complement the hysteresis studies, we asked the questions: How can the critical exponents of a spin glass be experimentally accessed in an isolated quantum system, where temperature scaling is absent? Does a spin glass phase exist in the dipolar-interacting Heisenberg XY model, and if so, is it connected to a quantum phase transition driven by an external magnetic field? To address them, we analyzed the critical behavior of a dipolar-interacting Heisenberg XY model. Determining whether a spin glass transition occurs is central to advancing the theoretical understanding of spin glasses. The two dominant frameworks, the Parisi replica-symmetry-breaking mean-field solution [16, 68], recently recognized with a Nobel Prize, and the droplet scaling model by Fisher and Huse [17, 18], make contrasting predictions about the existence of an Ising spin glass phase in the presence of a finite transverse magnetic field. In conventional spin glasses, critical exponents are measured through susceptibility scalings as a function of temperature (see Chap. 2). These protocols cannot be applied to isolated spin glasses, where tuning of a bath temperature is not available. Moreover, we aim to identify a quantum phase transition as a function of magnetic field rather than a thermal phase transition. For experimental feasibility, the protocol must rely solely on global measurements, as local spin-spin correlations are difficult to access in three-dimensional systems. These constraints motivated the development of a robust and scalable method applicable to three-dimensional spin glasses.

We therefore extended the generalized Kibble-Zurek mechanism to reverse quench protocols and showed analytically that, under suitable assumptions, the resulting defect density follows the same scaling as in forward-quench Kibble-Zurek dynamics. This implies that, whenever a system undergoes a continuous quantum phase transition into a paramagnetic phase, global magnetization measurements can approximate the Kibble-Zurek defect density. We verified these predictions using exact numerical simulations of the one-dimensional uniform and bond-disordered transverse-field Ising models. We then applied the reverse-quench protocol to the disordered dipolar XY model, complementing the hysteresis measurements. In the weakly disordered regime, where no bifurcation between the ZFA and FA magnetization was observed, we found no signatures of criticality. By contrast, in the strongly disordered regime, where energetic-magnetic hysteresis is pronounced, the reverse quench magnetization showed behavior consistent with a continuous quantum phase transition. Assuming point-like

Kibble-Zurek defects and using the literature value of the correlation length exponent ν from a disordered dipolar Ising system [105], we obtain $z\nu = 17(4)$. Such an anomalously large critical exponent product is absent in magnetically ordered phases but typical of spin glass materials, where comparable values were measured using AC susceptibilities [94].

Taken together, our measurements provide, within experimental uncertainties, tentative evidence that a spin glass may exist as a genuine quantum thermodynamic phase exhibiting a quantum phase transition as a function of magnetic field. Future studies using Hamiltonian engineering (Chap. 6) could apply this on our Rydberg quantum simulation platform to further investigate the role of a transverse magnetic field in dipolar Ising spin glasses [39–41]. Finally, the reverse-quench approach offers a versatile and experimentally accessible way to extract dynamical critical exponents using only global control. This is especially useful in disordered three-dimensional systems, where local observables are inaccessible and no prior protocol enabled probing criticality in large isolated systems. To further validate the theoretical analysis, it would be highly interesting to apply this protocol on an annealed quantum computing platform and compare the resulting KZM exponent with the one obtained from dynamical finite-size scaling [110].

Complementing our studies on glassy behavior, we asked the questions: Does a finite-size dipolar interacting quantum system show indications of many-body localization? How can localization and ETH effects be experimentally characterized in a power law interacting, bond-disordered system? What is the nature of the localized phase in a bond-disordered power law interacting system? To adress these questions, we explored the possibility of characterizing localization in a putative dipolar spin glass. While spin glasses [11, 80] and many-body localization (MBL) [45] have been extensively studied individually, much less is known about their interplay. To contribute to this open question, we focused on studying localization using time reversal based protocols, which offer high sensitivity.

To assess experimental realizability, we first examined how coherent transfer pulses in different spin encodings could effectively reverse time evolution in a dipolar-interacting XY model implemented on our Rydberg platform [48]. The efficiency of the transfer pulse constituted the primary experimental limitation at short times, and we developed strategies to enhance it and to minimize undesired interaction terms that reduced reversal fidelity at longer times.

To build a theoretical foundation for how localization manifests in time-reversal based protocols, we numerically investigated a small finite-size toy model, examining the interplay between many-body localization and bond-disordered power law interactions. We first analyzed the time decay of the Loschmidt echo. In contrast to

exponentially localized MBL systems, where the Loschmidt echo is expected to decay as a power law [252], we observed a stretched exponential decay—slower than the exponential decay in thermalizing systems, but faster than the power law decay of exponentially localized MBL systems. We additionally studied the width of the multiple quantum coherence (MQC) spectra for both final fidelity and final magnetization measurements. For the fidelity MQC width, which is proportional to the quantum Fisher information of the magnetization operator, we observed logarithmic growth at intermediate times, as in algebraically localized MBL systems, and double-logarithmic growth at longer times, similar to exponentially localized MBL systems. Together, these findings indicate that bond-disordered power-law interacting systems exhibit a qualitatively distinct localization mechanism compared to other MBL systems, consistent with Ref. [136]. These protocols could, in principle, be implemented on small system-size optical lattices, where fidelity can be experimentally measured [286, 287]. This approach is particularly promising for studies of two-dimensional systems, where numerical evaluation is more costly and the bulk-to-boundary ratio is less favorable for finite system sizes.

We also simulated the time evolution of the magnetization MQC and observed a very slow, yet algebraic, increase of the MQC spectral width on the simulated timescales. While the magnetization MQC is directly experimentally implementable, its behavior in the localized regime differs from the thermalizing regime primarily in its slower growth. It would therefore be instructive to simulate the magnetization MQC width in exponentially localized MBL systems as well, to determine whether it exhibits qualitatively distinct behavior and thereby deepen the understanding of different localization mechanisms at finite system sizes. Another avenue of investigation is to explore whether a universal power law growth exists in the magnetization MQC, similar to the universal power law growth of entanglement entropy in power law interacting systems with onsite disorder [133]. These studies could potentially allow different types of localization to be characterized using only global magnetization measurements.

In summary, we have experimentally and theoretically extended the study of bond-disordered, dipolar-interacting isolated spin systems. We showed that such a bond-disordered XY model exhibits strong energetic-magnetic hysteresis at low energies and high disorder, providing a first indication of glassy behavior. This observation was further supported by tentative evidence of quantum critical behavior, consistent with typical spin glass critical exponents. Finally, from a broader perspective, we demonstrated that time-reversal based protocols can reveal that bond-disordered, power-law interacting models exhibit a qualitatively distinct form of many-body localization at finite size.

CHAPTER A

Preparation and State Population Detection in a Frozen Rydberg Gas

In the main body of this thesis, Chap. 3 and 4, we used a Rydberg simulation platform, to implement disordered Heisenberg spin models and study their behavior. Where this platform was briefly introduced in Chap. 3 to explain the experimental results, the aim of this chapter is to explain and motivate the platform in full detail.

The aim of the platform is to implement disordered Heisenberg spin Hamiltonians of interacting 2-level pseudospin systems with tunable disorder. The spin-spin interaction is encoded by the dipole-dipole interaction of Rydberg atoms, as introduced in Chap. D, and we are interested in the unitary dynamics under these Hamiltonians. As a consequence, the platform must fulfill several conditions.

1. We want to study unitary dynamics under a model with quenched disorder. As a consequence, atoms may not move during experimental timescales. As a consequence, the atoms need to be cooled down to low temperatures such that their motional energy is negligible compared to the Rydberg-Rydberg interaction. This is the regime of a frozen Rydberg gas. In addition, the Rydberg-Rydberg interaction should be large compared to the black-body decay rate of the participating Rydberg states. As the Rydberg-Rydberg interaction decreases with distance, the cold atomic cloud must be prepared at a high density.

2. The platform needs to allow for the implementation of a pseudospin. Thus, it needs to be able to excite a well-defined Rydberg state, which may be coupled to only one more Rydberg state.

3. After mapping the Rydberg states to a spin model, we want to measure different

magnetization components. As a consequence, the platform must allow for a tomographic readout of different Rydberg state coherences.

4. To precisely determine the magnetization in the realized spin models, the platform must be able to extract ion numbers after a given protocol, averaged over different disorder realizations. Achieving high accuracy requires averaging over many realizations. Consequently, shot-to-shot fluctuations in the prepared atom number must be minimized.

In the following, we will show that the platform that has already been described in different works [153, 154, 156, 157, 161, 178, 288, 289] is well suited to achieve these points. The experimental sequence, which serves as an outline for this chapter, is sketched in Fig. A.1.

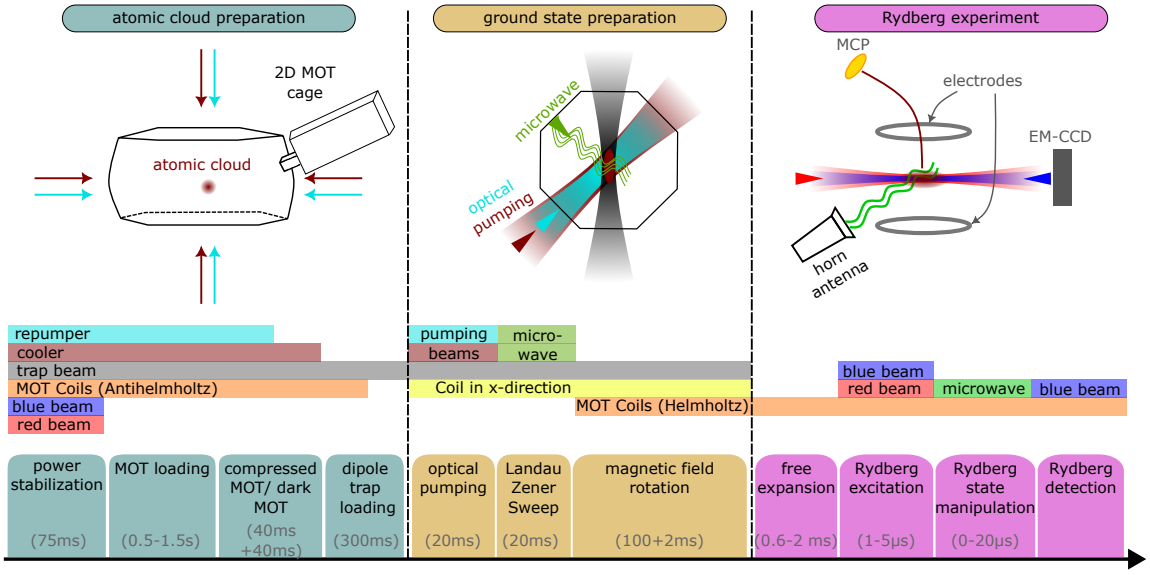

Figure A.1: *Schematic experimental sequence.* A cold and dense atomic cloud is prepared by pre-cooling atoms in a 2D MOT, followed by cooling a 3D MOT and loading into a dipole trap. Applying an optical pumping scheme and potentially also a Landau-Zener sweep, followed by rotation of the magnetic field, prepares all atoms in a single hyperfine ground state that serves as a starting point for the Rydberg experiments performed in the main part of this thesis. The vertical bars below the sketch indicate the presence of laser and magnetic fields, while the lowest row indicates the timing of the sequence. For details of the sequence see the text in this chapter. Figure inspired by [289].

First, the atoms are cooled using a magneto-optical trap [290] and loaded into an optical dipole trap [291], enabling the preparation of a dense thermal cloud with adjustable density (see Sec. A.1). Optical pumping [292] is then used to prepare a specific hyperfine ground state, which can be further refined using Landau-Zener sweeps [293] (see Sec. A.2). This procedure allows the excitation of a well-defined Rydberg state from this hyperfine ground state using dipole transition rules and large magnetic fields to separate magnetic sublevels. The strong Zeeman splitting ensures that this state can couple to only a single other Rydberg state, even under large Rabi frequencies. A tomographic readout pulse then detects coherences between Rydberg states, enabling magnetization readout (see Sec. A.3).

A.1 Preparation of a cold dense atomic cloud

To produce a cold and dense cloud of rubidium atoms, we employ established laser cooling and trapping techniques widely used in ultracold atom experiments [294]. The atoms are first precooled in a two-dimensional magneto-optical trap (2D MOT) before being transferred into a three-dimensional MOT (3D MOT) for final cooling. The high atomic mass of rubidium, combined with a strong dipole matrix element on the cooling transition and the large excited-state decay rate $\Gamma_e = 2\pi \times 6.065\,\mathrm{MHz}$, enables rapid and efficient trapping. This two-stage cooling scheme yields atomic samples containing several hundred thousand atoms at temperatures of a few tens of microkelvin, with peak densities reaching $2 \times 10^{11}\,\mathrm{cm}^{-3}$. After cooling, the atoms are loaded into an optical dipole trap [295] where they are allowed to thermalize. Where the MOT stages ensure a fast loading of many atoms and fast cooling, the dipole trap allows for a deterministic trap geometry, which will be crucial in tuning and characterizing the positional disorder of the atoms. Both the MOT stages and the dipole trap have been well characterized in prior work [153, 154, 161, 296], and most recently in [157, 289]. In the following, I will present the experimental sequence and the key aspects of these traps, closely following Refs. [289] and [157].

Power stabilization

To minimize shot-to-shot fluctuations in the number of excited atoms, we stabilize the power of the Rydberg excitation lasers before atom loading. A small portion of the beam power of both the red and blue excitation laser (1 mW) is coupled out from the excitation path and directed onto a photodiode. A PID controller regulates the RF power driving the acousto-optical modulator (AOM) that controls the excitation beams, ensuring the photodiode current matches a predefined setpoint. This feedback

loop reduces fluctuations in the number of excited Rydberg atoms and enables more consistent initial conditions with respect to atom number. During atom loading, the excitation beams are turned off again.

2D MOT

Our objective is to load a larger number of atoms into a 3D MOT and cool them to microkelvin temperatures. However, a 3D MOT typically captures only atoms with velocities below approximately $10\,\mathrm{m\,s^{-1}}$ [294]. Atoms emitted from a dispenser generally have velocities of several hundred meters per second, far exceeding this capture threshold. For the experiments presented in the main body of this thesis, no dispenser was used, as repeated use in previous studies [43, 157, 161, 289] caused Rubidium adsorption on the glass cell enclosing the 2D MOT. To conserve dispenser material while maintaining sufficient atom loading, we employ a UV lamp to induce photodesorption of Rubidium atoms from the glass surface. Since the cell is at room temperature, the desorbed atoms also exhibit velocities on the order of several hundred meters per second. To enable capture by the 3D MOT, these atoms must be decelerated. One possible approach is a Zeeman slower, which cools atoms along a spatially varying magnetic field using a laser that propagates in opposite direction to the atoms [294]. However, Zeeman slowers are typically large and impose significant geometric constraints. Additionally, they offer no cooling in directions transverse to the laser beam.

To address these limitations, we employ a 2D MOT [161, 297], where atoms are transversely laser-cooled in a magnetic quadrupole field. An additional pushing beam, aligned along the desired propagation direction, generates a slow atomic beam. This cold beam enters the main vacuum chamber through a differential pumping stage. A careful alignment of the atomic beam on the pumping stage ensures that predominantly ^{87}Rb atoms reach the main chamber.

3D MOT

In the main chamber, atoms are cooled using six laser beams intersecting along three orthogonal directions, as illustrated in Fig. A.1. A magnetic quadrupole field is generated by a pair of coils in anti-Helmholtz configuration. Additional compensation coils allow precise adjustment of the field center, thereby enabling control over the MOT position. As shown in Fig. A.2, the cooling laser is red-detuned by $\Delta_c = 3\Gamma_e$ from the $\left|5S_{1/2}, F = 2\right\rangle \rightarrow \left|5P_{3/2}, F = 2\right\rangle$ transition. To prevent optical pumping into the dark state $\left|5S_{1/2}, F = 1\right\rangle$, an additional repumper laser is applied, resonant with

the $\left|5S_{1/2}, F = 1\right\rangle \rightarrow \left|5P_{3/2}, F = 2\right\rangle$ transition. This efficient laser cooling is enabled by the large hyperfine splittings in both the $\left|5P_{3/2}\right\rangle$ and $\left|5S_{1/2}\right\rangle$ manifolds, on the order of several hundred MHz and several GHz, respectively, allowing for individual addressing of the relevant states. Once the 3D MOT is loaded with a high number of atoms, the density is further increased and the temperature further reduced by employing a compressed MOT phase [298], followed by a dark MOT phase [299, 300]. These steps also ensure that the atoms accumulate in the $\left|5S_{1/2}, F = 1\right\rangle$ ground state, providing a well-defined initial state for preparing a specific ground state with a defined magnetic sublevel.

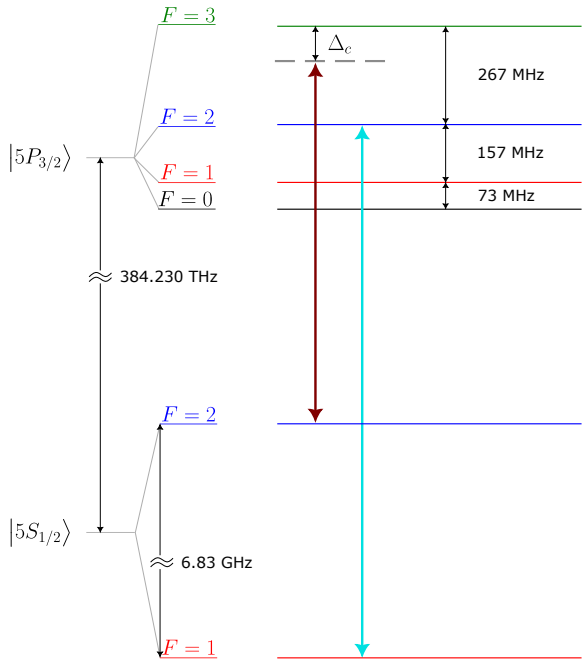

Figure A.2: *Level diagram of Rubidium during 3D MOT cooling.* At the center of the MOT, all different magnetic sublevels are degenerate and thus not depicted. Different hyperfine levels in the ground state and the excited $\left|5P_{3/2}\right\rangle$ excited state are depicted as vertical lines. The repumper transition is indicated by a cyan arrow, while the cooler transition is indicated by a brown arrow. The cooler is detuned from resonance by a detuning Δ_c. Black arrows indicate energy differences between levels given in units of Planck's constant times frequency.

Optical Dipole Trap

To achieve high atomic densities and a well-defined, deterministic spatial distribution, atoms are loaded into an optical dipole trap [291, 295, 301]. We use a high-power 1064 nm laser beam, red-detuned from both the D1 and D2 lines of Rubidium, which attracts atoms toward regions of high intensity.

Although a single focused Gaussian beam can, in principle, confine atoms in all three dimensions, the radial confinement is typically weak. To improve trapping efficiency, we implement a crossed optical dipole trap [301]. It is formed by retro-reflecting the initial high-intensity Gaussian beam back into the chamber through the same viewport. This configuration results in two beams with orthogonal linear polarizations intersecting at an angle of 9°, where the angle is limited by the retro-reflection geometry. The beam waist was optimized to maximize the spatial overlap with the 3D MOT, ensuring efficient transfer of atoms into the trap [302]. The resulting atomic distribution is thus a 3D Gaussian distribution, where the width is proportional to the waist of the dipole trap.

A.2 Ground state preparation

To study long-range magnetism with Rydberg atoms, we aim to prepare a gas in which long-range interactions are significant on experimental timescales. This requires rapidly exciting many closely spaced ground-state atoms to a Rydberg state, such that the excitation time remains negligible compared to the Rydberg state lifetime, and the interatomic distance between Rydberg atoms is small. This process is facilitated by the collective enhancement of the Rabi frequency within a Rydberg blockade radius [162]. To exploit this effect, it is essential to create a dense ensemble of atoms prepared in an identical ground state. To lift the degeneracy of the magnetic sublevels, a weak magnetic field is first applied to define the quantization axis. The atoms are then prepared in the $\left|5S_{1/2}, F = 2, m_F = 2\right\rangle$ state using optical pumping [292]. Additional atoms can be transferred to this state using Landau-Zener sweeps [293]. Due to geometric constraints, the magnetic field, and thus the quantization axis, is subsequently rotated onto the axis defined by the MOT coils. In this configuration, ground-state atoms can be resonantly excited to a single Rydberg state. Furthermore, excitation along this axis allows for spectral isolation of the target Rydberg states, as the MOT coils operated in Helmholtz configuration can generate a strong magnetic field, resulting in a large Zeeman splitting of the states in the Rydberg manifold. The preparation of ground-state atoms in a single hyperfine sublevel has been discussed in detail in Refs. [157, 288, 289], while the magnetic field rotation was briefly

addressed in Ref. [157]. In the following, I summarize the main elements of the sequence, following primarily Ref. [289], with a particular focus on the experimental implementation.

Optical Pumping

The goal of the optical pumping scheme is to deterministically transfer all atoms initially in the $F = 1$ manifold of the $\left|5S_{1/2}\right\rangle$ ground state into the single Zeeman sublevel $\left|5S_{1/2}, F = 2, m_F = 2\right\rangle$. Therefore, we couple 200 µW of repumper light, originally used in the 2D MOT, into the path of the Rydberg excitation laser via an optical fiber. As shown in Fig. A.3, the repumper, which is σ^+ polarized, drives the transition $\left|5S_{1/2}, F = 1, m_F\right\rangle \rightarrow \left|5P_{3/2}, F = 2, m_F + 1\right\rangle$, for $m_F \in \{0, \pm 1\}$.

From the excited state $\left|5P_{3/2}, F = 2, m_F\right\rangle$, atoms can decay via dipole-allowed transitions to ground-state sublevels with magnetic quantum numbers m_F, $m_F + 1$, or $m_F + 2$, populating either the $F = 1$ or $F = 2$ manifold of the $\left|5S_{1/2}\right\rangle$ ground state. As a result, continued cycling with the repumper laser accumulates population in the $\left|5S_{1/2}, F = 2, m_F\right\rangle$ states with $m_F \in \{-1, 0, 1, 2\}$. To further drive the population into a single Zeeman sublevel, we simultaneously couple approximately 2.1 µW of the cooling laser, originally used in the 2D MOT, into the excitation path. The frequency of this laser is shifted using an acousto-optic modulator (AOM) driven by a direct digital synthesizer (DDS), such that it is red-detuned by $\Delta_c \approx \Gamma_e$ from the $\left|5S_{1/2}, F = 2, m_F\right\rangle \rightarrow \left|5P_{3/2}, F = 2, m_F + 1\right\rangle$ transition. This combined optical pumping scheme ensures that nearly all atoms are transferred to the target state $\left|5S_{1/2}, F = 2, m_F = 2\right\rangle$, which is a dark state to this pumping scheme.

Landau-Zener Sweep

Imperfections in the optical pumping process, such as finite σ^- and π polarization, can lead to some remanent population in non-targeted magnetic sublevels of the $\left|5S_{1/2}, F = 2\right\rangle$ manifold. To remove these atoms, it is possible to apply an adiabatic Landau–Zener passage [293] on the $\left|5S_{1/2}, F = 1, m_F = 1\right\rangle \rightarrow \left|5S_{1/2}, F = 2, m_F = 2\right\rangle$ transition, which transfers all atoms in the desired target state to the state $\left|5S_{1/2}, F = 1, m_F = 1\right\rangle$. A subsequent pulse of 3D MOT cooling light, resonant with the $\left|5S_{1/2}, F = 2, m_F = 2\right\rangle \rightarrow \left|5P_{3/2}, F = 3, m_F = 3\right\rangle$ transition, removes the remaining atoms in the $F = 2$ manifold. A second Landau–Zener passage transfers the atoms back to the $\left|5S_{1/2}, F = 2, m_F = 2\right\rangle$ state. This procedure allows to prepare approximately 95 % of the atoms in the desired target state. By reducing the

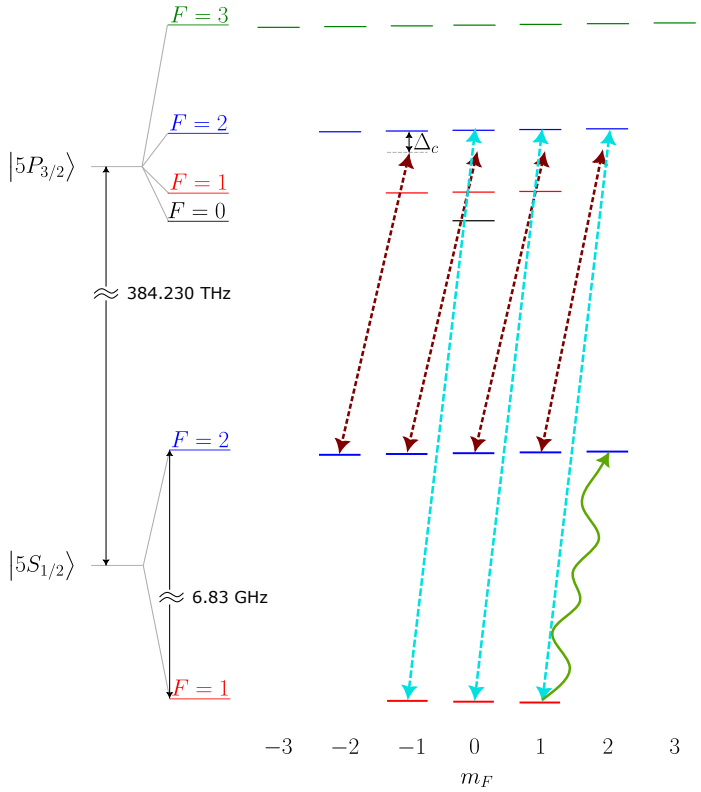

Figure A.3: *Level diagram of Rubidium during optical pumping.* The relevant energy levels of the Rubidium D2 line are represented by horizontal lines. Levels with the same total angular momentum F are shown in the same color. Black arrows indicate energy differences between levels, expressed in units of Planck's constant times frequency. Laser-driven transitions from the 2D repumper and 2D cooler are indicated by cyan and brown dashed arrows, respectively. The green wavy arrow represents the transition used for the Landau-Zener sweep.

duration of the second passage, the transfer becomes more diabatic, thus lowering the population in the target state. This allows for tunable preparation of the atom density in the target state.

The $\left|5S_{1/2}, F = 1, m_F = 1\right\rangle \rightarrow \left|5S_{1/2}, F = 2, m_F = 2\right\rangle$ transition has a resonance frequency of 6.8 GHz, placing it in the microwave regime. As this transition is electric dipole forbidden but allowed via magnetic dipole coupling, it is intrinsically weak. The required microwave signal is generated using a signal generator and delivered via a coaxial cable to an antenna positioned inside the vacuum chamber. The antenna's proximity to the atomic cloud and its directivity enable a Rabi frequency of $2\pi \times$

5.3(6) kHz. The Landau–Zener passage is implemented by initially applying microwave radiation blue-detuned from the transition, such that $\left|5S_{1/2}, F = 2, m_F = 2\right\rangle$ is the system's ground state. As the detuning is swept adiabatically to the red side, the ground state evolves into $\left|5S_{1/2}, F = 1, m_F = 1\right\rangle$. The achieved Rabi frequency ensures adiabaticity over a sweep duration of 10 ms.

Magnetic field rotation

Efficient optical pumping requires a magnetic field that is sufficiently small to keep all magnetic sublevels near-resonant with the pumping light, and aligned along the propagation direction of the optical pumping beams, such that circularly polarized light may drive only σ^+ transitions. To generate such a field, we use the compensation coils originally employed to control the position of the 3D MOT. These coils are designed to produce stable magnetic fields up to 30 G, making them well-suited for this purpose. Furthermore, their alignment with the optical pumping beams is fixed by design, eliminating the need for additional alignment.

After Rydberg excitation, we aim to drive microwave transitions between Rydberg states with Rabi frequencies exceeding 30 MHz. This requires a large energy separation between states in the Rydberg manifold, which can be achieved by applying a strong magnetic field to induce significant Zeeman splitting. To generate such fields, we use the MOT coils, which are designed to carry currents up to 200 A and can produce magnetic fields exceeding 200 G. However, two limitations arise when repurposing the MOT coils for this task:

1. During MOT loading, the coils operate in an anti-Helmholtz configuration. To generate a homogeneous field, the current in one coil must be reversed to switch to a Helmholtz configuration.

2. The magnetic field generated by the MOT coils is oriented perpendicular to the field used during optical pumping. Since the quantization axis is defined by the magnetic field, applying the MOT field effectively rotates this axis.

To switch to a Helmholtz configuration, two approaches are possible. One option is to use separate power supplies for each coil, connected via a common ground. However, this requires an additional power supply and introduces potential error sources due to the need for a stable shared ground reference. Instead, we adopt a second approach, in which the current passing through the first MOT coil is routed to the second coil via an H-bridge. The H-bridge allows precise control over the current direction, enabling a seamless switch between Helmholtz and anti-Helmholtz configurations.

This setup eliminates the need to match currents manually and simplifies the overall operation.

We begin the magnetic field rotation by operating the H-bridge such that the MOT coils are in Helmholtz configuration. The current through the MOT coils is then increased to generate a magnetic field aligned with the axis defined by the MOT coils. If the field was instantaneously quenched to its final value, the quantization axis would be quenched to a direction perpendicular to that used during optical pumping. In this case, the atomic state $|F = 2, m_F = 2\rangle$, initially defined with respect to the optical pumping axis, is projected onto an angular momentum basis defined with respect to the new quantization axis. The resulting state is

$$|2,2\rangle_{\text{quenched}} = \frac{1}{4}|2,-2\rangle + \frac{1}{4}|2,2\rangle - \frac{1}{2}|2,1\rangle + \sqrt{\frac{3}{8}}|2,0\rangle\,, \tag{A.1}$$

where we use the shorthand $|F, m_F\rangle \equiv \left|5S_{1/2}, F = F, m_F = m_F\right\rangle$, where the m_F are defined with respect to the quantization axis defined by the MOT coils, and the coefficients are determined by the corresponding Wigner d-matrix elements [179]. As a result, only 6.25 % of the population remains in the target state $|2,2\rangle$ when expressed in the new basis. To prevent this substantial reduction, we ramp the MOT field to its final value of 185 G over 100 ms. During this ramp, the 2 G compensation field in direction of the optical pumping beams remains active to maintain a finite Zeeman splitting, ensuring adiabatic following of the eigenstates. After the ramp, the compensation field is quenched to zero within 2 ms. Since the MOT field dominates, this fast quench remains adiabatic and preserves the state transfer.

In the current setup, direct optical pumping along the quantization axis defined by the MOT coils is not possible, as optical access is obstructed by one of the MOT beams. In a possible future implementation, this beam, currently entering from the top of the vacuum chamber, could be redirected to enter at an angle into the chamber. While this adjustment may reduce the MOT cooling efficiency, it provides access along the quantization axis and thereby makes direct optical pumping along the MOT coil axis possible. This would eliminate the need to rotate the magnetic field during state preparation.

A.3 Rydberg excitation and detection

The aim of the Rydberg excitation is to generate a cloud of Rydberg atoms with tunable spatial disorder. This can be achieved by two complementary methods: modifying the disorder of the ground-state atoms prior to excitation, or adjusting

the number of Rydberg atoms during the excitation process. Both approaches are employed in this work. To tune the initial ground-state configuration, the optical dipole trap is switched off before excitation, allowing the cloud to expand freely for 600 µs to 2000 µs. Owing to the anisotropic shape of the initial cloud, this thermal expansion can, in principle, alter its geometry. However, the Rydberg excitation is defined by the spatial profile of the laser beams, whose waists are smaller than the size of the expanded cloud. As a result, the geometry of the Rydberg atom distribution is mainly determined by the laser beam profiles, not by the overall atomic cloud.

Several methods are available for Rydberg excitation. A direct single-photon excitation from the state $\left|5S_{1/2}, F = 2, m_F = 2\right\rangle$ to a Rydberg level is, in principle, feasible. However, the dipole matrix element is extremely small, requiring a high-power laser. In addition, such transitions demand ultraviolet wavelengths; for instance, reaching the $|40S\rangle$ state necessitates UV light at 297 nm. At these wavelengths, optical components are prone to damage, and frequency modulation, which is required to excite different Rydberg states, becomes technically demanding. Moreover, generating UV light typically involves multiple frequency conversion stages, which increases sensitivity to amplitude and phase noise. Dipole selection rules further restrict direct excitation to Rydberg p-states, whose strongly anisotropic interactions hinder the study of weakly disordered systems. In contrast, when the blockade determines the interparticle distance, isotropic interactions are preferable to ensure uniform excitation spacing. To overcome these constraints, we employ a two-photon transition via the D2-line, using lasers in the optical regime. This allows direct excitation to a Rydberg S-state, which exhibits isotropic interactions and thus a nearly spherical blockade radius at low magnetic fields. The Rydberg excitation process and the subsequent detection schemes have been already discussed in detail in prvious works [156, 157]. In the following, I will summarize the main techniques, and adapt the discussion to the experiments performed in the main part of this thesis. During the summary, I will mainly follow [157].

Rydberg excitation

To excite the Rydberg state, as illustrated in Fig. A.4, we use a two-photon scheme. A red beam at 780 nm, blue-detuned by $\Delta = 2\pi \times 97\,\mathrm{MHz}$ from the $\left|5S_{1/2}, F = 2, m_F = 2\right\rangle \rightarrow \left|5P_{3/2}, F = 3, m_F = 3\right\rangle$ transition, provides the first excitation step. A counter-propagating blue beam at 480 nm is simultaneously applied, red-detuned by the same amount Δ from the $\left|5P_{3/2}, F = 3, m_F = 3\right\rangle \rightarrow \left|61S_{1/2}, m_J = 1/2\right\rangle$ transition. This configuration ensures two-photon resonance with the Rydberg state. The large detuning Δ minimizes population in the intermediate

level, allowing for its adiabatic elimination and reducing the system to an effective two-level model. The counter-propagating geometry leads to minimal momentum transfer, adding a velocity of only $3.7\,\mathrm{nm\,\mu s^{-1}}$ to the Rydberg atoms—significantly lower than the $15.5\,\mathrm{nm\,\mu s^{-1}}$ imparted in a co-propagating setup.

Figure A.1 shows that, due to the experimental geometry, the excitation beams enter the vacuum chamber perpendicular to the quantization axis, which is defined by the magnetic field of the MOT coils. As a result, circular polarization along the quantization axis cannot be achieved. Instead, we use linearly polarized light in the transverse plane, which decomposes equally into σ^+ and σ^- components. Consequently, only half of the laser power contributes to the Rydberg excitation scheme shown in Fig. A.4. As discussed in the section on magnetic field rotation, enabling optical access along the quantization axis from the top of the chamber would allow the use of circularly polarized excitation light. This would increase the effective two-photon Rabi frequency and additionally enhance state selectivity in the Rydberg manifold through polarization-dependent selection rules.

Microwave manipulation

Microwave control within the Rydberg manifold is achieved using a Keysight M8195A arbitrary waveform generator (AWG), which offers a digital sampling rate of 64 GSa, an analog bandwidth of 25 GHz, and a typical rise time of 18 ps. These parameters allow precise amplitude and phase modulation on picosecond timescales at gigahertz frequencies. As discussed in Chapter 3, the pseudospin is encoded in the states $\left|61S_{1/2}, m_J = 1/2\right\rangle$ and $\left|61P_{1\pm1/2}, m_J = 1/2\right\rangle$, which are coupled by a transition near 16 GHz. This frequency lies within the analog bandwidth of the AWG and can therefore be generated and modulated directly, without the need for frequency up-conversion. Avoiding conversion suppresses spurious sidebands that could induce Rydberg light shifts or unwanted couplings, thus maintaining the validity of the two-level approximation. The microwave signal is delivered to a Pasternack PE9852/2F-20 horn antenna with a nominal gain of 20 dB. Although this antenna is specified for the 18 GHz to 26.5 GHz range, we operate it slightly below specification at 16 GHz, where we expect a reduced gain. This can be compensated by increasing the output power of the AWG. Due to the long microwave wavelength, the antenna's near field is spatially inhomogeneous and lacks a well-defined polarization, while the far field is divergent, causing rapid power loss over distance. To generate a uniform, high-intensity microwave field inside the vacuum chamber, the radiation is refocused using a parabolic mirror. A wire grid polarizer is placed in the beam path to enforce π-polarization relative to the quantization axis, ensuring selective excitation of π-

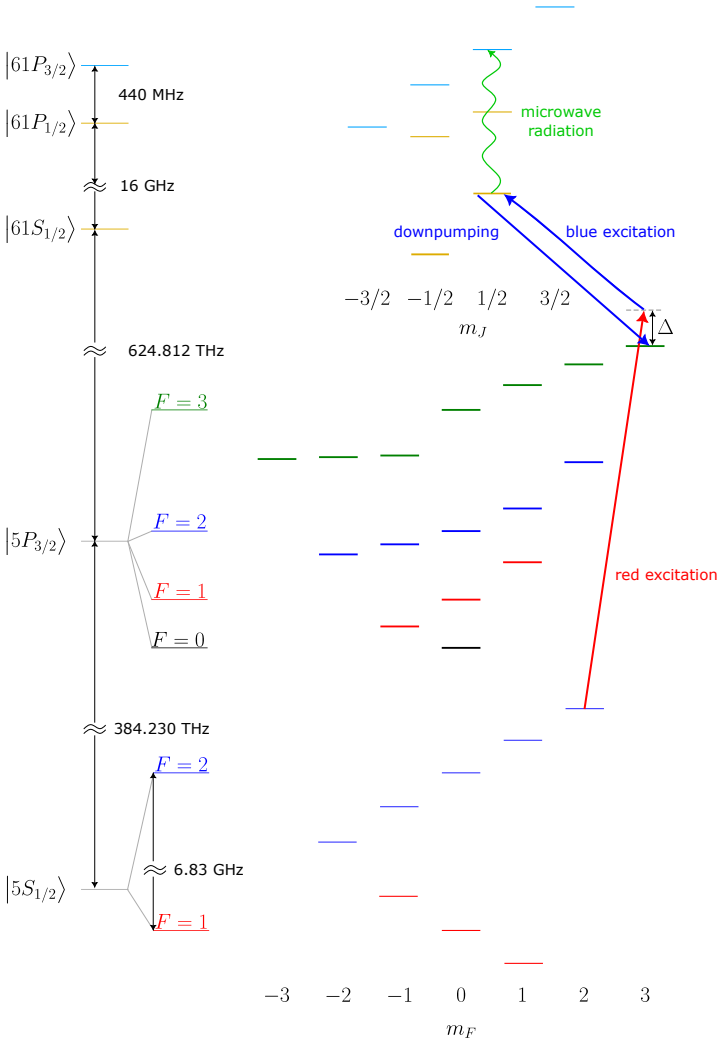

Figure A.4: *Level diagram of rubidium during Rydberg excitation and detection.* Horizontal lines represent energy levels at a magnetic field of 185 G. The ground state $|5S_{1/2}\rangle$ and the excited state $5P_{3/2}$ are color-coded by their total angular momentum F, and horizontally shifted according to the magnetic quantum number m_F. In the Rydberg manifold, hyperfine splitting is negligible; levels are therefore color-coded by their total angular momentum J, and arranged by their magnetic quantum number m_J. Black arrows indicate transition frequencies at zero magnetic field. Red and blue arrows show the transitions for excitation and detection. The green wavy line illustrates a typical microwave transition between Rydberg states. Further details are provided in the main text.

transitions only. Within the Rydberg manifold, the application of a strong magnetic field enables the splitting of magnetic sublevels by more than 300 G. This Zeeman splitting exceeds even strong Rabi frequencies of more than $2\pi \times 100$ MHz, thus allowing for state-selective addressing even under strong driving conditions.

Rydberg atom detection

To study Heisenberg spin systems using the Rydberg platform, we aim to measure the magnetization in the effective spin model. As discussed below, this corresponds to determining the population in the two Rydberg states that encode the pseudospin. In principle, state-selective field ionization could be employed for this purpose, as detailed in Ref. [156]. However, this technique relies on a large energy separation between the involved Rydberg states, which is not present between $\left|61S_{1/2}, m_J = 1/2\right\rangle$ and $\left|61P_{1\pm1/2}, m_J = 1/2\right\rangle$. Consequently, we detect only the population in one of the Rydberg states, specifically $\left|61P_{1\pm1/2}, m_J = 1/2\right\rangle$. This is achieved by applying a strong laser pulse using the blue excitation beam, whose frequency is shifted via a combination of a DDS and an AOM, to be resonant with the $\left|5P_{3/2}, F = 3, m_F = 3\right\rangle \rightarrow \left|61S_{1/2}, m_J = 1/2\right\rangle$ transition. As is outlined in Ref. [178], a downpumping pulse of 5 µs is sufficient to completely depopulate the Rydberg state $\left|5P_{3/2}, F = 3, m_F = 3\right\rangle \rightarrow \left|61S_{1/2}, m_J = 1/2\right\rangle$. The remaining population in $\left|61P_{1\pm1/2}, m_J = 1/2\right\rangle$ is ionized by applying a strong electric field generated by electrodes inside the vacuum chamber. The resulting ions are steered onto a microchannel plate (MCP) detector using deflection electrodes. The geometric acceptance of the MCP limits its theoretical detection efficiency to 40 % [161]. However, the experimentally measured efficiency, determined via comparison with depletion imaging [166], is approximately 10 %. This reduced efficiency is attributed primarily to incomplete ionization of the Rydberg atoms.

Tomographic magnetization readout

While the population in the state $\left|61P_{1\pm1/2}, m_J = 1/2\right\rangle$ can be directly accessed via field ionization, inferring the population in $\left|61S_{1/2}, m_J = 1/2\right\rangle$ requires additional reference measurements. These are also necessary to convert ion counts into quantitative magnetization values. To reconstruct the full magnetization vector, including the x- and y-components, we perform a tomographic readout, following the protocols described in Refs. [155–157]. For clarity, we define the state $\left|61S_{1/2}, m_J = 1/2\right\rangle$ as

$|\downarrow\rangle$, and $\left|61P_{1\pm1/2}, m_J = 1/2\right\rangle$ as $|\uparrow\rangle$. The populations in these Rydberg states are denoted as $N_\downarrow$ and $N_\uparrow$, respectively.

- To determine the total number of Rydberg atoms N_{tot}, we proceed as follows. After Rydberg excitation to the state $|\downarrow\rangle$, a microwave $\pi/2$-pulse creates the superposition state $1/\sqrt{2}\,(|\uparrow\rangle + |\downarrow\rangle)$. After a delay t, all Rydberg atoms are field-ionized. The resulting signal $N_{\text{tot}}(t)$ serves as a reference for the sum $N_\uparrow(t) + N_\downarrow(t)$, accounting for decay due to black-body radiation. This process is discussed in detail in Chap. 4.

- To isolate background contributions, we excite all atom in the Rydberg state $|\downarrow\rangle$, wait for a time t, apply the downpumping pulse, and perform field ionization. Ideally, all Rydberg atoms are depopulated, leaving no ions. In practice, a residual signal N_{dp} remains due to imperfections like black-body induced decay to nearby Rydberg states. These states are treated as a background, since their interaction with atoms in the states $|\uparrow\rangle$ and $|\downarrow\rangle$ is typically negligible.

- To obtain a reference for the ion number associated with the z-magnetization, we apply a downpumping pulse at the end of an experimental sequence and subsequently field-ionize the remaining Rydberg atoms. The resulting ion number N_z serves as a reference for the z-magnetization.

After an experimental sequence, all magnetization components are determined using the tomographic readout scheme described in [157]. At the end of the sequence, a Rabi $\pi/2$-pulse with adjustable phase ϕ is applied, where ϕ is varied over the discrete set $\{0, \pi/3, 2\pi/3, \pi, 4\pi/3, 5\pi/3, 2\pi\}$. After this readout pulse, a downpumping pulse is applied, followed by field ionization to measure the population in the state $|\uparrow\rangle$, denoted as $N_\uparrow^\phi$.

The measured $N_\uparrow^\phi(\phi)$ is fitted to the oscillatory function $N_{\text{offset}} + N_a \cos(\phi + \phi_0)$, as shown in Fig. A.5. From this fit, the magnetization components are extracted using the reference measurements N_{tot} and N_{dp}.

The z-component of the magnetization is calculated from N_{offset} as

$$M_z = \frac{2N_{\text{offset}} - N_{\text{tot}} - N_{\text{dp}}}{2(N_{\text{tot}} - N_{\text{dp}})}. \tag{A.2}$$

We verify consistency by confirming $N_{\text{offset}} = N_z$ within the experimental error bars. The x- and y-components are given by

$$M_x = \frac{2N_a - N_{\text{tot}} - N_{\text{dp}}}{2(N_{\text{tot}} - N_{\text{dp}})} \cos(\phi_0), \quad M_y = \frac{2N_a - N_{\text{tot}} - N_{\text{dp}}}{2(N_{\text{tot}} - N_{\text{dp}})} \sin(\phi_0). \tag{A.3}$$

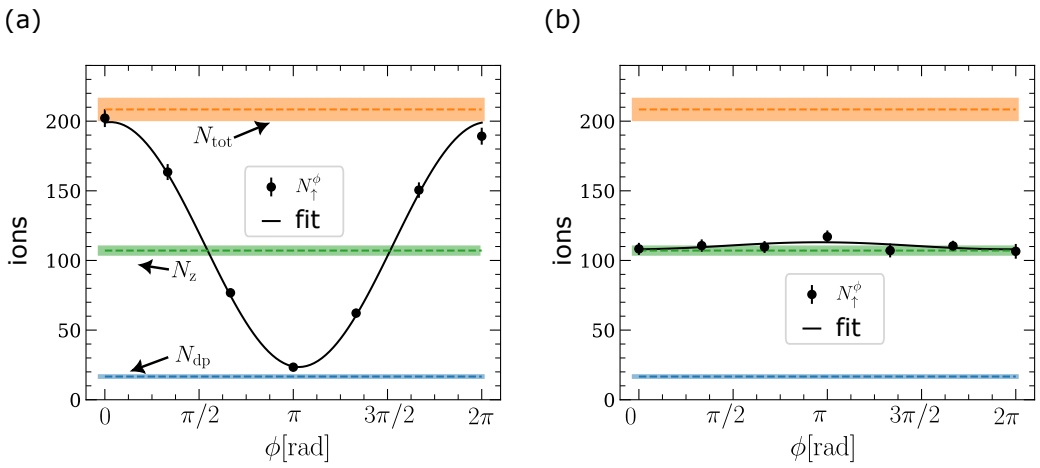

Figure A.5: *Tomographic readout of the magnetization.* Ion numbers are shown for a relaxation experiment as a function of the phase ϕ of the readout pulse. In (a), the system is initialized in the fully spin polarized state, while (b) shows the ion measurement after the magnetization has decayed. The fit line fits a sine function to the experimentally obtained data $N_{\uparrow}^{\phi}$. Different reference measurements are indicated by color horizontal dashed horizontal lines. Their standard deviations is shown as colored vertical bars. Data were taken in the characterization of the experiments in Chap. 3. See details of the protocol and interpretation in the main text. Figure layout inspired by Ref. [157].

Since the individual ion number measurements are randomized within each experimental sequence, the extracted magnetization components are robust against slow environmental drifts. Furthermore, using six phase points reduces statistical uncertainty, enabling more precise magnetization detection.

CHAPTER B

Additional Plots for the Reverse Quench Experiment

This short chapter provides a clearer illustration of the experiment presented in Chap. 4. The study focuses on a reverse quench protocol, in which the spin-lock and reverse-quench magnetizations are measured as functions of the quench time τ_Q. The experiment is conducted in both weakly and strongly disordered regimes. The full experimental protocol is detailed in Chap. 4.

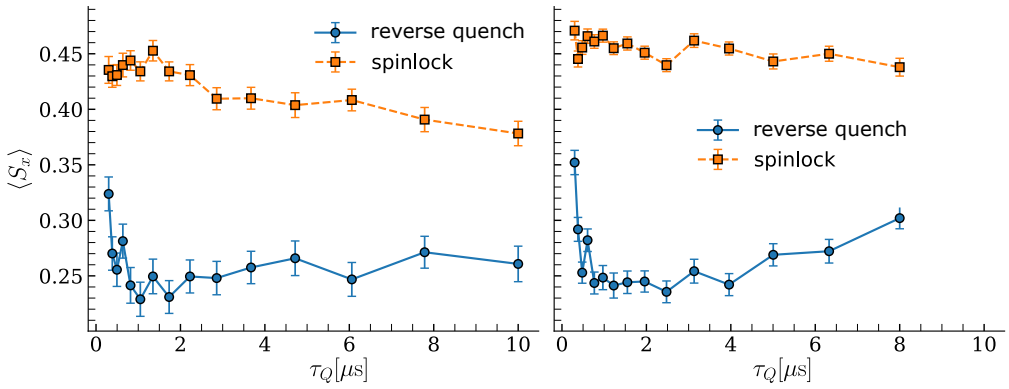

Figure B.1: *Magnetization measurements for the reverse quench protocol.* Magnetization measurements for the reverse quench (blue) and spinlock protocol (orange) for the weakly (left) and strongly (right) disordered regime as a function of quench time τ_Q in µs. Error bars are calculated from averaging over repeated measurements, and taking the standard deviation from the mean.

In the main body of this thesis, data are presented as a function of interaction cycles per quench, represented by the dimensionless parameter $J_{\mathrm{med}}\tau_Q/2\pi$. This normalization facilitates comparison across regimes with different median interaction strengths J_{med}. However, rescaling by J_{med} does not provide information about the total experimental duration, which is important for assessing the system's validity as an isolated quantum system. When the experimental timescale approaches the Rydberg state lifetime, effects induced by black-body radiation must be considered. Figure B.1 shows that the total experimental duration in the strongly disordered regime is significantly shorter than in the weakly disordered regime. Despite this, the reverse quench magnetization increases more markedly at long quench times in the strongly disordered regime. Therefore, this increase cannot be attributed solely to dynamics induced by black-body radiation decay.

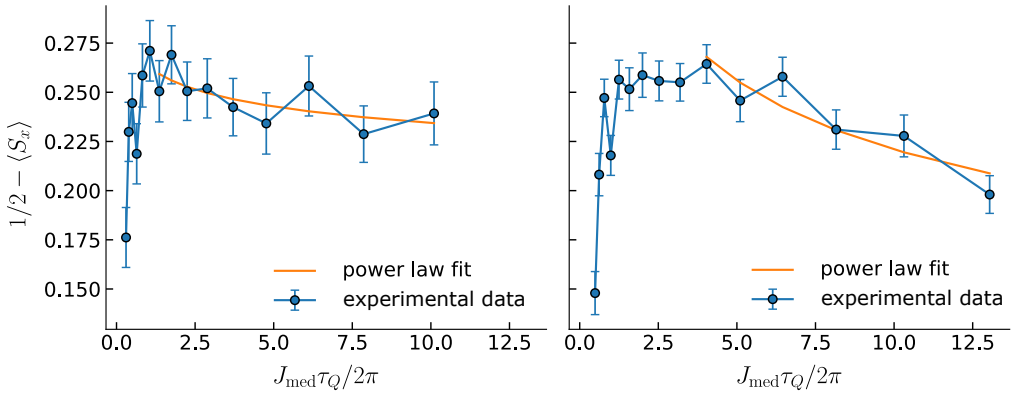

Figure B.2: *Power law fit to the estimated defect density.* Measured magnetization is converted via Eq. 4.53 into an estimated defect density (blue). Error bars are propagated from the magnetization measurement. In the weakly disordered regime (left), the last 9 points are fitted a power law (orange). In the strongly disordered regime (right), only the last 6 points are used to fit a power law. The plot is presented as a linear-linear plot, in order to highlight the nonlinearity of the fit-function, and directly present the experimental data as they were taken.

To illustrate the accuracy of the power law description of defect densities derived from magnetization measurements, we present the data on linear axes in Fig. B.2. Although the power law decay fits well within the measured range, a linear decay cannot be excluded.

CHAPTER C

Additional Plots for the Loschmidt Echo

As discussed in Chap. 5, the aim of this section is to serve as a supplemental comment on the short time-behavior in a bond-disordered power law interacting spin-1/2 model. The first section concentrates on early initial times where time-dependent perturbation theory may still be applied.

C.1 Power law behavior for short times

Here, we will shortly compare very early timescales of the Loschmidt echo as a function of time. As outlined in [253], the Loschmidt echo is expected to deviate quadratically from its initial value, i.e.

$$\overline{|S(t)|^2} \approx 1 - ct^2, \tag{C.1}$$

where c is a constant depending on the Hamiltonian and the perturbation during the time reversal in the Loschmidt echo protocol. Therefore, we expect that $1 - \overline{|S(t)|^2}$ increases according to a power law in time, with exponent 2. As for early times, there is no significant dependence of the Loschmidt echo on system size, we will fit a power law to $1 - \overline{|S(t)|^2}$ for $J_{\text{med}}t/(2\pi) \leq 1e-2$, i.e. for time-scales where the median spin-spin coupling J_{med} does not induce a full interaction cycle.

The results are shown in Fig. C.1. We fit the data with the function At^γ, where A is the amplitude and γ the exponent. In the thermalizing regime at weak disorder $W = 0.03$, we obtain $\gamma = 3.992(2)$, which is very close to 4. This suggests that, in the fully ordered case at $W = 0$, a symmetry of the power-law Hamiltonian may

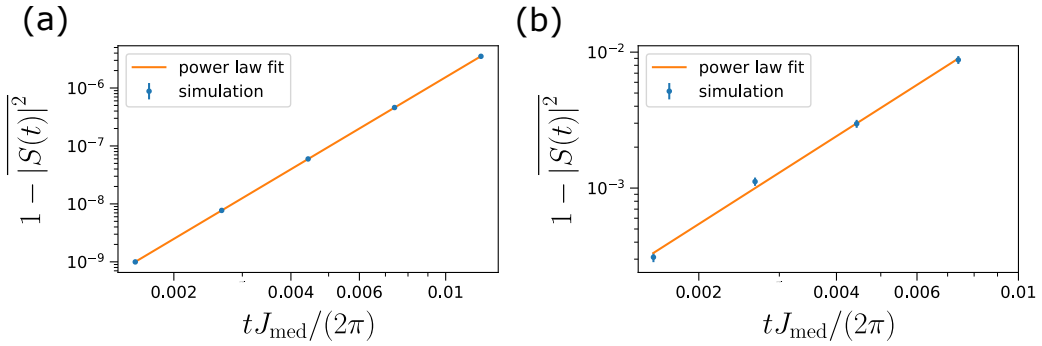

Figure C.1: *Short-time behavior of the Loschmidt echo.* Simulated values of $1-\overline{|S(t)|^2}$ (blue dots) are shown against the evolution time in terms of median interaction cycles on a log-log scale. Error bars are calculated from the standard deviation of the mean for a disorder average. Values are shown both for a thermalizing (a) and localized (b) regime. The data is fitted a power law (orange line).

force the quadratic prefactor c in Eq. C.1 to vanish. Since the Loschmidt echo has a local maximum at $t = 0$, the leading-order term must then be at least quartic. The extracted exponent $\gamma \approx 4$ indicates that this quartic term dominates the short-time dynamics. The fit yields a reduced $\chi^2 = 0.18$, demonstrating very good agreement with the data.

In contrast to the quartic behavior observed in the thermalizing regime with weak disorder, we find a nearly quadratic decay of the Loschmidt echo in the strongly localized regime with $W = 2.0$. A power law fit yields $\gamma = 2.14(7)$, which is consistent with the predicted value of 2 within a two-sigma confidence interval. However, the fit gives a reduced $\chi^2 = 1.62$, which we attribute to the fact that, in the strongly disordered regime, several spin-spin interaction couplings exceed J_{med}, leading to the emergence of few-body dynamics that disturb the t^2 behavior.

C.2 Exponential decay in the weakly disordered model

In Chapter 5, the long-time behavior is discussed in detail. Here, we focus on the intermediate time scales within the thermalizing regime. It is generally assumed that, in this regime, the Loschmidt echo reaches equilibrium exponentially fast [150]. As demonstrated in Chapter 5, the system eventually reaches an equilibrium plateau that remains constant over all numerically accessible time scales. Therefore, we use

the value of the Loschmidt echo at $tJ_{\mathrm{med}}/(2\pi) \approx 1.23 \times 10^6$, which lies within the plateau, as an estimate of the equilibrium value, i.e.,

$$\overline{|S_{\mathrm{eq}}|^2} \coloneqq \overline{|S(t = 1.23 \times 10^6)|^2}. \tag{C.2}$$

In Chapter 5, we observe that shortly before the plateau is reached, the Loschmidt echo drops below its equilibrium value. Consequently, we expect the Loschmidt echo to decay to this equilibrium value only prior to the drop. To illustrate this, we present the deviation of the Loschmidt echo for times where this deviation is positive in Fig. C.2. Furthermore, we restrict our analysis to times where $tJ_{\mathrm{med}}/(2\pi) > 1$ to focus on the many-body dynamics.

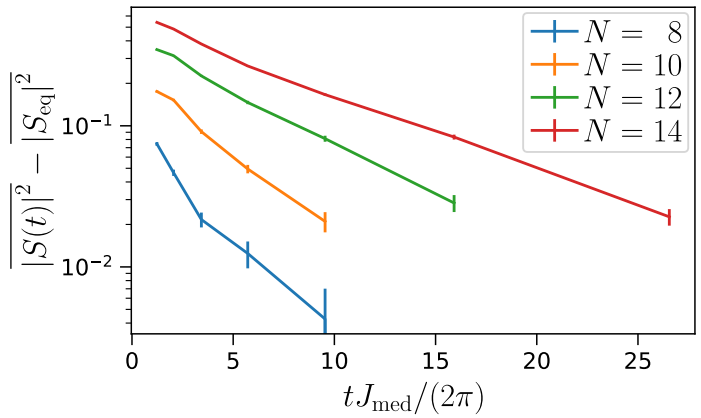

Figure C.2: *Exponential decay of the Loschmidt echo.* Deviation of the Loschmidt echo from its equilibrium value is shown as a function of evolution time for four different system sizes N. Error bars are propagated from the values of the Loschmidt echo and its equilibrium value. The ordinate axis is logarithmically scaled.

As the ordinate axis is logarithmically scaled, a linear behavior of the Loschmidt echo indicates an exponential decay. A linear trend is observed for all simulated particle numbers. Furthermore, with increasing particle number, the decay increasingly resembles an exponential, and the fit improves over longer time scales. This suggests that, in the thermodynamic limit, the decay might be exponential, further confirming the weakly disordered regime as thermalizing.

CHAPTER D

Perturbative Rydberg Calculations in Arbitrary Field Configurations

In the main part of this thesis, we consider a frozen Rydberg gas, where atoms are sufficiently separated such that their thermal deBroglie wavelength is much smaller than the interatomic distance. Under these conditions, atoms are distinguishable by their spatial position.

For the parameters relevant to this work, the temperature of the cloud of Rubidium atoms is 11 µK, corresponding to a thermal deBroglie wavelength of 56 nm. This is significantly smaller than the typical blockade radius of 8 µm. A similar regime occurs in Rydberg tweezer arrays [303–305]. Here, individual atoms can be cooled down to 3 µK via Raman sideband techniques [306], such that they have a deBroglie wavelength of 109 nm, which is still much smaller than the typical tweezer spacing of 2.5 µm.

This spatial separation offers two key advantages:

1. Distinguishability of atoms: Since the atoms are well separated, the total wavefunction need not be fully anti-symmetrized as in a molecule.

2. Non-overlapping charge distributions: A very large separation compared to the atomic radii of each atom ensures that Rydberg atoms behave as spatially distinct charge distributions. This allows the Rydberg-Rydberg interaction to be expanded in a multipole series, enabling truncation of the full Hilbert space to a few relevant states driving the dynamics.

In many experimental settings involving pairs of atoms, only a finite number of states are significantly populated. These states define a reduced model space. Choosing this model space carefully is essential: states within it must couple only

weakly and off-resonantly to states outside, referred to as the outer space, ensuring that population remains confined to the model space.

A central goal is to determine an effective Hamiltonian H_{eff} that accurately captures the dynamics within this space. A naive approach would be a simple projection of the Hamiltonian on to the model space. This typically fails, as it neglects off-resonant couplings that can shift energy levels and modify effective interactions within the model space. A notable example in Rydberg physics is the Förster resonance [307], where two near-resonant pair states become strongly coupled through virtual transitions to a far-detuned intermediate state.

To account for couplings between the model space and the full Hilbert space, we use a perturbative method based on the Bloch expansion. This approach offers a simpler structure and lower computational cost compared to the more general Schrieffer-Wolff transformation [308]. While the Schrieffer-Wolff transformation generally produces an effective Hermitian Hamiltonian, the Bloch expansion, derived from Rayleigh-Schrödinger perturbation theory, typically yields a non-Hermitian effective Hamiltonian [309]. To obtain a Hermitian effective Hamiltonian H_{eff}, we decompose the Bloch operator into its Hermitian and anti-Hermitian parts and retain only the Hermitian component $H_{\text{eff}} = \frac{H_{\text{RS}}+H_{\text{RS}}^{\dagger}}{2}$. Up to third order in perturbation theory, this procedure preserves the eigenvalues and eigenvectors of the original Bloch operator [310].

The algorithm presented in this appendix was developed by the author and has since been implemented as part of a dedicated software package, *PairInteraction* [167], which is maintained by Sebastian Weber and Johannes Mögerle. During the development phase, an early version of the algorithm was made available to Matthias Lotze, who applied it to selected examples as part of his bachelor thesis [249], which was supervised by the author. The bachelor thesis includes an application and a partial description of the algorithm based on this early code version. This appendix provides a complete and updated description of the algorithm, incorporating refinements and implementation improvements made since its original conception. After describing the algorithm, we show how it can be used in two prototypical experimental examples, namely in strong magnetic fields and in strong electric fields.

D.1 Modeling Alkali Rydberg atoms

For clarity, we restrict our discussion in this chapter to alkali atoms. However, the perturbative treatment of Rydberg–Rydberg interactions—central to this chapter—is equally applicable to alkaline-earth atoms. The only requirement for the construction

of the interaction matrix is the ability to efficiently evaluate electric multipole and magnetic dipole operators.

The numerical construction of the Hamiltonian for a single Rydberg atom follows the procedure outlined in [167], which we adopt here. The underlying theoretical framework is well established and can be found in standard references such as [27].

In alkali Rydberg atoms, the outermost electron is excited to a high-lying state, where its wavefunction overlaps only weakly with the nuclear region. As a result, the atom is effectively hydrogen-like: the core electrons shield the nuclear charge, and the outer electron behaves similarly to the single electron in hydrogen. The effective potential is spherical, allowing separation of the wavefunction into radial and angular parts. The angular part is described by spin spherical harmonics, which can be calculated analytically. The radial part is treated as hydrogenic at large distances and modeled using a core potential at short distances, where the finite extent of the nuclear charge distribution becomes relevant.

Consequently, the eigenstates can be labeled using the same quantum numbers as in hydrogen. The energy levels are given by

$$E_{nLJ} = -\frac{\mathrm{Ry}^*}{(n - \delta_{nLJ})^2}, \tag{D.1}$$

where Ry^* denotes the modified Rydberg constant, corrected for the finite nuclear mass, and δ_{nLJ} is the quantum defect. The quantum defect primarily depends on the orbital angular momentum L and accounts for deviations from the hydrogenic spectrum due to the finite size and structure of the nucleus. Since the nuclear potential is difficult to calculate from first principles, quantum defects are determined from spectroscopic measurements [311–314]. These values can then be used to infer the radial Rydberg wavefunction, either via Coulomb wavefunctions [27] or a model potential [315–317]. In both approaches, the Coulomb wavefunction or model potential is optimized to reproduce the observed energy levels corresponding to the measured quantum defects. Once the radial and angular parts of the eigenstates are known, calculations of operator matrix elements and interactions between atoms and external fields become possible.

The interaction with a static, homogeneous electric field $\vec{E}$, discussed in more detail in Chapter E, is described by

$$H_{\mathrm{el}} = -\vec{d} \cdot \vec{E}, \tag{D.2}$$

where $\vec{d} = e\vec{r}$ is the electric dipole operator of the Rydberg electron in position space. Electric field interactions are typically strong in Rydberg atoms due to

their large polarizability. For instance, even a weak field of $20\,\mathrm{mV\,cm^{-1}}$ induces a coupling of 32 MHz (in units where $h = 1$) between the states $\left|61S_{1/2}, m_J = 1/2\right\rangle$ and $\left|61P_{1/2}, m_J = 1/2\right\rangle$.

The interaction of a Rydberg atom with a static, homogeneous magnetic field $\vec{B}$ is given by

$$H_{\mathrm{mag}} = \mu_B \left(g_S \vec{S} + g_L \vec{L}\right) \cdot \vec{B} + \frac{1}{8m_e} \left(\vec{d} \times \vec{B}\right)^2, \tag{D.3}$$

where $g_S = 2$ is the Landé g-factor for the electron spin, and $g_L \approx 1$ is the g-factor for the orbital angular momentum. The exact value of g_L is given by $g_L = 1/(1+m_e/m_n)$, but the correction due to the finite nuclear mass is typically negligible.

The first, linear term describes the Zeeman interaction, coupling the magnetic field to the spin and orbital angular momentum of the Rydberg electron. The second, quadratic term describes the diamagnetic interaction, which couples to the electric dipole operator $\vec{d}$. This contribution becomes relevant at large magnetic fields or when electric and magnetic fields are both present. For a typical weak field of 30 G, the diamagnetic shift is negligible, while the Zeeman term induces an energy shift of 42 MHz.

For comparison, the fine-structure splitting between the $\left|61P_{1/2}\right\rangle$ and $\left|61P_{3/2}\right\rangle$ states is 437 MHz. This indicates that, in the presence of weak fields, the dominant energy scale arises from the interaction between the Rydberg electron and the ionic core, with external electric and magnetic fields treated perturbatively. However, in the experiments considered in the main body of this thesis, this assumption does not hold: the interaction with an external magnetic field can be comparable to the fine-structure splitting, inducing strong mixing between the unperturbed atomic eigenstates. Consequently, the relevant excited states are not the unperturbed eigenstates, but the eigenstates of the full single-atom Hamiltonian including the external fields. To account for this, we first diagonalize the single-atom Rydberg Hamiltonian in the presence of electric and magnetic fields. This choice of basis forms the starting point for the perturbative treatment of the Rydberg–Rydberg interaction. It also allows the method to remain valid even in regimes where external fields induce energy shifts comparable to, or larger than, the fine-structure splitting.

The bare atomic Hamiltonians, diagonalized in the presence of static electric and magnetic fields, which may differ for each atom, can be represented by the diagonal operators H_1 and H_2. The total Hamiltonian for two non-interacting Rydberg atoms is then given by

$$H_0 = H_1 \otimes \mathbb{1} + \mathbb{1} \otimes H_2, \tag{D.4}$$

where the system basis is the product basis of the individual atomic states. This

Hamiltonian H_0 serves as the unperturbed starting point for the perturbative treatment.

D.2 Perturbative treatment of the atom-atom interaction

As discussed above, when the separation between two Rydberg atoms is sufficiently large, they can be treated as non-overlapping charge distributions. This separation is quantified by the Leroy radius,

$$r_{\text{Leroy}} = 2\left(\sqrt{\langle r_1^2\rangle} + \sqrt{\langle r_2^2\rangle}\right), \tag{D.5}$$

where r_1 and r_2 denote the distances of the Rydberg electrons from their respective atomic centers, and the expectation values are taken with respect to the populated Rydberg states. For states with principal quantum numbers below 100, the Leroy radius is typically less than 4 µm, justifying the approximation of treating the atoms as non-overlapping charge distributions.The Rydberg–Rydberg interaction can be expressed as a multipole expansion in terms of the vector $\vec{R}$ separating the two atoms,

$$H_{\text{int}}(\vec{R}) = \sum_{\kappa_1,\kappa_2=1}^{\infty} \frac{V_{\kappa_1\kappa_2}}{4\pi\epsilon_0 \left|\vec{R}\right|^{1+\kappa_1+\kappa_2}}, \tag{D.6}$$

where the z-axis is chosen as the quantization axis. The matrix elements $V_{\kappa_1\kappa_2}$ are proportional to the multipole moments of order κ_1 and κ_2 in atoms 1 and 2, respectively. The parameter $\rho = 1 + \kappa_1 + \kappa_2$ determines the interaction's multipole order and spatial decay.

At $\rho = 3$, the interaction corresponds to dipole–dipole coupling. Dipole–quadrupole interactions ($\rho = 4$) can typically be neglected for low-angular-momentum states, except at very short interatomic distances below the blockade radius, a regime discussed in Chapter E. Higher-order multipole interactions, including dipole–quadrupole terms, also become significant in the context of Rydberg macrodimers [318, 319]. The constructed Rydberg–Rydberg interaction Hamiltonian $H_{\text{int}}(\vec{R})$, evaluated at a fixed interatomic separation $\vec{R}$, will serve as the perturbation V in our perturbative treatment. Consequently, the effective Hamiltonian we will construct provides information on how the instantaneous eigenstates, defined in the presence of finite external fields, interact through the Rydberg–Rydberg interaction.

D.2.1 The Bloch expansion

The Bloch expansion, grounded in Rayleigh-Schrödinger perturbation theory, was originally developed as an extension of perturbation theory to the Hamiltonian operator [309, 310]. A comprehensive derivation, including higher-order terms and various diagrammatic techniques, is presented in [320]. In this work, we primarily follow the pedagogical approach outlined in [321].

We assume that the full Hilbert space $\mathcal{H}$ can be partitioned into a model space $\mathcal{M}$ and an outer space $\mathcal{O}$, which contains all states not included in $\mathcal{M}$. The total Hamiltonian is written as $H = H_0 + V$, where H_0 is diagonal and V introduces couplings between $\mathcal{M}$ and $\mathcal{O}$. Let P denote the projection operator onto the model space, and $Q = \mathbb{1} - P$ the projection onto the outer space.

Our goal is to construct an effective Hamiltonian H_{eff} that acts entirely within the model space, such that for any eigenstate $|\Psi\rangle \in \mathcal{H}$ with eigenvalue E, the Schrödinger equation takes the form:

$$H_{\text{eff}} P |\Psi\rangle = E P |\Psi\rangle . \tag{D.7}$$

Since H_0 is diagonal by construction, it commutes with both projectors, i.e., $[H_0, P] = [H_0, Q] = 0$

A crucial step in the construction of the effective Hamiltonian is the introduction of the wave operator Ω, which is defined by the relation

$$\Omega P |\Psi\rangle = |\Psi\rangle , \tag{D.8}$$

where $|\Psi\rangle$ is an eigenstate of the full Hamiltonian H. While such a relation would not uniquely define Ω for arbitrary vectors, the requirement that $|\Psi\rangle$ is an eigenstate of H imposes sufficient constraints to define Ω uniquely. Moreover, this operator allows us to write down the effective Hamiltonian immediately as

$$H_{\text{eff}} = PH\Omega P, \tag{D.9}$$

which naturally fulfills Eq. D.7. The problem to define an effective Hamiltonian has thus become equivalent to the problem of finding an expression for Ω. We plug Eq. D.8 into the Schrödinger equation $H |\Psi\rangle = E |\Psi\rangle$ to obtain

$$(E - H_0) |\Psi\rangle = E |\Psi\rangle - H_0 \Omega P |\Psi\rangle = V \Omega P |\Psi\rangle . \tag{D.10}$$

Multiplying ΩP from the left we obtain

$$\begin{aligned} \Omega P (E - H_0) P |\Psi\rangle = E \Omega P |\Psi\rangle - \Omega P H_0 P |\Psi\rangle = E |\Psi\rangle - \Omega H_0 P^2 |\Psi\rangle \\ = E |\Psi\rangle - \Omega H_0 P |\Psi\rangle = \Omega P V \Omega P |\Psi\rangle . \end{aligned} \tag{D.11}$$

Subtracting Eq. D.11 from D.10 leads to the identity

$$[\Omega, H_0]P\,|\Psi\rangle = (\mathbb{1} - \Omega P)\,V\Omega P\,|\Psi\rangle\,. \tag{D.12}$$

This is a self-consistent equation for the wave operator Ω, depending only on the unperturbed Hamiltonian H_0 and the perturbation V.

To develop a perturbation theory in powers of V, we expand Ω as a power series,

$$\Omega = \sum_{k=0}^{\infty} \Omega_k, \tag{D.13}$$

where each term Ω_k is of order V^k. We choose $\Omega_0 = \mathbb{1}$, since the identity operator commutes with H_0, and the right-hand side of Eq. D.12 contains at least one factor of V, implying that Ω_0 captures the unperturbed limit.

Expanding Eq. D.9 we thus obtain

$$H_{\text{eff}} = P(H_0 + V)\Omega P = \underbrace{PH_0P}_{H_{\text{eff}}^{(0)}} + \underbrace{PVP}_{H_{\text{eff}}^{(1)}} + \underbrace{PV\Omega_1P}_{H_{\text{eff}}^{(2)}} + \underbrace{PV\Omega_2P}_{H_{\text{eff}}^{(3)}} + \ldots, \tag{D.14}$$

where H_{eff}^{i} denotes the i-th order in perturbation of the effective Hamiltonian. H_0 and H_1 are the projections of H onto the model space. Corrections due to couplings between $\mathcal{M}$ and $\mathcal{O}$ start from second order processes quadratic in V. These are exactly the processes leading to van-der-waals interactions in Rydberg atoms, where V is the dipole-dipole coupling. Expanding Eq. D.12 returns the recursive formula

$$[\Omega_n, H_0] = QV\Omega_{n-1} - \sum_{j=1}^{n-1} \Omega_j PV\Omega_{n-j-1}. \tag{D.15}$$

This allows calculate the matrix elements for two states $|a\rangle, |b\rangle \in \mathcal{M}$. We thus obtain

$$\langle a|H_{\text{eff}}^{(2)}|b\rangle = \langle a|\,V\frac{1}{E_b - H_0}QV\,|b\rangle\,. \tag{D.16}$$

Introducing an identiy matrix $\mathbb{1} = \sum_{|s\rangle\in\mathcal{H}} |s\rangle\langle s|$ yields

$$\langle a|H_{\text{eff}}^{(2)}|b\rangle = \sum_{|s\rangle\in\mathcal{O}} \langle a|V|s\rangle \frac{1}{E_b - E_s}\langle s|\,V\,|b\rangle\,. \tag{D.17}$$

The third order in perturbation theory reads

$$\begin{aligned}\langle a|H_{\text{eff}}^{(3)}|b\rangle &= \langle a|\,V\frac{1}{E_b - H_0}QV\frac{1}{E_b - H_0}QV\,|b\rangle \\ &- \sum_{|c\rangle\in\mathcal{M}} \langle a|\,V\frac{1}{E_b - H_0}\frac{1}{E_c - H_0}QV\,|c\rangle\langle c|\,V\,|b\rangle\,.\end{aligned} \tag{D.18}$$

This equation can also be brought into a more compact form by summing over states in the outer space

$$\begin{aligned}\langle a|H_{\text{eff}}^{(3)}|b\rangle = &\sum_{|r\rangle\in\mathcal{O},|s\rangle\in\mathcal{O}} \langle a|V|s\rangle \frac{\langle s|V|r\rangle}{E_b - E_s}\frac{\langle r|V|b\rangle}{E_b - E_r} \\ &- \sum_{|c\rangle\in\mathcal{M},|s\rangle\in\mathcal{O}} \frac{\langle a|V|s\rangle}{E_b - E_s}\frac{\langle s|V|c\rangle}{E_c - E_s}\langle c|V|b\rangle\,.\end{aligned} \tag{D.19}$$

D.2.2 Perturbed Eigenvectors

The effective Hamiltonians H_{eff}^i reproduce the eigenvalues within the model space incorporating corrections up to order V^i. When symmetrized to ensure Hermiticity, $H_{\text{eff}}^i = \left(H_{\text{eff}}^i + H_{\text{eff}}^{i\,\dagger}\right)/2$, they retain the same eigenstates and eigenvectors up to order $i = 3$ [310]. However, the Bloch expansion does not assess how accurately the system dynamics remains confined to the model space. It provides no criterion for the quality of this approximation, and contributions from states outside the model space may still play a significant role in the full dynamics.

As a quality check, we also construct the eigenstates in the model space using standard Rayleigh-Schrödinger perturbation theory, as detailed in classical references [322, 323]. The summations are defined such that each term sums only over the states involved in that specific term. The perturbed eigenstate $|m\rangle \in \mathcal{M}$ is given by

$$\begin{aligned}|m\rangle &= \left|m^0\right\rangle + \left|m^1\right\rangle + \left|m^2\right\rangle + \ldots\,, \\ H_0\left|m^0\right\rangle &= E_m\left|m^0\right\rangle\,, \\ \left|m^1\right\rangle &= \sum_{|m\rangle\neq|r\rangle\in\mathcal{H}} \frac{\langle r|V|m\rangle}{E_m - E_r}|r\rangle\,, \\ \left|m^2\right\rangle &= \sum_{|m\rangle\neq|r\rangle,|s\rangle\in\mathcal{H}} \left(\frac{\langle r|V|s\rangle}{E_m - E_r}\frac{\langle s|V|m\rangle}{E_m - E_s} - \frac{\langle m|V|m\rangle\ \langle r|V|m\rangle}{\left(E_m - E_r\right)^2}\right)|r\rangle \\ &\quad - \frac{1}{2}\left(\frac{\langle m|V|r\rangle\ \langle r|V|m\rangle}{\left(E_r - E_m\right)^2}\right)|m\rangle\,.\end{aligned} \tag{D.20}$$

We simplify these expressions by first noting that, by construction, $\langle m|V|m\rangle = 0$. Moreover, since the effective Hamiltonian theory accounts for all couplings within the model space, we retain only those terms involving at least one coupling to a state in the outer space. Consequently, the perturbed eigenstates arising from interactions with states in $\mathcal{O}$ are given by

$$\left|m^1\right\rangle = \sum_{|r\rangle\in\mathcal{O}} \frac{\langle r|V|m\rangle}{E_m - E_r} |r\rangle \,. \tag{D.21}$$

At the next order, the perturbed eigenstate $|m^2\rangle$ decomposes as $|m^2\rangle = |m^2_{\mathcal{M}}\rangle + |m^2_{\mathcal{O}}\rangle$. Here, $|m^2_{\mathcal{M}}\rangle$ represents corrections to the amplitudes within the model space, while $|m^2_{\mathcal{O}}\rangle$ corresponds to contributions in the outer space. Those contributions are given as

$$\begin{aligned}
\left|m^2_{\mathcal{M}}\right\rangle &= \sum_{|m\rangle\neq|n\rangle\in\mathcal{M},|r\rangle\in\mathcal{O}} \left(\frac{\langle n|V|r\rangle}{E_m - E_n}\frac{\langle r|V|m\rangle}{E_m - E_r}\right)|n\rangle - \frac{1}{2}\left(\frac{\langle m|V|r\rangle\ \langle r|V|m\rangle}{(E_r - E_m)^2}\right)|m\rangle \,, \\
\left|m^2_{\mathcal{O}}\right\rangle &= \sum_{|m\rangle\neq|n\rangle\in\mathcal{M},|r\rangle\in\mathcal{O}} \left(\frac{\langle r|V|n\rangle}{E_m - E_r}\frac{\langle n|V|m\rangle}{E_m - E_n}\right)|r\rangle + \sum_{|r\rangle,|s\rangle\in\mathcal{O}} \left(\frac{\langle r|V|s\rangle}{E_m - E_r}\frac{\langle s|V|m\rangle}{E_m - E_s}\right)|r\rangle \,.
\end{aligned} \tag{D.22}$$

To evaluate the validity of the assumption that the dynamics remain confined to the model space, we compute the perturbed eigenstate at order i as $|m\rangle = \sum_{j=0}^{i-1} |m^j\rangle$. If this state overlaps with $|m^0\rangle$ by less than 90 %, we identify and report all outer space states with populations exceeding 0.5 %, as these may become significantly populated through the dynamics induced by V, and thus should be included in the model space.

D.2.3 Numerical implementation

We numerically implement the construction of the effective Hamiltonian by allowing the following inputs:

- A Hamiltonian $H = H_0 + V$ as a sparse matrix, where H_0 is assumed to be the diagonal of the Hamiltonian, and V is assumed to be purely off-diagonal.
- A list m_inds of the indexes spanning up the model space
- The order of perturbation theory, which may be chosen between 0 and 3.

In a first step, we resort the basis states of the Hamiltonian, such that the first $d = \dim(\mathcal{M})$ states are exactly the states defined by the list m_inds. As we will see later, this allows for an efficient matrix product formulation of the perturbation theory.

We extract the following quantities:

- H_0 as the diagonal of H, which is a one-dimensional array, and $V = H - H_0$, which is a $N \times N$ matrix, , where $N = \dim(H)$.

- The projections of H_0 onto the model and outer spaces: $H_m = H_0[1:d]$ and $H_e = H_0[d+1:N]$.

- The components of V coupling states within the model space $V_{mm} = V[1:d, 1:d]$, within the outer space $V_{ee} = V[d+1:N, d+1:N]$, and between model and outer spaces $V_{me} = V[1:d, d+1:N]$. Consequently, V has the block structure

$$V = \begin{pmatrix} V_{mm} & V_{me} \\ V_{me}^{\dagger} & V_{ee} \end{pmatrix}, \tag{D.23}$$

  where the hermiticity of V is used.

- An empty sparse array of size $d \times N$ is initialized to store the perturbed eigenvectors.

At second order, energy differences between model space and outer space states must be considered. We construct the matrix $\Delta E_{em} = 1/(H_m[\texttt{new axis}, :] - H_e[\texttt{new axis}, :])$. If any entry in ΔE_{em} is infinite, a warning is raised indicating the presence of a resonance. To identify the resonance location, the normalized eigenstate is computed, where the infinite value occurs at the index of the resonant state.

At third order, constructing perturbed eigenvectors requires accounting for energy differences within the model space. We define the matrix ΔE_{mm} by $(\Delta E_{mm})_{ij} = 1/\left((H_m)_i - (H_m)_j\right)$, where i and j denote the row and column indices, respectively. To construct this matrix efficiently, we employ the `numpy.newaxis` method, which replicates rows and columns as needed before applying matrix operations. This yields the compact expression $\Delta E_{mm} = 1/\left(H_m[\text{np.newaxis}, :] - H_m[:, \text{np.newaxis}]\right)$. Elements that diverge to infinity are replaced by zero. Consequently, terms of the form $\langle n|V|m\rangle / (E_m - E_n)$ vanish when $E_n = E_m$. This is consistent with degenerate perturbation theory, where the states $|m\rangle$ and $|n\rangle$ are replaced by linear combinations $|m'\rangle$ and $|n'\rangle$ such that $\langle n'|V|m'\rangle = 0$. After this transformation, $V_{nm} = 0$, and these terms no longer contribute to the expansion of the perturbed eigenvectors. However, this does not guarantee that the new states $|m'\rangle$ and $|n'\rangle$ maintain the same couplings to other model-space or outer-space states, which may affect the perturbed eigenstates. Therefore, a warning is currently issued: the third-order eigenstates are accurate under this method only if the model space contains a single state. In future versions, an algorithm will be needed to construct $|m'\rangle$ and $|n'\rangle$ efficiently, calculate the eigenstates, and then transform back to the original $|m\rangle$ and $|n\rangle$ basis.

Using these matrices, both the effective Hamiltonian at all perturbation orders and the perturbed eigenvectors can be constructed via matrix multiplication or element-wise multiplication. For instance,

$$H_{\text{eff}}^{(0)} = H_m, \quad H_{\text{eff}}^{(1)} = V_{mm}, \quad H_{\text{eff}}^{(2)} = V_{me}\left(V_{me}^{\dagger} \odot \Delta E_{em}\right). \tag{D.24}$$

Similarly, $H_{\text{eff}}^{(3)}$ and the perturbed eigenvectors can be expressed as matrix products in an analogous way. To optimize performance, all matrices are stored in compressed sparse row format, allowing efficient transformation to compressed sparse column format for matrix multiplications.

At each perturbative order, the effective eigenvectors are summed directly, while the effective Hamiltonians at each order are stored separately. This separation is essential for extracting dispersion coefficients, as discussed in the next section. We will demonstrate experimentally relevant examples where this algorithm is applied to obtain key insights into Rydberg interactions under strong magnetic and electric fields.

D.3 Example 1: Rydberg excitation in strong magnetic fields

In this first example, which is partially based on the supplemental material of [169] and from which parts of the text have been taken verbatim, we consider strong magnetic fields, relevant for the experiments discussed in Chapters 3 and 4. We truncate the multipole interaction from Eq. D.6 at $1 + \kappa_1 + \kappa_2 = 3$, resulting in the dipole-dipole Hamiltonian

$$\begin{aligned} H_{\text{DDI}} = \frac{1}{4\pi\epsilon_0}\Bigg[& \frac{1-3\cos^2\theta}{2r^3}\left(2d_1^0 d_2^0 + d_1^+ d_2^- + d_1^- d_2^+\right) \\ & -\frac{3\sin\theta\cos\theta}{\sqrt{2}r^3}\left((d_1^+ d_2^0 + d_1^0 d_2^+)e^{-i\phi} - (d_1^0 d_2^- + d_1^- d_2^0)e^{i\phi}\right) \\ & -\frac{3\sin^2\theta}{2r^3}\left(d_1^+ d_2^+ e^{-2i\phi} + d_1^- d_2^- e^{2i\phi}\right)\Bigg]. \end{aligned} \tag{D.25}$$

Here, θ denotes the angle between the interatomic axis and the quantization axis, which is chosen along a magnetic field of $B = 185\,\text{G}$. The azimuthal angle ϕ describes the orientation of the interatomic axis around this quantization axis, and r is the

interatomic distance. The quantities $d_i^{0,\pm}$ represent the spherical components of the dipole moment of atom i.

In the absence of a magnetic field, we select the model space as either:

- The resonant pair states (used in the weakly disordered regime):

$$\left|61S_{1/2}, m_J = 1/2\right\rangle \left|61P_{1/2}, m_J = 1/2\right\rangle, \quad \left|61P_{1/2}, m_J = 1/2\right\rangle \left|61S_{1/2}, m_J = 1/2\right\rangle$$

- Or the resonant pair states (used in the strongly disordered regime):

$$\left|61S_{1/2}, m_J = 1/2\right\rangle \left|61P_{3/2}, m_J = 1/2\right\rangle, \quad \left|61P_{3/2}, m_J = 1/2\right\rangle \left|61S_{1/2}, m_J = 1/2\right\rangle$$

However, the large magnetic field leads to a strong admixing between the states $\left|61P_{1/2}, m_J = 1/2\right\rangle$ and $\left|61P_{3/2}, m_J = 1/2\right\rangle$, such that the above mentioned pairstates need to be replaced by the adiabatically connected eigenstates at large magnetic field. We thus want to study the influence of this admixture on the dispersion coefficients, which can be obtained by first and second-order perturbation theory. For an atom in the $|nS\rangle$ and an atom in the $|nP\rangle$ states, the two-atom states $|nS, nP\rangle$ and $|nP, nS\rangle$ are degenerate. If we set the energy level of these two states to zero by gauge freedom, the Hamiltonian in this basis reads

$$\hat{H} = \frac{1 - 3\cos(\theta)^2}{r^3} \frac{1}{4\pi\epsilon_0} \frac{2\hat{d}_1^0\hat{d}_2^0 + \hat{d}_1^+\hat{d}_2^- + \hat{d}_1^-\hat{d}_2^+}{2} \tag{D.26}$$

$$= \frac{1 - 3\cos(\theta)^2}{r^3} \underbrace{\frac{1}{4\pi\epsilon_0} \frac{\left\langle 2\hat{d}_1^0\hat{d}_2^0 + \hat{d}_1^+\hat{d}_2^- + \hat{d}_1^-\hat{d}_2^+ \right\rangle}{2}}_{C_3} \begin{pmatrix} 0 & 1 \\ 1 & 0 \end{pmatrix} \tag{D.27}$$

$$= \frac{1 - 3\cos(\theta)^2}{r^3} C_3 \begin{pmatrix} 0 & 1 \\ 1 & 0 \end{pmatrix}, \tag{D.28}$$

where the angle brackets denote the matrix element evaluated between the states $|nS, nP\rangle$ and $|nP, nS\rangle$. This defines the dispersion coefficient C_3. It is obtained from the first-order contribution to the effective Hamiltonian, $H_{\text{eff}}^{(1)}$, where the perturbation corresponds to the dipole-dipole interaction at a distance r and polar angle θ. The coefficient C_3 is then extracted by multiplying the off-diagonal matrix element by the factor $r^3/\left(1 - 3\cos^2(\theta)\right)$.

At strong magnetic fields, the atomic eigenstates in the P-manifold become superpositions of the states $\left|61P_{1/2}, m_J = 1/2\right\rangle$ and $\left|61P_{3/2}, m_J = 1/2\right\rangle$. As a result, the coefficient C_3 becomes magnetic-field dependent. This is because the electric dipole

matrix elements between the bare states $\left|61S_{1/2}, m_J = 1/2\right\rangle$ and $\left|61P_{1/2}, m_J = 1/2\right\rangle$ differ from those between the corresponding eigenstates in the presence of the field.

For a magnetic field of 185 G, this leads to a reduction of the C_3 coefficient to $C_3 = 875\,\mathrm{MHz}\,\mu\mathrm{m}^3$ (from $1626\,\mathrm{MHz}\,\mu\mathrm{m}^3$ at $B = 0$) for the eigenstates adiabatically connected to $\left|61S_{1/2}, m_J = 1/2\right\rangle$ and $\left|61P_{1/2}, m_J = 1/2\right\rangle$. Conversely, for the eigenstates connected to $\left|61S_{1/2}, m_J = 1/2\right\rangle$ and $\left|61P_{3/2}, m_J = 1/2\right\rangle$, the coefficient increases to $C_3 = 3876\,\mathrm{MHz}\,\mu\mathrm{m}^3$ (from $3151\,\mathrm{MHz}\,\mu\mathrm{m}^3$ at $B = 0$) ($h = 1$).

For two atoms in the same Rydberg state, exemplified by the state $\left|61S_{1/2}, m_J = 1/2\right\rangle$, the first-order perturbative energy shift vanishes, since the electric dipole matrix element between states of equal parity is zero. As a result, the interaction energy arises only at second order in perturbation theory:

$$\Delta E = \sum_{\alpha\beta} \frac{\langle nS, nS|\hat{H}_{\mathrm{DDI}}|\alpha, \beta\rangle \ \langle \alpha, \beta|\hat{H}_{\mathrm{DDI}}|nS, nS\rangle}{2E_{nS} - E_\alpha - E_\beta} = \frac{C_6}{r^6}. \tag{D.29}$$

This defines the van der Waals coefficient C_6. It is obtained from multiplying the second-order contribution $H_{\mathrm{eff}}^{(2)}$ by r^6, where the perturbation is again the dipole-dipole interaction, and the model space consists of a single pairstate.

In the absence of a magnetic field, all magnetic sublevels m_J within a given $|nL_J\rangle$ manifold are degenerate. Consequently, the sum over all contribution from intermediate pair states $|\alpha\beta\rangle$, with fixed n, L, and J, is isotropic. The resulting energy shift is thus direction-independent. Furthermore, since the dipole-dipole interaction scales as r^{-3}, the second-order shift scales as r^{-6}.

In a finite magnetic field, the energies E_α and E_β are magnetic field dependent, and different m_J states are not degenerate anymore. This leads to an anisotropy in the energy shift

$$\Delta E = \frac{C_6(\theta)}{r^6}, \tag{D.30}$$

being dependent on the angle θ of the interatomic axis with the magnetic field.

Numerically evaluating equation (D.29) and using our algorithm for the effective Hamiltonian at $r = 16\,\mu\mathrm{m}$ for different θ, we found convergence including states $|\alpha\beta\rangle = |nL_Jm_J\rangle\,|n'L'_{J'}m'_J\rangle$ for $n, n' \in \{57, \ldots, 65\}$, $L, L' \in \{0, 1, 2, 3\}$, all possible values of J, J' for these states, and $m_J, m'_J \in \{-0.5, 0.5, 1.5\}$. The results are shown in figure D.1. Unlike at zero magnetic field, where the C_6 coefficient is isotropic, we observe a strong increase of the energy shift in the direction perpendicular to the magnetic field. This anisotropy in the Rydberg interaction introduces a positional anisotropy during excitation of atoms to the Rydberg state $\left|61S_{1/2}, m_J = 1/2\right\rangle$ due to the Rydberg blockade effect discussed in Chap. 3.

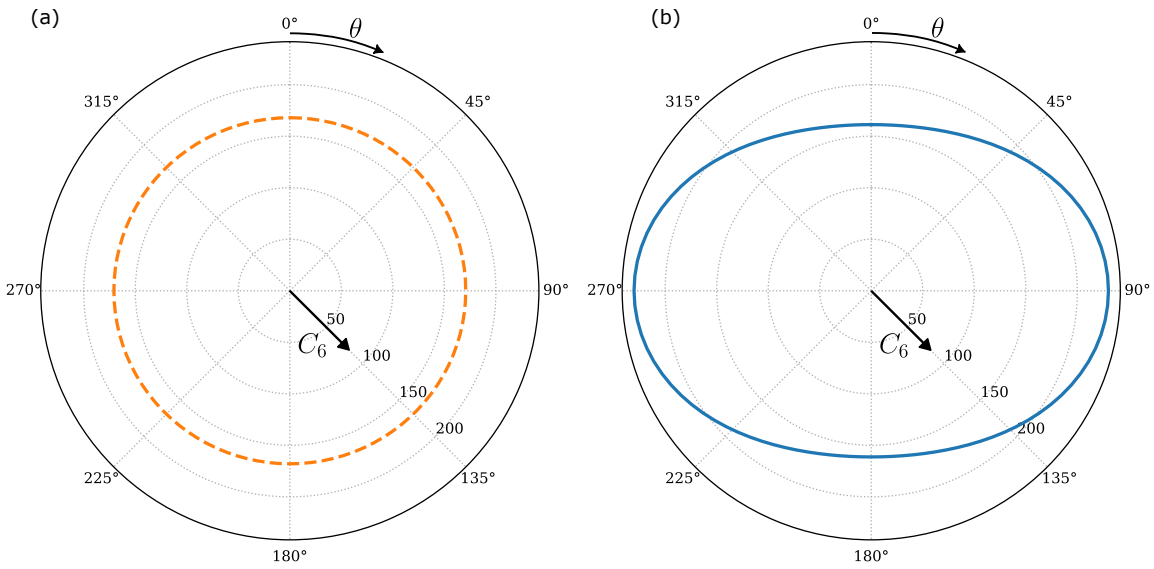

Figure D.1: *Angular dependence of the C_6 coefficient in strong magnetic fields.* Polar plot of the C_6 coefficient in GHz µm^6 as a function of the angle θ between interatomic axis and magnetic field direction for the state $\left|61S_{1/2}, m_J = 1/2\right\rangle$ in Rubidium. (a) No magnetic field is present, C_6 represented by orange dashed line. (b) Magnetic field of 185 G is present, C_6 represented by blue solid line.

D.4 Example 2: Rydberg excitation and interaction in strong electric fields

In my bachelor thesis, I devised a protocol based on strong electric fields for generating spiral spin states with Rubidium Rydberg atoms [324]. In my subsequent master thesis [219], I extended this work by analyzing how the protocol duration can be minimized, assuming non-interacting atoms. I found that an optimal spin encoding is realized in the states $\left|48P_{3/2}, m_J = 1/2\right\rangle = |\downarrow\rangle$ and $\left|47D_{5/2}, m_J = 1/2\right\rangle = |\uparrow\rangle$.

These states are not the bare atomic eigenstates, but rather the eigenstates at a finite electric field of 3.3 V cm^{-1}, adiabatically connected to the corresponding zero-field states.

To better control positional disorder in the Rydberg state, we propose initializing the system in the state $\left|48S_{1/2}, m_J = 1/2\right\rangle$, which allows for a direct excitation and results in an isotropic blockade radius. Microwave radiation can then be used to coherently transfer all atoms into the $|\downarrow\rangle$ state.

The strong electric field induces permanent electric dipole moments in the eigen-

states, significantly modifying both the Rydberg-Rydberg interactions and the energy levels. In the first part of this section, we analyze how the electric field alters the interaction-induced energy shift of the state $\left|48S_{1/2}, m_J = 1/2\right\rangle$, which in turn affects the Rydberg blockade radius.

In the second part, we show how an effective four-level Hamiltonian can be mapped onto a pseudospin model, enabling a description of Rydberg-Rydberg interactions in terms of effective spin couplings.

Building on this framework, the third part is devoted to computing the effective Hamiltonian in the model space spanned by $|\uparrow\uparrow\rangle, |\uparrow\downarrow\rangle, |\downarrow\uparrow\rangle, |\downarrow\downarrow\rangle$, where the dipole-dipole interaction is treated as a perturbation. We then analyze how the presence of the electric field modifies the pseudospin couplings in the resulting spin Hamiltonian.

D.4.1 Rydberg excitation in strong electric fields

In order to calculate the C_6 coefficient, we again calculate $C_6 = H_{\text{eff}}^{(2)} r^6$ at distance $r = 16\,\mu\text{m}$ as a function of the angle θ at a smaller magnetic field of 70 G that lifts the magnetic quantum number degeneracy, but does not introduce anisotropies in the C_6 coefficient. The results are presented in Fig. D.2.

We observe that, unlike a strong magnetic field, a strong electric field does not modify the anisotropy of the C_6 coefficient. However, in the case considered here, it shifts off-resonant intermediate states further away from resonance. As a result, the magnitude of the C_6 coefficient decreases, leading to a reduced Rydberg blockade radius. This, in turn, allows atoms to be excited in closer proximity to one another.

D.4.2 Mapping the effective Hamiltonian to a spin Hamiltonian

In the main body of this thesis, the Rydberg-Rydberg interaction is typically described using spin Hamiltonians. This approach is justified by demonstrating how an effective Rydberg-Rydberg Hamiltonian, restricted to the model space spanned by the four pair states $|\uparrow\uparrow\rangle, |\uparrow\downarrow\rangle, |\downarrow\uparrow\rangle, |\downarrow\downarrow\rangle$, can be mapped onto a pseudospin Hamiltonian. This methodology is also described in other theses from our group [157, 249].

We begin by assuming a Hermitian effective Hamiltonian of the form

$$H = \begin{pmatrix} H_{11} & H_{12} & H_{13} & H_{14} \\ H_{12}^* & H_{22} & H_{23} & H_{24} \\ H_{13}^* & H_{23}^* & H_{22} & H_{34} \\ H_{14}^* & H_{24}^* & H_{34}^* & H_{44} \end{pmatrix}, \tag{D.31}$$

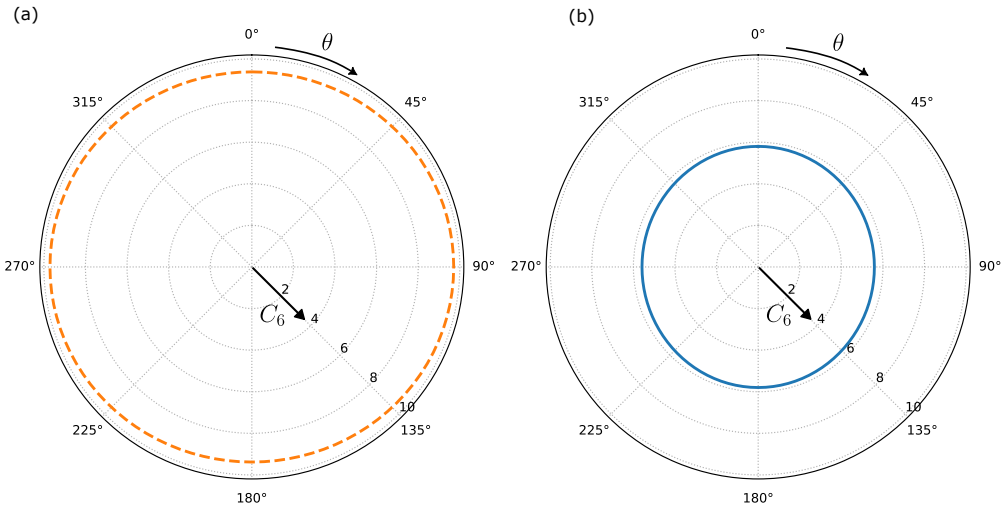

Figure D.2: *Angular dependence of the C_6 coefficient in strong electric fields.* Polar plot of the C_6 coefficient in GHz µm^6 as a function of the angle θ between interatomic axis and magnetic field direction for the state $\left|61S_{1/2}, m_J = 1/2\right\rangle$ in Rubidium. (a) No electric field is present, C_6, represented by orange dashed line, averaged over all directions is given as 9.542(12) GHz µm^6. (b) Electric field of 3.3 V cm^{-1} is present, C_6 represented by blue solid line, averaged over all directions is given as 5.689(7) GHz µm^6.

where we assume that the states $|\uparrow\downarrow\rangle$ and $|\downarrow\uparrow\rangle$ are degenerate. This assumption is justified, as these are symmetric product states of individual atoms, and their non-interacting energies are simply additive. Furthermore, interaction-induced energy shifts arising from couplings to states outside the model space respect exchange symmetry and thus contribute equally to both states. As a result, the degeneracy between $|\uparrow\downarrow\rangle$ and $|\downarrow\uparrow\rangle$ is preserved.

In this Hamiltonian, the off-diagonal terms represent dipole-dipole coupling elements, typically on the order of a few MHz. In contrast, the diagonal entries correspond to the pairstate energies, which differ by several tens of GHz. Let ω denote the energy difference between the single-particle states $|\uparrow\rangle$ and $|\downarrow\rangle$.

To proceed, we transform the Hamiltonian into a frame rotating at frequency ω. In this rotating frame, the Hamiltonian reads

$$H_{\text{rotated}} = \begin{pmatrix} H_{11} - 2\omega & H_{12}e^{i\omega t} & H_{13}e^{i\omega t} & H_{14}e^{2i\omega t} \\ H_{12}^* e^{-i\omega t} & H_{22} - \omega & H_{23} & H_{24}e^{i\omega t} \\ H_{13}^* e^{-i\omega t} & H_{23}^* & H_{22} - \omega & H_{34}e^{i\omega t} \\ H_{14}^* e^{-2i\omega t} & H_{24}^* e^{-i\omega t} & H_{34}^* e^{-i\omega t} & H_{44} \end{pmatrix}. \tag{D.32}$$

Since the off-diagonal elements H_{ij} are small compared to ω, we apply the rotating wave approximation (RWA), neglecting all fast-oscillating terms proportional to $e^{\pm i\omega t}$ and $e^{\pm 2i\omega t}$. This yields the simplified Hamiltonian

$$H_{\mathrm{RWA}} = \begin{pmatrix} H_{11} - 2\omega & 0 & 0 & 0 \\ 0 & H_{22} - \omega & H_{23} & 0 \\ 0 & H_{23}^* & H_{22} - \omega & 0 \\ 0 & 0 & 0 & H_{44} \end{pmatrix}. \tag{D.33}$$

The trace of this Hamiltonian contributes only a global phase and can be neglected. Moreover, by appropriately redefining the phases of the basis states $|\uparrow\rangle$ and $|\downarrow\rangle$, we can take H_{23} to be real without loss of generality.

We define the traceless effective Hamiltonian as $\tilde{H} = H_{\mathrm{RWA}} - \frac{1}{4}\,\mathrm{Tr}(H_{\mathrm{RWA}})\mathbb{1}$, which yields

$$\tilde{H} = \begin{pmatrix} \tilde{H}_{11} & 0 & 0 & 0 \\ 0 & \tilde{H}_{22} & \tilde{H}_{23} & 0 \\ 0 & \tilde{H}_{23} & \tilde{H}_{22} & 0 \\ 0 & 0 & 0 & \tilde{H}_{44} \end{pmatrix}. \tag{D.34}$$

This Hamiltonian corresponds to a Heisenberg XXZ spin model with a magnetic field oriented along the z-axis. Additional spin–spin interaction terms are neglected because they are either far off-resonant—such as terms proportional to $S^+S^+ + S^-S^-$—or they break the $U(1)$ symmetry intrinsic to the Rydberg–Rydberg interaction Hamiltonian

$$\begin{aligned} H_{\mathrm{XXZ}} &= J_\perp \left(S_x^{(1)} S_x^{(2)} + S_y^{(1)} S_y^{(2)} \right) + J_\parallel S_z^{(1)} S_z^{(2)} + h_z \left(S_z^{(1)} + S_z^{(2)} \right) \\ &= \begin{pmatrix} J_\parallel/4 + h_z & 0 & 0 & 0 \\ 0 & -J_\parallel/4 & J_\perp/2 & 0 \\ 0 & J_\perp/2 & -J_\parallel/4 & 0 \\ 0 & 0 & 0 & J_\parallel/4 - h_z \end{pmatrix}. \end{aligned} \tag{D.35}$$

A comparison of coefficients thus leads to

$$J_\parallel = \tilde{H}_{11} + \tilde{H}_{44} - 2\tilde{H}_{22}, \tag{D.36}$$

$$J_\perp = \tilde{H}_{23}, \tag{D.37}$$

$$h_z = \left(\tilde{H}_{11} - \tilde{H}_{44} \right)/2. \tag{D.38}$$

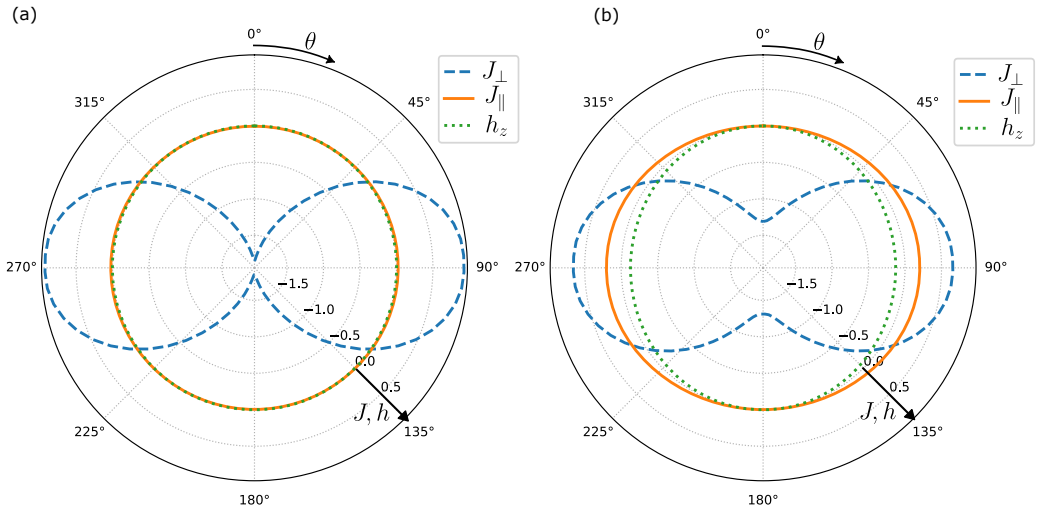

Figure D.3: *Angular dependence of effective Hamiltonian couplings in strong electric fields as a polar plot.* The couplings $J_\perp$ (blue dashed line), $J_\parallel$ (orange solid line) and h_z (green dotted line) in MHz are shown as a function of the angle θ both (a) without electric field and (b) in the presence of an electric field of $3.3\,\mathrm{V\,cm^{-1}}$. In order to plot the full range of $J_\perp$, the center of the polar plot does not coincide with zero, but with the strongest negative interaction.

D.4.3 Effective spin Hamiltonian in the presence of strong electric fields

We thus construct the different components of the spin Hamiltonian as described above. The results are presented as polar plots in Fig. D.3 and as linear plots in Fig. D.4. We observe that the angular dependence of $J_\perp$ is strongly connected to the C_3 coefficient and thus shares the $1-3\cos^2(\theta)$ angular dependence. The terms $J_\parallel$ and h_z arise from second order contribution, and are thus smaller. This beomes especially apparent at zero field when the interaction strengths are plotted linearly in Fig. D.3(a).

The finite electric field, leading to permanent electric dipole moments in the eigenstates, reduces the strength of $J_\perp$, as electric dipole moments tend to align with the electric field and a dipole moment flip, corresponding to a spin flip induced by $J_\perp$ becomes energetically less favorable. On the other hand, the electric field favor spin alignment towards the electric field, thus leading to an increase of $J_\parallel$ and h_z. As a consequence, the terms J_z and h_z, which we typically neglected in the thesis in the absence of electric fields, need to be taken into account once electric fields are applied.

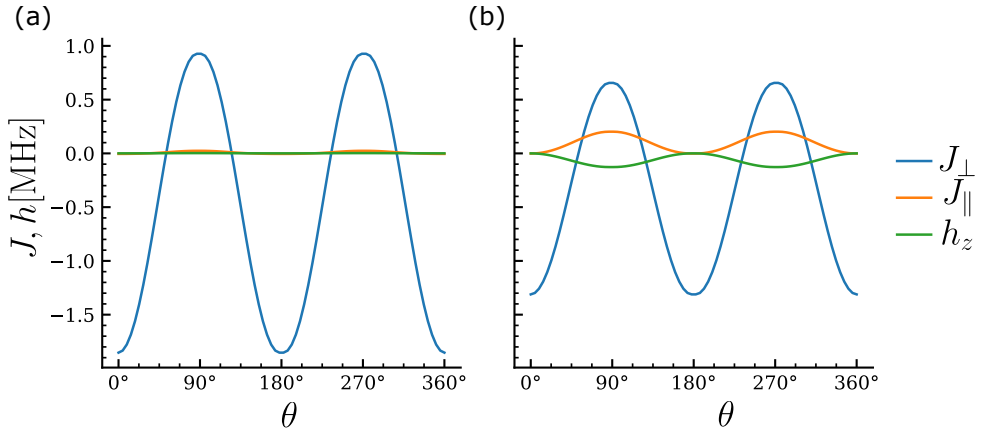

Figure D.4: *Angular dependence of effective Hamiltonian couplings strength in strong electric fields as linear plots.* The couplings $J_\perp$ (blue), $J_\parallel$ (orange) and h_z (green) in MHz are shown as a function of the angle θ in degree both (a) without electric field and (b) in the presence of an electric field of $3.3\,\mathrm{V\,cm^{-1}}$.

Another interesting regime where these terms become essential, is the application of time-reversal, where $J_\perp$ can be completely flipped, but the terms J_z and h_z are typically rather unaffected. This effect was further studied under the supervision of the author in [249].

CHAPTER E

Microwave Engineering of Ultrafast Rydberg Interactions

In the main body of this thesis, we explored a regime in which the Rydberg-Rydberg interaction is typically weaker than or comparable to the coupling between Rydberg atoms and the applied microwave drive. In contrast, during a research internship at the Institute for Molecular Science (IMS) in Japan, I investigated a complementary regime where the Rydberg-Rydberg interaction dominates the energy scale. When two Rydberg atoms are sufficiently close together, the dipole-dipole approximation, discussed in Appendix D, breaks down and higher-order processes, such as dipole-quadrupole interactions, become relevant. Consequently, the two-level approximation that underpinned much of the analysis in this thesis is no longer valid, and the system must instead be described as a genuine multilevel atom.

An important feature of this strongly interacting regime is its fast dynamics: interaction strengths can reach hundreds of MHz, leading to interaction cycles on the order of nanoseconds. This rapid timescale is particularly attractive for quantum information processing, as it offers the potential for implementing ultrafast entangling gates. However, achieving high-fidelity gate operations in this context requires precise control over the multilevel atomic structure. In this work, we analyze in detail how spatial uncertainties and microwave coupling affect the performance and robustness of such entangling gates.

E.1 Realization of an ultrafast Rydberg gate

This subsection focuses on the numerical analysis of the entangling gate. Therefore, we omit a detailed description of the experimental setup for Rydberg excitation,

which can be found in [306]. Instead, we provide a brief summary of the experimental concept before discussing the dynamics within the Rydberg manifold. The atomic Hamiltonian is constructed using the *PairInteraction* library [167], and the time evolution is simulated with the *QuTiP* library [325]. Throughout this chapter, we will give all units of energy as frequencies, not as angular frequencies, following the unit convention of the *PairInteraction* package.

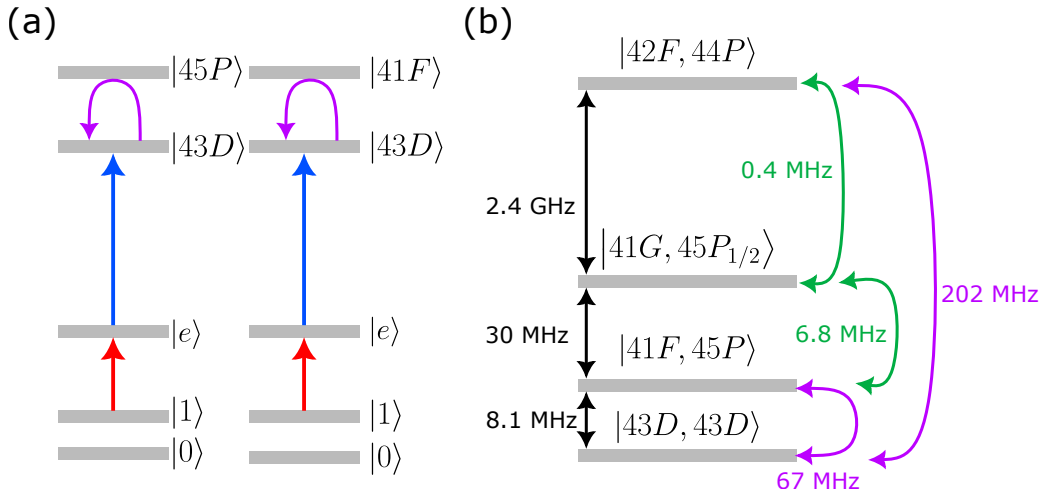

Figure E.1: *Realization of an ultrafast Rydberg entanglement gate.* (a) Idea behind the CZ gate: The 780 nm-pulse is only resonant if both atoms are in the logical state $|1\rangle$. After excitation to $|e\rangle$, which is metastable on a nanosecond timescale, the atoms are excited to the Rydberg state $|43D\rangle$. In the Rydberg manifold due to Förster resonance, the pairstate $|43D, 43D\rangle$ undergoes an oscillation to the pairstate $|45P, 41F\rangle$, where in a 2-level approximation a phase of π would accumulate. (b) Level diagram of Rydberg states with a buildup of more than 1 % during the gate. Energy differences are indicate by black arrows, dipole-dipole interaction energies by violet arrows and dipole-quadrupole interactions by green arrows.

Figure E.1(a) illustrates the concept of implementing an ultrafast entangling gate. The platform is based on Rubidium, which features a large ground-state hyperfine splitting of 6.8 GHz [177]. This allows qubit encoding in the two hyperfine levels $|0\rangle = \left|5S_{1/2}, F = 1, m_F = 1\right\rangle$ and $|1\rangle = \left|5S_{1/2}, F = 2, m_F = 2\right\rangle$, which remain effectively stable over a typical experimental cycle of 1 s.

An ultrashort laser pulse at 780 nm with a duration of 2 ps excites atoms from state $|1\rangle$ to the intermediate state $|e\rangle = \left|5P_{3/2}, F = 3, m_F = 3\right\rangle$. A second pulse at 480 nm, lasting 17 ps, then drives the excitation to the Rydberg level $\left|43D_{5/2}, m_J = 5/2\right\rangle$.

To implement a CZ gate, the spectral bandwidth of both pulses must be precisely controlled to ensure that only the $|1\rangle \rightarrow |e\rangle \rightarrow |r\rangle$ transition is resonant, isolating this excitation pathway. In the current setup, this condition is met for the $|e\rangle \rightarrow |r\rangle$ transition. However, the 2 ps laser pulse used for the $|1\rangle \rightarrow |e\rangle$ transition is too short to resolve the hyperfine splitting in Rubidium. To address this limitation, a new laser source is being prepared, capable of producing pulses tunable between 100 ps to 1000 ps. Due to the large hyperfine splitting in Rubidium, a pulse duration of 200 ps is sufficient to resolve the 6.8 GHz splitting [177]. The ultrashort 480 nm pulse is tailored to a spectral bandwidth of approximately 100 GHz, which exceeds the energy shifts due to Rydberg interactions. As a result, the Rydberg blockade effect (see Chapter 3) ceases to apply, allowing simultaneous excitation of two atoms to the Rydberg state even at short distances.

We introduce the following notation conventions for atomic finestructure states to improve clarity:

1. When only the principal quantum number n and orbital angular momentum L are specified, $|nL\rangle$ denotes the state within that manifold with the highest total angular momentum J and magnetic quantum number m_J, i.e.,$|nL\rangle = \left|nL_{(L+1)/2},\, m_J = (L+1)/2\right\rangle$.

2. If the total angular momentum J is given, the state $|nL_J\rangle$ corresponds to the substate with the maximal magnetic quantum number, $|nL_J\rangle = |nL_J,\, m_J = J\rangle$.

3. For two-atom states, the notation $|S1, S2\rangle$ lists the state of atom 1 followed by that of atom 2. For example, $|43D, 43D\rangle$ indicates both atoms are in the $|43D\rangle$ state.

4. The two-atom state $|S1, S2\rangle$ in the case $|S1\rangle \neq |S2\rangle$ is identified with the symmetric superposition $|S1, S2\rangle = \frac{1}{\sqrt{2}}\left(|S1, S2\rangle + |S2, S1\rangle\right)$. Since the Hamiltonian is symmetric under particle exchange (atom 1 $\leftrightarrow$ atom 2) and the initial state is the symmetric state $|11\rangle$, only these symmetric states are populated.

Within the Rydberg manifold, a Förster resonance occurs between the states $|43D, 43D\rangle$ and $|45P, 41F\rangle$. By restricting the dynamics to these two pair states, one interaction cycle transforms the initial state $|43D, 43D\rangle$ into $-|43D, 43D\rangle$. Reapplying the pulses with adjusted phases then coherently deexcites the system from the Rydberg state to $-|11\rangle$. If both atoms are initially in $|0\rangle$, no evolution occurs. For the case where one atom is in $|0\rangle$ and the other in $|1\rangle$, the atom in $|0\rangle$ remains unchanged, while the atom in $|1\rangle$ is excited to the Rydberg state and subsequently deexcited back to $|1\rangle$ without phase alteration. This sequence implements a controlled-Z (CZ) gate.

However, as illustrated in Fig. E.1(b), additional near-resonant pair states perturb the otherwise isolated Förster resonance at an interatomic distance of $r = 2.5\,\mu\text{m}$. This specific distance is chosen because it enables the entangling gate to operate on nanosecond timescales, while only two perturbing states acquire populations exceeding 0.1 % during the evolution.

The state $|42F, 44P\rangle$ is detuned by $\Delta = 2.4\,\text{GHz}$ and couples to $|43D, 43D\rangle$ with an interaction strength of $V = 202\,\text{MHz}$. Additionally, the state $\left|41G, 45P_{1/2}\right\rangle$ is detuned by only $\Delta = 30\,\text{MHz}$ and is weakly coupled to $|41F, 45P\rangle$ via a dipole-quadrupole interaction with a coupling strength of $V = 6.8\,\text{MHz}$.

This chapter aims to examine how the interaction between relevant Rydberg pair states depends on interatomic distance and orientation. It also investigates whether microwave radiation, previously shown to reduce perturbations from residual electric fields [326, 327], can stabilize the Förster resonance against nearby off-resonant states. Stabilizing the resonance in this way could improve the fidelity of the intended CZ gate.

E.1.1 The effect of positional uncertainty

For entanglement gates applied in neutral atom platforms based on tweezer arrays[29, 304], the atoms typically suffer from positional uncertainty due to the Heisenberg uncertainty of the motional ground state. This leads to uncertainty both in the distance of the atoms, as well as in the orientation. We study first the case of positional uncertainty. When tightly trapped and cooled to the motional ground state, positional uncertainties as low as 35 nm have been experimentally achieved[306]. For a worst-case scenario, we assume a positional uncertainty of 50 nm. We analyze the time evolution of a two-atom system initialized in the state $|43D, 43D\rangle$ for entanglement gates at distances of 2.45 µm and 2.55 µm. The overlap between the instantaneous eigenstates and all states populated above 0.1 % during the evolution is plotted. Additionally, the total population of these states is plotted and remains close to 1, as expected. This confirms the numerical accuracy of the code.

The populations of the four relevant states identified in Fig. E.1(b) remain stable. However, the dynamics slow down as the distance increases. Consequently, the gate duration extends from 7 ns at $r = 2.45\,\mu\text{m}$ to nearly 8 ns at $r = 2.55\,\mu\text{m}$.

If the Rydberg states are transferred back to the ground state at 7.7 ns at $r = 2.5\,\mu\text{m}$, a phase error arises and some population is lost within the Rydberg manifold. This error can be mitigated by reducing the positional uncertainty, for example by employing tighter traps. In the current setup, Raman sideband cooling is employed so that the positional uncertainty is dominated by the spatial extent

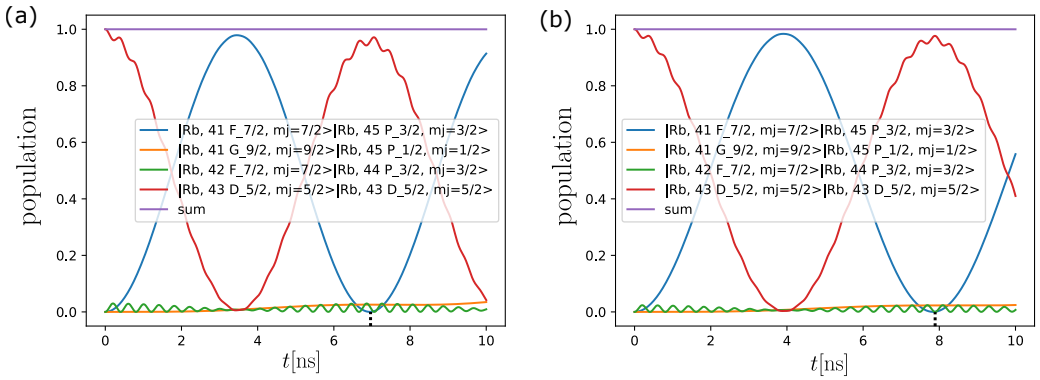

Figure E.2: *Effect of positional uncertainty.* Time evolution of state popoulations of pairstates with a population build-up of more than 1 % and the sum of their populations as a function of evolution time t. The minimum of the popoulation in $|41F, 45P\rangle$, which marks the gate duration, is indicated by a black dotted line. (a) Distance set at $r = 2.45\,\mu\text{m}$. (b) Distance set at $r = 2.55\,\mu\text{m}$.

of the motional ground state, given by $\sigma_x = \sqrt{\hbar/(m\omega_x)}$ [306]. Here, ω_x denotes the trap frequency, which scales proportional to $\sqrt{P}$, where P is the trap laser power [301]. Consequently, the positional uncertainty scales as $P^{-1/4}$. A reduction of the positional uncertainty by a factor of two therefore requires an increase in trap power by a factor of sixteen. One alternative would be the use of motional squeezed states, where a reduction in positional uncertainty is treated for increased momentum uncertainty [328]. Alternatively, the experiment may be performed at a larger interatomic distance, where the mentioned phase error may be reduced at the cost of a longer gate duration.

E.1.2 The effect of orientational uncertainty

To investigate the effect of orientational uncertainty, we again assume a positional uncertainty of 50 nm. If atom 1 is displaced by 50 nm perpendicular to the interatomic axis, and atom 2 is shifted by the same amount in the opposite direction, the resulting tilt of the interatomic axis is $\theta = 2 \times \frac{50\,\text{nm}}{2.5\,\mu\text{m}} = 40\,\text{mrad}$.

In experiments, the quantization axis is defined by a magnetic field with a fixed direction. This tilt thus corresponds to a shift in the quantization axis. By rotating the coordinate system by θ around the axis perpendicular to both the quantization and interatomic axes, the system becomes equivalent to atoms aligned along the quantization axis, but with a magnetic field component perpendicular to it.

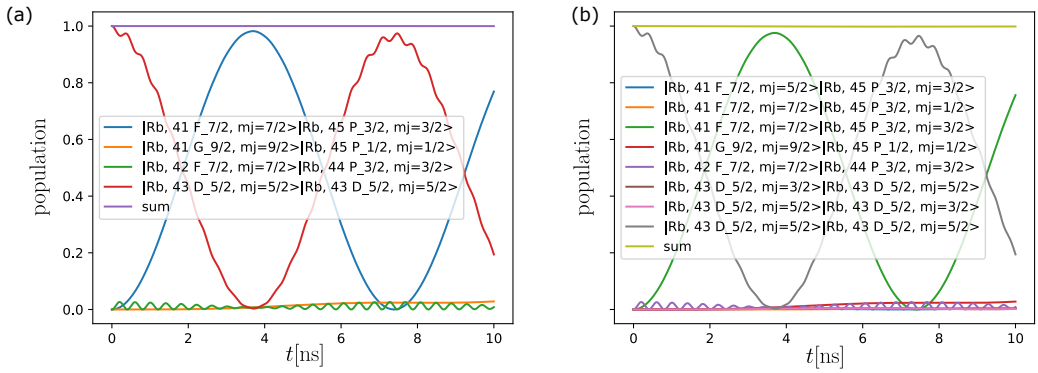

Figure E.3: *Effect of orientational uncertainty.* Time evolution of state popoulations of pairstates with a population build-up of more than 1 % and the sum of their populations as a function of evolution time t. (a) Angle between interatomic axes and quantization axis at $\theta = 0\,\text{mrad}$. (b) Angle between interatomic axes and quantization axis at $\theta = 50\,\text{mrad}$.

In Fig. E.3, we simulate the time evolution of two atoms initialized in the state $|43D, 43D\rangle$. We plot the populations of all states that exceed a maximum occupation of 0.1 % during evolution, for two angles between the interatomic and quantization axis: $\theta = 0\,\text{mrad}$ and $\theta = 50\,\text{mrad}$, representing the best- and worst-case scenarios.

As the angle between the interatomic and quantization axes increases, the overall dynamics remains largely unchanged, and the gate duration stays close to 7.7 ns. However, states with different magnetic quantum numbers m_J become admixed due to the magnetic field component perpendicular to the quantization axis. This admixture reduces the gate fidelity.

To quantify this effect, we define a *relevant fidelity* $\mathcal{F}$. It assumes that any error within the four relevant states identified in Fig. E.1 can be perfectly corrected. The quantity $\mathcal{F}$ therefore measures the fidelity loss due solely to orientational errors.

$\mathcal{F}$ can be understood as the overlap between the system's state and its state after a rotation by an angle θ. Geometrically, the overlap of a vector with itself after rotation scales as $\cos(\theta) \approx 1 - \theta^2/2$ for small angles.

For angular momentum states, a rotation by an angle θ transforms the eigenstate $|j, m\rangle$ into a superposition of other $|j, m'\rangle$ states, governed by the Wigner d-matrices:

$$R(\alpha, \beta, \gamma)\,|j, m\rangle = \sum_{m'} d^j_{m,m'}(\beta)\, e^{-im\alpha} e^{-im'\gamma}\,|j, m'\rangle\,. \tag{E.1}$$

Here, α, β, γ are the Euler angles, and R denotes the rotation operator. A rotation of the quantization axis by an angle θ corresponds to the specific choice

$(\alpha, \beta, \gamma) = (0, \theta, 0)$. In this case, the overlap between the rotated and original states becomes:

$$\langle j, m|\, R(0, \theta, 0)\, |j, m\rangle = \left(\cos\frac{\theta}{2}\right)^{2m} P_{j-m}^{(0,2m)}(\cos\theta), \tag{E.2}$$

where $P_{j-m}^{(0,2m)}$ are Jacobi polynomials, and we assume $m > 0$ [329].

Since this expression depends only on θ^2, the fidelity $\mathcal{F}$ can be approximated for small θ as

$$\mathcal{F} \approx 1 - a\theta^2. \tag{E.3}$$

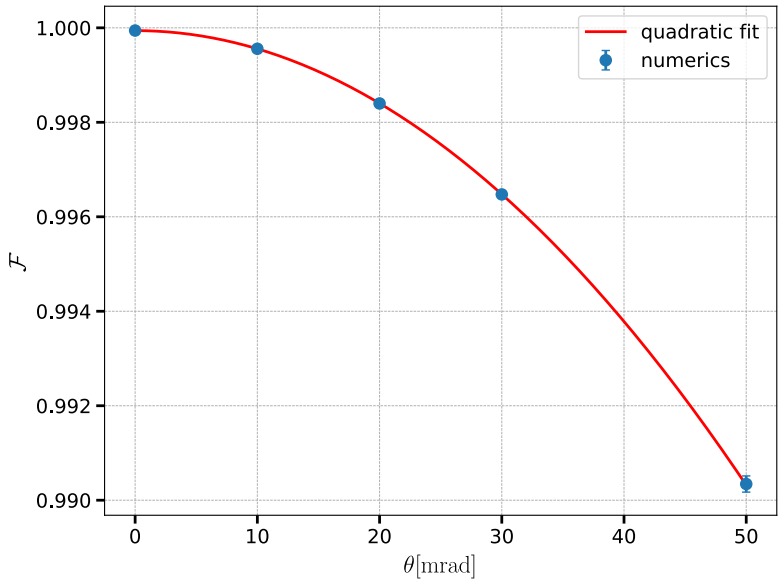

Figure E.4: *Influence of the angle on relevant fidelity.* Population contribution $\mathcal{F}$ of the four relevant pairstates shown in Fig. E.1(b) as a function of angle θ between interatomic axes and magnetic field. Errorbars of are estimated from standard error of the mean when averaging $\mathcal{F}$ in the interval $6\,\text{ns} \leq t \leq 8\,\text{ns}$. The admixture of other states due to the component of the magnetic field perpendicular to quantization axis is fitted by a quadratic function (solid red line).

We simulate $\mathcal{F}$ for angles $\theta = [0, 10, 20, 30, 50]$ mrad and observe excellent agreement with a quadratic dependence. From the fit, we extract the coefficient $a = 3.849(5) \times 10^{-6}\,\text{mrad}^{-2}$.

To maintain a fidelity above 99.9 %, which is commonly considered sufficient for fault tolerance below the surface code threshold of 1 %[330], the rotation angle must satisfy $\theta < 16\,\text{mrad}$. This corresponds to a positional uncertainty of less than 20 nm.

E.2 A microwave setup for the creation of microwave radiation with arbitrary polarization

This chapter aims to estimate how microwave radiation can stabilize the previously introduced CZ gate. To this end, we consider microwave-driven transitions between the relevant states shown in Fig. E.1(b), with typical transition frequencies in the tens of gigahertz. Since several transitions in this frequency range are important, I briefly present a setup capable of generating such radiation. The focus lies on achieving high control over both frequency and polarization. We present a setup capable to generate both σ^+- and σ^--, as well as linearly polarized radiation, ranging from 24 GHz to 50 GHz.

To generate circularly polarized microwave radiation, we use the QRH67E horn antenna from RF-Spin. This antenna features two input channels, with polarization determined by their relative phase. Circular polarization requires equal power at both input ports.

The initial part of the setup, illustrated in Fig. E.5, is designed to produce these two coherent channels. We employ the Signal Core SC5511B signal generator, which covers frequencies from 100 MHz to 20 000 MHz, with a maximum output power of 13 dBm For optimal signal quality, we operate it at a low power of 0 dBm, where sideband noise is small. Further amplification is performed at a later stage using a low-noise amplifier.

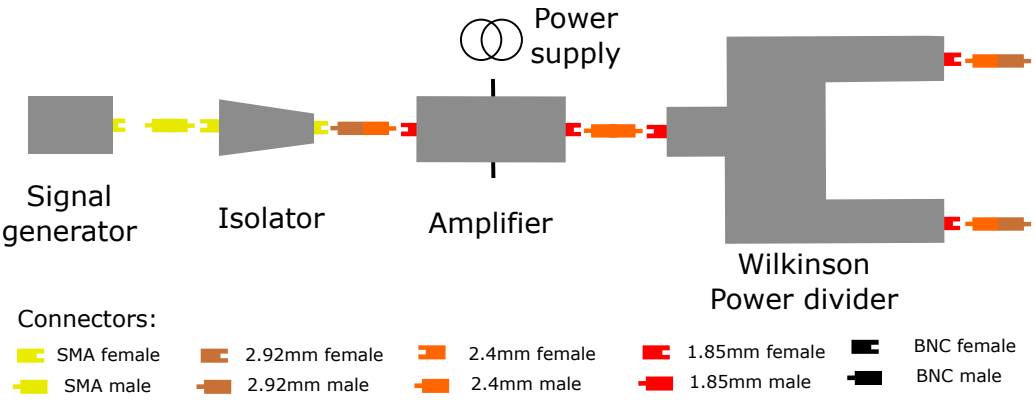

Figure E.5: *Setup for the generation of two phase-stable output channels.* Individual components are marked by gray boxes, while there connectors and cables by colore bars. Connector legend is shown below the setup.

To protect the signal generator from potentially damaging reflections, it is con-

nected to the DMI6018 isolator from DiTOM Microwave, which provides more than 13 dB of isolation over the full frequency range from 6 GHz to 18 GHz, thereby supporting broad frequency tunability. The output is then amplified using the DR-AN-20-MO amplifier from Exail, offering an adjustable gain between 28 dB to 30 dB. We operate it at 28 dB, where the output remains stable even at high amplitudes and frequencies.

The total output power of 28 dBm is split into two equal-power channels with identical phase. As no passive power divider is both lossless and phase-coherent, one of these conditions must be relaxed. To prioritize low noise and phase coherence, we use a Wilkinson divider, which introduces an insertion loss between 2 dB to 5 dB, depending on the input frequency. Since we operate below 20 GHz, the expected loss is 2 dB. The resulting output consists of two phase-matched channels, tunable from 0.1 GHz to 20 GHz, each with an amplitude of 13 dBm.

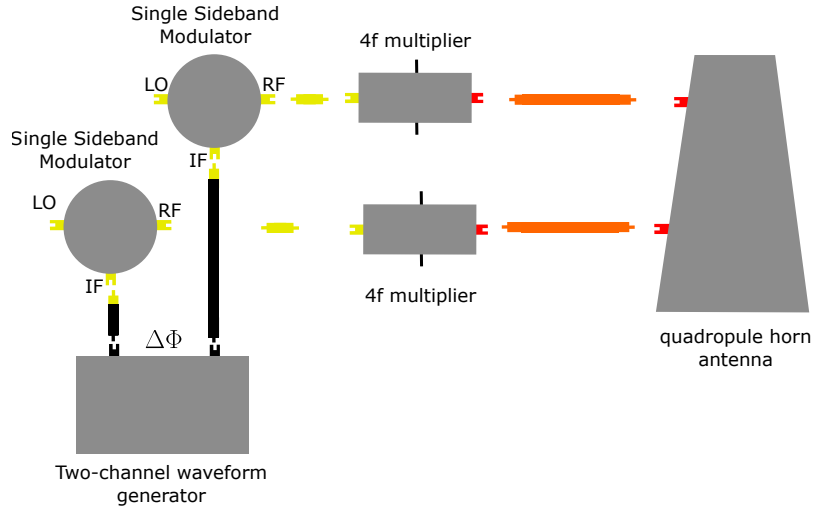

Figure E.6: *Setup for the generation of microwave radiation with tunable polarization.* Individual components are marked by gray boxes, while there connectors and cables by colore bars. Connector legend is shown below the setup.

In order to achieve microwave radiation at arbitrary polarization, we need to adjust the phases of the individual channels, or in the case of linear polarization, switch each channel separately on and off. Therefore, we employ single-sideband mixers (SSBs). A SSB has three connection ports: One input port at high frequency ν_L which is called the local oscillator (LO), one input port at an intermediate frequency ν_I (IF) and an output port for a radio frequency ν_R (RF). What the SSB does is it takes the IF input signal and mixes it with IF signal to produce a new signal at the RF port of

$\nu_R = \nu_I + \nu_L$. The SSB has in our setup two main purposes:

1. The output power of the RF port is proportional to the IF input power. So by switching on and off the IF signal, the SSB works as a switch for microwave radiation.

2. The SSB is phase additive, i.e. the output port adds the phases of the LO and IF signals.

As shown in Fig. E.6, each output of the Wilkinson divider is connected to the LO port of a single-sideband (SSB) mixer, ensuring a common LO phase across both mixers. The IF inputs are driven by a dual-channel waveform generator, configured to introduce a constant phase offset $\Delta\Phi$ between its two outputs. Since the LO phase is identical for both SSBs and the IF signals differ by $\Delta\Phi$, the resulting RF outputs also exhibit a stable phase difference of $\Delta\Phi$. The setup employs the SSB-0618LXW-1 mixer from Marki Microwave, selected for its broad LO frequency range from 6 GHz to 18 GHz and low conversion loss of 7.5 dB. This mixer uses internal double-balanced mixers and therefore requires a high LO drive, which is provided by the Wilkinson divider outputs. The IF signals are generated using a Keysight 33600A waveform generator, chosen for its fine frequency resolution in the MHz range and its phase-stabilized dual-channel mode, which maintains both a constant phase offset and equal output power between the channels. Both the SSB mixers and the isolator limit the maximum RF output frequency to 18 GHz. To reach higher frequencies, we employ a $\times 4$ frequency multiplier, enabling outputs up to 50 GHz. These frequencies are essential for driving specific transitions within the Rydberg manifold, as discussed later. The AQA-2156 amplifier from Marki Microwave is used, as it supports frequencies beyond 50 GHz and offers a broad tuning range from 21 GHz to 56 GHz. It delivers a stable output power of 20 dBm and strongly suppresses the frequency-doubled signal by 26 dBc relative to the carrier at the fourth harmonic. The output is transmitted via a TMM cable from Thorlabs to the quadrupole horn antenna.

To estimate a typical Rabi frequency achievable in this setup, we consider the Rydberg transition $\left|43D_{5/2}, m_J = 5/2\right\rangle \rightarrow \left|42F_{7/2}, m_J = 7/2\right\rangle$, which has a transition frequency of 30 GHz and a dipole matrix element of 1.97 GHz/(V/cm). At this frequency, the antenna provides a gain of $G = 9$ dBi, corresponding to 9 dB relative to isotropic radiation for an input power of $P = 20$ dBm. Assuming the microwave source is positioned at a distance of $d = 1$ m from the atoms, the electric field amplitude E at the atomic position is

$$E = \sqrt{\frac{2GP}{4\pi\epsilon_0 c d^2}} = 0.069\,\mathrm{V\,cm^{-1}}. \tag{E.4}$$

This field corresponds to a Rabi frequency of 136 MHz, expressed in units of frequency rather than angular frequency. Higher Rabi frequencies can be achieved by placing the antenna closer to the atoms. Since the electric field amplitude is inversely proportional to the distance, the Rabi frequency, being proportional to the electric field amplitude, scales equally. For instance, positioning the antenna at 50 cm increases the Rabi frequency to 272 MHz, whereas a distance of 2 m reduces it to 68 MHz.

In summary, the setup enables frequency generation in the range from 24 GHz to 50 GHz. The lower bound is determined by the minimum frequency at which the SSB mixers operate reliably. The upper limit is set by the maximum frequency the TMM cable can transmit effectively. Coarse frequency tuning is achieved by adjusting the signal generator directly. Fine tuning is performed via the two-channel waveform generator, which also serves as a computer-controlled switch. The polarization of the emitted radiation depends on the configuration of the waveform generator outputs. Linearly polarized radiation is generated when one channel is turned off and the other delivers finite power. Circular polarization occurs when both channels are active with a phase difference of $\pm\pi/2$.

E.3 An algorithm to construct an effective time-independent atom-light Hamiltonian

In the previous section, we presented a setup for generating microwave radiation with tunable polarization. We now turn to its interaction with Rydberg atoms. For clarity, we first consider the case of a single atom exposed to microwave radiation. We then extend the analysis to a pair of interacting Rydberg atoms.

For our analysis, we consider an atom described by an internal Hamiltonian H_0, where the energy eigenstates are labelled by $|nL_Jm_J\rangle$. The atom is exposed to an electromagnetic wave with a time- and space-dependent electric field, a monochromatic plane wave given by

$$\vec{E}(\vec{r},t) = \begin{pmatrix} E_x \\ E_y \\ E_z \end{pmatrix} \exp\left(i\left(\vec{k}\cdot\vec{r} - \omega t\right)\right) + \text{c.c.}, \tag{E.5}$$

where $\vec{k}$ is the wavevector, ω the angular frequency, and the components E_x, E_y, E_z determine the polarization and amplitude of the field. We will follow from here the standard approach of linear electrodynamics, where for the calculations we neglect the complex conjugation part, and reintroduce it only at a final step. This yields the same math as long as only linear operations are performed on the electric field.

E.3.1 Electric dipole and quadrupole transitions

As the interaction of atoms with electromagnetic radiation is textbook knowledge [179], here we will shortly review the most important assumptions and approximations relevant for the numerical simulations we want to implement. For most parts, we will follow [179]. In the semiclassical framework, the atom is modeled as a charge distribution $\rho(\vec{r})$ interacting with the electric potential $\Phi(\vec{r})$ of the electromagnetic wave introduced above. The interaction energy is given by the integral

$$\int d^3r\, \rho(\vec{r})\Phi(\vec{r}). \tag{E.6}$$

Expanding $\Phi(\vec{r})$ in a Taylor series around the origin yields a multipole expansion:

$$\begin{aligned}\int d^3r\, \rho(\vec{r})\Phi(\vec{r}) &= \int d^3r\, \rho(\vec{r}) \left(\Phi(0) + \vec{r}\cdot\nabla\Phi(0) + \frac{1}{2}\vec{r}^T\left(\vec{\nabla}\otimes\vec{\nabla}\Phi(0)\right)\vec{r} + \mathcal{O}(|\vec{r}|^3)\right) \\ &= \int d^3r\, \rho(\vec{r}) \left(\Phi(0) - \vec{r}\cdot\vec{E}(0) - \frac{1}{2}r_i r_j \partial_i E_j(0) + \mathcal{O}(|\vec{r}|^3)\right),\end{aligned}$$

where we used $\vec{E} = -\vec{\nabla}\Phi$.

Evaluating the integrals defines the multipole moments:

$$Q = \int d^3r\, \rho(\vec{r}), \quad \vec{d} = \int d^3r\, \rho(\vec{r})\vec{r}, \quad Q_{ij} = \int d^3r\, \rho(\vec{r}) \left(3r_i r_j - \delta_{ij} r^2\right). \tag{E.7}$$

Thus, the interaction energy approximates to

$$U = Q\Phi(0) - \vec{E}(0)\cdot\vec{d} - \frac{1}{6}\partial_i E_j(0) Q_{ij}. \tag{E.8}$$

Since the atom is neutral, $Q = 0$ by definition. The leading term is therefore the dipole interaction $-\vec{E}(0)\cdot\vec{d}$. The next significant contribution arises from the quadrupole interaction involving the quadrupole moment Q_{ij}. We include this term explicitly, as it plays a crucial role in the analysis of the Rydberg gate, particularly influencing the state $|41G\rangle$.

To gain deeper insight into these terms, we express them in the spherical basis. This representation offers an intuitive interpretation: the dipole moment corresponds to the absorption of a single photon from the electromagnetic field, while the quadrupole interaction can be viewed as a two-photon process, involving one photon from the oscillating electric field $\vec{E}$, and another associated with its momentum $\vec{k}$.

We first note that as the atomic Hamiltonian H_0 is isotropic, the angular momentum eigenstates are also energy eigenstates. For this reason, it is convenient to

describe both the atomic wavefunctions and the electric field using spherical basis vectors, defined as follows:

$$\hat{e}_+ = -\frac{1}{\sqrt{2}}\begin{pmatrix}1\\ i\\ 0\end{pmatrix} \tag{E.9}$$

$$\hat{e}_- = \frac{1}{\sqrt{2}}\begin{pmatrix}1\\ -i\\ 0\end{pmatrix} \tag{E.10}$$

$$\hat{e}_0 = \begin{pmatrix}0\\ 0\\ 1\end{pmatrix} \tag{E.11}$$

and the components are given by

$$E_+ = -\frac{1}{\sqrt{2}}(E_x - iE_y) \tag{E.12}$$

$$E_- = \frac{1}{\sqrt{2}}(E_x + iE_y) \tag{E.13}$$

$$E_0 = E_z \tag{E.14}$$

$$\tag{E.15}$$

The same can also be applied for the electric dipole operator $\vec{d} = e\vec{r}$, where e denotes the electron charge

$$d_+ = -\frac{1}{\sqrt{2}}(d_x + id_y) = er\sqrt{\frac{4\pi}{3}}Y_1^1 \tag{E.16}$$

$$d_- = \frac{1}{\sqrt{2}}(d_x - id_y) = er\sqrt{\frac{4\pi}{3}}Y_{-1}^1 \tag{E.17}$$

$$d_0 = d_z = er\sqrt{\frac{4\pi}{3}}Y_0^1 \tag{E.18}$$

This framework reveals the connection between spherical harmonics Y_m^ℓ and the dipole operator expressed in the spherical basis. Since angular momentum eigenstates are described by spherical harmonics, an operator proportional to Y_m^ℓ induces transitions changing the orbital angular momentum quantum number L by ℓ and the magnetic quantum number m_J by m. In the semiclassical picture, the dipole operator in the

spherical basis corresponds to the absorption or emission of a single photon, where the photon's polarization determines the selection rules and the direction of the angular momentum change.

Because the quadrupole and higher-order terms involve spatial derivatives of the electric field, the dipole term is the sole contributor in the multipole expansion when the electric field is spatially homogeneous. This assumption, known as the "dipole approximation" [179], is generally well justified for optical-wavelength laser radiation, since the wavelength is much larger than the atomic charge distribution.

In the spherical basis, the interaction thus reads

$$U_{\text{dipole}} = -\vec{d}\vec{E}(0) = -\left(E_+ d_+ + E_- d_- + E_0 d_0\right) \exp(-i\omega t) \tag{E.19}$$

In the spherical basis, all polarization components of the electric field do clearly couple to only one respective component of the dipole operator. To perform calculations at higher accuracy where perturbations due to electric quadrupole transitions may become significant, we extend the same framework to the quadrupole interaction. We first calculate the spatial derivative of the electric field as $\partial_i E_j(0) = ik_i E_j(0)$. This leads yields the quadrupole interaction energy

$$U_{\text{quadrupole}} = -i/6 k_i E_j(0) Q_{ij} \exp(-i\omega t) \tag{E.20}$$

in the cartesian basis, and

$$U_{\text{quadrupole}} = -i/6 k_{q_k} E_{q_E}(0) Q_{q_k q_E} \exp(-i\omega t) \tag{E.21}$$

where we use the Einstein summation convention. Expressing the quadrupole moment tensor Q_{ij} in the spherical basis yields the matrix

$$Q_{q_k q_E} = \begin{pmatrix} \sqrt{6}R^2_2 & R^2_0 & \sqrt{3}R^2_1 \\ R^2_0 & \sqrt{6}R^2_{-2} & \sqrt{3}R^2_{-1} \\ \sqrt{3}R^2_1 & \sqrt{3}R^2_{-1} & 2R^2_0 \end{pmatrix}, \tag{E.22}$$

where the regular solid harmonics are defined as

$$R^\ell_m(\mathbf{r}) = \sqrt{\frac{4\pi}{2\ell+1}}\, r^\ell\, Y^m_\ell(\theta, \phi). \tag{E.23}$$

This form highlights that a quadrupole transition can be interpreted as a "two-photon" excitation process: one unit of angular momentum is contributed by the polarization of the electric field, and another by the momentum of the propagating wave. This momentum from the propagating wave is proportional to $\left|\vec{k}\right| = \omega/c$, where the factor of $1/c \sim \alpha$, where α is the finestructure constant, shows that quadrupole transitions are weaker than dipole transitions.

E.3.2 Magnetic dipole transitions

According to Maxwell's equations, every electromagnetic wave consists of both an oscillating electric field and a corresponding magnetic field. Applying Faraday's law to the plane wave introduced above yields the magnetic field as

$$\vec{B}(\vec{r},t) = \frac{\vec{k}}{\omega} \times \vec{E}(\vec{r},t) \tag{E.24}$$

This expression shows that the magnetic field is in phase with the electric field but lies in a plane perpendicular to it. As a consequence, when the the electric field is circular polarized, the magnetic field is so as well. When the electric field is linearly polarized, the magnetic field is also linearly polarized, but in a plane perpendicular to the electric field.

A similar approach as above for the electric interaction energy, replacing the charge distribution with a current distribution and the scalar potential Φ with the vector potential $\vec{A}$, leads to the magnetic interaction energy [179]. In the dipole approximation, this contribution is given by

$$U_{\text{mag}} = -\left(B_+\mu_+ + B_-\mu_- + B_0\mu_0\right)\exp(-i\omega t) \tag{E.25}$$

where $\vec{\mu}$ denotes the atomic magnetic dipole moment, and again, each component in the spherical basis corresponds to a polarization of the magnetic field. As the amplitude of the magnetic field is proportional to $|k|/\omega = 1/c \sim \alpha$, the strength of the magnetic dipole transitions is also suppressed by a factor of α, and thus the magnetic dipole transitions have a strength similar to the electric quadrupole transitions.

E.3.3 The Floquet Hamiltonian

The complete Hamiltonian that describes the atom-light interaction is thus given as

$$H_{al} = -\sum_{q_E=-1}^{1}\left(d_{q_E}E_{q_E} + i\frac{\omega}{6c}\sum_{q_k=-1}^{1}k_{q_k}E_{q_E}Q_{q_kq_E} + \frac{1}{c}\mu_{\tilde{q_E}}E_{\tilde{q_E}}\right)\exp(-i\omega t) + \text{h.c.} \tag{E.26}$$

where $\tilde{q_E}$ takes into account that for $q_E = 0$, the magnetic field is linear polarized orthogonal to the π-polarized direction, and thus for $q_E = 0$, we define $\mu_{\tilde{q_E}=0}E_{\tilde{q_E}=0} = \mu_+E_+ + \mu_-E_-$. In the circular polarized cases, $\tilde{q_E} = q_E = \pm 1$. The Hermitian conjugate stems from reintroducing the complex conjugate part of the electric field.

In a complex multi-level system, multiple near-resonant transitions can generally be present, as illustrated later in Fig. E.7. Consequently, counter-rotating terms may

induce dynamics on other near-resonant transitions, and multiphoton processes may occur. Therefore, in such systems, the rotating wave approximation is typically not valid [179]. Instead, we apply the Floquet theorem, which solves the dynamics of a periodically driven system exactly, and which is reviewed in the context of many-body physics in [331, 332], and in the case for a two-level system in [333]. For the following discussion, we will mainly follow [332]. The idea behind the Floquet theorem is that a periodic Hamiltonian that satisfies $H(t) = H(t+T)$, where T is the period time, can be replaced by a time-independent Floquet Hamiltonian H_F such that the dynamics for the multiple integers of the period time, the time evolution can be replaced by an evolution with the Floquet Hamiltonian, i.e.

$$\mathcal{T} \exp\left(-\int_0^T H(t)dt\right) = \exp\left(-iH_F T\right), \tag{E.27}$$

where $\mathcal{T}$ denotes the time-ordering operator. Our goal is to find a numerical expression of H_F, as it accurately covers the dynamics on every integer multiple of T. For radiation at 24 GHz, which is the lowest frequency we can generate with the apparatus presented above, $T \approx 4\,\text{ps}$, which is three orders of magnitude smaller compared to the the experimental timescales of 4 ns to 8 ns. The Floquet-Hamiltonian thus captures the, compared to T, slow dynamics, which are relevant for the gate fidelity, while fast oscillations on timescales shorter than T are averaged out.

To numerically calculate H_F, we proceed by rewriting the Hamiltonian E.26 as

$$H = H_0 + H_{la} = H_0 + V\exp(-i\omega t) + V^\dagger \exp(i\omega t) \tag{E.28}$$

The Hamiltonian is of the form $H(t) = H(t+T)$ with $T = 2\pi/\omega$. According to the Floquet theorem, due to this discrete time-translation symmetry, the eigenstates $|\Psi_n\rangle$ follow

$$|\Psi_n(t)\rangle = e^{-i\epsilon_n t}\,|\Phi_n(t)\rangle\,; \quad |\Phi_n(t+T)\rangle = |\Phi_n(t)\rangle \tag{E.29}$$

where ϵ_n is the quasienergy of the Floquetstate Φ_n. Plugging this back into the Schrödinger equation, we find

$$\left(\epsilon_n + i\frac{d}{dt}\right)|\Phi_n(t)\rangle = H(t)\Phi_n(t) \tag{E.30}$$

Performing a Fourier series both on the Floquet states $|\Phi_n(t)\rangle = \sum_{m=-\infty}^{\infty} e^{-im\omega t}\left|\phi_n^{(m)}\right\rangle$ and on the Hamiltonian $H(t) = \sum_{m=-\infty}^{\infty} e^{-im\omega t}H^{(m)}$ and plugging the results into the Schrödinger equation yields

$$(\epsilon_n + m\omega)\left|\phi_n^{(m)}\right\rangle = \sum_{m'} H^{(m-m')}\left|\phi_n^{(m')}\right\rangle \tag{E.31}$$

By expanding the Hilbert space by "stacking up" the $\left|\phi_n^{(m)}\right\rangle$ for all m at a fixed n and subtracting the $m\omega$ contribution for each block, we obtain an eigenvalue equation [332]

$$\begin{pmatrix} \dots & \ddots & H^{(-1)} & H^{(-2)} & \dots \\ \dots & H^{(1)} & H^{(0)} - m\omega & H^{(-1)} & \dots \\ \dots & H^{(2)} & H^{(1)} & H^{(0)} - (m+1)\omega & \dots \\ \dots & \vdots & \vdots & \vdots & \ddots \end{pmatrix} \begin{pmatrix} \vdots \\ \phi_n^{(m)} \\ \phi_n^{(m+1)} \\ \vdots \end{pmatrix} = \epsilon_n \begin{pmatrix} \vdots \\ \phi_n^{(m)} \\ \phi_n^{(m+1)} \\ \vdots \end{pmatrix} \tag{E.32}$$

In our case of Eq. E.28, the only non-vanishing components of $H^{(m)}$ are found for $m = 0, \pm 1$, leading to a tri-diagonal matrix, which we truncate at $m = \pm n_{\text{photon}}$

$$H = \begin{pmatrix} H_0 + n_{\text{photon}}\omega & V & 0 & \dots \\ V^\dagger & H_0 + (n_{\text{photon}} - 1)\omega & V & \dots \\ \vdots & \ddots & \vdots & \vdots \\ 0 & \dots & V^\dagger & H_0 - n_{\text{photon}}\omega \end{pmatrix} \tag{E.33}$$

It becomes apparent why we chose the name n_{photon}. The atom-light interaction term V can be interpreted as the term where one virtual photon of energy ω is absorbed from the drive, thus increasing the energy of the bare hamiltonian by ω. The states we obtain by diagonalizing this Hamiltonian are the $\left|\phi_n^{(m)}\right\rangle$, where we write down H by taking $2n_{\text{photon}} + 1$ exact copies of the basis of H_0. This allows us to extract the exact time-tependence of a single Floquet state approximately:

$$|\Phi_n\rangle(t) = \sum_{m=-n_{\text{photon}}}^{n_{\text{photon}}} e^{-im\omega t} |\phi_n^m\rangle \tag{E.34}$$

This summation is possible because for every copy of the Hamiltonian, we used an identical basis. As we are not interested on the dynamics faster than T, it is sufficient to calculate

$$|\Phi_n\rangle \coloneqq |\Phi_n(t=0)\rangle = \sum_{m=-n_{\text{photon}}}^{n_{\text{photon}}} |\phi_n^m\rangle \tag{E.35}$$

However, from the dimension of the Hamiltonian, it becomes evident that by this construction, we obtain $(2n_{\text{photon}} + 1)\dim(H)$ eigenvectors, where we expect only $\dim(H)$. This redundant information comes from the definition of the $|\Phi_n(t)\rangle$, and is an artifact of the discrete time-translation symmetry.

Taking the Floquet theorem E.29 and shifting the quasienergy ϵ_n by a multiple integer of ω, we find

$$\begin{aligned} |\Psi_n(t)\rangle &= e^{-i\epsilon_n t} \sum_{m=-\infty}^{\infty} e^{-im\omega t} \left|\phi_n^{(m)}\right\rangle \\ &= e^{-i(\epsilon_n + m'\omega)t} \sum_{m=-\infty}^{\infty} e^{-i(m-m')\omega t} \left|\phi_n^{(m)}\right\rangle \\ &= e^{-i(\epsilon_n + m'\omega)t} \sum_{m=-\infty}^{\infty} e^{-im\omega t} \left|\phi_n^{(m+m')}\right\rangle \end{aligned} \tag{E.36}$$

Thus, eigenvectors with the same eigenenergy ϵ_n up to multiple integers of the drive frequency represent the same Floquet eigenstate. As such, these states are not linear independent, and at time $t = 0$, even identical, as $\sum_{m=-\infty}^{\infty} \left|\phi_n^{(m+m')}\right\rangle = \sum_{m=-\infty}^{\infty} \left|\phi_n^{(m)}\right\rangle$. We thus devise the following method to numerically extract the physical Floquet eigenstates:

1. We create the expanded Hilbert space and the diagonalize the Hamiltonian E.33, and obtain $(2n_{\text{photon}} + 1)\dim(H)$ eigenvectors with $(2n_{\text{photon}} + 1)\dim(H)$ entries each. For each eigenvector, we store the corresponding eigenenergy.

2. We numerically calculate the Floquet eigenvector at time zero, which corresponds to a block-wise summation of components within each individual eigenvector. This leads to $(2n_{\text{photon}} + 1)\dim(H)$ eigenvectors with $\dim(H)$ entries each. Each eigenvector is now presented in the basis of H_0 and V.

3. For each eigenenergy, we add or subtract multiple integers of ω until the eigenenergy is in an energy window of range ω. As the procedure is independent of the choice of the window, for convenience we use the window $(-\omega/2, \omega/2)$. We thus obtain an array of quasienergies for each of the $(2n_{\text{photon}} + 1)\dim(H)$ states.

4. We sort the quasienergies in increasing order, and group them in packages of $2n_{\text{photon}} + 1$. In the limit of $n_{\text{photon}} \to \infty$, the quasienergies in each of these windows should be exactly identical. Due to truncation, the exact quasienergy may vary slightly. We thus keep only a fraction p of the quasienergies in the center of each of the $2n_{\text{photon}} + 1$ package, as these values are almost identical and do not suffer from the truncation, while the highest and lowest value are stronger affected by truncation. For each package containing $p\,(2n_{\text{photon}} + 1)$, we take the mean and standard deviation of the mean as the numerically estimated value of the Floquet quasienergy ϵ_n.

5. We sort the eigenvectors in the exact same way as the quasienergies, and obtain packages of $p\,(2n_{\text{photon}}+1)$ eigenvectors. All of these vectors should be identical. We test this assumption by grouping these column vectors into a matrix and perform a singular value decomposition (SVD) on this matrix. We test that this matrix has rank zero, and the basis of this space is returned by the one-column matrix u in the SVD. This value u is the Floquet state to the quasienergy ϵ.

We thus arrive at $\dim(H)$ quasienergies ϵ_n with corresponding Floquet states $|u_n\rangle$, given in the basis specified for H and V. The Floquet Hamiltonian is thus the diagonal matrix containing all quasienergies ϵ_n on the diagonal, and the basis of the matrix is given by the corresponding Floquet states u_n. This procedure is applicable to all Hamiltonians of the form E.28, with one caveat: If there are l degenerate quasienergies, the eigenvectors in the $p\,(2n_{\text{photon}}+1)$ package are not identical, as they are linear combinations of the l basisvectors spanning the degenerate subspace. We thus need to adjust the algorithm in order to be able to detect these degeneracies. Therefore, we devise the following procedure after step 3.:

1. Sort the quasienergies in increasing order, and group them in packages of $2n_{\text{photon}}+1$.
2. Set $l=1$
3. Take the next package of $l\,(2n_{\text{photon}}+1)$ quasienergies. Keep only the $pl(2n_{\text{photon}}+1)$ central values.
4. Construct a matrix of the eigenvectors corresponding to these values. Perform an SVD on this matrix. If the rank of the matrix is larger than l: Increase $l \to l+1$ and go to 2.
5. If the rank equals l, the matrix U from the SVD contains in each column one eigenvector in the degenerate subspace. The corresponding Floquet energy is calculated by the mean of the $pl(2n_{\text{photon}}+1)$ quasienergy values.

This method thus enables the construction of the Floquet Hamiltonian. However, the SVD numerically needs to distinguish the value zero from numerical errors. In the SVD, we say a value if zero if its modulus is below the tolerance. The effectivity of the algorithm thus depends on an elaborate choice of the tolerance. If we take for example as tolerance the machine precision, the matrix will always have full rank, and the algorithm will not work.

In a best case scenario, there should be no quasienergy degeneracies. The problem of degeneracies arises in two cases:

- Two levels of H_0 differ numerically exactly (close to machine precision!) by the drive frequency ω and are **not!** coupled by V. This case is extremely rare.
- Two levels of H_0 are numerically exactly (close to machine precision!) degenerate and are **not!** coupled by V. In the case of a single atom, this is also almost never the case, while in the two-atom case, this happens multiple times, as will be discussed later. We will discuss how the validity of the numerics are verified in this case later.

If the incident radiation is weak, its effect on the system remains perturbative. In this regime, each Floquet eigenvector can be uniquely associated with the bare atomic eigenstate to which it has the largest overlap. This identification provides a natural labeling scheme for the dressed states. The corresponding Floquet eigenenergies then represent the energy shifts of these dressed states.

E.4 Numerical calculation of Rydberg atoms in the presence of a microwave drive

E.4.1 The effect of microwave radiation on a single multi-level Rydberg atom

We begin by validating our algorithm on a single Rubidium atom. This analysis focuses on the four relevant states introduced in Fig. E.1(b). Based on that level diagram, we define two main objectives:

1. Detune the two-level state $\left|41G, 45P_{1/2}\right\rangle$ from resonance. Since the $|41G\rangle$ state has negligible dipole-coupling to low L states, the microwave drive primarily affects the $\left|45P_{1/2}\right\rangle$ component.
2. Tune the interaction dynamics between the Förster resonances $|43D, 43D\rangle \leftrightarrow |41F, 45P\rangle$ and $|43D, 43D\rangle \leftrightarrow |42F, 44P\rangle$. These processes occur on a megahertz interaction scale, and thus require light shifts of comparable magnitude on the participating states to significantly alter their dynamics.

We now shift our focus from the two-atom level diagram in Fig. E.1(b) to the single-atom level structure shown in Fig. E.7. The pair states relevant for the Rydberg interaction are marked by green arrows. To strongly influence the dynamics between the two Förster resonances, we propose applying microwave radiation near-resonant with the $|43D\rangle \leftrightarrow |42F\rangle$ transition. This approach allows simultaneous tuning of the

detuning for both resonances. The microwave field is assumed to be σ_+-polarized, as required by selection rules. To suppress quadrupole coupling to the $|41G\rangle$ state, we consider light propagating along the z-axis, i.e., $\vec{k} = k_0\hat{e}_0$, which restricts allowed quadrupole transitions to those with $\Delta m_J = \pm 1$. Moreover, both the $|41F\rangle$ state and all states in the $45P$ manifold exhibit strong electric dipole couplings to nearby levels. As a result, these states are expected to experience large lightshifts.

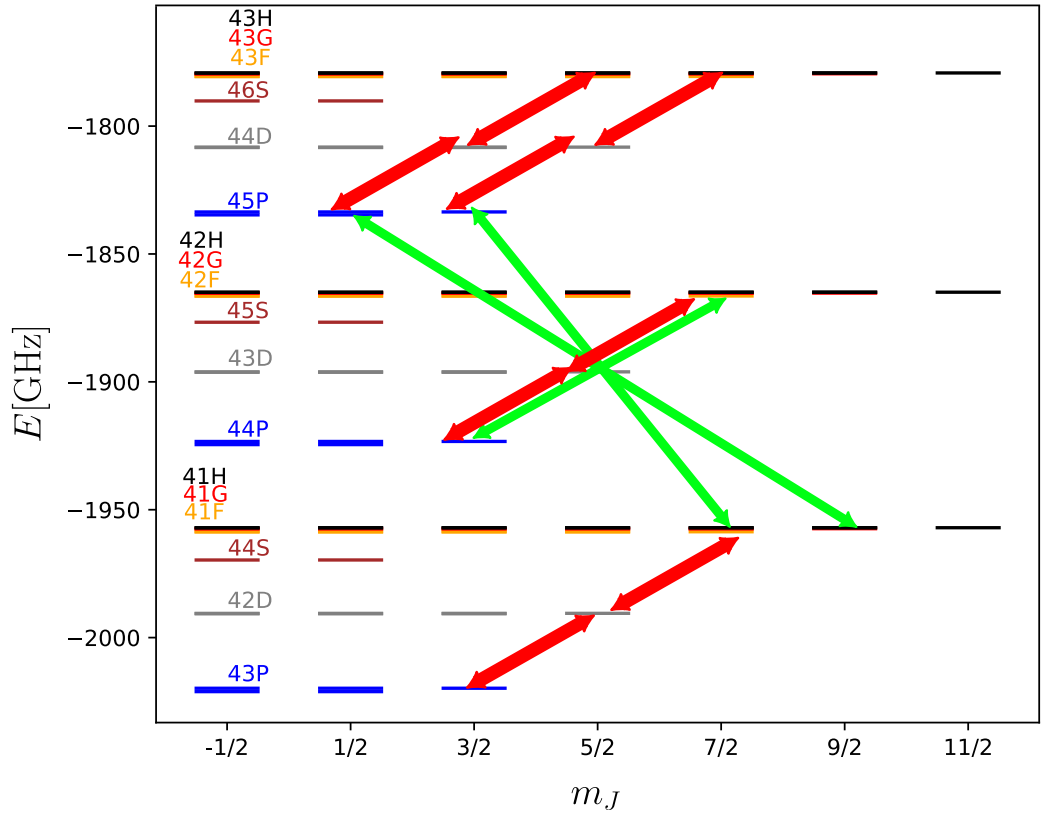

Figure E.7: *Level diagram of the most relevant states for a single atom.* P-states are shown as blue, D-states as gray, F-states as orange, G-states as red, and H-states as black bars. Green arrows denote the transitions to the pair states as shown in Fig. E.1(b). Red lines indicate transitions nearly resonant to the targeted transition.

All near-resonant transitions that couple to single-atom states populated during the entanglement gate are indicated by red arrows. In Tab. E.1 we list all the transition frequencies we calculated for a single Rubidium atom at an external field of 3 G, along which we choose to be aligned to the z-axis.

We observe that all these transitions are, up to a range from 1 GHz to 4 GHz,

Initial State	**Final State**	**Transition Frequency** [GHz]	**Dipole Moment** GHz/V/cm
$\|43P\rangle$	$\|42D\rangle$	29.28	1.82
$\|42D\rangle$	$\|41F\rangle$	31.89	1.87
$\|44P\rangle$	$\|43D\rangle$	27.22	1.91
$\|43D\rangle$	$\|42F\rangle$	29.66	1.97
$\|45P\rangle$	$\|44D\rangle$	25.34	2.00
$\|44D\rangle$	$\|43F\rangle$	27.63	2.06
$\left\|45P_{1/2}\right\rangle$	$\left\|44D_{3/2}\right\rangle$	26.34	1.81
$\left\|45D_{3/2}\right\rangle$	$\left\|43F_{7/2}\right\rangle$	27.77	1.99

Table E.1: Transition properties between the adressed single-particle states.

resonant with one-another, and that the dipole moments, relevant for coupling strength, is similar, thus leading to similar on-resonance Rabi frequencies on all these transitions.

We first want to test that our algorithm works on a single atoms. Therefore, we construct a Hamiltonian including the states depicted in the leveldiagram in Fig. E.7. We then extract the electric dipole and quadrupole moments as well as the magnetic dipole moments to calculate

$$V = -E\left(d_+ + \frac{1}{c}\mu_+\frac{i}{6}kQ_0^+\right) \tag{E.37}$$

where E is the strength of the electric field. We take the transition $|43D\rangle \leftrightarrow |42F\rangle$ as a reference and define the detuning as the difference of the microwave frequency with respect to that transition. We also characterize the electric field strength by the on-resonance Rabi frequency Ω on that transition. As a consequence, we calculate the free parameters E and k in the construction of V in Eq. E.37 as a function of Ω and Δ. For the algorithm to calculate the Floquet Hamiltonian, we choose $n_{\text{photon}} = 5$ and $p = 0.2$. As for the single atom we are mainly interested in the spectrum, we omit the full construction of the Hamiltonian, and construct only the Floquet energies. The light shift of a certain state is calculated by subtracting the obtained Floquet energy from the Floquet energy at $\Delta = \Omega = 0$.

Before discussing the results, we consider the general expectation that the relevant atomic states may either couple resonantly to a single nearby state or far off-resonantly to a few distant states, depending on the drive frequency. In such cases, a two-level approximation is often valid.

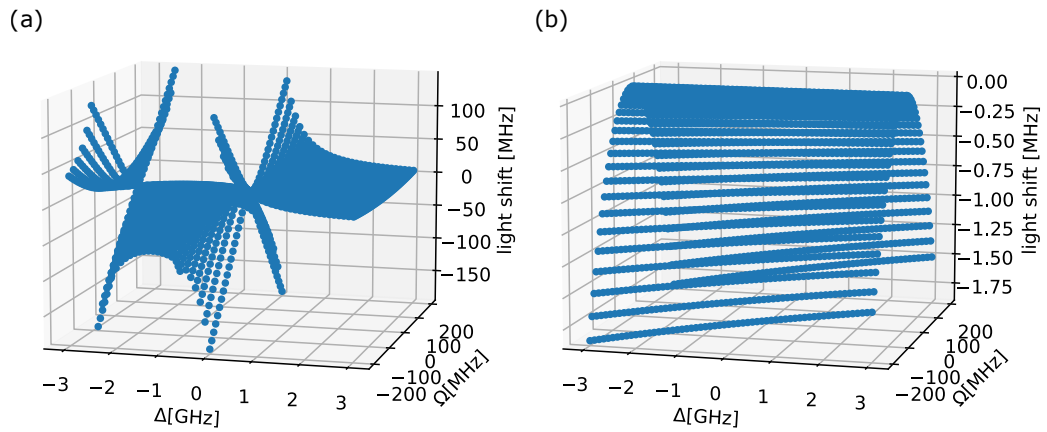

Figure E.8: *Lightshift of different staes in Rubidium.* The lightshift is shown as a function of detuning Δ and Rabi frequency Ω on the $|43D\rangle \leftrightarrow |42F\rangle$ transition. (a) The lighshift of the state $|43D\rangle$. (b) The lightshift of the state $|42G\rangle$.

Within this approximation, and under the rotating wave approximation (RWA), the light shift ΔE of a state coupled to another by a microwave field detuned by Δ from resonance is given by

$$\Delta E = \frac{\Omega^2}{4\Delta} \tag{E.38}$$

provided that the detuning satisfies $\Delta \gg \Omega$, where Ω is the on-resonance Rabi frequency.

The results are presented in Fig. E.8. For the level shift of the state $|43D\rangle$, we observe the expected $\frac{1}{\Delta}$ scaling predicted by the RWA [179]. Furthermore, the light shift exhibits a quadratic dependence on the Rabi frequency Ω for sufficiently small Ω. Two resonances appear where the sign of the light shift changes. The first, at $\Delta = 0$, corresponds to the $|43D\rangle \leftrightarrow |42F\rangle$ transition. The second, near $\Delta \approx -2\,\mathrm{GHz}$, is associated with the $|43D\rangle \leftrightarrow |44P\rangle$ transition. Between these two resonances, the $|43D\rangle$ state experiences negligible light shift, while the $|42F\rangle$ and $|44P\rangle$ states show increasing light shifts with Ω. This regime provides an optimal point for tuning the energy of the $|42F, 44P\rangle$ two-level system without significantly perturbing the $|43D, 43D\rangle$ state.

As a reference for a weakly interacting state, we chose the state $|42G\rangle$. Here, we observe that the lightshift is almost independent of the detuning, and shows only a weak linear increase, which signals in the light of the RWA a coupling to a far off-resonant state. The fact that even at high drive amplitudes, corresponding to a 200 MHz Rabi frequency on the $|43D\rangle \leftrightarrow |42F\rangle$ transition, the light shift increases

quadratically with the electric field, further corroborates this.

A brief analysis confirms that the observed light shift originates primarily from far off-resonant electric dipole transitions, rather than from electric quadrupole or magnetic dipole couplings. For an electric field strength of $E = 0.1\,\mathrm{V\,cm^{-1}}$, corresponding to $\Omega = 200\,\mathrm{MHz}$ on the $|43D\rangle \leftrightarrow |42F\rangle$ transition, the Rabi frequency of the dipole transition between $|42G\rangle$ and $|42F\rangle$ is 224 MHz. At a detuning of 27.5 GHz, this results in a light shift of 0.5 MHz, which constitutes the dominant contribution to the total light shift of 1.5 MHz. A comparable contribution arises from the transition to $\left|42H_{11/2}, m_J = 11/2\right\rangle$.

In contrast, the strongest electric quadrupole transition, to $\left|42G_{9/2}, m_J = 7/2\right\rangle$, yields a Rabi frequency of only 3.0 kHz. Given a detuning of 28.6 GHz, the resulting light shift is merely 0.08 mHz, and thus negligible. The strongest magnetic dipole coupling to $|42F\rangle$ produces an even smaller light shift of 0.03 mHz. This demonstrates that both magnetic dipole and electric quadrupole contributions are of the same negligible order of magnitude.

E.4.2 The effect of off-resonant microwave radiation on an ultrafast Rydberg gate

As the Floquet energies are accurately described by the Floquet quasienergies we constructed, we now apply the same method to the case of two interacting Rydberg atoms. We construct the two-atom Hilbert space as the product space of two single-atom Hilbert spaces. In order to reduce computational complexity, we truncate the single-atom Hilbert space to the 12 states listed in Tab. E.1, together with the state $|41G\rangle$. In order to be at the optimal point where the pairstate $|43D, 43D\rangle$ experiences a negligible light shift, while the pairstate $|42F, 44P\rangle$ shifts strongly, we choose to operate at a detuning of $\Delta = -1\,\mathrm{GHz}$, corresponding to a microwave frequency of 27.66 GHz. At this point, we examine the influence of the power of the microwave radiation. Therefore, we construct V according to Eq. E.37 for both $\Omega = 1\,\mathrm{Hz}$ and $\Omega = 1\,\mathrm{MHz}$. The construction for $\Omega = 1\,\mathrm{Hz}$ serves as a reference case to check that, at negligible field, the dynamics without field, as seen in Fig. E.3(a), is reproduced. We choose $\Omega = 1\,\mathrm{MHz}$ to test the behavior of the two-atom system at moderate drive power.

We construct the two-atom Hamiltonian including all pairstate combinations from the single-atom Hamiltonian, and take multipole interactions up to dipole-quadrupole interactions into account. We choose a distance of $r = 2.5\,\mu\mathrm{m}$ and assume a perfect alignment of $\theta = 0$ with the external magnetic field of 3 G. This constructed two-atom Hamiltonian $H_{\mathrm{two-atom}}$ serves as the time-independent Hamiltonian for the

Floquet algorithm. The time-dependent part arises solely due to the individual atoms interacting with the microwave drive. We thus obtain for the time-dependent part of the Hamiltonian

$$V_{\text{two-atom}} = V \otimes \mathbb{1} + \mathbb{1} \otimes V \tag{E.39}$$

From here, we can apply our algorithm that we used to calculate Floquet quasienergies and Floquet States. For the algorithm, we truncate at $n_{\text{photon}} = 3$, and use only a fraction of $p = 0.45$ of the quasienergies in a package. In order to test the consistency of the algorithm, we apply two sanity checks:

1. We test the orthogonality of the obtain Floquet states. We can group the Floquet states to a quadratic matrix B of dimension $\dim(H_{\text{two-atom}}) \times \dim(H_{\text{two-atom}})$ and varify for both values of Ω that

$$\max_{i,j} \left| \left(B^\dagger B - \mathbb{1} \right)_{ij} \right| < 1E-5 \tag{E.40}$$

2. We test the independence of the results on the tolerance. In both cases, we obtain the same Hamiltonian if we vary the tolerance from 5×10^{-7} to 1×10^{-11}, which are all orders of magnitude higher than the machine precision.

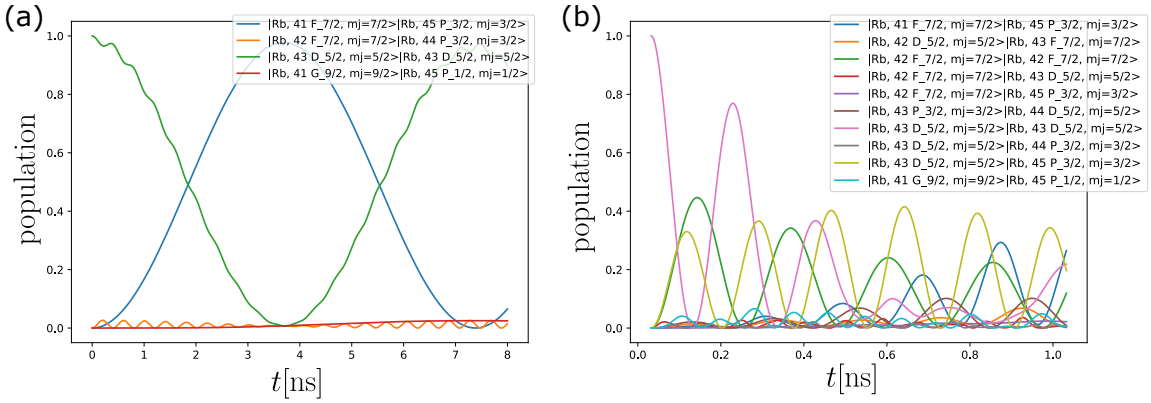

Figure E.9: *The effect of microwave radiation.* Population of all states with a contribution of more than 1 % are shown as a function of evolution time. (a). The Rabi frequency is set to $\Omega = 1\,\text{Hz}$ to test for the consistency of the simulation method. (b). The Rabi frequency is set to $\Omega = 1\,\text{MHz}$.

For the time evolution, the system is assumed to be initially in the state $|43D, 43D\rangle$, rather than in the dressed state with the largest overlap. This choice is justified

because the excitation pulse has a Rabi frequency of 60 GHz, which significantly exceeds any Rydberg-Rydberg or Rydberg-microwave interaction energy scale. At a microwave Rabi frequency of 1 Hz, Fig. E.9(a) shows that the time evolution of the Rydberg states in the entanglement gate remains unchanged, as expected.

At a moderate resonant Rabi frequency of 1 MHz on the $|43D\rangle \leftrightarrow |42F\rangle$ transition, detuned by 1 GHz, the numerical calculation suggests that multiple additional levels become off-resonantly populated, as shown in Fig. E.9(b). Remarkably, these levels exhibit significant dynamics on sub-nanosecond timescales, even though Rydberg interactions are on the order of 100 MHz and the drive frequency is detuned by at least 1 GHz from all single-photon transitions in the Hamiltonian of a single atom.

On possible explanation might already be found in the highly nonlinear dynamics of multilevel atomic systems. To further illuicated on this interpretation, we focus on the dynamics of the state $\left|41G, 45P_{1/2}\right\rangle$ in the absence of microwave radiation. As shown in Fig. E.1(b), this pair state is only weakly off-resonantly coupled, with a coupling strength of 6.8 MHz, to $|41F, 45P\rangle$, which in turn is strongly coupled to $|43D, 43D\rangle$. Assuming the states $|43D, 43D\rangle$ and $|41F, 45P\rangle$ are nearly degenerate, a simple Rabi model predicts that the population build-up over 8 ns, given a detuning of 30 MHz, is approximately 0.3 %. This prediction overestimates the actual population, since not all population is initially in $|41F, 45P\rangle$. However, in our simulation we observe the population exceeding even 2 %.

We conjecture that the unexpectedly large amplitude may stem from an interference between two Rydberg interaction coupling pathways. The first pathway is

$$|43D, 43D\rangle \leftrightarrow |41F, 45P\rangle \leftrightarrow \left|41G, 45P_{1/2}\right\rangle,$$

and the second is

$$|43D, 43D\rangle \leftrightarrow |42F, 44P\rangle \leftrightarrow \left|41G, 45P_{1/2}\right\rangle.$$

We thus may conjecture that in the presence of microwave radiation, similar effects may arise from multiple coupling paths connecting states such as $|43D, 43D\rangle$ and $|42F, 42F\rangle$. The Rydberg interaction strongly couples $|43D, 43D\rangle$ to $|42F, 44P\rangle$, which is near two-photon resonance with $|42F, 42F\rangle$ via the microwave drive. Additionally, the microwave off-resonantly couples $|43D, 43D\rangle$ directly to $|42F, 42F\rangle$, detuned by 2 GHz. We hypothesize that this complex multi-level structure, combined with GHz detunings, might be able to produce fast dynamics and unexpectedly large amplitudes, analogous to the population growth observed in $\left|41G, 45P_{1/2}\right\rangle$ on short timescales in the absence of microwave radiation. However, the dynamics exhibit large population variations exceeding 40 % on sub-nanosecond timescales. Therefore, it is

possible that, in the calculation of the Floquet eigenstates, some eigenvectors were numerically miscalculated due to the mentioned problem of degenerate subspaces, which could explain the observed strong dynamics.

We summarize that the $|43D\rangle \leftrightarrow |42F\rangle$ transition is the most effective for shifting the pair state $|42F, 44P\rangle$ relative to $|43D, 43D\rangle$, which is already visible from a single atom calculation. However, this transition is near-resonant to many other transitions. As a result, and suggested by the two-atom numerics, the system's dynamics cannot be accurately described by a model involving only three pairstates, making this transition unsuitable for realizing a high-fidelity CZ gate.

To improve the fidelity of a potential CZ gate, it is advantageous to minimize the number of involved states. One promising approach is to near-resonantly drive the $|45S\rangle \leftrightarrow |45P\rangle$ transition, which has a frequency of 43.12 GHz, and is nearly resonant with the $\left|45S_{-1/2}\right\rangle \leftrightarrow \left|45P_{1/2}\right\rangle$ transition at 41.98 GHz. This enables selective shifting of the pair states $\left|41G, 45P_{1/2}\right\rangle$ and $|41F, 45P\rangle$.

An optimal light shift occurs when the frequency is slightly red-detuned from the $\left|45S_{-1/2}\right\rangle \leftrightarrow \left|45P_{1/2}\right\rangle$ transition, for instance at 41.5 GHz. At this detuning, the pair state $\left|41G, 45P_{1/2}\right\rangle$ is shifted out of resonance, while $|41F, 45P\rangle$ is only slightly affected. Alternatively, blue-detuning the frequency above the $|45S\rangle \leftrightarrow |45P\rangle$ transition, for example at 43.7 GHz, enhances the lightshift on $|41F, 45P\rangle$, while still shifting $\left|41G, 45P_{1/2}\right\rangle$ out of resonance. This stronger lightshift may also give a further possibility to change the Förster detunings of the two Förster resonances depicted in Fig. E.1(b).

However, this blue-detuned approach also increases the admixture of the state $|45S, 41F\rangle$ in the gate dynamics. Since $|45S, 41F\rangle$ experiences only weak dipole-quadrupole interactions to $|43D, 43D\rangle$ and has a larger Förster detuning from $|43D, 43D\rangle$, it might be treated as approximately non-interacting during the gate operation. Therefore, dressing this transition may improve gate fidelity without significant admixture of other states.

E.4.3 Conclusion

In summary, complementing the main body of this thesis, we investigated the interaction between two strongly interacting Rydberg atoms beyond the two-level approximation, treating the atoms as multilevel systems. We explored how these interactions can be harnessed to implement a CZ gate on a nanosecond timescale. First, we studied the impact of positional uncertainties, finding that at a separation of 2.5 µm, the positional uncertainty must remain below 16 nm to limit gate fidelity

loss to less than 1×10^{-3}.

Next, we examined tuning Rydberg interactions via microwave radiation, aiming to modify the Förster defects between different pair states in the Rydberg manifold. To calculate light shifts affecting these defects, we developed an algorithm to construct the Floquet Hamiltonian and devised a method to overcome challenges posed by accidental degeneracies. This algorithm can be further improved by separately treating the two symmetry sectors arising from particle exchange, thereby avoiding most degeneracies.

Testing the algorithm on single-atom light shifts, we identified that driving the $|43D, 42F\rangle$ transition with a detuning of $\Delta = -1\,\mathrm{GHz}$ optimally tunes the Förster resonance between pair states relevant for the CZ gate. We analyzed how this drive influences gate fidelity: small microwave amplitudes leave the Rydberg dynamics largely unaffected, whereas the numerics suggest that already moderate amplitudes might induce population admixture of many additional Rydberg states, which would further reduce instead of improve the overall gate fidelity.

To improve gate stability, we proposed microwave dressing blue-detuned from the $|45S\rangle \leftrightarrow |45P\rangle$ transition, arguing that this approach may avoid the couplings to many untargeted Rydberg states as is likely the case for the $|43D\rangle \leftrightarrow |42F\rangle$ transition.

Bibliography

[1] Claudine Lacroix, Philippe Mendels, and Frédéric Mila, eds. *Introduction to Frustrated Magnetism: Materials, Experiments, Theory*. Vol. 164. Springer Series in Solid-State Sciences. Berlin, Heidelberg: Springer Berlin Heidelberg, 2011. ISBN: 978-3-642-10588-3. DOI: 10.1007/978-3-642-10589-0.

[2] Sergio Cecotti. "Frustrated and Quenched Systems". In: *Statistical Mechanics: A Concise Advanced Textbook*. Ed. by Sergio Cecotti. Cham: Springer Nature Switzerland, 2024, pp. 323–355. ISBN: 978-3-031-67874-5. DOI: 10.1007/978-3-031-67874-5_7.

[3] N. Davier et al. "Combined approach to analyze and classify families of classical spin liquids". In: *Physical Review B* 108.5 (2023), p. 054408. DOI: 10.1103/PhysRevB.108.054408.

[4] Han Yan et al. "Classification of classical spin liquids: Detailed formalism and suite of examples". In: *Physical Review B* 109.17 (2024), p. 174421. DOI: 10.1103/PhysRevB.109.174421.

[5] Yi Zhou, Kazushi Kanoda, and Tai-Kai Ng. "Quantum spin liquid states". In: *Reviews of Modern Physics* 89.2 (2017), p. 025003. DOI: 10.1103/RevModPhys.89.025003.

[6] C. Broholm et al. "Quantum spin liquids". In: *Science* 367.6475 (2020), eaay0668. DOI: 10.1126/science.aay0668.

[7] G. Semeghini et al. "Probing topological spin liquids on a programmable quantum simulator". In: *Science* 374.6572 (2021), pp. 1242–1247. DOI: 10.1126/science.abi8794.

[8] J.A. Mydosh. "Disordered magnetism and spin glasses". In: *Journal of Magnetism and Magnetic Materials* 157-158 (1996), pp. 606–610. ISSN: 03048853. DOI: 10.1016/0304-8853(95)01272-9.

[9] Ada Altieri and Marco Baity-Jesi. "An introduction to the theory of spin glasses". In: *Encyclopedia of Condensed Matter Physics (Second Edition)*. Ed. by Tapash Chakraborty. Oxford: Academic Press, 2024, pp. 361–370. ISBN: 978-0-323-91408-6. DOI: 10.1016/B978-0-323-90800-9.00249-3.

[10] Eric Vincent. "Spin glass experiments". In: *Encyclopedia of Condensed Matter Physics (Second Edition)*. Ed. by Tapash Chakraborty. Oxford: Academic Press, 2024, pp. 371–387. ISBN: 978-0-323-91408-6. DOI: 10.1016/B978-0-323-90800-9.00070-6.

[11] E. D. Dahlberg et al. *Spin-glass dynamics: experiment, theory and simulation*. arXiv:2412.08381 [cond-mat] version: 1. 2024. DOI: 10.48550/arXiv.2412.08381.

[12] Jennifer Freedberg and E. Dan Dahlberg. "A brief review of spin glass magnetometry techniques". In: *Frontiers in Physics* 12 (2024). ISSN: 2296-424X. DOI: 10.3389/fphy.2024.1447018.

[13] Eric Vincent et al. "Slow dynamics and aging in spin glasses". In: *Complex Behaviour of Glassy Systems*. Ed. by Miguel Rubí and Conrado Pérez-Vicente. Berlin, Heidelberg: Springer, 1997, pp. 184–219. ISBN: 978-3-540-69123-5. DOI: 10.1007/BFb0104827.

[14] M. Baity-Jesi et al. "Memory and rejuvenation effects in spin glasses are governed by more than one length scale". In: *Nature Physics* 19.7 (2023), pp. 978–985. ISSN: 1745-2481. DOI: 10.1038/s41567-023-02014-6.

[15] I. Paga et al. "Quantifying Memory in Spin Glasses". In: *Physical Review Letters* 133.25 (2024), p. 256704. ISSN: 0031-9007, 1079-7114. DOI: 10.1103/PhysRevLett.133.256704.

[16] G. Parisi. "Infinite Number of Order Parameters for Spin-Glasses". In: *Physical Review Letters* 43.23 (1979), pp. 1754–1756. DOI: 10.1103/PhysRevLett.43.1754.

[17] Daniel S. Fisher and David A. Huse. "Equilibrium behavior of the spin-glass ordered phase". In: *Physical Review B* 38.1 (1988), pp. 386–411. DOI: 10.1103/PhysRevB.38.386.

[18] Daniel S. Fisher and David A. Huse. "Nonequilibrium dynamics of spin glasses". In: *Physical Review B* 38.1 (1988), pp. 373–385. DOI: 10.1103/PhysRevB.38.373.

[19] Benedikt Placke et al. *Topological Quantum Spin Glass Order and its realization in qLDPC codes*. arXiv:2412.13248 [quant-ph]. 2024. DOI: 10.48550/arXiv.2412.13248.

[20] G. Kucsko et al. "Critical Thermalization of a Disordered Dipolar Spin System in Diamond". In: *Physical Review Letters* 121.2 (2018), p. 023601. DOI: 10.1103/PhysRevLett.121.023601.

[21] E. J. Davis et al. "Probing many-body dynamics in a two-dimensional dipolar spin ensemble". In: *Nature Physics* 19.6 (2023), pp. 836–844. ISSN: 1745-2481. DOI: 10.1038/s41567-023-01944-5.

[22] Lillian B. Hughes et al. "Strongly Interacting, Two-Dimensional, Dipolar Spin Ensembles in (111)-Oriented Diamond". In: *Physical Review X* 15.2 (2025), p. 021035. DOI: 10.1103/PhysRevX.15.021035.

[23] Bo Yan et al. "Observation of dipolar spin-exchange interactions with lattice-confined polar molecules". In: *Nature* 501.7468 (2013), pp. 521–525. ISSN: 1476-4687. DOI: 10.1038/nature12483.

[24] Lysander Christakis et al. "Probing site-resolved correlations in a spin system of ultracold molecules". In: *Nature* 614.7946 (2023), pp. 64–69. ISSN: 1476-4687. DOI: 10.1038/s41586-022-05558-4.

[25] Jun-Ru Li et al. "Tunable itinerant spin dynamics with polar molecules". In: *Nature* 614.7946 (2023), pp. 70–74. ISSN: 1476-4687. DOI: 10.1038/s41586-022-05479-2.

[26] Annie J. Park et al. "Extended Rotational Coherence of Polar Molecules in an Elliptically Polarized Trap". In: *Physical Review Letters* 131.18 (2023), p. 183401. DOI: 10.1103/PhysRevLett.131.183401.

[27] Thomas F. Gallagher. *Rydberg Atoms*. Cambridge Monographs on Atomic, Molecular and Chemical Physics. Cambridge: Cambridge University Press, 1994. ISBN: 978-0-521-02166-1. DOI: 10.1017/CBO9780511524530.

[28] Thomas F. Gallagher and Pierre Pillet. "Dipole–Dipole Interactions of Rydberg Atoms". In: *Advances In Atomic, Molecular, and Optical Physics*. Vol. 56. Elsevier, 2008, pp. 161–218. ISBN: 978-0-12-374290-2. DOI: 10.1016/S1049-250X(08)00013-X.

[29] M. Morgado and S. Whitlock. "Quantum simulation and computing with Rydberg-interacting qubits". In: *AVS Quantum Science* 3.2 (2021), p. 023501. ISSN: 2639-0213. DOI: 10.1116/5.0036562.

[30] Lingbang Zhu et al. “Probing Dipolar Interactions between Rydberg Atoms and Ultracold Polar Molecules”. In: *Physical Review Letters* 135.15 (2025), p. 153001. DOI: 10.1103/48rk-sxfs.

[31] T. F. Rosenbaum et al. “Dipolar ferromagnets and glasses (invited)”. In: *Journal of Applied Physics* 70.10 (1991), pp. 5946–5951. ISSN: 0021-8979, 1089-7550. DOI: 10.1063/1.350087.

[32] D. H. Reich et al. “Dipolar magnets and glasses: Neutron-scattering, dynamical, and calorimetric studies of randomly distributed Ising spins”. In: *Physical Review B* 42.7 (1990), pp. 4631–4644. ISSN: 0163-1829, 1095-3795. DOI: 10.1103/PhysRevB.42.4631.

[33] J. A. Quilliam et al. “Evidence of Spin Glass Dynamics in Dilute $LiHo_xY_{1-x}F_4$”. In: *Physical Review Letters* 101.18 (2008), p. 187204. DOI: 10.1103/PhysRevLett.101.187204.

[34] D. H. Reich, T. F. Rosenbaum, and G. Aeppli. “Glassy relaxation without freezing in a random dipolar-coupled Ising magnet”. In: *Physical Review Letters* 59.17 (1987), pp. 1969–1972. ISSN: 0031-9007. DOI: 10.1103/PhysRevLett.59.1969.

[35] S. Ghosh et al. “Coherent Spin Oscillations in a Disordered Magnet”. In: *Science* 296.5576 (2002), pp. 2195–2198. DOI: 10.1126/science.1070731.

[36] S. Ghosh et al. “Entangled quantum state of magnetic dipoles”. In: *Nature* 425.6953 (2003), pp. 48–51. ISSN: 1476-4687. DOI: 10.1038/nature01888.

[37] Moshe Schechter and Nicolas Laflorencie. “Quantum Spin Glass and the Dipolar Interaction”. In: *Physical Review Letters* 97.13 (2006), p. 137204. DOI: 10.1103/PhysRevLett.97.137204.

[38] Juan Carlos Andresen et al. “Existence of a Thermodynamic Spin-Glass Phase in the Zero-Concentration Limit of Anisotropic Dipolar Systems”. In: *Phys. Rev. X* 4.4 (2014), p. 041016. ISSN: 2160-3308. DOI: 10.1103/PhysRevX.4.041016.

[39] Wenhao Wu et al. “From classical to quantum glass”. In: *Physical Review Letters* 67.15 (1991), pp. 2076–2079. DOI: 10.1103/PhysRevLett.67.2076.

[40] Wenhao Wu et al. “Quenching of the nonlinear susceptibility at a T=0 spin glass transition”. In: *Physical Review Letters* 71.12 (1993), pp. 1919–1922. DOI: 10.1103/PhysRevLett.71.1919.

[41] J. Brooke et al. “Quantum Annealing of a Disordered Magnet”. In: *Science* 284.5415 (1999), pp. 779–781. DOI: 10.1126/science.284.5415.779.

[42] T. Franz et al. “Observation of anisotropy-independent magnetization dynamics in spatially disordered Heisenberg spin systems”. In: *Physical Review Research* 6.3 (2024), p. 033131. DOI: 10.1103/PhysRevResearch.6.033131.

[43] Titus Franz et al. *Absence of thermalization in an interacting system of thousands of quantum spins*. arXiv:2207.14216 [cond-mat, physics:physics, physics:quant-ph]. 2022. DOI: 10.48550/arXiv.2207.14216.

[44] Adolfo del Campo and Wojciech H. Zurek. “Universality of phase transition dynamics: Topological defects from symmetry breaking”. In: *International Journal of Modern Physics A* 29.08 (2014), p. 1430018. ISSN: 0217-751X. DOI: 10.1142/S0217751X1430018X.

[45] Piotr Sierant et al. “Many-body localization in the age of classical computing*”. In: *Reports on Progress in Physics* 88.2 (2025), p. 026502. ISSN: 0034-4885. DOI: 10.1088/1361-6633/ad9756.

[46] Jonas A. Kjäll, Jens H. Bardarson, and Frank Pollmann. “Many-Body Localization in a Disordered Quantum Ising Chain”. In: *Physical Review Letters* 113.10 (2014), p. 107204. DOI: 10.1103/PhysRevLett.113.107204.

[47] C. R. Laumann, A. Pal, and A. Scardicchio. “Many-Body Mobility Edge in a Mean-Field Quantum Spin Glass”. In: *Phys. Rev. Lett.* 113.20 (2014), p. 200405. ISSN: 0031-9007, 1079-7114. DOI: 10.1103/PhysRevLett.113.200405.

[48] Sebastian Geier et al. “Time-reversal in a dipolar quantum many-body spin system”. In: *Physical Review Research* 6.3 (2024), p. 033197. DOI: 10.1103/PhysRevResearch.6.033197.

[49] Matthew Newville et al. *LMFIT: Non-Linear Least-Squares Minimization and Curve-Fitting for Python*. 2025. DOI: 10.5281/zenodo.16175987.

[50] G. H. Wannier. “Antiferromagnetism. The Triangular Ising Net”. In: *Physical Review* 79.2 (1950), pp. 357–364. ISSN: 0031-899X. DOI: 10.1103/PhysRev.79.357.

[51] Sam Mugiraneza and Alannah M. Hallas. “Tutorial: a beginner’s guide to interpreting magnetic susceptibility data with the Curie-Weiss law”. In: *Communications Physics* 5.1 (2022), p. 95. ISSN: 2399-3650. DOI: 10.1038/s42005-022-00853-y.

[52] Steven T. Bramwell and Michel J. P. Gingras. “Spin Ice State in Frustrated Magnetic Pyrochlore Materials”. In: *Science* 294.5546 (2001), pp. 1495–1501. DOI: 10.1126/science.1064761.

[53] C. Castelnovo, R. Moessner, and S. L. Sondhi. "Spin Ice, Fractionalization, and Topological Order". In: *Annual Review of Condensed Matter Physics* 3.Volume 3, 2012 (2012), pp. 35–55. ISSN: 1947-5454, 1947-5462. DOI: 10.1146/annurev-conmatphys-020911-125058.

[54] Cristiano Nisoli, Roderich Moessner, and Peter Schiffer. "*Colloquium* : Artificial spin ice: Designing and imaging magnetic frustration". In: *Reviews of Modern Physics* 85.4 (2013), pp. 1473–1490. ISSN: 0034-6861, 1539-0756. DOI: 10.1103/RevModPhys.85.1473.

[55] Sandra H. Skjærvø et al. "Advances in artificial spin ice". In: *Nature Reviews Physics* 2.1 (2020), pp. 13–28. ISSN: 2522-5820. DOI: 10.1038/s42254-019-0118-3.

[56] Luca Berchialla, Gavin M. Macauley, and Laura J. Heyderman. "Focus on three-dimensional artificial spin ice". In: *Applied Physics Letters* 125.22 (2024), p. 220501. ISSN: 0003-6951. DOI: 10.1063/5.0229120.

[57] Rawnak Sultana et al. *Artificial Spin Ice: A Tutorial on Design and Control of Geometry, Microstate, Magnon Dynamics & Neuromorphic Computing*. arXiv:2504.06548 [cond-mat]. 2025. DOI: 10.48550/arXiv.2504.06548.

[58] P. W. Anderson. "Resonating valence bonds: A new kind of insulator?" In: *Materials Research Bulletin* 8.2 (1973), pp. 153–160. ISSN: 0025-5408. DOI: 10.1016/0025-5408(73)90167-0.

[59] R. Moessner and S. L. Sondhi. "Resonating Valence Bond Phase in the Triangular Lattice Quantum Dimer Model". In: *Physical Review Letters* 86.9 (2001), pp. 1881–1884. ISSN: 0031-9007, 1079-7114. DOI: 10.1103/PhysRevLett.86.1881.

[60] Maissam Barkeshli et al. "Symmetry fractionalization, defects, and gauging of topological phases". In: *Physical Review B* 100.11 (2019), p. 115147. ISSN: 2469-9950, 2469-9969. DOI: 10.1103/PhysRevB.100.115147.

[61] Jinsheng Wen et al. "Experimental identification of quantum spin liquids". In: *npj Quantum Materials* 4.1 (2019), p. 12. ISSN: 2397-4648. DOI: 10.1038/s41535-019-0151-6.

[62] Steven Kivelson and Shivaji Sondhi. "50 years of quantum spin liquids". In: *Nature Reviews Physics* 5.7 (2023), pp. 368–369. ISSN: 2522-5820. DOI: 10.1038/s42254-023-00596-x.

[63] Chandan Dasgupta and Shang-keng Ma. “Low-temperature properties of the random Heisenberg antiferromagnetic chain”. In: *Physical Review B* 22.3 (1980), pp. 1305–1319. DOI: 10.1103/PhysRevB.22.1305.

[64] R. N. Bhatt and P. A. Lee. “Scaling Studies of Highly Disordered Spin-1/2 Antiferromagnetic Systems”. In: *Physical Review Letters* 48.5 (1982), pp. 344–347. DOI: 10.1103/PhysRevLett.48.344.

[65] Daniel S. Fisher. “Random antiferromagnetic quantum spin chains”. In: *Physical Review B* 50.6 (1994), pp. 3799–3821. DOI: 10.1103/PhysRevB.50.3799.

[66] Ferenc Iglói and Cécile Monthus. “Strong disorder RG approach – a short review of recent developments”. In: *The European Physical Journal B* 91.11 (2018), p. 290. ISSN: 1434-6036. DOI: 10.1140/epjb/e2018-90434-8.

[67] Huan Tran and N. E. Bonesteel. “Valence bond entanglement and fluctuations in random singlet phases”. In: *Physical Review B* 84.14 (2011), p. 144420. DOI: 10.1103/PhysRevB.84.144420.

[68] Giorgio Parisi. “Nobel Lecture: Multiple equilibria”. In: *Reviews of Modern Physics* 95.3 (2023), p. 030501. DOI: 10.1103/RevModPhys.95.030501.

[69] Maria Chiara Angelini et al. “Unexpected Upper Critical Dimension for Spin Glass Models in a Field Predicted by the Loop Expansion around the Bethe Solution at Zero Temperature”. In: *Physical Review Letters* 128.7 (2022), p. 075702. ISSN: 0031-9007, 1079-7114. DOI: 10.1103/PhysRevLett.128.075702.

[70] F. Krzakala and O. C. Martin. “Spin and Link Overlaps in Three-Dimensional Spin Glasses”. In: *Physical Review Letters* 85.14 (2000), pp. 3013–3016. DOI: 10.1103/PhysRevLett.85.3013.

[71] Matteo Palassini and A. P. Young. “Nature of the Spin Glass State”. In: *Physical Review Letters* 85.14 (2000), pp. 3017–3020. DOI: 10.1103/PhysRevLett.85.3017.

[72] C. M. Newman and D. L. Stein. “Simplicity of state and overlap structure in finite-volume realistic spin glasses”. In: *Physical Review E* 57.2 (1998), pp. 1356–1366. DOI: 10.1103/PhysRevE.57.1356.

[73] C. M. Newman and D. L. Stein. “Finite-Dimensional Spin Glasses: States, Excitations, and Interfaces”. In: *Annales Henri Poincaré* 4.1 (2003), pp. 497–503. ISSN: 1424-0661. DOI: 10.1007/s00023-003-0939-5.

[74] M. A. Moore. "Droplet-scaling versus replica symmetry breaking debate in spin glasses revisited". In: *Physical Review E* 103.6 (2021), p. 062111. DOI: 10.1103/PhysRevE.103.062111.

[75] Ronen M. Kroeze et al. "Directly observing replica symmetry breaking in a vector quantum-optical spin glass". In: *Science* 389.6765 (2025), pp. 1122–1126. DOI: 10.1126/science.adu7710.

[76] Bharadwaj Vedula, M. A. Moore, and Auditya Sharma. "Nature of spin glass order in physical dimensions". In: *Physical Review E* 111.3 (2025), p. 034102. DOI: 10.1103/PhysRevE.111.034102.

[77] Benedikt Placke et al. *Expansion creates spin-glass order in finite-connectivity models: a rigorous and intuitive approach from the theory of LDPC codes*. arXiv:2507.13342 [cond-mat]. 2025. DOI: 10.48550/arXiv.2507.13342.

[78] T. Mizoguchi et al. "Measurement of the Spin-Glass Order Parameter in Amorphous $Gd_{0.37}Al_{0.63}$". In: *Physical Review Letters* 38.2 (1977), pp. 89–92. DOI: 10.1103/PhysRevLett.38.89.

[79] E. Vincent. "Ageing, Rejuvenation and Memory: The Example of Spin-Glasses". In: *Ageing and the Glass Transition*. Ed. by Malte Henkel, Michel Pleimling, and Roland Sanctuary. Lecture Notes in Physics. Berlin, Heidelberg: Springer, 2007, pp. 7–60. ISBN: 978-3-540-69684-1. DOI: 10.1007/3-540-69684-9_2.

[80] Kurt Binder and Allan Peter Young. "Spin glasses: Experimental facts, theoretical concepts, and open questions". In: *Rev. Mod. Phys.* 58.4 (1986), pp. 801–976. ISSN: 0034-6861. DOI: 10.1103/RevModPhys.58.801.

[81] P. A. Joy, P. S. Anil Kumar, and S. K. Date. "The relationship between field-cooled and zero-field-cooled susceptibilities of some ordered magnetic systems". In: *J. Phys.: Condens. Matter* 10.48 (1998), p. 11049. ISSN: 0953-8984. DOI: 10.1088/0953-8984/10/48/024.

[82] P A Joy and S K Date. "Comparison of the zero-field-cooled magnetization behavior of some ferromagnetic and ferrimagnetic systems". In: *Journal of Magnetism and Magnetic Materials* (2000).

[83] H. Mamiya et al. "Comparison of field-cooled, zero-field-cooled, and thermoremanent magnetization in nanomagnet, random magnet, and bulk ferromagnet". In: *Journal of Magnetism and Magnetic Materials*. Proceedings of the Joint European Magnetic Symposia 316.2 (2007), e535–e537. ISSN: 0304-8853. DOI: 10.1016/j.jmmm.2007.03.042.

[84] F. Tournus and A. Tamion. "Magnetic susceptibility curves of a nanoparticle assembly II. Simulation and analysis of ZFC/FC curves in the case of a magnetic anisotropy energy distribution". In: *Journal of Magnetism and Magnetic Materials* 323.9 (2011), pp. 1118–1127. ISSN: 03048853. DOI: 10.1016/j.jmmm.2010.11.057.

[85] E. B. Peixoto et al. "Analysis of zero field and field cooled magnetization curves of $Co\,Fe_2\,O_4$ nanoparticles with a T-dependence on the saturation magnetization". In: *Journal of Alloys and Compounds* 721 (2017), pp. 525–530. ISSN: 0925-8388. DOI: 10.1016/j.jallcom.2017.05.246.

[86] Sahil Pradhan et al. "Investigation of experimental signatures of spin glass transition temperature". In: *Frontiers in Physics* 12 (2024). ISSN: 2296-424X. DOI: 10.3389/fphy.2024.1482907.

[87] Sudip Pal et al. "Field-cooled state of the canonical spin glass revisited". In: *Physical Review B* 101.18 (2020), p. 180402. DOI: 10.1103/PhysRevB.101.180402.

[88] Sudip Pal et al. "Non-equilibrium magnetic response in concentrated spin-glass $Au_{0.89}Fe_{0.11}$ alloy". In: *Journal of Magnetism and Magnetic Materials* 570 (2023), p. 170504. ISSN: 0304-8853. DOI: 10.1016/j.jmmm.2023.170504.

[89] Dinesh Martien. *Introduction to AC Susceptibility*. URL: https://api.semanticscholar.org/CorpusID:38382001. 2001.

[90] V. Cannella and J. A. Mydosh. "Magnetic Ordering in Gold-Iron Alloys". In: *Physical Review B* 6.11 (1972), pp. 4220–4237. DOI: 10.1103/PhysRevB.6.4220.

[91] E. D. Dahlberg et al. "High-Frequency ac Susceptibility and ESR of a Spin-Glass". In: *Physical Review Letters* 42.6 (1979), pp. 401–404. DOI: 10.1103/PhysRevLett.42.401.

[92] J. L. Tholence. "On the frequency dependence of the transition temperature in spin glasses". In: *Solid State Communications* 35.2 (1980), pp. 113–117. ISSN: 0038-1098. DOI: 10.1016/0038-1098(80)90225-2.

[93] C. A. M. Mulder, A. J. van Duyneveldt, and J. A. Mydosh. "Frequency and field dependence of the ac susceptibility of the Au Mn spin-glass". In: *Physical Review B* 25.1 (1982), pp. 515–518. DOI: 10.1103/PhysRevB.25.515.

[94] Mouli Roy-Chowdhury, Mohindar S. Seehra, and Subhash Thota. "Optimized analysis of the AC magnetic susceptibility data in several spin-glass systems using the Vogel–Fulcher and Power laws". In: *AIP Advances* 13.11 (2023), p. 115020. ISSN: 2158-3226. DOI: 10.1063/5.0169800.

[95] Cheng Tien et al. "$Ce_2 Cu Ge_3$: A nonmagnetic atom-disorder spin glass". In: *Physical Review B* 61.18 (2000), pp. 12151–12158. DOI: 10.1103/PhysRevB.61.12151.

[96] Ajay Kumar, Anis Biswas, and Yaroslav Mudryk. *Unconventional magnetic glassiness in non-centrosymmetric Sm_7Pd_3: Interplay of magnetic frustration, long-range order, and frozen domains*. arXiv:2505.09532 [cond-mat]. 2025. DOI: 10.48550/arXiv.2505.09532.

[97] Anzar Ali et al. "Cluster spin glass state in $Ba_3 Sb_{1+x} Co_{2-x} O_{9-\delta}$: Cation disorder and mixed-valence Co dimers". In: *Physical Review B* 112.2 (2025), p. 024409. DOI: 10.1103/k7mm-g2zc.

[98] Zhen Ma et al. "Spin-Glass Ground State in a Triangular-Lattice Compound $Yb Zn Ga O_4$". In: *Physical Review Letters* 120.8 (2018), p. 087201. DOI: 10.1103/PhysRevLett.120.087201.

[99] Rahul Kumar, Premakumar Yanda, and A. Sundaresan. "Cluster-glass behavior in the two-dimensional triangular lattice Ising-spin compound $Li_2Mn_3O_7$". In: *Physical Review B* 103.21 (2021), p. 214427. DOI: 10.1103/PhysRevB.103.214427.

[100] S. Shtrikman and E.P. Wohlfarth. "The theory of the Vogel-Fulcher law of spin glasses". In: *Physics Letters A* 85.8-9 (1981), pp. 467–470. ISSN: 03759601. DOI: 10.1016/0375-9601(81)90441-2.

[101] J. L. Tholence. "A.C. susceptibility of Cu Mn and Ag Mn spin-glasses". In: *Physica B+C* 108.1 (1981), pp. 1287–1288. ISSN: 0378-4363. DOI: 10.1016/0378-4363(81)90943-8.

[102] Subir Sachdev. *Quantum Phase Transitions*. 2nd ed. Cambridge: Cambridge University Press, 2011. ISBN: 978-0-521-51468-2. DOI: 10.1017/CBO9780511973765.

[103] K. Gunnarsson et al. "Static scaling in a short-range Ising spin glass". In: *Physical Review B* 43.10 (1991), pp. 8199–8203. DOI: 10.1103/PhysRevB.43.8199.

[104] Laurent P. Lévy. "Critical dynamics of metallic spin glasses". In: *Physical Review B* 38.7 (1988), pp. 4963–4973. DOI: 10.1103/PhysRevB.38.4963.

[105] Tushar Kanti Bose, Roderich Moessner, and Arnab Sen. "Dipolar spin glass transition in three dimensions". In: *Phys. Rev. B* 100.6 (2019), p. 064425. DOI: 10.1103/PhysRevB.100.064425.

[106] Kai-Cheng Zhang, Yong Liu, and Feng Chi. "Dynamical Properties of a Diluted Dipolar-Interaction Heisenberg Spin Glass". In: *Communications in Theoretical Physics* 61.2 (2014), p. 257. ISSN: 0253-6102. DOI: 10.1088/0253-6102/61/2/19.

[107] Kai-Cheng Zhang, Gui-Bin Liu, and Yan Zhu. "Chiral-glass transition in a diluted dipolar-interaction Heisenberg system". In: *Physics Letters A* 375.20 (2011), pp. 2041–2046. ISSN: 03759601. DOI: 10.1016/j.physleta.2011.04.005.

[108] Sudip Mukherjee, Sabyasachi Nag, and Arti Garg. "Many-body localization-delocalization transition in the quantum Sherrington-Kirkpatrick model". In: *Physical Review B* 97.14 (2018), p. 144202. DOI: 10.1103/PhysRevB.97.144202.

[109] Louk Rademaker and Dmitry A. Abanin. "Slow Nonthermalizing Dynamics in a Quantum Spin Glass". In: *Physical Review Letters* 125.26 (2020), p. 260405. DOI: 10.1103/PhysRevLett.125.260405.

[110] Andrew D. King et al. "Quantum critical dynamics in a 5,000-qubit programmable spin glass". In: *Nature* 617.7959 (2023), pp. 61–66. ISSN: 1476-4687. DOI: 10.1038/s41586-023-05867-2.

[111] Hao Zhang, Kelly Boothby, and Alex Kamenev. "Cyclic quantum annealing: searching for deep low-energy states in 5000-qubit spin glass". In: *Scientific Reports* 14.1 (2024), p. 30784. ISSN: 2045-2322. DOI: 10.1038/s41598-024-80761-z.

[112] Mark Srednicki. "The approach to thermal equilibrium in quantized chaotic systems". In: *Journal of Physics A: Mathematical and General* 32.7 (1999), p. 1163. ISSN: 0305-4470. DOI: 10.1088/0305-4470/32/7/007.

[113] Rahul Nandkishore and David A. Huse. "Many-Body Localization and Thermalization in Quantum Statistical Mechanics". In: *Annual Review of Condensed Matter Physics* 6.1 (2015), pp. 15–38. ISSN: 1947-5454, 1947-5462. DOI: 10.1146/annurev-conmatphys-031214-014726.

[114] Luca D'Alessio et al. "From quantum chaos and eigenstate thermalization to statistical mechanics and thermodynamics". In: *Advances in Physics* 65.3 (2016), pp. 239–362. ISSN: 0001-8732. DOI: 10.1080/00018732.2016.1198134.

[115] Takashi Mori et al. “Thermalization and prethermalization in isolated quantum systems: a theoretical overview”. In: *Journal of Physics B: Atomic, Molecular and Optical Physics* 51.11 (2018), p. 112001. ISSN: 0953-4075. DOI: 10.1088/1361-6455/aabcdf.

[116] Masahito Ueda. “Quantum equilibration, thermalization and prethermalization in ultracold atoms”. In: *Nature Reviews Physics* 2.12 (2020), pp. 669–681. ISSN: 2522-5820. DOI: 10.1038/s42254-020-0237-x.

[117] J. M. Deutsch. “Quantum statistical mechanics in a closed system”. In: *Physical Review A* 43.4 (1991), pp. 2046–2049. DOI: 10.1103/PhysRevA.43.2046.

[118] Mark Srednicki. “Chaos and quantum thermalization”. In: *Physical Review E* 50.2 (1994), pp. 888–901. DOI: 10.1103/PhysRevE.50.888.

[119] P. W. Anderson. “Absence of Diffusion in Certain Random Lattices”. In: *Physical Review* 109.5 (1958), pp. 1492–1505. DOI: 10.1103/PhysRev.109.1492.

[120] E. Abrahams et al. “Scaling Theory of Localization: Absence of Quantum Diffusion in Two Dimensions”. In: *Physical Review Letters* 42.10 (1979), pp. 673–676. DOI: 10.1103/PhysRevLett.42.673.

[121] I. V. Gornyi, A. D. Mirlin, and D. G. Polyakov. “Interacting Electrons in Disordered Wires: Anderson Localization and Low-T Transport”. In: *Physical Review Letters* 95.20 (2005), p. 206603. DOI: 10.1103/PhysRevLett.95.206603.

[122] D. M. Basko, I. L. Aleiner, and B. L. Altshuler. “Metal–insulator transition in a weakly interacting many-electron system with localized single-particle states”. In: *Annals of Physics* 321.5 (2006), pp. 1126–1205. ISSN: 0003-4916. DOI: 10.1016/j.aop.2005.11.014.

[123] Vadim Oganesyan and David A. Huse. “Localization of interacting fermions at high temperature”. In: *Physical Review B* 75.15 (2007), p. 155111. DOI: 10.1103/PhysRevB.75.155111.

[124] John Z. Imbrie, Valentina Ros, and Antonello Scardicchio. “Local integrals of motion in many-body localized systems”. In: *Annalen der Physik* 529.7 (2017), p. 1600278. ISSN: 1521-3889. DOI: 10.1002/andp.201600278.

[125] Dmitry A. Abanin et al. “Colloquium: Many-body localization, thermalization, and entanglement”. In: *Reviews of Modern Physics* 91.2 (2019), p. 021001. DOI: 10.1103/RevModPhys.91.021001.

[126] Louk Rademaker, Miguel Ortuño, and Andres M. Somoza. "Many-body localization from the perspective of Integrals of Motion". In: *Annalen der Physik* 529.7 (2017), p. 1600322. ISSN: 1521-3889. DOI: 10.1002/andp.201600322.

[127] Maksym Serbyn, Z. Papić, and D. A. Abanin. "Quantum quenches in the many-body localized phase". In: *Physical Review B* 90.17 (2014), p. 174302. ISSN: 1098-0121, 1550-235X. DOI: 10.1103/PhysRevB.90.174302.

[128] Piotr Sierant, Dominique Delande, and Jakub Zakrzewski. "Many-body localization due to random interactions". In: *Physical Review A* 95.2 (2017), p. 021601. DOI: 10.1103/PhysRevA.95.021601.

[129] L. S Levitov. "Absence of Localization of Vibrational Modes Due to Dipole-Dipole Interaction". In: *Europhysics Letters (EPL)* 9.1 (1989), pp. 83–86. ISSN: 0295-5075, 1286-4854. DOI: 10.1209/0295-5075/9/1/015.

[130] L. S. Levitov. "Delocalization of vibrational modes caused by electric dipole interaction". In: *Physical Review Letters* 64.5 (1990), pp. 547–550. DOI: 10.1103/PhysRevLett.64.547.

[131] N. Y. Yao et al. "Many-Body Localization in Dipolar Systems". In: *Physical Review Letters* 113.24 (2014), p. 243002. DOI: 10.1103/PhysRevLett.113.243002.

[132] Giuseppe De Tomasi. "Algebraic many-body localization and its implications on information propagation". In: *Physical Review B* 99.5 (2019), p. 054204. DOI: 10.1103/PhysRevB.99.054204.

[133] Xiaolong Deng et al. "Universal Algebraic Growth of Entanglement Entropy in Many-Body Localized Systems with Power-Law Interactions". In: *Physical Review Letters* 125.1 (2020), p. 010401. ISSN: 0031-9007, 1079-7114. DOI: 10.1103/PhysRevLett.125.010401.

[134] X. Deng et al. "Duality in Power-Law Localization in Disordered One-Dimensional Systems". In: *Physical Review Letters* 120.11 (2018), p. 110602. DOI: 10.1103/PhysRevLett.120.110602.

[135] Thomas Botzung et al. "Algebraic localization from power-law couplings in disordered quantum wires". In: *Physical Review B* 100.15 (2019), p. 155136. ISSN: 2469-9950, 2469-9969. DOI: 10.1103/PhysRevB.100.155136.

[136] Adith Sai Aramthottil et al. "Phenomenology of Many-Body Localization in Bond-Disordered Spin Chains". In: *Physical Review Letters* 133.19 (2024), p. 196302. DOI: 10.1103/PhysRevLett.133.196302.

[137] Shenglong Xu and Brian Swingle. "Scrambling Dynamics and Out-of-Time-Ordered Correlators in Quantum Many-Body Systems". In: *PRX Quantum* 5.1 (2024), p. 010201. DOI: 10.1103/PRXQuantum.5.010201.

[138] A. I. Larkin and Yu. N. Ovchinnikov. "Quasiclassical Method in the Theory of Superconductivity". In: *Soviet Journal of Experimental and Theoretical Physics* 28 (1969), p. 1200. ISSN: 1063-7761.

[139] Juan Maldacena, Stephen H. Shenker, and Douglas Stanford. "A bound on chaos". In: *Journal of High Energy Physics* 2016.8 (2016), p. 106. ISSN: 1029-8479. DOI: 10.1007/JHEP08(2016)106.

[140] J. Baum et al. "Multiple-quantum dynamics in solid state NMR". In: *The Journal of Chemical Physics* 83.5 (1985), pp. 2015–2025. ISSN: 0021-9606, 1089-7690. DOI: 10.1063/1.449344.

[141] Michael Munowitz, Alexander Pines, and Michael Mehring. "Multiple-quantum dynamics in NMR: A directed walk through Liouville space". In: *The Journal of Chemical Physics* 86.6 (1987), pp. 3172–3182. ISSN: 0021-9606. DOI: 10.1063/1.452028.

[142] Gonzalo A. Álvarez, Dieter Suter, and Robin Kaiser. "Localization-delocalization transition in the dynamics of dipolar-coupled nuclear spins". In: *Science* 349.6250 (2015), pp. 846–848. DOI: 10.1126/science.1261160.

[143] Beni Yoshida and Norman Y. Yao. "Disentangling Scrambling and Decoherence via Quantum Teleportation". In: *Physical Review X* 9.1 (2019), p. 011006. ISSN: 2160-3308. DOI: 10.1103/PhysRevX.9.011006.

[144] Federico D. Domínguez et al. "Decoherence scaling transition in the dynamics of quantum information scrambling". In: *Physical Review A* 104.1 (2021), p. 012402. DOI: 10.1103/PhysRevA.104.012402.

[145] Gonzalo A. Álvarez and Dieter Suter. "NMR Quantum Simulation of Localization Effects Induced by Decoherence". In: *Physical Review Letters* 104.23 (2010), p. 230403. DOI: 10.1103/PhysRevLett.104.230403.

[146] Gonzalo A. Álvarez, Robin Kaiser, and Dieter Suter. "Quantum simulations of localization effects with dipolar interactions". In: *Annalen der Physik* 525.10-11 (2013), pp. 833–844. ISSN: 1521-3889. DOI: 10.1002/andp.201300096.

[147] Ken Xuan Wei, Chandrasekhar Ramanathan, and Paola Cappellaro. "Exploring Localization in Nuclear Spin Chains". In: *Physical Review Letters* 120.7 (2018), p. 070501. DOI: 10.1103/PhysRevLett.120.070501.

[148] Martin Gärttner et al. “Measuring out-of-time-order correlations and multiple quantum spectra in a trapped-ion quantum magnet”. In: *Nature Physics* 13.8 (2017), pp. 781–786. ISSN: 1745-2473, 1745-2481. DOI: 10.1038/nphys4119.

[149] Martin Gärttner, Philipp Hauke, and Ana Maria Rey. “Relating Out-of-Time-Order Correlations to Entanglement via Multiple-Quantum Coherences”. In: *Physical Review Letters* 120.4 (2018), p. 040402. DOI: 10.1103/PhysRevLett.120.040402.

[150] Maksym Serbyn and Dmitry A. Abanin. “Loschmidt echo in many-body localized phases”. In: *Physical Review B* 96.1 (2017), p. 014202. DOI: 10.1103/PhysRevB.96.014202.

[151] Pablo R. Zangara et al. “Loschmidt echo as a robust decoherence quantifier for many-body systems”. In: *Physical Review A* 86.1 (2012), p. 012322. ISSN: 1050-2947, 1094-1622. DOI: 10.1103/PhysRevA.86.012322.

[152] J. Smith et al. “Many-body localization in a quantum simulator with programmable random disorder”. In: *Nature Physics* 12.10 (2016), pp. 907–911. ISSN: 1745-2481. DOI: 10.1038/nphys3783.

[153] Christoph Hofmann. “Emergence of correlations in strongly interacting ultracold Rydberg gases”. PhD thesis. 2013.

[154] Hanna Schempp. “Formation of Aggregates and Energy Transport in Ultracold Rydberg Interacting Gases”. PhD thesis. 2014.

[155] A. Signoles et al. “Glassy Dynamics in a Disordered Heisenberg Quantum Spin System”. In: *Phys. Rev. X* 11.1 (2021), p. 011011. DOI: 10.1103/PhysRevX.11.011011.

[156] Titus Franz. “Studies of out-of-equilibrium dynamics of disordered Heisenberg spin models on a Rydberg quantum simulator - How the emergence of localized clusters induces glassy dynamics and inhibits thermalization”. PhD thesis. 2022.

[157] Sebastian Jonas Geier. “Shaping the Hamiltonian of many-body spin systems on a Rydberg-atom quantum simulator - How periodic driving and spin-encoding states tune the dynamics of strongly interacting quantum systems”. PhD thesis. 2024.

[158] W. R. Anderson, J. R. Veale, and T. F. Gallagher. “Resonant Dipole-Dipole Energy Transfer in a Nearly Frozen Rydberg Gas”. In: *Physical Review Letters* 80.2 (1998), pp. 249–252. ISSN: 0031-9007, 1079-7114. DOI: 10.1103/PhysRevLett.80.249.

[159] I. Mourachko. "Many-Body Effects in a Frozen Rydberg Gas". In: *Physical Review Letters* 80.2 (1998), pp. 253–256. DOI: 10.1103/PhysRevLett.80.253.

[160] M. Reetz-Lamour. "Rabi Oscillations and Excitation Trapping in the Coherent Excitation of a Mesoscopic Frozen Rydberg Gas". In: *Physical Review Letters* 100.25 (2008). DOI: 10.1103/PhysRevLett.100.253001.

[161] C. S. Hofmann et al. "An experimental approach for investigating many-body phenomena in Rydberg-interacting quantum systems". In: *Frontiers of Physics* 9.5 (2014), pp. 571–586. ISSN: 2095-0470. DOI: 10.1007/s11467-013-0396-7.

[162] M. D. Lukin et al. "Dipole Blockade and Quantum Information Processing in Mesoscopic Atomic Ensembles". In: *Phys. Rev. Lett.* 87.3 (2001), p. 037901. DOI: 10.1103/PhysRevLett.87.037901.

[163] Hendrik Weimer et al. "Quantum Critical Behavior in Strongly Interacting Rydberg Gases". In: *Physical Review Letters* 101.25 (2008), p. 250601. ISSN: 0031-9007, 1079-7114. DOI: 10.1103/PhysRevLett.101.250601.

[164] Alpha Gaëtan et al. "Observation of collective excitation of two individual atoms in the Rydberg blockade regime". In: *Nature Phys* 5.2 (2009), pp. 115–118. ISSN: 1745-2481. DOI: 10.1038/nphys1183.

[165] E. Urban et al. "Observation of Rydberg blockade between two atoms". In: *Nature Phys* 5.2 (2009), pp. 110–114. ISSN: 1745-2481. DOI: 10.1038/nphys1178.

[166] M Ferreira-Cao et al. "Depletion imaging of Rydberg atoms in cold atomic gases". In: *Journal of Physics B: Atomic, Molecular and Optical Physics* 53.8 (2020), p. 084004. ISSN: 0953-4075. DOI: 10.1088/1361-6455/ab7427.

[167] Sebastian Weber et al. "Calculation of Rydberg interaction potentials". In: *J. Phys. B: At. Mol. Opt. Phys.* 50.13 (2017), p. 133001. ISSN: 0953-4075. DOI: 10.1088/1361-6455/aa743a.

[168] Sebastian Geier et al. "Floquet Hamiltonian engineering of an isolated many-body spin system". In: *Science* 374.6571 (2021), pp. 1149–1152. DOI: 10.1126/science.abd9547.

[169] Moritz Hornung et al. *Observation of hysteresis in an isolated quantum system of disordered Heisenberg spins*. arXiv:2508.18197 [quant-ph]. 2025. DOI: 10.48550/arXiv.2508.18197.

[170] Daniel Barredo et al. "Coherent Excitation Transfer in a Spin Chain of Three Rydberg Atoms". In: *Physical Review Letters* 114.11 (2015), p. 113002. DOI: 10.1103/PhysRevLett.114.113002.

[171] Sylvain Ravets et al. “Measurement of the angular dependence of the dipole-dipole interaction between two individual Rydberg atoms at a Förster resonance”. In: *Physical Review A* 92.2 (2015), p. 020701. DOI: 10.1103/PhysRevA.92.020701.

[172] A.P. Piñeiro Orioli et al. “Relaxation of an Isolated Dipolar-Interacting Rydberg Quantum Spin System”. In: *Physical Review Letters* 120.6 (2018), p. 063601. ISSN: 0031-9007. DOI: 10.1103/PhysRevLett.120.063601.

[173] Cheng Chen et al. “Continuous symmetry breaking in a two-dimensional Rydberg array”. In: *Nature* 616.7958 (2023), pp. 691–695. ISSN: 1476-4687. DOI: 10.1038/s41586-023-05859-2.

[174] Guillaume Bornet et al. “Enhancing a Many-Body Dipolar Rydberg Tweezer Array with Arbitrary Local Controls”. In: *Physical Review Letters* 132.26 (2024), p. 263601. DOI: 10.1103/PhysRevLett.132.263601.

[175] B. W. Silverman. *Density Estimation for Statistics and Data Analysis*. Monographs on Statistics and Applied Probability. Boston, MA: Springer, 1986. ISBN: 978-1-4899-3324-9. DOI: 10.1007/978-1-4899-3324-9.

[176] David W. Scott. *Multivariate density estimation: theory, practice, and visualization*. Second edition. Hoboken, New Jersey: John Wiley & Sons, Inc, 2015. ISBN: 978-0-471-69755-8.

[177] Daniel A. Steck. *Rubidium 87 D Line Data*. http://steck.us/alkalidata. Revision 2.3.4, 8 August 2025. 2025.

[178] Miguel Ferreira Cao. “Control and characterisation of a Rydberg spin system to explore many-body physics”. PhD thesis. 2017.

[179] Daniel A. Steck. *Quantum and Atom Optics*. http://steck.us/teaching. Revision 0.16.5, 18 August 2025. 2025.

[180] Hornung, Moritz. “Memory Effects and Aging - Ergodicity Breaking Behaviour in Isolated Quantum Systems”. MA thesis. 2023.

[181] Philipp Hauke et al. “Perspectives of quantum annealing: methods and implementations”. In: *Rep. Prog. Phys.* 83.5 (2020), p. 054401. ISSN: 0034-4885. DOI: 10.1088/1361-6633/ab85b8.

[182] Ryogo Kubo. “Statistical-Mechanical Theory of Irreversible Processes. I. General Theory and Simple Applications to Magnetic and Conduction Problems”. In: *J. Phys. Soc. Jpn.* 12.6 (1957), pp. 570–586. ISSN: 0031-9015. DOI: 10.1143/JPSJ.12.570.

[183] R Kubo. "The fluctuation-dissipation theorem". In: *Reports on Progress in Physics* 29.255 (1966).

[184] M. Wolf, J. Gleitzmann, and W. Gey. "Relaxation-caused suppression of magnetization in superconducting $YBa_2Cu_3O_{7-\delta}$ single crystals". In: *Phys. Rev. B* 47.13 (1993), pp. 8381–8384. ISSN: 0163-1829, 1095-3795. DOI: 10.1103/PhysRevB.47.8381.

[185] Sultan Mahmud. "Field cooled and zero-field cooled magnetic effect on Cr-substituted Fe based amorphous $Fe_{73.5-x}Cr_xCu_1Nb_3Si_{13.5}B_9$ alloys". In: *International Journal of Materials Science (IJoMS)* 12 (2017), pp. 17–23.

[186] Adrian Braemer et al. "Pair localization in dipolar systems with tunable positional disorder". In: *Physical Review B* 106.13 (2022), p. 134212. DOI: 10.1103/PhysRevB.106.134212.

[187] Daniel S. Fisher. "Random transverse field Ising spin chains". In: *Physical Review Letters* 69.3 (1992), pp. 534–537. DOI: 10.1103/PhysRevLett.69.534.

[188] Ferenc Iglói and Cécile Monthus. "Strong disorder RG approach of random systems". In: *Physics Reports* 412.5 (2005), pp. 277–431. ISSN: 0370-1573. DOI: 10.1016/j.physrep.2005.02.006.

[189] P. Nordblad et al. "Time decay of the remanent magnetization in a CuMn spin glass". In: *Physical Review B* 33.1 (1986), pp. 645–648. DOI: 10.1103/PhysRevB.33.645.

[190] Michel J. P. Gingras and Patrik Henelius. "Collective Phenomena in the $LiHo_xY_{1-x}F_4$ Quantum Ising Magnet: Recent Progress and Open Questions". In: *Journal of Physics: Conference Series* 320.1 (2011), p. 012001. ISSN: 1742-6596. DOI: 10.1088/1742-6596/320/1/012001.

[191] T. W. B. Kibble. "Topology of cosmic domains and strings". In: *Journal of Physics A: Mathematical and General* 9.8 (1976), p. 1387. ISSN: 0305-4470. DOI: 10.1088/0305-4470/9/8/029.

[192] W. H. Zurek. "Cosmological experiments in superfluid helium?" In: *Nature* 317.6037 (1985), pp. 505–508. ISSN: 1476-4687. DOI: 10.1038/317505a0.

[193] W. H. Zurek. "Cosmological experiments in condensed matter systems". In: *Physics Reports* 276.4 (1996), pp. 177–221. ISSN: 0370-1573. DOI: 10.1016/S0370-1573(96)00009-9.

[194] Erica Grant. "Benchmarking Quantum Annealing Controls with Portfolio Optimization". In: *Physical Review Applied* 15.1 (2021). DOI: 10.1103/PhysRevApplied.15.014012.

[195] David Subires. “Benchmarking quantum annealing dynamics: The spin-vector Langevin model”. In: *Physical Review Research* 4.2 (2022). DOI: 10.1103/PhysRevResearch.4.023104.

[196] Seongmin Kim et al. “Quantum annealing for combinatorial optimization: a benchmarking study”. In: *npj Quantum Information* 11.1 (2025), p. 77. ISSN: 2056-6387. DOI: 10.1038/s41534-025-01020-1.

[197] M. C. Cross and P. C. Hohenberg. “Pattern formation outside of equilibrium”. In: *Reviews of Modern Physics* 65.3 (1993), pp. 851–1112. ISSN: 0034-6861, 1539-0756. DOI: 10.1103/RevModPhys.65.851.

[198] S. Ducci et al. “Order Parameter Fragmentation after a Symmetry-Breaking Transition”. In: *Physical Review Letters* 83.25 (1999), pp. 5210–5213. ISSN: 0031-9007, 1079-7114. DOI: 10.1103/PhysRevLett.83.5210.

[199] S. Casado, W. González-Viñas, and H. Mancini. “Testing the Kibble-Zurek mechanism in Rayleigh-Bénard convection”. In: *Physical Review E* 74.4 (2006), p. 047101. DOI: 10.1103/PhysRevE.74.047101.

[200] S. Casado et al. “The birth of defects in pattern formation: Testing of the Kibble–Zurek mechanism”. In: *The European Physical Journal Special Topics* 146.1 (2007), pp. 87–98. ISSN: 1951-6401. DOI: 10.1140/epjst/e2007-00171-2.

[201] Peter Ashcroft and Tobias Galla. “Pattern formation in individual-based systems with time-varying parameters”. In: *Physical Review E* 88.6 (2013), p. 062104. DOI: 10.1103/PhysRevE.88.062104.

[202] M. A. Miranda et al. “Frozen dynamics and synchronization through a secondary symmetry-breaking bifurcation”. In: *Physical Review E* 87.3 (2013), p. 032902. ISSN: 1539-3755, 1550-2376. DOI: 10.1103/PhysRevE.87.032902.

[203] C. J. O. Reichhardt, A. del Campo, and C. Reichhardt. “Kibble-Zurek mechanism for nonequilibrium phase transitions in driven systems with quenched disorder”. In: *Communications Physics* 5.1 (2022), p. 173. ISSN: 2399-3650. DOI: 10.1038/s42005-022-00952-w.

[204] K. Sengupta, Diptiman Sen, and Shreyoshi Mondal. “Exact Results for Quench Dynamics and Defect Production in a Two-Dimensional Model”. In: *Physical Review Letters* 100.7 (2008), p. 077204. ISSN: 0031-9007, 1079-7114. DOI: 10.1103/PhysRevLett.100.077204.

[205] A. del Campo, T. W. B. Kibble, and W. H. Zurek. "Causality and non-equilibrium second-order phase transitions in inhomogeneous systems". In: *Journal of Physics: Condensed Matter* 25.40 (2013), p. 404210. ISSN: 0953-8984. DOI: 10.1088/0953-8984/25/40/404210.

[206] F. J. Gómez-Ruiz and A. del Campo. "Universal Dynamics of Inhomogeneous Quantum Phase Transitions: Suppressing Defect Formation". In: *Physical Review Letters* 122.8 (2019), p. 080604. ISSN: 0031-9007, 1079-7114. DOI: 10.1103/PhysRevLett.122.080604.

[207] S. Ulm et al. "Observation of the Kibble–Zurek scaling law for defect formation in ion crystals". In: *Nature Communications* 4.1 (2013), p. 2290. ISSN: 2041-1723. DOI: 10.1038/ncomms3290.

[208] Adolfo Del Campo. "Universal Statistics of Topological Defects Formed in a Quantum Phase Transition". In: *Physical Review Letters* 121.20 (2018), p. 200601. ISSN: 0031-9007, 1079-7114. DOI: 10.1103/PhysRevLett.121.200601.

[209] Fernando J. Gómez-Ruiz, Jack J. Mayo, and Adolfo del Campo. "Full Counting Statistics of Topological Defects after Crossing a Phase Transition". In: *Physical Review Letters* 124.24 (2020), p. 240602. DOI: 10.1103/PhysRevLett.124.240602.

[210] Yuki Bando et al. "Probing the universality of topological defect formation in a quantum annealer: Kibble-Zurek mechanism and beyond". In: *Physical Review Research* 2.3 (2020), p. 033369. ISSN: 2643-1564. DOI: 10.1103/PhysRevResearch.2.033369.

[211] Jin-Ming Cui et al. "Experimentally testing quantum critical dynamics beyond the Kibble–Zurek mechanism". In: *Communications Physics* 3.1 (2020), pp. 1–7. ISSN: 2399-3650. DOI: 10.1038/s42005-020-0306-6.

[212] Jack J. Mayo et al. "Distribution of kinks in an Ising ferromagnet after annealing and the generalized Kibble-Zurek mechanism". In: *Physical Review Research* 3.3 (2021), p. 033150. DOI: 10.1103/PhysRevResearch.3.033150.

[213] Fan Zhang and H. T. Quan. "Work statistics across a quantum critical surface". In: *Physical Review E* 105.2 (2022), p. 024101. ISSN: 2470-0045, 2470-0053. DOI: 10.1103/PhysRevE.105.024101.

[214] Victor Mukherjee, Amit Dutta, and Diptiman Sen. "Defect generation in a spin-1 2 transverse X Y chain under repeated quenching of the transverse field". In: *Physical Review B* 77.21 (2008), p. 214427. ISSN: 1098-0121, 1550-235X. DOI: 10.1103/PhysRevB.77.214427.

[215] Uma Divakaran and Amit Dutta. "Reverse quenching in a one-dimensional Kitaev model". In: *Physical Review B* 79.22 (2009), p. 224408. ISSN: 1098-0121, 1550-235X. DOI: 10.1103/PhysRevB.79.224408.

[216] H. T. Quan and W. H. Zurek. "Testing quantum adiabaticity with quench echo". In: *New Journal of Physics* 12.9 (2010), p. 093025. ISSN: 1367-2630. DOI: 10.1088/1367-2630/12/9/093025.

[217] Han-Chuan Kou and Peng Li. "Interferometry based on the quantum Kibble-Zurek mechanism". In: *Physical Review B* 106.18 (2022), p. 184301. ISSN: 2469-9950, 2469-9969. DOI: 10.1103/PhysRevB.106.184301.

[218] Daniel Rubin. "Exploring the Quantum Kibble-Zurek Mechanism by Passing the Critical Point Twice". Bachelor Thesis. 2024.

[219] Eduard Jürgen Braun. "Driving of a quantum many-body spin system of Rydberg atoms out of equilibrium". MA thesis. 2022.

[220] Xiao-Ye Xu et al. "Quantum Simulation of Landau-Zener Model Dynamics Supporting the Kibble-Zurek Mechanism". In: *Physical Review Letters* 112.3 (2014), p. 035701. DOI: 10.1103/PhysRevLett.112.035701.

[221] Nir Navon et al. "Critical dynamics of spontaneous symmetry breaking in a homogeneous Bose gas". In: *Science* 347.6218 (2015), pp. 167–170. DOI: 10.1126/science.1258676.

[222] Jin-Ming Cui et al. "Experimental Trapped-ion Quantum Simulation of the Kibble-Zurek dynamics in momentum space". In: *Scientific Reports* 6.1 (2016), p. 33381. ISSN: 2045-2322. DOI: 10.1038/srep33381.

[223] Ming Gong et al. "Simulating the Kibble-Zurek mechanism of the Ising model with a superconducting qubit system". In: *Scientific Reports* 6.1 (2016), p. 22667. ISSN: 2045-2322. DOI: 10.1038/srep22667.

[224] Adolfo del Campo et al. "Universal statistics of vortices in a newborn holographic superconductor: beyond the Kibble-Zurek mechanism". In: *Journal of High Energy Physics* 2021.6 (2021), p. 61. ISSN: 1029-8479. DOI: 10.1007/JHEP06(2021)061.

[225] Stefano Gherardini, Lorenzo Buffoni, and Nicolò Defenu. "Universal Defects Statistics with Strong Long-Range Interactions". In: *Physical Review Letters* 133.11 (2024). DOI: 10.1103/PhysRevLett.133.113401.

[226] Bin Yan et al. "Nonadiabatic Phase Transition with Broken Chiral Symmetry". In: *Physical Review Letters* 126.7 (2021), p. 070602. ISSN: 0031-9007, 1079-7114. DOI: 10.1103/PhysRevLett.126.070602.

[227] Jacek Dziarmaga. "Dynamics of a Quantum Phase Transition: Exact Solution of the Quantum Ising Model". In: *Physical Review Letters* 95.24 (2005), p. 245701. DOI: 10.1103/PhysRevLett.95.245701.

[228] Yan He and Hao Guo. "The boundary effects of transverse field Ising model". In: *Journal of Statistical Mechanics: Theory and Experiment* 2017.9 (2017), p. 093101. ISSN: 1742-5468. DOI: 10.1088/1742-5468/aa85b0.

[229] András Grabarits, Federico Balducci, and Adolfo Del Campo. "Driving a quantum phase transition at an arbitrary rate: Exact solution of the transverse-field Ising model". In: *Physical Review A* 111.4 (2025), p. 042207. ISSN: 2469-9926, 2469-9934. DOI: 10.1103/PhysRevA.111.042207.

[230] E.C.G. Stueckelberg. "Theorie der unelastischen Stösse zwischen Atomen". In: *Helvetica Physica Acta* 5.VI (1932), p. 369. ISSN: 0018-0238. DOI: 10.5169/seals-110177.

[231] S. N. Shevchenko, S. Ashhab, and Franco Nori. "Landau–Zener–Stückelberg interferometry". In: *Physics Reports* 492.1 (2010), pp. 1–30. ISSN: 0370-1573. DOI: 10.1016/j.physrep.2010.03.002.

[232] Oleh V. Ivakhnenko, Sergey N. Shevchenko, and Franco Nori. "Nonadiabatic Landau–Zener–Stückelberg–Majorana transitions, dynamics, and interference". In: *Physics Reports*. Nonadiabatic Landau-Zener-Stückelberg-Majorana transitions, dynamics, and interference 995 (2023), pp. 1–89. ISSN: 0370-1573. DOI: 10.1016/j.physrep.2022.10.002.

[233] Christopher Rackauckas and Qing Nie. "DifferentialEquations.jl–a performant and feature-rich ecosystem for solving differential equations in Julia". In: *Journal of Open Research Software* 5.1 (2017). DOI: 10.5334/jors.151.

[234] Daniel S. Fisher. "Critical behavior of random transverse-field Ising spin chains". In: *Physical Review B* 51.10 (1995), pp. 6411–6461. DOI: 10.1103/PhysRevB.51.6411.

[235] A. P. Young and H. Rieger. "Numerical study of the random transverse-field Ising spin chain". In: *Physical Review B* 53.13 (1996), pp. 8486–8498. ISSN: 0163-1829, 1095-3795. DOI: 10.1103/PhysRevB.53.8486.

[236] Jacek Dziarmaga. "Dynamics of a quantum phase transition in the random Ising model: Logarithmic dependence of the defect density on the transition rate". In: *Physical Review B* 74.6 (2006), p. 064416. ISSN: 1098-0121, 1550-235X. DOI: 10.1103/PhysRevB.74.064416.

[237] Sebastian Krämer et al. "QuantumOptics.jl: A Julia framework for simulating open quantum systems". In: *Computer Physics Communications* 227 (2018), pp. 109–116. ISSN: 0010-4655. DOI: 10.1016/j.cpc.2018.02.004.

[238] Jeff Bezanson et al. "Julia: A fresh approach to numerical computing". In: *SIAM Review* 59.1 (2017), pp. 65–98. DOI: 10.1137/141000671.

[239] M. Schechter, P. C. E. Stamp, and N. Laflorencie. "Quantum spin glass in anisotropic dipolar systems". In: *Journal of Physics: Condensed Matter* 19.14 (2007), p. 145218. ISSN: 0953-8984, 1361-648X. DOI: 10.1088/0953-8984/19/14/145218.

[240] C. Ancona-Torres et al. "Quantum and Classical Glass Transitions in $LiHo_xY_{1-x}F_4$". In: *Physical Review Letters* 101.5 (2008), p. 057201. DOI: 10.1103/PhysRevLett.101.057201.

[241] Na Xu et al. "Dynamic scaling in the two-dimensional Ising spin glass with normal-distributed couplings". In: *Physical Review E* 96.5 (2017), p. 052102. ISSN: 2470-0045, 2470-0053. DOI: 10.1103/PhysRevE.96.052102.

[242] Harald Günther. *NMR spectroscopy: basic principles, concepts, and applications in chemistry*. Third, completely revised and updated edition. Weinheim: Wiley-VCH Verlag GmbH & Co. KGaA, 2013. ISBN: 978-3-527-33004-1.

[243] N. Šibalić et al. "ARC: An open-source library for calculating properties of alkali Rydberg atoms". In: *Computer Physics Communications* 220 (2017), pp. 319–331. ISSN: 0010-4655. DOI: 10.1016/j.cpc.2017.06.015.

[244] P. L. Stanwix. "Coherence of nitrogen-vacancy electronic spin ensembles in diamond". In: *Physical Review B* 82.20 (2010). DOI: 10.1103/PhysRevB.82.201201.

[245] R. Harris et al. "Phase transitions in a programmable quantum spin glass simulator". In: *Science* 361.6398 (2018), pp. 162–165. DOI: 10.1126/science.aat2025.

[246] D. Linnemann et al. "Quantum-Enhanced Sensing Based on Time Reversal of Nonlinear Dynamics". In: *Physical Review Letters* 117.1 (2016), p. 013001. DOI: 10.1103/PhysRevLett.117.013001.

[247] Kevin A. Gilmore et al. "Quantum-enhanced sensing of displacements and electric fields with two-dimensional trapped-ion crystals". In: *Science* 373.6555 (2021), pp. 673–678. DOI: 10.1126/science.abi5226.

[248] Simone Colombo et al. “Time-reversal-based quantum metrology with many-body entangled states”. In: *Nature Physics* 18.8 (2022), pp. 925–930. ISSN: 1745-2481. DOI: 10.1038/s41567-022-01653-5.

[249] Matthias Lotze. “Effects of second order quantum corrections on a time reversal protocol for a dipolar many-body system”. Bachelor Thesis. 2025.

[250] Braemer, Adrian. *SpinModels.jl*. URL: https://github.com/abraemer/SpinModels.jl. 2025.

[251] Alfréd Rényi. “On a One-Dimensional Problem Concerning Random Space-Filling”. In: *Publ. Math. Inst. Hung. Acad. Sci.* 3 (1958), pp. 109–127.

[252] Maksym Serbyn, Z. Papić, and Dmitry A. Abanin. “Criterion for Many-Body Localization-Delocalization Phase Transition”. In: *Physical Review X* 5.4 (2015), p. 041047. DOI: 10.1103/PhysRevX.5.041047.

[253] Tomaž Prosen, Thomas H. Seligman, and Marko Žnidarič. “Theory of Quantum Loschmidt Echoes”. In: *Progress of Theoretical Physics Supplement* 150 (2003), pp. 200–228. ISSN: 0375-9687. DOI: 10.1143/PTPS.150.200.

[254] Arseni Goussev et al. “Loschmidt echo”. In: *Scholarpedia* 7.8 (2012), p. 11687. ISSN: 1941-6016. DOI: 10.4249/scholarpedia.11687.

[255] Utkarsh Mishra, R. Jafari, and Alireza Akbari. “Disordered Kitaev chain with long-range pairing: Loschmidt echo revivals and dynamical phase transitions”. In: *Journal of Physics A: Mathematical and Theoretical* 53.37 (2020), p. 375301. ISSN: 1751-8121. DOI: 10.1088/1751-8121/ab97de.

[256] B. V. Fine et al. “Absence of exponential sensitivity to small perturbations in nonintegrable systems of spins 1/2”. In: *Physical Review E* 89.1 (2014), p. 012923. DOI: 10.1103/PhysRevE.89.012923.

[257] Evert P. L. van Nieuwenburg, Sebastian D. Huber, and R. Chitra. “Single spin probe of many-body localization”. In: *Physical Review B* 94.18 (2016), p. 180202. DOI: 10.1103/PhysRevB.94.180202.

[258] David J. Griffiths and Darrell F. Schroeter. *Introduction to quantum mechanics*. Third edition. Cambridge ; New York, NY: Cambridge University Press, 2018. ISBN: 978-1-107-18963-8.

[259] Luca Schmid, Charlotte Muth, and Laurent Schmalen. *Uncertainty Propagation in the Fast Fourier Transform*. arXiv:2504.10136 [cs]. 2025. DOI: 10.48550/arXiv.2504.10136.

[260] Luca Pezzé and Augusto Smerzi. "Entanglement, Nonlinear Dynamics, and the Heisenberg Limit". In: *Physical Review Letters* 102.10 (2009), p. 100401. DOI: 10.1103/PhysRevLett.102.100401.

[261] Philipp Hyllus et al. "Fisher information and multiparticle entanglement". In: *Physical Review A* 85.2 (2012), p. 022321. DOI: 10.1103/PhysRevA.85.022321.

[262] Géza Tóth. "Multipartite entanglement and high-precision metrology". In: *Physical Review A* 85.2 (2012), p. 022322. DOI: 10.1103/PhysRevA.85.022322.

[263] Pasquale Calabrese and Andrea Gambassi. "Ageing properties of critical systems". In: *Journal of Physics A: Mathematical and General* 38.18 (2005), R133. ISSN: 0305-4470. DOI: 10.1088/0305-4470/38/18/R01.

[264] L. F. Cugliandolo and J. Kurchan. "Analytical solution of the off-equilibrium dynamics of a long-range spin-glass model". In: *Physical Review Letters* 71.1 (1993), pp. 173–176. ISSN: 0031-9007. DOI: 10.1103/PhysRevLett.71.173.

[265] L. F. Cugliandolo and J. Kurchan. "On the out-of-equilibrium relaxation of the Sherrington-Kirkpatrick model". In: *Journal of Physics A: Mathematical and General* 27.17 (1994), p. 5749. ISSN: 0305-4470. DOI: 10.1088/0305-4470/27/17/011.

[266] Gérard Ben Arous, Amir Dembo, and Alice Guionnet. "Cugliandolo-Kurchan equations for dynamics of Spin-Glasses". In: *Probability Theory and Related Fields* 136.4 (2006), pp. 619–660. ISSN: 1432-2064. DOI: 10.1007/s00440-005-0491-y.

[267] G. M. Schütz and S. Trimper. "Relaxation and aging in quantum spin systems". In: *Europhysics Letters* 47.2 (1999), p. 164. ISSN: 0295-5075. DOI: 10.1209/epl/i1999-00367-8.

[268] Sebastian Von Ohr, Markus Manssen, and Alexander K. Hartmann. "Aging in the three-dimensional random-field Ising model". In: *Phys. Rev. E* 96.1 (2017), p. 013315. ISSN: 2470-0045, 2470-0053. DOI: 10.1103/PhysRevE.96.013315.

[269] Henrik Christiansen et al. "Aging in the Long-Range Ising Model". In: *Physical Review Letters* 125.18 (2020), p. 180601. DOI: 10.1103/PhysRevLett.125.180601.

[270] Jad C. Halimeh and Mohammad F. Maghrebi. "Quantum aging and dynamical universality in the long-range $O(N \to \infty)$ model". In: *Physical Review E* 103.5 (2021), p. 052142. DOI: 10.1103/PhysRevE.103.052142.

[271] G. G. Kenning et al. “Observation of critical scaling in spin glasses below Tc using thermoremanent magnetization”. In: *Frontiers in Physics* 12 (2024). ISSN: 2296-424X. DOI: 10.3389/fphy.2024.1443298.

[272] L. C. E. Struik. *Physical aging in amorphous polymers and other materials*. Amsterdam ; New York : New York: Elsevier Scientific Pub. Co. ; distributors for the U.S. and Canada, Elsevier North-Holland, 1978. ISBN: 978-0-444-41655-1.

[273] Bernd Rinn, Philipp Maass, and Jean-Philippe Bouchaud. “Hopping in the glass configuration space: Subaging and generalized scaling laws”. In: *Physical Review B* 64.10 (2001), p. 104417. DOI: 10.1103/PhysRevB.64.104417.

[274] Henrik Christiansen et al. *Finite-Size Effects in Aging can be Interpreted as Sub-Aging*. arXiv:2501.04843 [cond-mat]. 2025. DOI: 10.48550/arXiv.2501.04843.

[275] C. Djurberg, K. Jonason, and P. Nordblad. “Magnetic relaxation phenomena in a CuMn spin glass”. In: *The European Physical Journal B - Condensed Matter and Complex Systems* 10.1 (1999), pp. 15–21. ISSN: 1434-6036. DOI: 10.1007/s100510050824.

[276] Qiang Zhai, Raymond L. Orbach, and Deborah L. Schlagel. “Evidence for temperature chaos in spin glasses”. In: *Physical Review B* 105.1 (2022), p. 014434. DOI: 10.1103/PhysRevB.105.014434.

[277] Malay Bandyopadhyay and Sushanta Dattagupta. “Memory in nanomagnetic systems: Superparamagnetism versus spin-glass behavior”. In: *Physical Review B* 74.21 (2006), p. 214410. DOI: 10.1103/PhysRevB.74.214410.

[278] M. Sasaki et al. “Aging and memory effects in superparamagnets and superspin glasses”. In: *Physical Review B* 71.10 (2005), p. 104405. ISSN: 1098-0121, 1550-235X. DOI: 10.1103/PhysRevB.71.104405.

[279] I. Paga et al. “Superposition principle and nonlinear response in spin glasses”. In: *Physical Review B* 107.21 (2023), p. 214436. DOI: 10.1103/PhysRevB.107.214436.

[280] Andre Neubauer. *DFT - Diskrete Fourier-Transformation: Elementare Einführung*. Wiesbaden: Vieweg+Teubner Verlag, 2012. ISBN: 978-3-8348-1997-0.

[281] Yan Xin and Xiaogang Su. *Linear regression analysis: theory and computing*. Singapore Hackensack, N.J: World Scientific Pub. Co, 2009. ISBN: 978-981-283-411-9.

[282] Arnab Sen and R. Moessner. "Topological Spin Glass in Diluted Spin Ice". In: *Physical Review Letters* 114.24 (2015), p. 247207. DOI: 10.1103/PhysRevLett.114.247207.

[283] V. Russier and J.-J. Alonso. "Phase diagram of a three-dimensional dipolar Ising model with textured Ising axes". In: *Journal of Physics: Condensed Matter* 32.13 (2020), p. 135804. ISSN: 0953-8984, 1361-648X. DOI: 10.1088/1361-648X/ab6047.

[284] J. S. Waugh, L. M. Huber, and U. Haeberlen. "Approach to High-Resolution nmr in Solids". In: *Physical Review Letters* 20.5 (1968), pp. 180–182. ISSN: 0031-9007. DOI: 10.1103/PhysRevLett.20.180.

[285] U. Haeberlen and J. S. Waugh. "Coherent Averaging Effects in Magnetic Resonance". In: *Physical Review* 175.2 (1968), pp. 453–467. DOI: 10.1103/PhysRev.175.453.

[286] Jochen Braumüller et al. "Probing quantum information propagation with out-of-time-ordered correlators". In: *Nature Physics* 18.2 (2022), pp. 172–178. ISSN: 1745-2481. DOI: 10.1038/s41567-021-01430-w.

[287] Zi-Hang Zhu et al. *Probing false vacuum decay on a cold-atom gauge-theory quantum simulator*. arXiv:2411.12565 [cond-mat]. 2024. DOI: 10.48550/arXiv.2411.12565.

[288] Vladislav Gavryusev. "Imaging of Rydberg Impurities in an Ultracold Atomic Gas". PhD thesis. 2016.

[289] Annika Tebben. "Rydberg Electromagnetically Induced Transparency - A vanishing linear response, resonances, and a stationary Rydberg polariton". PhD thesis. 2021.

[290] E. L. Raab et al. "Trapping of Neutral Sodium Atoms with Radiation Pressure". In: *Physical Review Letters* 59.23 (1987), pp. 2631–2634. ISSN: 0031-9007. DOI: 10.1103/PhysRevLett.59.2631.

[291] Steven Chu et al. "Experimental Observation of Optically Trapped Atoms". In: *Physical Review Letters* 57.3 (1986), pp. 314–317. ISSN: 0031-9007. DOI: 10.1103/PhysRevLett.57.314.

[292] William Happer. "Optical Pumping". In: *Reviews of Modern Physics* 44.2 (1972), pp. 169–249. ISSN: 0034-6861. DOI: 10.1103/RevModPhys.44.169.

[293] Clarence Zener. “Non-adiabatic crossing of energy levels”. In: *Proceedings of the Royal Society of London. Series A, Containing Papers of a Mathematical and Physical Character* 137.833 (1932), pp. 696–702. DOI: 10.1098/rspa.1932.0165.

[294] Harold J. Metcalf and Peter Van Der Straten. *Laser Cooling and Trapping*. Ed. by R. Stephen Berry et al. Graduate Texts in Contemporary Physics. New York, NY: Springer, 1999. ISBN: 978-0-387-98728-6. DOI: 10.1007/978-1-4612-1470-0.

[295] S. J. M. Kuppens et al. “Loading an optical dipole trap”. In: *Physical Review A* 62.1 (2000), p. 013406. ISSN: 1050-2947, 1094-1622. DOI: 10.1103/PhysRevA.62.013406.

[296] Georg Günter. “Interfacing Rydberg atoms with light and observing their interaction driven dynamics”. PhD thesis. 2014.

[297] K. Dieckmann et al. “Two-dimensional magneto-optical trap as a source of slow atoms”. In: *Physical Review A* 58.5 (1998), pp. 3891–3895. ISSN: 1050-2947, 1094-1622. DOI: 10.1103/PhysRevA.58.3891.

[298] Wolfgang Petrich et al. “Behavior of atoms in a compressed magneto-optical trap”. In: *JOSA B* 11.8 (1994), pp. 1332–1335. ISSN: 1520-8540. DOI: 10.1364/JOSAB.11.001332.

[299] Wolfgang Ketterle et al. “High densities of cold atoms in a *dark* spontaneous-force optical trap”. In: *Physical Review Letters* 70.15 (1993), pp. 2253–2256. ISSN: 0031-9007. DOI: 10.1103/PhysRevLett.70.2253.

[300] C. G. Townsend et al. “High-density trapping of cesium atoms in a dark magneto-optical trap”. In: *Physical Review A* 53.3 (1996), pp. 1702–1714. ISSN: 1050-2947, 1094-1622. DOI: 10.1103/PhysRevA.53.1702.

[301] Rudolf Grimm, Matthias Weidemüller, and Yurii B. Ovchinnikov. “Optical Dipole Traps for Neutral Atoms”. In: *Advances In Atomic, Molecular, and Optical Physics* 42 (2000), pp. 95–170. DOI: 10.1016/S1049-250X(08)60186-X.

[302] Annika Tebben. “Resonant Enhancement of the Optical Nonlinearity in a Rydberg Gas”. MA thesis. 2018.

[303] M. Saffman, T. G. Walker, and K. Mølmer. “Quantum information with Rydberg atoms”. In: *Reviews of Modern Physics* 82.3 (2010), pp. 2313–2363. ISSN: 0034-6861, 1539-0756. DOI: 10.1103/RevModPhys.82.2313.

[304] M Saffman. "Quantum computing with atomic qubits and Rydberg interactions: progress and challenges". In: *Journal of Physics B: Atomic, Molecular and Optical Physics* 49.20 (2016), p. 202001. ISSN: 0953-4075. DOI: 10.1088/0953-4075/49/20/202001.

[305] Antoine Browaeys and Thierry Lahaye. "Many-body physics with individually controlled Rydberg atoms". In: *Nature Physics* 16.2 (2020), pp. 132–142. ISSN: 1745-2481. DOI: 10.1038/s41567-019-0733-z.

[306] Y. Chew et al. "Ultrafast energy exchange between two single Rydberg atoms on a nanosecond timescale". In: *Nature Photonics* 16.10 (2022), pp. 724–729. ISSN: 1749-4893. DOI: 10.1038/s41566-022-01047-2.

[307] Th. Förster. "Zwischenmolekulare Energiewanderung und Fluoreszenz". In: *Annalen der Physik* 437.1-2 (1948), pp. 55–75. ISSN: 1521-3889. DOI: 10.1002/andp.19484370105.

[308] Sergey Bravyi, David P. DiVincenzo, and Daniel Loss. "Schrieffer–Wolff transformation for quantum many-body systems". In: *Annals of Physics* 326.10 (2011), pp. 2793–2826. ISSN: 0003-4916. DOI: 10.1016/j.aop.2011.06.004.

[309] I Lindgren. "The Rayleigh-Schrodinger perturbation and the linked-diagram theorem for a multi-configurational model space". In: *Journal of Physics B: Atomic and Molecular Physics* 7.18 (1974), pp. 2441–2470. ISSN: 0022-3700. DOI: 10.1088/0022-3700/7/18/010.

[310] V. Kvasnička. "Construction of model hamiltonians in framework of Rayleigh-Schrödinger perturbation theory". In: *Czechoslovak Journal of Physics B* 24.6 (1974), pp. 605–615. ISSN: 1572-9486. DOI: 10.1007/BF01587295.

[311] Wenhui Li et al. "Millimeter-wave spectroscopy of cold Rb Rydberg atoms in a magneto-optical trap: Quantum defects of the ns , np , and nd series". In: *Physical Review A* 67.5 (2003), p. 052502. ISSN: 1050-2947, 1094-1622. DOI: 10.1103/PhysRevA.67.052502.

[312] K. Afrousheh et al. "Determination of the ^{85}Rb ng -series quantum defect by electric-field-induced resonant energy transfer between cold Rydberg atoms". In: *Physical Review A* 74.6 (2006), p. 062712. ISSN: 1050-2947, 1094-1622. DOI: 10.1103/PhysRevA.74.062712.

[313] Jianing Han et al. "Rb nf quantum defects from millimeter-wave spectroscopy of cold ^{85}Rb Rydberg atoms". In: *Physical Review A* 74.5 (2006), p. 054502. ISSN: 1050-2947, 1094-1622. DOI: 10.1103/PhysRevA.74.054502.

[314] Markus Mack et al. “Measurement of absolute transition frequencies of ^{87}Rb to nS and nD Rydberg states by means of electromagnetically induced transparency”. In: *Physical Review A* 83.5 (2011), p. 052515. ISSN: 1050-2947, 1094-1622. DOI: 10.1103/PhysRevA.83.052515.

[315] Constantine E. Theodosiou. “Lifetimes of alkali-metal—atom Rydberg states”. In: *Physical Review A* 30.6 (1984), pp. 2881–2909. DOI: 10.1103/PhysRevA.30.2881.

[316] M. Marinescu. “Dispersion coefficients for alkali-metal dimers”. In: *Physical Review A* 49.2 (1994), pp. 982–988. DOI: 10.1103/PhysRevA.49.982.

[317] M. Pawlak. “Highly excited Rydberg states of a rubidium atom: Theory versus experiments”. In: *Physical Review A* 89.4 (2014). DOI: 10.1103/PhysRevA.89.042506.

[318] Johannes Deiglmayr. “Observation of Dipole-Quadrupole Interaction in an Ultracold Gas of Rydberg Atoms”. In: *Physical Review Letters* 113.19 (2014). DOI: 10.1103/PhysRevLett.113.193001.

[319] Simon Hollerith and Johannes Zeiher. “Rydberg Macrodimers: Diatomic Molecules on the Micrometer Scale”. In: *The Journal of Physical Chemistry A* 127.18 (2023), pp. 3925–3939. ISSN: 1089-5639, 1520-5215. DOI: 10.1021/acs.jpca.2c08454.

[320] Kazuo Takayanagi. “Effective interaction in the Rayleigh–Schrödinger perturbation theory”. In: *Annals of Physics* 350 (2014), pp. 501–532. ISSN: 00034916. DOI: 10.1016/j.aop.2014.08.002.

[321] Yoshio Kuramoto. “Perturbation Theory and Effective Hamiltonian”. In: *Quantum Many-Body Physics: A Perspective on Strong Correlations*. Ed. by Yoshio Kuramoto. Tokyo: Springer Japan, 2020, pp. 1–11. ISBN: 978-4-431-55393-9. DOI: 10.1007/978-4-431-55393-9_1.

[322] Albert Messiah. *Quantum mechanics. Vol. 2*. OCLC: 779108599. Amsterdam: North-Holland, 1961. ISBN: 978-0-7204-0043-4.

[323] J. J. Sakurai and Jim Napolitano. *Modern Quantum Mechanics*. 3rd ed. Cambridge University Press, 2020. ISBN: 978-1-108-47322-4. DOI: 10.1017/9781108587280.

[324] Eduard Jürgen Braun. “Creation and relaxation dynamics of disordered spin spirals realized with ^{87}Rb-Rydberg atoms in a constant gradient electric field”. Bachelor Thesis. 2020.

[325] Neill Lambert et al. “QuTiP 5: The Quantum Toolbox in Python”. In: *Physics Reports* 1153 (2026), pp. 1–62. ISSN: 0370-1573. DOI: https://doi.org/10.1016/j.physrep.2025.10.001.

[326] Donald W. Booth, Joshua Isaacs, and M. Saffman. “Reducing the sensitivity of Rydberg atoms to dc electric fields using two-frequency ac field dressing”. In: *Physical Review A* 97.1 (2018), p. 012515. DOI: 10.1103/PhysRevA.97.012515.

[327] J. C. Bohorquez et al. “Reducing Rydberg-state dc polarizability by microwave dressing”. In: *Physical Review A* 108.2 (2023), p. 022805. DOI: 10.1103/PhysRevA.108.022805.

[328] Vincent Lienhard et al. *Generation of Motional Squeezed States for Neutral Atoms in Optical Tweezers*. arXiv:2505.10092 [physics]. 2025. DOI: 10.48550/arXiv.2505.10092.

[329] L. C. Biedenharn and James D. Louck. *Angular momentum in quantum physics: theory and application*. Encyclopedia of mathematics and its applications ; Section, Mathematics of physics v. 8. Cambridge University Press, 1984. ISBN: 978-0-521-30228-9.

[330] Austin G. Fowler et al. “Surface codes: Towards practical large-scale quantum computation”. In: *Physical Review A* 86.3 (2012), p. 032324. ISSN: 1050-2947, 1094-1622. DOI: 10.1103/PhysRevA.86.032324.

[331] Mark S. Rudner and Netanel H. Lindner. “Band structure engineering and non-equilibrium dynamics in Floquet topological insulators”. In: *Nature Reviews Physics* 2.5 (2020), pp. 229–244. ISSN: 2522-5820. DOI: 10.1038/s42254-020-0170-z.

[332] Mark S. Rudner and Netanel H. Lindner. *The Floquet Engineer’s Handbook*. arXiv:2003.08252 [cond-mat, physics:quant-ph]. 2020.

[333] Daniel Zeuch et al. “Exact Rotating Wave Approximation”. In: *Annals of Physics* 423 (2020), p. 168327. ISSN: 00034916. DOI: 10.1016/j.aop.2020.168327.

Acknowledgements

An dieser Stelle möchte ich all denen meinen Dank aussprechen, ohne deren Unterstützung diese Arbeit nicht möglich gewesen wäre:

... MATTHIAS WEIDEMÜLLER, meinem Betreuer und Mentor, für die bereichernde Zeit in seiner Gruppe, in der ich sowohl fachlich als auch persönlich reifen konnte. Besonders danke ich dir für die inspirierenden Diskussionen zu Rydberg-Atomen und Spingläsern sowie für die Ermöglichung meines Auslandsaufenthalts.

... MARKUS OBERTHALER, der nicht nur das Zweitgutachten dieser Arbeit übernommen hat, sondern mich bereits im Bachelorstudium durch seine Einführungsvorlesung in die Quantenmechanik für die Forschung begeistern konnte, sowie den weiteren Mitgliedern des Prüfungskomitees TILMAN ENSS und JÖRG EVERS.

... the RYDBERG TEAM, for the great times we shared while working together. First and foremost, I want to thank GERHARD ZÜRN, who always had not only the perfect solution but also the right tools for every electronics and optics problem. I greatly enjoyed our physics discussions and the positive atmosphere we maintained together. I also want to thank MENY MENASHES for the many engaging discussions on how to tackle one experimental problem after another. Moreover, I am grateful to my fellow doctoral students: SEBASTIAN GEIER, it was a pleasure running the lab together, and I will never forget our little "adventure" in Arizona; and PRAN BORA MAHARSHI, thank you for the inspiring discussions we had. I am especially grateful to all the Bachelor, Master, and internship students I had the privilege to work with, namely MAXIMILIAN MÜLLENBACH, DILLEN LEE, MORITZ HORNUNG, AMAR BELLAHSENE, REET MHASKE, BIRTE BEIER, DANIEL RUBIN, MARGAUX CARTIER, and MATTHIAS LOTZE. Your dedication, curiosity, and enthusiasm have been truly inspiring, and I wish you all the best for your future. Finally, I want to thank all the other Bachelor and Master students, LORENZ LUGER, COLIN HUNG, BERTHOLD HELBER, KAREN WADENPFUHL, and FLORIAN PLASWIG, for contributing to a collaborative and stimulating research environment.

... NIKLAS EULER, ADRIAN BRAEMER, and MARTIN GÄRTTNER, for your support with the numerics of spin systems and for introducing me to working with a CPU cluster. It was a pleasure discussing localization with you.

... the MIXTURES TEAM, namely TOBIAS KROM and MICHAEL RAUTENBERG, for the great discussions on spin echoes we had during lunch, and KILIAN WELZ, it was a fascinating journey exploring different CSS styles for the homepage with you.

... the DIGITAL TWINS team, namely CARLOS BRANDL and ANNA NITSCHKE; I greatly enjoyed the time we spent together and the pleasant atmosphere within the team.

... ADRIAN BRAEMER, TITUS FRANZ, MARTIN GÄRTTNER, SYLVAIN DE LÉSÉLEUC, MARKUS MÜLLER and THOMAS GASENZER for collaborating with us on the topics of this thesis. I have learned a lot from our joint work and from our insightful discussions, which shaped this work considerably.

... JOHANNES MÖGERLE, SEBASTIAN WEBER, and HENRI MENKE; collaborating with you on the *PairInteraction* project was a real pleasure. I will always appreciate the many hours we spent together demystifying CMake under Windows, as well as the invaluable lesson you taught me about the difference between "coding" and "software development".

... KENJI OHMORI SENSEI and SYLVAIN DE LÉSÉLEUC, for giving me the opportunity to work with them and for hosting me at the IMS in Japan. I am also grateful to YEELAI CHEW SAN for introducing me to the ultrafast Rydberg tweezer platform. I would like to thank TAKAFUMI TOMITA SAN, TAKUYA MATSUBARA SAN, HIKARU TAMURA SAN, and TITOUAN JAUNET-LAHARY for creating such a great atmosphere in the group and for the valuable scientific discussions. I truly appreciate all that I learned from you about pulsed laser generation. Furthermore, I wish to express my gratitude to all students and postdocs at the IMS: VIKAS SINGH CHAUHAN, MAHESH T. P., ROBIN KOCIK, OMAR KECIR, SAPNA HASSANALY, GENKI WATANABE SAN, JORGE MAURICIO, "BEAM" KITTISAK KETAIAM, ARNAB MAITY, KARTHIKEYAN GANESAN, "BEE" PHATWARACH SIRIWORAKOONCHAI, ISALINE DUPERON, AXEL-UGO LERICHE, MATHIS ROUSSEL, and AITO TANAKA SAN for the wonderful time we spent together, the inspiring discussions we had, and for introducing me to the rich and beautiful Japanese (and often additionally also to the French) culture.

... CLAUDIA KRÄMER, FERMAN ALKASARI, ALEXANDRA HOLTEN, IDA PACHOMOWA, FRANZISKA SCHNEYDER, DIANA HORNECK und GESINE HEINZELMANN für ihre stets zuverlässige Unterstützung und kompetente Beratung bei allen administrativen Prozessen, stets mit Sorgfalt und Engagement, unabhängig von ihrem

Umfang oder Schwierigkeitsgrad. Ich danke Ihnen herzlich für Ihre engagierte Arbeit.

... dem KONSTRUKTIONS-TEAM für die tatkräftige Unterstützung beim Druck der Poster sowie der MECHANISCHEN WERKSTATT und der ELEKTRONISCHEN WERKSTATT für die wertvolle Hilfe bei der Fertigung elektronischer Schaltungen und ihrer Gehäuse. Besonders danken möchte ich VENELIN ANGELOV für die ausführliche Einführung in Sample-and-Hold-Schaltungen, ESTEBAN RUBIO für die Unterstützung bei unserer allseits beliebten Laser-Indication-Box und OLIVER VORBACH sowohl für den fachlichen Rat als auch für den persönlichen Austausch. Ihre Expertise, Geduld und Hilfsbereitschaft haben die Arbeit im Labor erheblich erleichtert und bereichert.

... MAXIMILIAN MÜLLENBACH, GERHARD ZÜRN, SYLVAIN DE LÉSÉLEUC, EUGEN DIZER, JOHANNES MÖGERLE, MATTHIAS LOTZE, and MENY MENASHES for their careful proofreading of the manuscript.

... the DEUTSCHE FORSCHUNGSGEMEINSCHAFT (DFG, German Research Foundation) and the international Max Planck Research School for Quantum Dynamics in Physics, Chemistry and Biology (IMPRS-QD) for their financial and non-financial support during my thesis. I would also like to thank the Collaborative Research Center SFB 1225 (ISOQUANT), the DFG priority program GIRYD 1929, and the Horizon Europe programme HORIZON-CL4-2022-QUANTUM-02-SGA via project 101113690 (PASQUANS2.1), as well as the Heidelberg Center for Quantum Dynamics (CQD) and the state of Baden-Württemberg through bwHPC and the DFG via grant INST 35/1597-1 FUGG (Helix cluster).

... meinen FREUNDEN für eine schöne und unvergessliche Studien- und Promotionszeit. Besonders danken möchte ich FELIX HERZOG für sein offenes Ohr, seine wertvollen Ratschläge und unsere vielen interessanten Gespräche über Gott und die Welt – im wahrsten Sinne des Wortes. Außerdem gilt mein Dank ANNE VON LÖBEN und WERNER BORNEMANN-VON LÖBEN für ihre Unterstützung in jeder Hinsicht während meiner Promotion.

... meinen Eltern JOHANN BRAUN und FILORETA-MINA BRAUN, die mich meinen ganzen Lebensweg bis zu diesem Punkt immer unterstützt und begleitet haben, durch gute und auch durch schwere Zeiten. Vielen Dank, dass ihr immer an mich geglaubt und mich unterstützt habt.